Master's thesis

NTNU
Norwegian University of Science and Technology
Faculty of Information Technology and Electrical Engineering
Department of Electric Power Engineering

Claysius Dewanata Widjaja

Impedance Modelling and Stability Analysis of Virtual Synchronous Machine-based Wind Energy Conversion System

Master's thesis in Renewable Energy in the Marine Environment
Supervisor: Mohammad Amin
June 2022

NTNU
Norwegian University of Science and Technology

Claysius Dewanata Widjaja

Impedance Modelling and Stability Analysis of Virtual Synchronous Machine-based Wind Energy Conversion System

Master's thesis in Renewable Energy in the Marine Environment
Supervisor: Mohammad Amin
June 2022

Norwegian University of Science and Technology
Faculty of Information Technology and Electrical Engineering
Department of Electric Power Engineering

NTNU
Norwegian University of
Science and Technology

Summary

As the number of power electronics converters increases due to the increase in variable renewable energy, it has a significant impact on the dynamics and stability of power systems. Since power systems are traditionally dominated by synchronous machine-based physics and control, the dynamics are also determined by the response of the dominant synchronous machine. With how power converters are more interconnected to the grid, the conventional modelling for power system dynamics is not enough to capture all the desired phenomena available in power systems.

This thesis will examine the converter-driven stability of a Synchronverter-based wind energy conversion system (WECS) through a state-of-the-art stability assessment method: impedance-based stability analysis. The three main objectives of the thesis are: *to derive the impedance model of WECS analytically; comparing the accuracy of the derived analytical model with the frequency sweep model; to perform the converter-driven stability analysis of WECS interconnection to an AC weak grid by implementing the impedance-based stability analysis*.

A Synchronverter-based WECS, which is a type IV wind turbine connected to an infinite bus, will be modelled in Simulink. Both converter controls will use Synchronverter algorithms where Rotor Side Control will control the DC link voltage and Grid Side Control will control the active and reactive power transmitted to the grid. The model will be validated against the Texas Panhandle Wind Farm scenario.

The impedance model of the Synchronverter-based WECS will be derived analytically using the mathematical model of Synchronverter. The accuracy of the impedance obtained will be compared with the impedance obtained through the Single-Tone Sinusoidal Frequency Sweep in Simulink. The impedances will be presented in the Modified Sequence Domain.

Both impedances obtained will be used to assess the converter-driven stability of the WECS for weak AC grid interconnection. Generalized Nyquist Criterion (GNC) will be used to examine the systems' open-loop-pole characteristics. Sensitivity studies will be performed, where three parameters of the system will be varied: *Short Circuit Ratio (SCR); virtual attenuation; and virtual inertia*.

The results show that variation of SCR affects the stability of the system to a large extent, and that virtual damping and virtual inertia do not really affect the converter-driven stability of WECS, especially for weak grid interconnection. The simple impedance model derived also performed satisfactorily for the converter-driven stability assessment since it captures all the desired stability phenomena.

The simulation results also managed to show that the impedance-based technique combined with GNC is a powerful tool for assessing the power system's stability in the form of BIBO stability.

Sammendrag

Ettersom antallet kraftelektronikkomformere øker på grunn av økningen i variabel fornybar energi, har det en betydelig innvirkning på dynamikken og stabiliteten til kraftsystemer. Siden kraftsystemer tradisjonelt domineres av synkron maskinbasert fysikk og kontroll, bestemmes dynamikken også av responsen til den dominerende synkronmaskinen. Med hvordan kraftomformere er mer sammenkoblet med nettet, er ikke den konvensjonelle modelleringen for kraftsystemdynamikk nok til å fange opp alle de ønskede fenomenene som er tilgjengelige i kraftsystemer.

Denne oppgaven vil undersøke den omformerdrevne stabiliteten til et Synchronverter-basert vindenergikonverteringssystem (WECS) gjennom en state-of-the-art stabilitetsvurderingsmetode: impedansbasert stabilitetsanalyse. De tre hovedmålene med oppgaven er: å utlede impedansmodellen til WECS analytisk; å sammenligne nøyaktigheten til den avledede analytiske modellen med frekvenssveip-modellen; å utføre den omformerdrevne stabilitetsanalysen av WECS-sammenkobling til et AC-svak nett ved å implementere den impedansbaserte stabilitetsanalysen.

En Synchronverter-basert WECS, som er en type IV vindturbin koblet til en uendelig buss, skal modelleres i Simulink. Begge omformerkontrollene vil bruke Synchronverter-algoritmer der Rotor Side Control vil kontrollere DC-linkspenningen og Grid Side Control vil kontrollere den aktive og reaktive kraften som overføres til nettet. Modellen vil bli validert mot Texas Panhandle Wind Farm-scenario.

Impedansmodellen til Synchronverter-baserte WECS vil bli utledet analytisk ved å bruke den matematiske modellen til Synchronverter. Nøyaktigheten til impedansen som oppnås vil bli sammenlignet med impedansen oppnådd gjennom Single-Tone Sinusoidal Frequency Sweep i Simulink. Impedansene vil bli presentert i Modified Sequence Domain.

Begge impedansene som oppnås vil bli brukt til å vurdere den omformerdrevne stabiliteten til WECS for svak AC-nettforbindelse. Generalisert Nyquist Criterion (GNC) vil bli brukt for å undersøke systemenes åpen-sløyfe-polkarakteristikk. Sensitivitetsstudier vil bli utført, hvor tre parametere til systemet vil varieres: Short Circuit Ratio (SCR); virtuell demping; og virtuell treghet.

Resultatene viser at variasjon av SCR påvirker stabiliteten til systemet i stor grad, og at virtuell demping og virtuell treghet egentlig ikke påvirker den omformerdrevne stabiliteten til WECS, spesielt for svak nettsammenkobling. Den enkle impedansmodellen avledet utførte også tilfredsstillende for den omformerdrevne stabilitetsvurderingen siden den fanger opp alle de ønskede stabilitetsfenomenene.

Simuleringsresultatene klarte også å vise at den impedansbaserte teknikken kombinert med GNC er et kraftig verktøy for å vurdere kraftsystemets stabilitet i form av BIBO-stabilitet.

Preface

Praise and gratitude to God Almighty for His blessings and grace which allows me to complete this thesis, titled 'Impedance Modelling and Stability Analysis of Virtual Synchronous Machine-based Wind Energy Conversion System'. This thesis is submitted as a requirement to obtain the degree of Master of Science in Renewable Energy in the Marine Environment, organised by Department of Electric Power Engineering at the Norwegian University of Science and Technology.

I would like to thank various parties who have helped and guided the author in doing this final project, especially to:

1. My father who has given extensive prayers, moral and material support, as well as never-ending love.
2. Assoc. Prof. Mohammad Amin as my thesis supervisor, for his guidance, motivation, and help to complete this thesis
3. EMJMD REM consortium for their beliefs on me, so that I can be granted the opportunity to pursue graduate study in one of the best universities in Europe.
4. EMJMD REM class of 2020, especially friends from pathway B for their support throughout the master's journey.
5. Dr. Fathin Saifur Rahman (EP'08) and Dr.(cand) Fabiola Maria (EL'12) from Institut Teknologi Bandung for their helpful insights, software help, and theoretical discussion during my master's thesis writing.

Suggestions and constructive critics can be dropped at claysius@ieee.org to help advancing this research field further.

C.D.W.

Trondheim, June 2022

Contents

List of Figures

Abbreviations

AC	Alternating Current
ADC	Analog to Digital Converter
AVR	Automatic Voltage Regulator
APL	Active Power Loop
BTB	Back-to-Back
CIG	Converter-Interfaced Generation
CIL	Converter-Interfaced Load
CLTF	Closed Loop Transfer Function
CLTM	Closed Loop Transfer Matrix
DAC	Digital to Analog Converter
DC	Direct Current
DFIG	Doubly-Fed Induction Generator
DSP	Digital Signal Processing
EU	European Union
EMF	Back-Electromotive Force
FACTS	Flexible AC Transmission Systems
FFT	Fast Fourier Transform
FRC-WT	Fully Rated Converter Wind Turbine
FRT	Fault Ride Through
GFI	Grid Forming Inverters
GINC	Generalised Inverse Nyquist Criterion
GNC	Generalised Nyquist Criterion
GSC	Grid Side Converter

HAWT	Horizontal Axis Wind Turbine
HVDC	High Voltage Direct Current
IEA	International Energy Agency
IEEE	Institute of Electrical and Electronics Engineers
IGBT	Insulated-Gate Bipolar Transistor
IGE	Induction Generator Effect
IM	Induction Machine
LCOE	Levelized Cost of Energy
LNG	Liquefied Natural Gas
MIMO	Multi Input Multi Output
MLBS	Maximum Length Binary Sequence
MSD	Modified Sequence Domain
NSC	Nyquist Stability Criterion
OLTC	On-Load Tap Changer
OLTF	Open Loop Transfer Function
OLTM	Open Loop Transfer Matrix
PCC	Point of Common Coupling
PI	Proportional-Integral
PLL	Phase-Locked Loop
PF	Power Factor
PRBS	Pseudo-Random Binary Sequences
PWM	Pulse Width Modulation
RC	Resistor-Capacitor
RL	Resistor-Inductor
RHP	Right Half Plane
RSC	Rotor Side Converter
RoCoF	Rate of Change of Frequency

RPL	Reactive Power Loop
SCIG	Squirrel-Cage Induction Generator
SCR	Short Circuit Ratio
SG	Synchronous Generator
SIL	Surge Impedance Loading
SISO	Single Input Single Output
SLD	Single Line Diagram
SM	Synchronous Motor
SMIB	Single Machine to Infinite Bus
SPWM	Sinusoidal Pulse Width Modulation
SSO	Sub Synchronous Oscillation
SSR	Sub Synchronous Resonance
STATCOM	Static Synchronous Compensator
TOV	Transient Over-Voltage
TSR	Tip Speed Ratio
TSO	Transmission Systems Operator
UFLS	Under Frequency Load Shedding
USA	United States of America
VAWT	Vertical Axis Wind Turbine
VRE	Variable Renewable Energy
VSC	Voltage Source Converter
VSG	Virtual Synchronous Generator
WECS	Wind Energy Conversion System
WRIG	Wound-Rotor Induction Generator
WRSG	Wound-Rotor Synchronous Generator

Nomenclature

Units

Ω	Ohm
°	Degree
A	Ampere
H	Henry
Hz	Hertz
m	meter
N	Newton
p.u.	per unit
rad	Radian
s	second
V	Volt

Metric Prefix

μ	micro	10^{-6}
m	milli	10^{-3}
k	kilo	10^{3}
M	mega	10^{6}
G	giga	10^{9}
T	Tera	10^{12}

Chapter 1

Introduction

This chapter is written to make sure the reader has a better understanding of the background and the aim of the thesis. First, the motivation behind the thesis work is explained before the specific objectives are presented. The project significance is also elaborated together with the methodology, scope, limitations, and the overall thesis structure.

1.1 Background and Motivation

Energy has been one of the most significant drivers of economic growth. Due to the COVID-19 pandemic, the world has gone into a recession which causes the global electricity demand to drop by around 124 TWh in 2020 [1]. In 2021, the global electricity demand grew by 6%, which in absolute terms, was the highest ever recorded with over 1500 TWh [1]. With the recovery of the world's economy and extreme weather conditions, the electricity demand will inevitably keep growing by 2.7% per year on average until 2024 [1].

However, the sharp increase in energy demand is not balanced with the sources of the electricity supply due to the energy crisis. It started with the COVID-19 pandemic when the lockdown was implemented around the globe, causing electricity and gas usage to fall steeply. The lockdown, combined with the overproduction of oil and gases, drove the prices to crash. The crashing prices of oil and gases resulted in oil and gas companies decreasing their production to ensure they were operating profitably.

The electricity demand started recovering with the economic recovery, which drove the gas prices to hike. The prices, reaching a new high level [2], made the utilities operate in red without being able to pass the costs on since the government's energy price cap was too low. For example, 26 energy companies have collapsed in the UK due to the policy, affecting almost 4.3 million domestic customers [3]. Due to this, Ofgem in the UK has set a new, fairer price cap mechanism that allows energy companies to pass on the high production costs while ensuring customers pay a fair share of their electricity usage. This new mechanism, in the short run, is successful in helping the energy companies alleviate their losses. However, it was too taxing for the customers since the price suddenly increased and was too high for them to afford, especially during the long winter period.

This energy crisis reveals the bad energy policy being designed worldwide (especially in Europe), which focused only on one part of the energy trilemma: sustainability and environmental impacts, without putting too much attention on energy security. The EU aims to achieve at least a 40% share of renewable energy by 2030 [4], aiming to have net-zero CO_2 emissions by 2050 to establish Europe as the first climate-neutral continent in the world [5]. To achieve this, policymakers in Europe have focused on phasing-out conventional power plants such as coal and nuclear-based power plants. Also, they

emphasize reducing oil and gas production while increasing investment in wind farms and solar power plants.

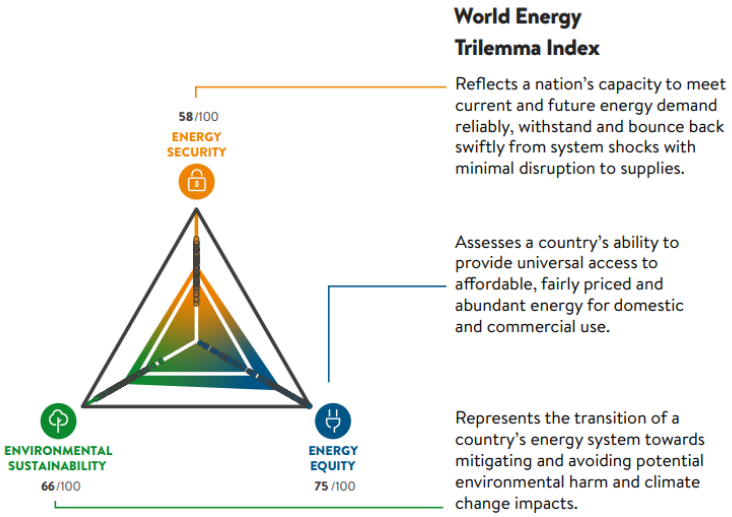

Figure 1.1 Example of The Energy Trilemma [6]

With the massive focus on sustainability, the policymakers have reformed the supply-side of the energy system while the demand-side reformation lag behind [7]. Currently, the EU heavily depends on natural gas imports and LNG from other countries, such as Russia, the USA, and Norway [8]. With how things progress so far, the current energy crisis will not have a short fix, and the prices can be expected to stay high in the upcoming years.

For that reason, the EU has announced another ambitious strategy called REPowerEU to make Europe independent from Russian fossil fuels before 2030 [9]. This strategy can be further discussed in two main parts: short-term and medium-term plans. The short-term program ensures that gas supply distribution is undisturbed by having the EU Energy Platform for common gas and LNG purchases. Also, the EU plans to have new energy partnerships with more reliable suppliers, rapid roll-out of solar and wind energy projects, and the approval of the first EU-wide hydrogen projects [9]. The support of the hydrogen project is an excellent move from the EU to ensure a variety of alternatives of green energy to keep the energy mix well-balanced. By having a more well-balanced energy mix, the intermittency of other VREs can be avoided, improving the continent's energy security while ensuring it is still affordable for consumers.

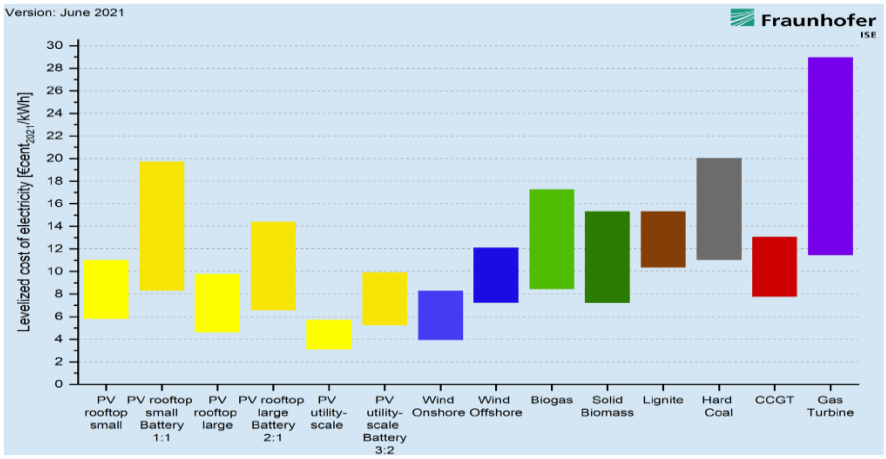

Figure 1.2 LCOE of Renewable Energy and Conventional Technologies in 2021 [10]

In the medium-term, the EU plans to increase the share of renewables from the previous 40% to 45% in 2030. Other things worth noting are the increase in investments in renewables and the new legislation and recommendations to accelerate renewable energy interconnections. The EU prepared a special solar energy strategy to double the installed capacity to 320 GW by 2025 and 420 GW by 2030 [9]. REPowerEU also wants wind energy to increase from 190 GW today to at least 480 GW in 2030. It is understandable since wind and solar power are already one of the cheapest forms of electricity generation in terms of LCOE [10].

With how the EU plans to integrate more wind energy into the systems, it is apparent that the shift from conventional power plants to VRE sources is growing at an extreme pace. Unfortunately, wind energy has its drawbacks compared to traditional power plants. One of the most popular ones is intermittency, which causes the output power from the wind power plants to vary depending on the weather. This intermittency issue provides technical challenges in balancing the generation and demand at all times. Compared to other conventional, dispatchable sources which can store their energy in the form of their primary energy source (water for hydropower power plants or coal for coal-fired power plants), wind energy cannot be stored, so the output varies depending on the available wind at that particular time or non-dispatchable. Due to this, the output of the wind turbines cannot be directly integrated into the electrical grid. With varying wind speeds, the rotation of the wind turbines will also vary, generating a variable frequency AC waveform.

By utilising power electronics converters, the integration of wind farms into the AC grid has been eased, and the AC waveforms can be converted to be compatible with the grid. However, as the number of power electronics converters increases, there is a significant impact on the power systems' dynamics and stability. Since traditionally, power systems are dominated by synchronous machine-based physics and control, the dynamics are also determined by the response of the dominant synchronous machine. With how power converters are interconnected more to the grids (from here onwards will be called CIG-Converter Interfaced Generation), the conventional modelling for power systems dynamics is not enough to capture all the desired phenomena available in power systems [11].

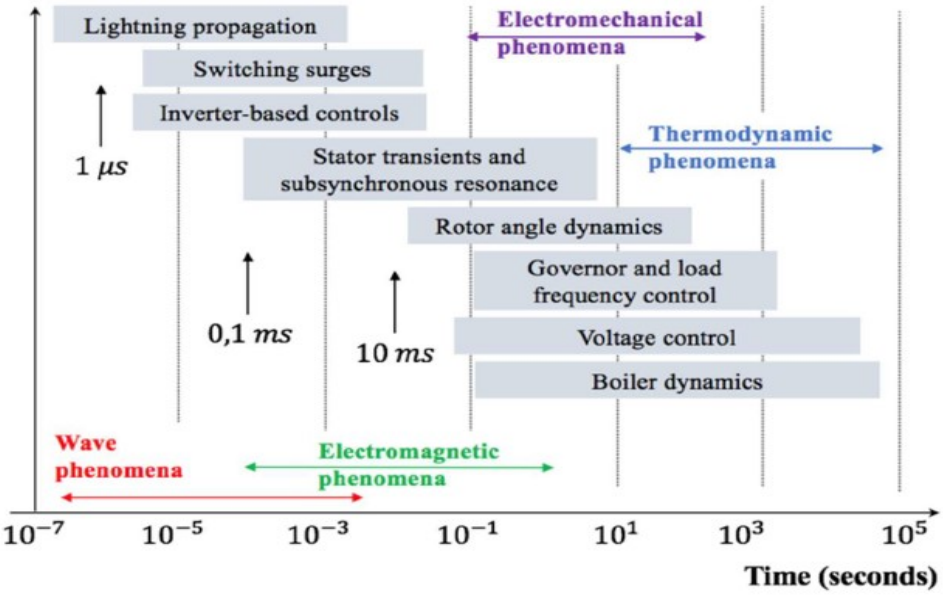

Figure 1.3 Power Systems Dynamic Time Scales [12]

When CIGs are connected to the grid, it can be seen from [12] that inverter-based control exist. This happened since the converter are interacting with the existing grid dynamics. This interaction may cause a lot of problems, from oscillation to small-signal stability problems [13], [14]. To analyse the interactions and their small-signal dynamics, usually linearised modelling is utilised. From the linearised model, there are two main ways to conduct the stability analysis. The first one is conducted in the time domain with state-space analysis method [15], and the second and the most recent and currently state-of-the-art one is in the frequency domain with impedance-based analysis method [16].

The difference between them is the state-space analysis comes from the differential equations of the state variables, obtained from a linearised model. Since the dynamics of the converter is modelled through the control systems, the physical components of the converter can be considered less important for dynamic studies. However, the control design is a very confidential information from the suppliers and will not be available. This will not be a problem if all converters came from the same vendor, since a general model then can be derived for the subsystems. In reality, there are many vendors supplying converters to the grid worldwide. Therefore, the TSO will have a challenge in obtaining data for each converters to conduct a proper and accurate dynamic studies [17].

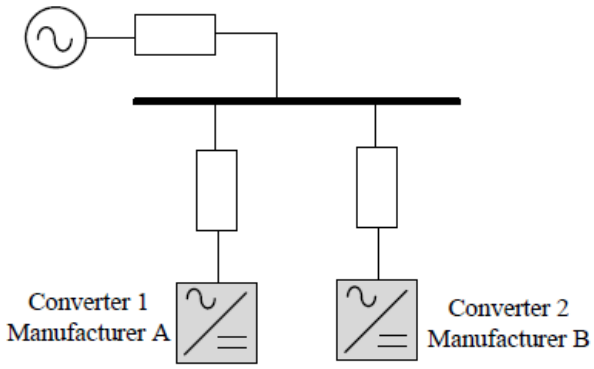

Figure 1.4 Illustration of the Challenge on Converter Interoperability [18]

Impedance-based modelling will consider both the converter 1 and 2 in [18] from the terminal equivalent or the grid PCC. From here, the converter control dynamics will be modelled as a transfer function (or an impedance model), defined as the voltage divided by the current. The interaction will be modelled as a feedback loop formed by the grid impedance and the converter impedance. With this technique, it allows 'black-box' way of modelling so that the control dynamics can be characterised simply through the input-output approach by transfer functions.

Even though impedance-based modelling has been a quite common field of research at the moment, it usually studies only a certain type of control, such as VSG [19], VSC HVDC control [20], MMC-based HVDC [21], and GFI [22]. To the best of the author's knowledge, there is no specific studies on impedance-based modelling and converter-driven stability analysis for Synchronverter-based WECS (from here onwards, WECS will refer to the Synchronverter-based control of WECS to simplify the terms). Therefore, in this thesis, an impedance-based modelling and converter-driven stability analysis will be conducted for the WECS. The thesis will propose and derive the analytical impedance model, so that it can be used as the baseline to tune the controller. Also, as a case study, it will be

demonstrated on how the impedance-based modelling combined with the GNC for converter-driven stability analysis can be utilised to investigate the impact of the WECS interconnection to a weak AC grid.

1.2 Objectives

The main objective of this master's thesis is to investigate the converter-driven stability of a power systems consisting of a Synchronverter-based WECS by means of impedance-based modelling and analysis. MATLAB/Simulink will be used to simulate the systems and implementing the method proposed.

Therefore, the three major objectives of the thesis are

- to analytically derive the impedance model of the WECS
- to compare the accuracy between the derived analytical model with the frequency sweep model
- to conduct the converter-driven stability analysis of the WECS connected to an AC weak grid by implementing the impedance-based stability analysis.

1.3 Thesis Significance

This thesis which studies the impedance-based modelling and stability analysis will contribute to the already established research on the topic by creating an analytical impedance model that can be used to investigate the Synchronverter small-signal dynamic response, and provide a detailed comparison between the model obtained from simulation and the derived analytical model. Furthermore, an in-depth study regarding the converter-driven stability will be conducted, and the impact of the different control parameters to the interconnection with weak AC grids will also be explored.

The result of this thesis will provide helpful feedback for the TSO to plan and prepare for the upcoming full transition to more power electronics-dominated power systems. The proposed, impedance-based method can also be designed and professionally implemented into a more well-known power systems analysis commercial software, such as DIgSILENT PowerFactory or PSCAD to conduct stability studies regarding CIGs. Another thing worth to mention is these studies will contribute indirectly to the environment and energy crisis since it will undoubtedly help alleviate one of the risks in VRE integration to the power systems. This will also benefit the electricity consumers since the research will help increase the reliability of the grids in terms of converter-driven stability of WECS.

In addition, from this thesis, 3 scientific papers will be written and submitted for publication. 2 of them is directly related to the thesis and 1 of them is only related to a certain extent.

- *Low Inertia Power Systems: A Comprehensive Review,* is currently in minor revision and is attached in Appendix
- *Sequence Domain Impedance Modelling of Synchronverter-based Wind Energy Conversion System*, is currently in major revision and will not be attached in Appendix
- *Converter-Driven Stability Analysis of Synchronverter-based Wind Energy Conversion System for Weak AC Grid Integration*, is currently in writing process, and will not be attached in the Appendix.

1.4 Method

Literature review of VSMs (especially Synchronverter) will be carried out first, complemented with literature review of relevant articles and papers related to impedance-based modelling and stability analysis of power electronics converters. The required mathematical modelling for the WECS will also be provided, including the mathematical concepts of wind turbine and the power extraction, the modelling of a synchronous generator and the Synchronverter control system.

Provided with relevant mathematical and background theory, the detailed model of the WECS will be built in Simulink. A validation of the model will be conducted from the scenarios on Texas Panhandle Wind Power System [23].

Next, analytical impedance model of the WECS will be derived from the mathematical model of the Synchronverter and the control schemes. Normal linearization approach will be used, and the Bode Plot of the impedance magnitude and the phase will be shown. To validate the analytical impedance model, a frequency sweep will be simulated with Simulink. The obtained, frequency sweep model will be compared with the analytical model from the Bode Plots.

Last, the converter-driven stability analysis will be conducted to see the impact of the WECS control parameters for the interconnection under weak AC grid conditions. A GNC method [24] will be used to analyse the converter-driven stability of the WECS. The Nyquist plot of both the impedance obtained from analytical model and the frequency sweep will be compared, and a time-domain simulation will also be performed to see the stability aspects in the form of active power, reactive power, frequency, and voltage waveforms.

1.5 Scope and Limitations

The scope of this thesis are as follows:

- Get up to date on the new, extended, classification of power systems stability in a power electronics-dominated power system
- Perform a comprehensive literature review on the state-of-art for Synchronverter
- Model the control and the dynamics of the Synchronverter-based WECS
- Derive analytically the impedance model of the WECS from the mathematical equation of Synchronverter
- Conduct a single-tone frequency sweep to obtain the impedance model of the WECS from simulation
- Use the obtained model to conduct a converter-driven stability analysis by means of the GNC
- Carry out a sensitivity analysis by varying the parameters of the WECS to understand the impact of the parameters of the WECS for weak AC grid interconnection
- Execute a time-domain simulation to analyse the current and voltage waveforms during the converter-driven stability studies

Notable limitations include the following:

- Simulations will be carried out on an SMIB using MATLAB/Simulink, which basically means that all system parameters are hypothetical and there will be no physical hardware implementations.
- An aggregated wind farm model is used, consisting of a wind turbine model, the GSC and RSC, the grid impedance, and the voltage source as the infinite bus.
- The details related to the WECS tuning and control design are not considered.
- The control of the wind turbine in detail, such as pitch control, aerodynamic model, tower model, gain scheduling control, etc are outside the scope of this thesis.
- Only one type of VSM will be studied which is Synchronverter. There will be no comparison studies performed between other topologies of VSM with Synchronverter.
- Only converter-driven stability is considered. Frequency, rotor angle, and voltage stability studies are thus not carried out.

1.6 Thesis Structure

The thesis follows a four-level format from the NTNU thesis template, in which A is the chapter number, B is the section number inside chapter A, and so on. Equations are formatted directly as (A) where A indicates the equation number, while figures, and tables are formatted as A.B, with B denoting the number of objects and A denoting the chapter.

The bibliography at the last part of the thesis is formatted in IEEE citation style, and references are identified by their reference number inside square brackets. The reference number will correspond to the number in the bibliography, and the references will be listed in chronological order depending on when they are first referenced in the thesis.

There are six chapters in this master's thesis, plus five appendices, including the introduction chapter. The format of the remaining five chapters and appendices, as well as a review of their contents, are given below.

Chapter 2 introduces the background theory that will be used sfor the research that will be conducted in this thesis. Before the wind turbine and permanent magnet synchronous generator are mathematically modelled, an introduction to wind power is given. Then there will be a quick rundown on power electronic converters. The swing equation which is the basic fundamental theory of Synchronverter will be introduced once the synchronous machine is modelled. Also included is a brief introduction to VSM. Finally, an introduction to the new, expanded classification of power system stability is provided, as well as a discussion of one of the newest types of stability from the classification: converter-driven stability.

Chapter 3 models the Synchronverter technique for both inverter control and rectifier control of the WECS. The system topology which will be modelled in Simulink is also described in detail, with the simulation and results of the validation from Texas Panhandle Wind Farm scenarios provided at the end of the chapter.

Chapter 4 derives the impedance model of the WECS which is connected an infinite bus. First, a brief introduction on several methods of impedance modelling will be elaborated. Also, a concise explanation in regards to obtaining the impedance model from measurement will be provided. Then, the impedance model of both the GSC and the RSC will be derived analytically from the governing equations of the Synchronverter control. To

validate the results, a single-tone frequency sweep will be conducted. The results and simulations providing insight into the system stability are provided, before being thoroughly discussed.

Chapter 5 investigates the converter-driven stability of the WECS by means of the GNC. First, an introduction on stability analysis for interconnection to a weak grid will be given. Next, a concise explanation about the weak grids and impedance-based stability analysis is provided, with emphasis on the GNC method. Lastly, simulations which centred on sensitivity analysis of the WECS control parameters are carried out to understand the impact of the parameters for converter-driven stability in regards of interconnection to a weak AC grid. A time-domain simulation will then be executed to see the effect on the current and voltage waveform of the PCC.

Chapter 6 present the conclusions for all the simulations and results obtained. Possible future works are also discussed based on the studies carried out in the thesis.

Last part of the thesis contains the appendix, which is given to complete the thesis as a whole.

Chapter 2

Background Theory

This chapter lays the theoretical foundation for the research that will be done in this thesis. An introduction to wind energy is given before the wind turbine and permanent magnet synchronous generator are mathematically modelled. After that, a short overview of power electronic converters will be given. Once the synchronous machine model has been introduced, the swing equation, which is the core fundamental theory of Synchronverter, will be introduced. A quick introduction to VSM is also presented. Finally, a description of the new, expanded classification of power system stability is presented, as well as an introduction to one of the newest types of stability: converter-driven stability.

2.1 Introduction to Wind Energy

2.1.1 Overview of the Wind Turbine Technology and Architectures

A wind turbine is a device which converts the wind energy into electricity [25]. A wind turbine consists of a tower and a nacelle that is mounted on top of the tower. This nacelle contains several components which is responsible for the energy conversion, such as the gearbox, the generator, and the transformer. When the wind blows past the wind turbine, the turbine blade will capture the energy and rotate. This rotation will rotate the shaft inside the hub. To increase the rotational speed, the shaft is connected to a gearbox, and this gearbox is connected to the generator to convert the kinetical energy to electricity. This electricity generated needs to be regulated by the power electronics converters to ensure it complies with the grid code. By having a larger rotor blade in terms of diameter, the energy it can capture will also be greater. However, larger rotor will needs higher tower to ensure that the height is high enough to capture faster winds so the rotor blade can rotate [26].

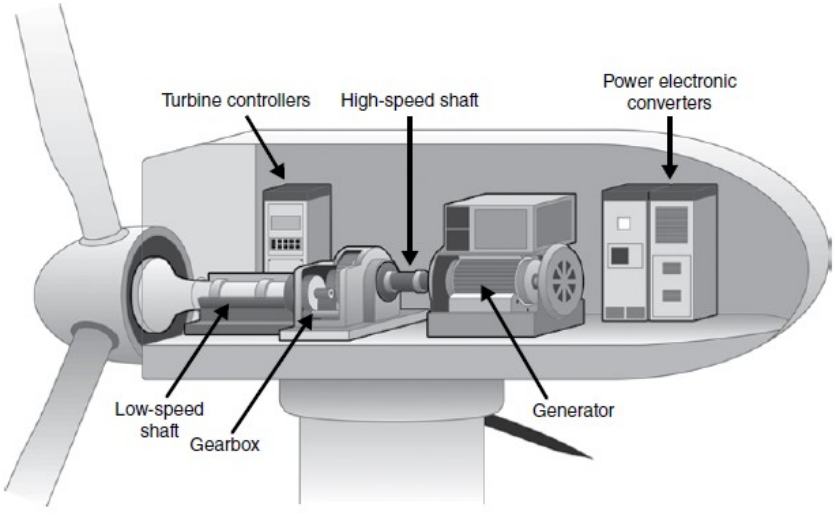

Figure 2.1 The Structure of Wind Turbine [27]

Wind turbines itself in general has 2 different orientation of the rotor shaft, more commonly known as VAWT and HAWT [28]. Even though VAWT can operate independently of the wind direction, in larger wind turbines in the modern era, VAWT have more disadvantages compared to the advantages such as dynamics issues, low efficiency, and weak wind speed issues [28]. In recent times, HAWT is the most dominating orientation type of wind turbine, especially for offshore applications where the sizes of the wind turbine itself is much larger compared to onshore applications. The largest as of January 2022, is the 14 MW GE Haliade-X with a rotor diameter of 220 meters [29].

Modern wind turbine generators can be categorised are into 2 categories as well depending on the operating type; fixed speed wind turbines (type I) and variable speed wind turbines (type II, III, and IV) [27]. Type I wind turbines uses an SCIG driven by a gearbox, and connected directly to the grid via a transformer. Therefore, the rotational speed of the generator is almost constant. To excite the SCIG, a PF compensator in forms of capacitor bank is required for reactive power supply to the SCIG. The disadvantage of such wind turbine is the low efficiency compared to the other types even though type I is cheaper and much simpler in terms of construction.

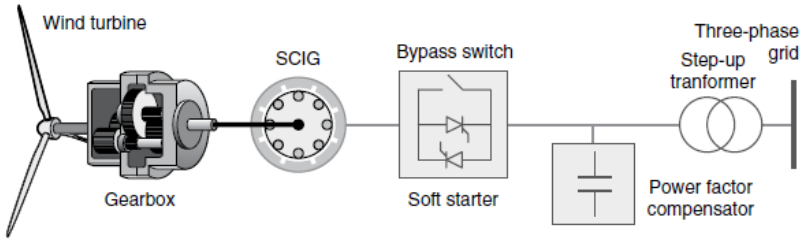

Figure 2.2 Type I Wind Turbine [27]

The difference between type II and the other two types (type III and IV) is on the way to achieve the variable speed operation. In type II wind turbine, the variable speed operation is obtained by controlling the rotor resistance of the WRIG. A variable resistor is connected to the WRIG in series, and it is controlled with a chopper circuit. From the way it operates, basically type II wind turbine is a modification from type I, where below the rated speed, it will act as type I wind turbine. Above the rated wind speed, the variable resistor will control the air-gap torque and slip speed, controlling the rotational speed of the generators [27].

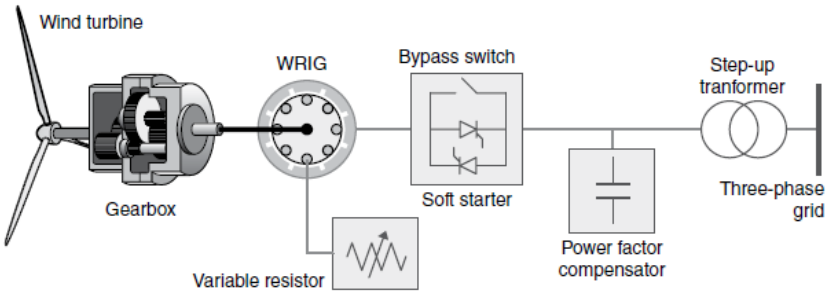

Figure 2.3 Type II Wind Turbine [27]

The most used topologies for variable speed wind turbines are type III and type IV, where type III is known as variable speed with partial power electronics conversion with typical DFIG configuration. This happened because the stator of the generator is connected in parallel with the converter. The variable speed operation is achieved by the use of a

controllable, variable frequency voltage in the rotor at a certain value of slip required. This effectively decoupled the mechanical speed of the DFIG with the grid frequency [27].

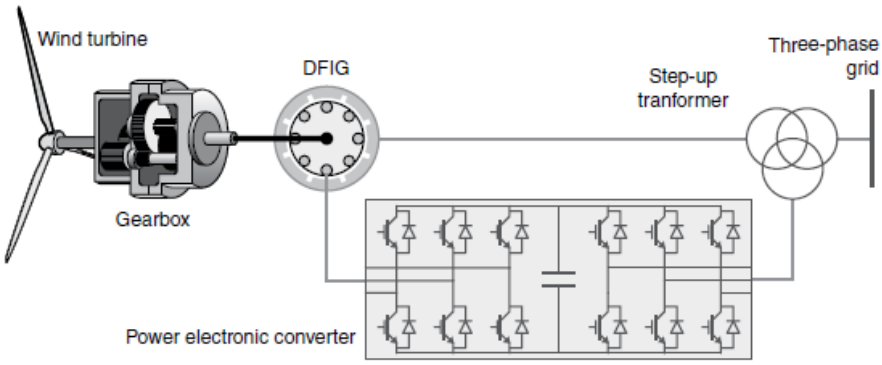

Figure 2.4 Type III Wind Turbine [27]

Type IV is known as FRC-WT, since all the power from the wind turbine is now being sent directly to the converters. Therefore, the generator is effectively isolated from the grid. FRC-WT is very flexible and can have a variety of generator types, such as PMSG, SCIG, or WRSG. The control of the wind turbine itself depends on the converter type used, so in reality, there are various control strategies depending on what to achieve [27]. In this thesis, the PMSG will be used and a simple PMSG model will be derived in the following section.

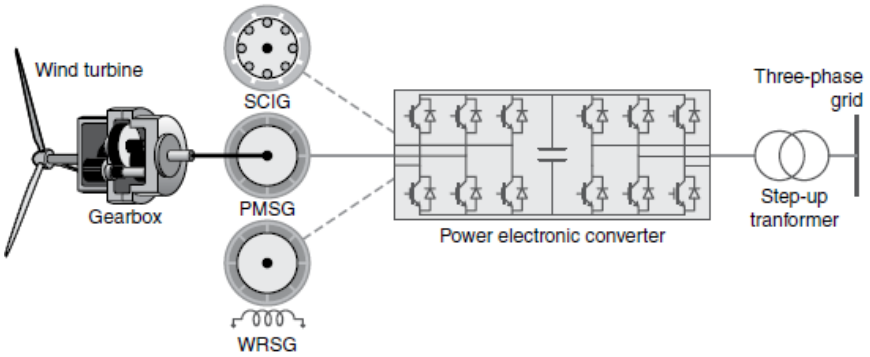

Figure 2.5 Type IV Wind Turbine [27]

2.1.2 Wind Energy Conversion System Modelling

As explained in the previous chapter, a Simulink model of the WECS will be built from scratch in this thesis. The model built will come from the mathematical formulation in this section.

2.1.2.1 Wind Turbine

In this thesis, without loss of generalisation, a simple wind turbine model will be used [30]–[32]. For a wind turbine with radius R, the mechanical power available to be extracted P_m, is given by (1)

$$P_m = \frac{1}{2}\rho\pi R^2 v_w^3 C_p(\lambda, \beta) \tag{1}$$

where ρ is the density of the air, v_w is the wind speed and C_p is the power coefficient. C_p is a coefficient which is dependent on the pitch angle β, and the TSR λ as defined in (2)

$$\lambda = \frac{\omega_m R}{v_w} \tag{2}$$

From the aerodynamic and foil design, every wind turbine type has its own empirical model between C_p as a function of $\boldsymbol{\lambda}$ and β. In this thesis, the empirical model used is cited from [31] and shown in (3).

$$C_p(\lambda, \beta) = 0.5\left(\frac{116}{\Lambda} - 0.4\beta - 5\right)e^{\frac{-21}{\Lambda}} \tag{3}$$

where,

$$\frac{1}{\Lambda} = \frac{1}{\lambda + 0.08\beta} - \frac{0.035}{1 + \beta^3} \tag{4}$$

From the equation given above, it is clear that to extract maximum power at any given wind speed, the wind turbines need to operate at its maximum efficiency $C_{p,max}$. To obtain this, the optimal TSR λ_{opt} needs to be determined. By plotting the C_p as a function of λ for various β, λ_{opt} can be easily determined as shown in the following figure.

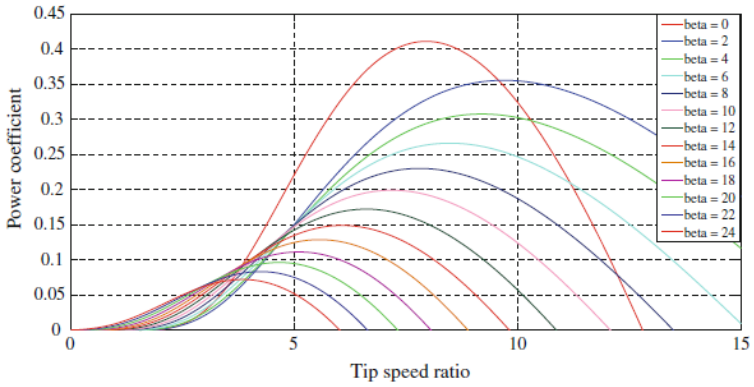

Figure 2.6 Plot of C_p vs λ

It can be seen from Figure 2.6 that the λ_{opt} is around 8 (7.95 to be exact) and the $C_{p,max}$ is around 0.41 for $\beta = 0$. This value will be needed for the MPPT algorithm which will be used to extract the maximum power from the wind turbine at all times.

2.1.2.2 Maximum Power Point Tracking (MPPT)

As explained in the closing sentence of the previous section, an MPPT algorithm will be used to extract maximum power at all times, i.e., to ensure the wind turbine operates at $C_{p,max}$. MPPT algorithm works by adjusting the active power set-point, which would regulate the speed of the generator. By doing so, ω_m will be the adjusted to obtain the desired TSR following (2). The MPPT algorithm presented here is the optimal torque control as presented in [33], [34].

Again, rearranging (2),

$$v_w = \frac{\omega_m R}{\lambda} \tag{5}$$

Substituting (5) to (1) results in

$$P_m = \frac{1}{2}\rho\pi R^5 \frac{\omega_m^3}{\lambda^3} C_p(\lambda, \beta) \tag{6}$$

Reflecting back to the MPPT concept to operate the wind turbine at $C_{p,max}$ and utilising the fact that $P_m = \omega_m T_m$, the following set of equations can be obtained.

$$P_{m,opt} = \frac{1}{2}\rho\pi R^5 \frac{\omega_m^3}{\lambda_{opt}^3} C_{p,max} = K_{p,opt}\omega_m^3 \tag{7}$$

$$K_{p,opt} = \frac{1}{2}\rho\pi R^5 \frac{C_{p,max}}{\lambda_{opt}^3} \tag{8}$$

If the wind speed measurement data is available, $P_{m,opt}$ will be straightforward since $C_{p,max}$ is known.

$$P_{m,opt} = \frac{1}{2}\rho\pi R^2 v_w^3 C_{p,max} \tag{9}$$

2.1.2.3 Permanent Magnet Synchronous Generator (PMSG)

PMSG is more or less a simplified version of a normal SG which will be explained further in section 2.3. The fundamental difference between SG and the PMSG is the rotor flux source. In a PMSG, the rotor flux is provided directly from the permanent magnet installed in the machine. Therefore, a PMSG does not need an external excitation to create the flux as compared to the normal SG [27].

Since the PMSG is a simplified version of the SG, the mathematical model is more or less the same as for the SG. Here, Ψ will be used to introduce as the permanent magnet-generated flux. Therefore, the mathematical models of the PMSG are

$$e = \Psi\dot{\theta_e}\,\widetilde{\sin\theta_e} \tag{10}$$

$$T_e = p\Psi\langle i, \widetilde{\sin\theta_e}\rangle \tag{11}$$

$$P_g = \dot{\theta_e}\Psi\langle i, \widetilde{\sin\theta_e}\rangle \tag{12}$$

$$Q_g = -\dot{\theta_e}\Psi\langle i, \widetilde{\cos\theta_e}\rangle \tag{13}$$

Here, $\dot{\theta_e}$ is the time derivative of the generator angle, i.e., electrical speed of the generator which can be related to the mechanical speed of the rotor by the following relation

$$\omega_e = p\omega_m \tag{14}$$

where p is the number of pole pairs of the machine.

2.2 Power Electronics Converters

As explained previously, to obtain a more proper and higher quality output from the wind turbines, power electronics converters are required. For wind turbine applications, the typical converters needed are rectifiers, inverters and DC-DC converters. There are several technical, operational, and economical requirements for the converters to be feasible to be used in wind turbine applications, such as initial cost, reliability and maintenance cost, efficiency, power quality, grid code compliance, power density and weight [27]. In reality,

power electronic converters are often divided into two parts; the physical part and the electronic part [35].

The switching devices and other physical components such as diodes, thyristors, capacitors and inductors make up the physical part of the converters. Because of their high current and voltage ratings, IGBTs are frequently employed in the converters for the applications in wind turbine [36], and the same component is also used for modelling in this thesis.

For the electronic part, it consists of the DSP device, signal condition unit, sensors, and PWM drivers [37]. It also has a DAC and an ADC, as well as additional monitoring output connections. The electronic part also contains the control strategies for the converter.

2.2.1 Back-to-Back Converters

BTB converter is a type of series connection between rectifiers and inverters. Rectifiers are used to convert AC to DC signals while inverters are used to convert DC to AC signals. Between the rectifier and the inverter, there will be a DC connection and more commonly called as DC bus [38]. Therefore, the BTB converters will transform the variable frequency or voltage output from the generator to DC and back to AC with fixed frequency or voltage which is now complies with the grid code [27]. Such a converter is often called as a VSC.
One thing worth to mention is in BTB converters, the power flow can be bidirectional. That is the reason why in type IV, various machine can be used, from SCIG, PMSG, and WRSG. Also, BTB can be classified as low voltage (less than 1 kV) and medium voltage (1 – 35 kV) [39]. An example of BTB configuration is shown in Figure 2.7 below.

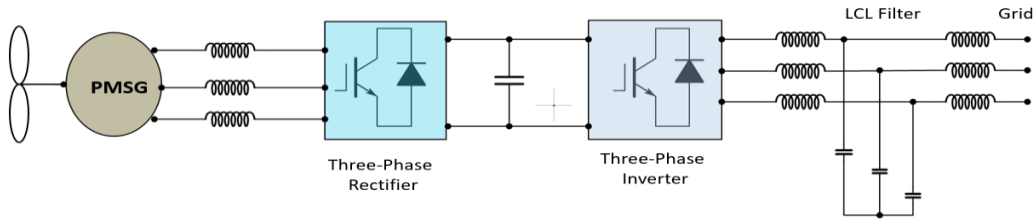

Figure 2.7 An Example of Type IV Wind Turbine with PMSG and LCL Filter

2.2.2 Pulse Width Modulation Technique

To control the IGBT of the converters, then the signal is commonly generated by a technique called PWM. There are several PWM techniques, such as sampling-based PWM with natural sampling or carrier-based, regular sampling PWM, SPWM, programmable PWM, and so on [35]. In general, the concept of PWM will be explained in the next paragraph.

A modulating signal or reference signal will be compared to a triangular carrier signal which frequency is equal to the switching frequency f_s of the IGBTs of the converters. This generates a sequence of pulses called the drive signals. The reference's frequency will regulate the output voltage's frequency, while the amplitude of the output voltage will be controlled by the modulation index [35]. The same concept applies to three-phase systems where three reference voltages are compared with the carrier, generating three sets of pulses to control the three different legs of the converter.

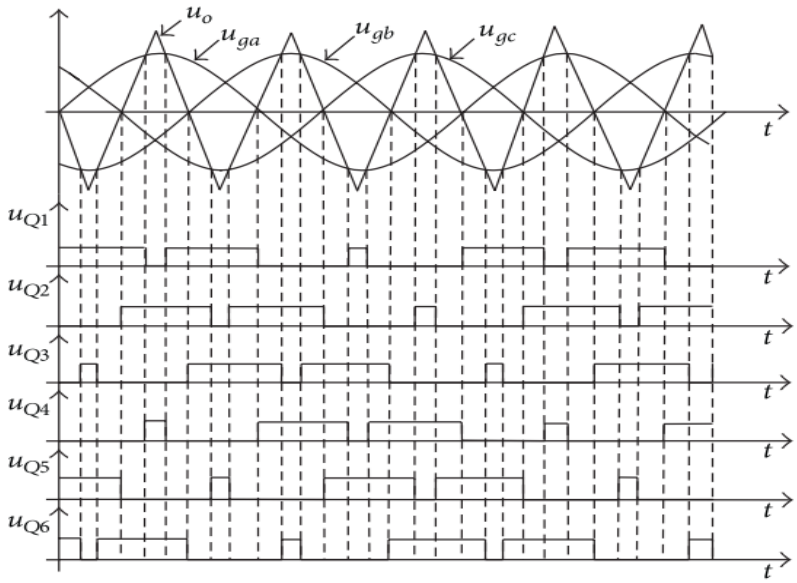

Figure 2.8 3-Phase Reference Signal, Carrier Signal, and the Control Signals [40]

2.3 Synchronous Machine Modelling

The model of synchronous machine is essential to be able to understand the Synchronverter control strategy that will be explained in Chapter 3. Even though SG and SM is similar, their mathematical models have some slight differences, and will therefore be described separately. The topology used in this thesis will be an ideal three-phase round-rotor machine i.e., all stator inductances are assumed to be constant. Additionally, the model has no damper winding, has one pole pair per phase, and there is assumed that no magnetic saturation effects in the core exist [41].

2.3.1 Synchronous Generator

Consider the following figure,

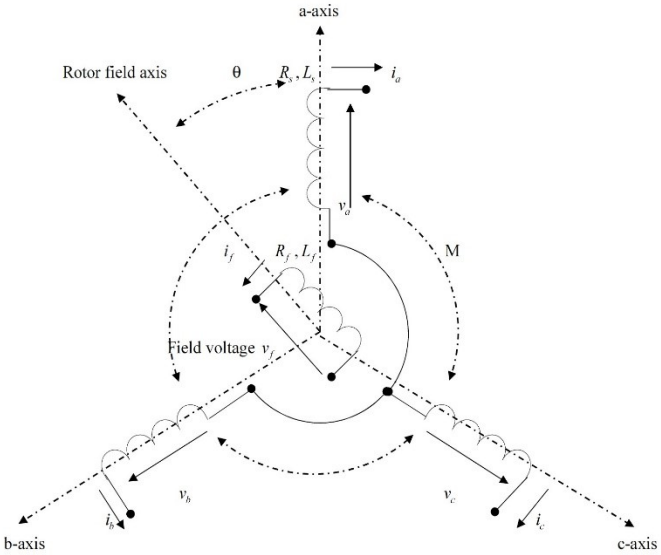

Figure 2.9 Ideal 3-phase Synchronous Generator [33]

From the assumption of an ideal round-rotor machine, it can be presumed that the air gap is uniform. In the section around the air gap, 3 stator windings are placed can assumed to be a concentrated coil with self-inductance L and mutual inductance M where $M > 0$ [33]. Additionally, R_s is the winding resistance, and L_f is the rotor winding's self inductance.

As the rotor turns, the mutual inductance between the rotor and stator windings M_f and the rotor angle θ varies. Therefore, M_f can be defined as follows [41].

$$M_{af} = M_f \cos\theta \tag{15}$$

$$M_{bf} = M_f \cos\left(\theta - \frac{2\pi}{3}\right) \tag{16}$$

$$M_{cf} = M_f \cos\left(\theta + \frac{2\pi}{3}\right) \tag{17}$$

To make the equation concise, the following vector expression will be used in this thesis onwards

$$\widetilde{\cos\theta} = \begin{bmatrix} \cos\theta \\ \cos\left(\theta - \frac{2\pi}{3}\right) \\ \cos\left(\theta + \frac{2\pi}{3}\right) \end{bmatrix} \qquad \widetilde{\sin\theta} = \begin{bmatrix} \sin\theta \\ \sin\left(\theta - \frac{2\pi}{3}\right) \\ \sin\left(\theta + \frac{2\pi}{3}\right) \end{bmatrix} \tag{18}$$

Furthermore, another 3-phase vector expressions for stator flux linkage Φ, the phase currents i, the EMF e, and the terminal phase voltages v can be defined as

$$\Phi = \begin{bmatrix} \Phi_a \\ \Phi_b \\ \Phi_c \end{bmatrix} \qquad i = \begin{bmatrix} i_a \\ i_b \\ i_c \end{bmatrix} \qquad e = \begin{bmatrix} e_a \\ e_b \\ e_c \end{bmatrix} \qquad v = \begin{bmatrix} v_a \\ v_b \\ v_c \end{bmatrix} \tag{19}$$

From (19) and the Figure 2.9, the flux linkage can be derived as follows,

$$\Phi_a = Li_a - Mi_b - Mi_c + M_{af} i_f \tag{20}$$

$$\Phi_b = -Mi_a + Li_b - Mi_c + M_{bf} i_f \tag{21}$$

$$\Phi_c = -Mi_a - Mi_b + Li_c + M_{cf} i_f \tag{22}$$

$$\Phi_f = M_{af} i_a + M_{bf} i_b + M_{cf} i_c + L_f i_f \tag{23}$$

It is noticeable from the expressions that subscript f indicates rotor while subscript abc indicates the stator. Also, in a balanced 3-phase circuits with no neutral line, the sum of all phase currents will be 0. By definition, $L_s = L + M$, therefore equation (20), (21), (22), and (23) can be re-written as

$$\Phi = L_s i + M_f i_f \widetilde{\cos\theta} \tag{24}$$

$$\Phi_f = L_f i_f + M_f \langle i, \widetilde{\cos\theta} \rangle \tag{25}$$

By assuming that i_f is constant, e and v can be defined as

$$e = M_f i_f \dot{\theta} \widetilde{\sin\theta} \tag{26}$$

$$v = -R_s i - \frac{d\Phi}{dt} = -R_s i - L_s \frac{di}{dt} + e \tag{27}$$

The electromagnetic torque, T_e generated by the SG is

$$T_e = M_f i_f \langle i, \widetilde{\sin\theta} \rangle \tag{28}$$

To simplify the control implementation, the active power P_g and reactive power Q_g will be expressed similar to (28) as follows,

$$P_g = \dot{\theta} M_f i_f \langle i, \widetilde{\sin\theta} \rangle \tag{29}$$

$$Q_g = -\dot{\theta} M_f i_f \langle i, \widetilde{\cos\theta} \rangle \tag{30}$$

2.3.2 Synchronous Motor

Consider the following figure,

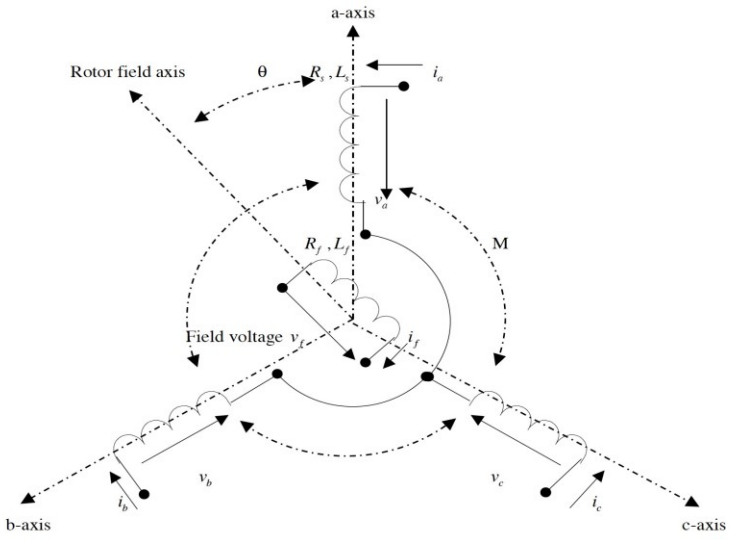

Figure 2.10 Ideal 3-phase Synchronous Motor [33]

It can be seen that Figure 2.10 is very similar to Figure 2.9. The main difference is that now, the currents are flowing into the motor. In SM, the EMF, e_m and the electromagnetic torque T_{em} still follows the same equation as explained in previous section.

Based on Figure 2.10, the vector of currents flowing into the motor $\boldsymbol{i_r}$ and the vector of voltages applied to the motor terminal $\boldsymbol{v_r}$ can be defined as

$$i_r = \begin{bmatrix} i_{ra} \\ i_{rb} \\ i_{rc} \end{bmatrix} \qquad v_r = \begin{bmatrix} v_{ra} \\ v_{rb} \\ v_{rc} \end{bmatrix} \tag{31}$$

From the direction of the current which flows into the motor, equation (27) can be redefined as [34]

$$v_r = R_s i_r + L_s \frac{di_r}{dt} + e \tag{32}$$

For the active and reactive powers of SM, equation (29) and (30) are still valid. But with the current flows in reverse now compared to SG, it will cause the power calculated from equation (29) and (30) to be negative, i.e., power is consumed by the motor.

2.4 The Swing Equation

Swing equation is one of the most fundamental equation in power systems stability [42], and one of the equation that builds the synchronverter [41]. In a typical SG, the driver and the drive train are the turbine and the shaft, respectively. Assuming a free-body rotation i.e. the turbine and generator inertia move together, the shaft can be modelled as a rigid body [43]. Under this assumption, a single mass model can be used to model the generator and each of the component inertias can be regarded as one total inertia J [44]. By treating the turbine and the generator systems as a one unit, the following equation can be obtained [43].

$$J\frac{d\omega_m}{dt} + D_d\omega_m = \tau_t - \tau_e \tag{33}$$

From equation (33), it can be seen the relation between the rate of change of machine rotational speed $\boldsymbol{\omega_m}$ is equal to the difference of the turbine torque τ_t and the electrical torque τ_e [43]. In synchronous operation, $\boldsymbol{\omega_m}$ is equal to the synchronous speed $\boldsymbol{\omega_{sm}}$. Therefore, the torques will be in balance, i.e.

$$\tau_t = \tau_e + D_d\omega_{sm} \qquad\qquad \tau_m = \tau_t - D_d\omega_{sm} = \tau_e \tag{34}$$

where τ_m is the net mechanical torque applied to the shaft obtained after subtracting rotational losses during synchronous operation. Now, in a synchronous machine, the rotor position is defined based on a rotating reference frame. Therefore, the rotor angle δ_m is measured with respect to the rotating reference frame and the machine rotational speed now can be defined as

$$\omega_m = \omega_{sm} + \Delta\omega_m = \omega_{sm} + \frac{d\delta_m}{dt} \tag{35}$$

where $\Delta\omega_m = \frac{d\delta_m}{dt}$ is defined as the speed deviation of the shaft from the synchronous speed. By substituting equation (35) to equation (33), the swing equation can now be rewritten in terms of $\frac{d\delta_m}{dt}$ as follows,

$$J\frac{d^2\delta_m}{dt^2} + D_d\frac{d\delta_m}{dt} = \tau_m - \tau_e \tag{36}$$

Equation (36) can also be rewritten in terms of the machine's angular momentum and active power. By using the expression of $P = \tau\omega$ and $\omega_m \approx \omega_{sm}$, and multiplying both sides of the equation (36) with ω_{sm}, the swing equation in terms of rotor dynamics can be obtained as follows [44],

$$M_m\frac{d^2\delta_m}{dt^2} + D_m\frac{d\delta_m}{dt} = P_m - P_e \tag{37}$$

where the angular momentum $M_m = J\omega_{sm}$ and damping coefficient $D_m = D_d\omega_{sm}$. From the relation, it is clear that the swing equation in the form of (37) is expressed in the form of mechanical properties of the machine. To express it in the form of electrical properties, however, it is algebraically simple since the angle and speed are related to the number of the pole pairs of the machine.

2.5 Virtual Synchronous Machines

It has been explained in Chapter 1 that the proliferation of VRE is increasing significantly throughout the years. Besides the CIGs interaction with the grid impedance that have been shortly introduced in the beginning of this thesis, one of the most important aspects in interconnecting CIGs are the reduction of the inertia of the power grids. Inertia is a tendency for a moving object to remain in motion. In the context of power grids, inertia is almost similar, and it refers to the amount of kinetic energy it stored in spinning generators [44]–[46]. To understand this aspect better, consider the following figure,

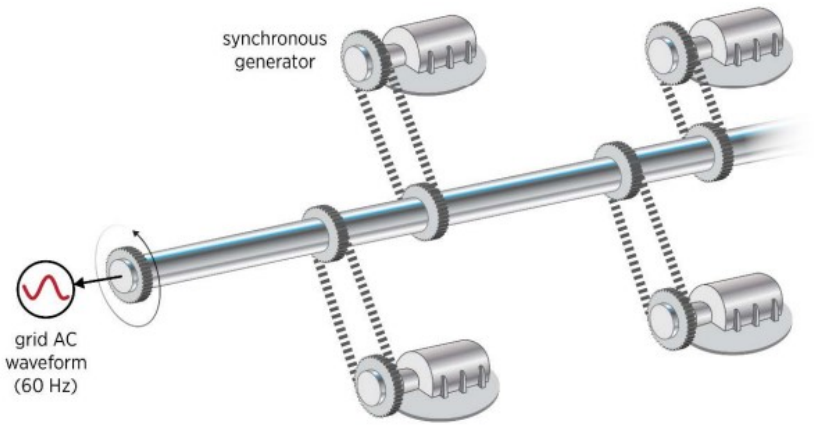

Figure 2.11 Visualisation of Synchronous Generators Operation in a Power Grid [45]

It can be seen in Figure 2.11 that all conventional generators are connected via a 'chain', which basically is the EMF. These chains indicate that all spinning generators will contribute to the grid inertia. Inertia is important for grid stability and security because it gives the TSO a leeway to respond to contingencies during grid faults. This happened since inertia resist frequency changes by providing temporary energy extracted from the spinning generators. Inertia will give the TSO ample time to rebalance the supply and demand, maintaining the grid stability.

By increasing more VRE and CIGs to the grid, it will reduce the available inertia since it does not provide power from a rotating machine. The following figure visualise what happened to a grid during a failure due to VRE penetrations.

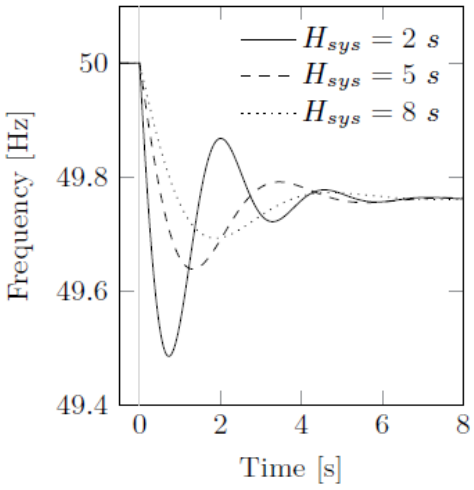

Figure 2.12 Frequency Trajectory for H=2, 5, and 8 s [47]

It can be seen from Figure 2.12 that with the reduction of inertia in the systems, the RoCoF will increase, causing the frequency nadir of the systems to decrease. The lower the frequency nadir, the more danger it brings to the power systems since in the worst case scenario, the UFLS can be triggered, causing a cascaded shutdown off the load, causing massive financial losses and immaterial losses.

Since VREs and CIGs have very small or almost no rotating mass, massive penetration of them will affect the frequency stability of the power grids. One of the solutions to this is by implementing VSM. VSM, is a concept of controlling the converters of CIGs to provide the benefits of SG such as inertia, droop, and damping properties, by mimicking the behavior and dynamics of a real SG [48]. To provide the additional inertia, a short-term energy storage is needed to be able to discharge the energy in times of need [46]. Therefore, VSM actually refers to a complete set of the VRE sources, short-term energy storage, the converters, and the control algorithms [46], [48]. However, academic and industrial applications usually refer VSM as the control algorithms since the VRE sources are typically solar and wind, while the short-term energy storage are usually the DC-link capacitors.

VSM is a relatively novel concept, and the first proposed algorithm was VISMA in [49]. VISMA is modelled by using the higher-order model of SG, and other VSM control algorithms modelled by utilising lower-order model of SG also started to bloom, such as VSYNC [50], Synchronous Power Controller [51], KHI [52], Ise's [53], and Synchronverter [41] which will be studied further in Chapter 3. Also, VSM has also been studied for IM, with the algorithm called Inducverter [54].

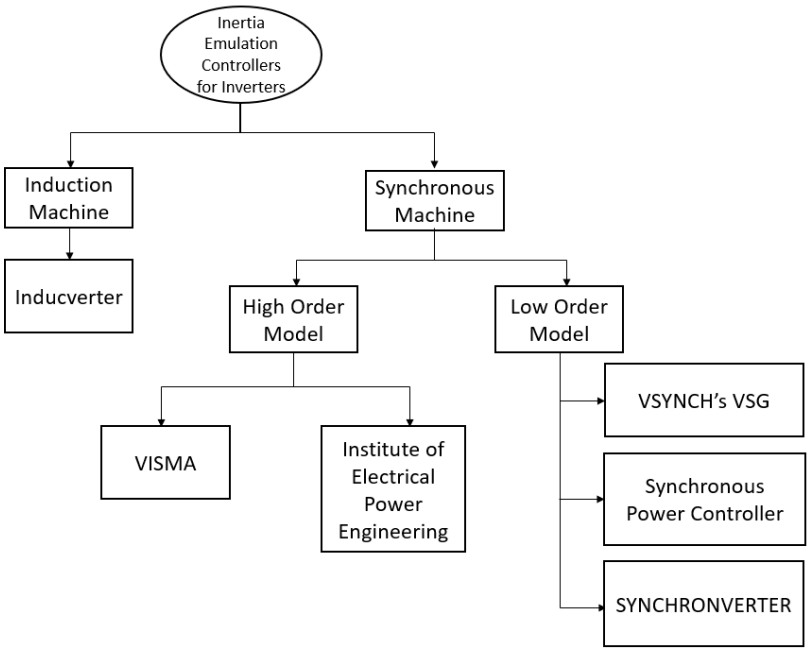

Figure 2.13 VSM Algorithms Tree

An in-depth review of VSM topology can be read further in [55]. As have been explained a bit previously, one of the major difference lies in the mathematical model used. Some implements higher order model, and other algorithms implements the lower order model. Higher order model brings some disadvantages, such as prone to numerical instability. This happened because the SG model involves many derivative and integrative operation. Hence, by having higher order model, it brings issues in numerical instability, slow calculation time, and has higher complexity.

2.6 Introduction to Power System Stability

The electric power systems are sometimes referred to be the world's largest and the most sophisticated system ever made by human. A power system is a network of components that is designed to efficiently transmit and distribute electrical energy. Since power system usually spans a large area, such as a continent or a whole island, maintaining the balance between generation and demand is one of challenge of the TSO. A very complex system will be prone to disturbances and interactions; therefore, it is important to understand how the dynamics and the interactions in power system works.

The formal definition of power system stability has been proposed by the IEEE PES Task Force. This definition is important to provide an easily understood and readily applied physical-based definition. The definition is as follows [12]:

> *"Power system stability is the ability of an electric power system, for a given initial operating condition, to regain a state of operating equilibrium after being subjected to a physical disturbance, with most system variables bounded so that practically the entire system remains intact."*

In conventional power systems stability definition, The IEEE Task Force has classified the power system stability into 3 categories: *rotor angle stability, voltage stability,* and *frequency stability* [56]. This classification is important to conduct the stability analysis, identification of critical elements that cause instabilities, and stability improvement easier. This classification is based on the simplifications, devices, and methods used, as well as the time period, size of the disturbance, and level of detail required to explore the various stability phenomena.

Rotor angle stability refers to the ability of the interconnected synchronous machine to remain in synchronism under normal operating conditions and to re-achieve synchronism after subjected to a small or large disturbances. This type of stability depends on the equilibrium between mechanical torque and electromagnetic torque based on the swing equation and the rotor dynamics [11].

Voltage stability refers to the ability of a power system to maintain steady voltage around the nominal value at all buses in the power systems after subjected to a disturbance. This type of stability depends on the equilibrium between load supply and load demand [11].

Frequency stability refers to the ability of a power system to maintain steady frequency after being subjected to a large contingency causing a significant imbalance between generation and load. This type of stability depends on the ability to restore equilibrium between system generation and load with minimum unintentional loss of load [56].

In 2016, due to the recognition of the issues brought by massive penetration of CIGs to the power systems, a task force has been created by IEEE to analyse the power system dynamics performance, resulting in a new, extended, classification of power system stability in 2020 [12]. This is important since CIGs bring different dynamic behavior compared to the conventional SG. There are 3 main causes for power system stability issues in CIGs: *control interaction, reduction in inertia, low short circuit power* [12]. While reduction in inertia is dominantly affecting the frequency stability and low short circuit power is dominantly affecting the voltage stability, the control interaction here is not properly discussed in the classic definition of power system stability in [56]. Therefore, 2 new categories regarding the control interaction stability were added: *resonance stability* and *converter-driven stability.*

The extended classification of power systems stability can be seen in the following figure.

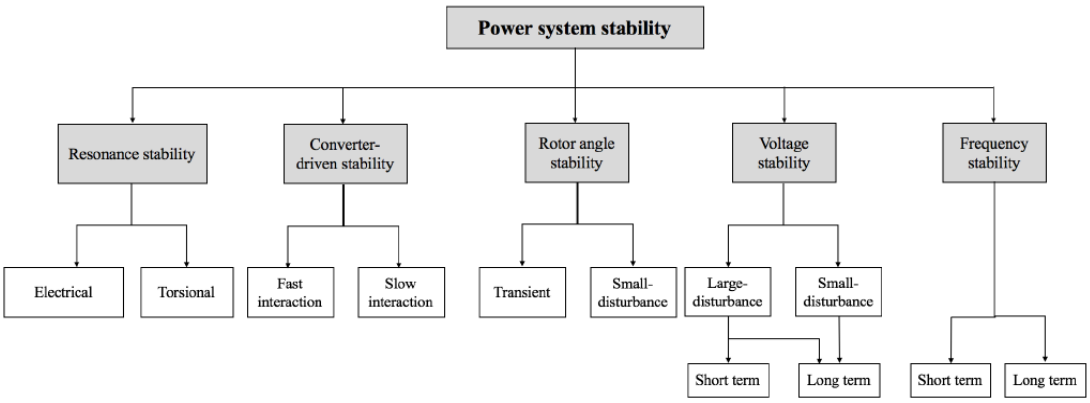

Figure 2.14 New Classification of Power System Stability [11]

Resonance stability refers to the ability of a power system and its component to maintain a non-oscillatory or a bounded, damped, oscillatory energy exchange periodically in terms of voltage or current or torque magnitude. Resonance stability here includes the classic interaction of SSR/SSO, which firstly proposed in 1979 [57]. This type of stability depends on the damping ability of the components [11]. Resonance can happened due to torsional interactions between series compensated transmission lines and the mechanical shaft of the generator's turbine i.e. torsional resonance, or due to pure electrical resonance between the inductance of the IM and the series capacitor i.e. IGE [11].

In this thesis, converter-driven stability will be the focus, and will be explained further in detail in Section 2.7.

2.7 Converter-driven Stability

Converter-driven stability, as one of the newest classifications of power system stability is defined as the ability of the power systems to maintain its stability, generally in terms of synchronising stability and voltage stability in spite of the fast or slow dynamics of the converter controls. It has been explained that the dynamic characteristics of CIG is very different with conventional SG. To understand better, consider the following figure.

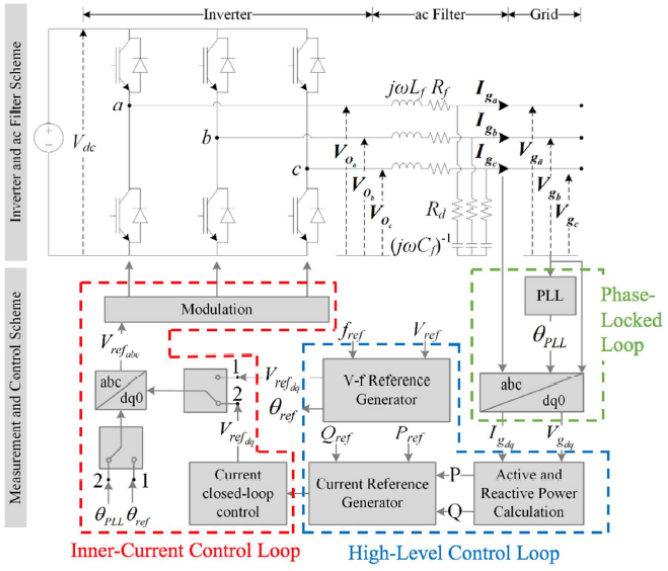

Figure 2.15 Typical Converter Interface and the Control Scheme [12]

Figure 2.15 shows a typical converter interface and control schemes for CIGs. It can be seen that there are 4 major components in a CIGs [12]:

1. The main circuit: consists of the DC bus (which is modelled as a general DC voltage source in Figure 2.15) and the inverter bridge which is responsible to convert the DC signal to AC for interconnection to the power grid.
2. The PLL is responsible to sense and keep track of the frequency and the voltage of the grid to ensure synchronisation between the converter and the power grid. It generates the reference angle for variable transformations (from abc to $dq0$) for control implementations.
3. The high level inverter controls/the outer loop control is the essential control functions which basically provide all the basic and additional features of the converters such as voltage control, active power control, black-start capability, FRT capability, capacity firming, and other ancillary services.
4. The inner loop control is the current control loop to be feeded to the grid based on the output of the outer loop control. This type of control is also known for the much faster response compared to the outer loop control.

To evaluate the CIGs dynamic performance, there are several things that is important to be mulled over:

1. CIGs can only provide limited short circuit current, from 0 p.u to 1.5 p.u [58].
2. PLL and inner loop control is often to have an oscillatory response due to their typical high gain constant. Also, this might happen when the PLL cannot quickly synchronise with the grids. A typical SCR for this event to be possible is around 1.5 to 2 [12].
3. The overall dynamic response of CIGs is largely determined by the characteristics of the PLL, the inner loop control, and the outer loop control [12].

In power electronics switches, the switching frequency can vary in the kHz range, while most other controllers in power systems frequency is typically in around 1 to 10 Hz. Therefore, CIGs can impact a wide range of dynamic phenomena, ranging from electromagnetic phenomena to electromechanical phenomena as shown in Figure 1.3. The fast and slow interaction converter-driven stability are differentiated based on the frequency of the observed scenario [12]. A short overview on each of the two types of converter-driven stability will be discussed in the following sections.

2.7.1 Fast-Interaction Converter-driven Stability

As explained previously, fast-interaction converter-driven stability happened due to the fast dynamic interactions between the control systems of the converters with fast response component of power systems. The converters being discussed is not limited to CIGs, but it also includes HVDC, CIL, FACTS, etc. Fast response component of power systems refers to not only conventional components such as stator dynamics, LCL filters, or other converters. The typical frequency range for fast-interaction converter-driven stability is from >50 Hz, to hundreds and even kHz [12], [59]. This type of stability has also been referred to as harmonic stability [59].

Several examples of fast-interaction instability issues have been recorded and studied. For example, interactions that appears due to the coupling between converters and grids [60]. Another example is some high frequency oscillations due to large scale wind farms connected to VSC-HVDC [61], [62]. LCL filter interactions with its own converter controls and other nearby inverters can also cause high frequency oscillations [63]. Other example are interactions between STATCOM and weak grids in China, causing oscillations at 2.5 Hz

and 97.5 Hz [64]. Having a high frequency oscillation due to mutual interaction between the control loops of converters is also possible [65]. A high frequency oscillation is also recorded for a CPL in microgrid [66].

2.7.2 Slow-Interaction Converter-driven Stability

While fast-interaction converter-driven stability happened due to the fast dynamic interaction, a slow-interaction converter-driven stability happened due to the slow dynamic interactions of the converter's control systems such as PLL and the outer loop, with the slow response component of power systems i.e., generator AVR and governor. The typical frequency range for slow-interaction converter-driven stability is from <50 Hz, sometimes even reaching <10 Hz [12], [59]. Slow-interaction converter-driven stability in a sense is similar to voltage stability. The difference lies in the driver of the stability, i.e. for voltage stability, it depends on loads while for converter-driven, it depends on the converter controls [12].

One of the most important factor in a low frequency oscillation is the grid strength, indicated by the value of SCR. Typically, a weak grid has SCR < 2 or 3 [67]–[72], and the characteristics of a weak grid will be explained further in chapter 5. One thing that can be confirmed is that in a weak grid, low frequency oscillation have a higher tendency to appear and can grows into an undamped oscillation [12].

Other factors that might have an effect on low frequency oscillation is due to the PLL. It has been recorded that the high gain value of PLL might introduce a negative admittance as seen from the system, causing an error in the value for angle tracking [16]. CIGs capacity and the control strategies and tuning parameter might also cause a low frequency oscillation as seen in [73]–[75].

Chapter 3

Synchronverter-based Technology for Wind Energy Conversion System

This chapter will dive deeper to understand the Synchronverter control technique of both inverter and rectifier for WECS application. The SLD of the system will be explained in detail, and a model validation will be conducted as well with a simulation scenario from Texas Panhandle Wind Power System [23]. This chapter will mostly involve material from [33], [34], [41], [76] *for the basic theory regarding Synchronverter-based WECS.*

3.1 Grid Side - Inverter Control

Synchronverter was first introduced in 2011 as one of the earliest topology of VSM [41]. As explained in the previous chapter that a VSM is a control strategy for a converter to mimic a SM, Synchronverter can be considered one of the pioneer of the VSM [77].

The first Synchronverter schemes being proposed at [41] discussed about the inverter application with an ideal DC voltage source. Therefore, the first section of this thesis will discuss the GSC or the inverter control part to introduce the basic knowledge of Synchronverter. Consider the following figure.

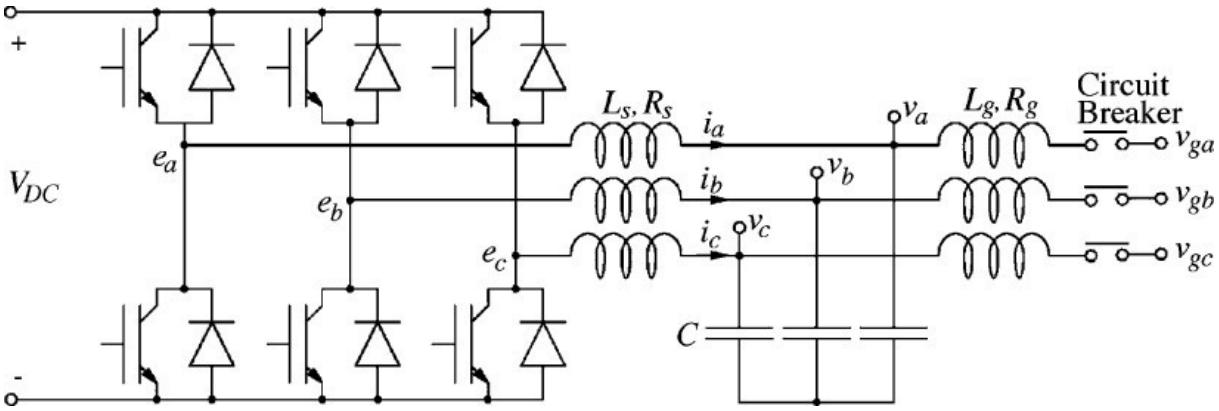

Figure 3.1 Schematics of a Typical Inverter [41]

From Figure 3.1, L_s and R_s are the stator inductance and resistance of the virtual SG [41]. Therefore, it can be deduced that the terminal voltages of the Synchronverter will be the capacitor voltages, and the output of the inverter will be the EMF, e. The capacitor here acts as a filter to alleviate the ripple effect.

The Synchronverter controller will implement the mathematical model derived in Section 2.3.1. Besides the swing equation, the 4 equations derived in Section 2.3.1, namely equation (26), (28), (29), and (30) will be used as well [41]. The output from the control system will generate a signal for the PWM, which will be used to control the IGBT switching of the inverter. The GSC's objective here is for active and reactive power injection to the

grid. The GSC will consider the MPPT set-point, the grid voltage, and the frequency. The control scheme can be seen in the following figure.

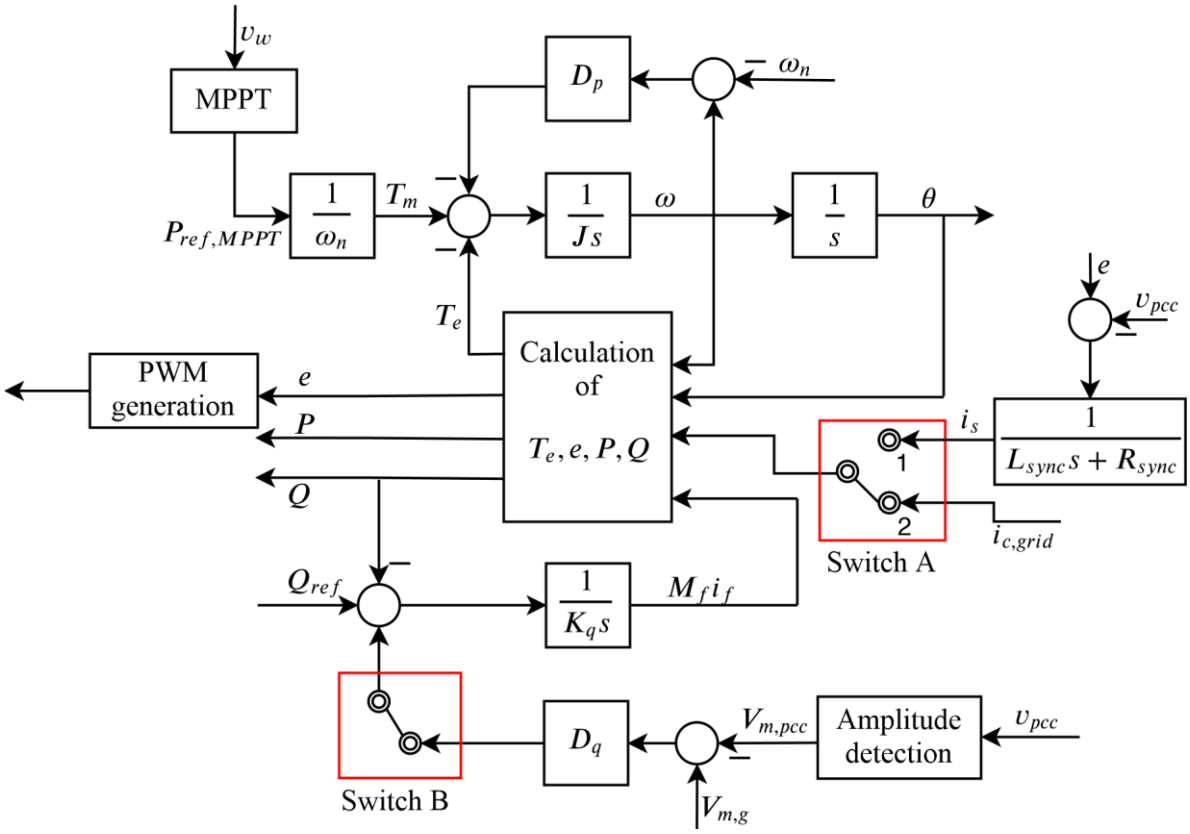

Figure 3.2 WECS-GSC Control Structure [34], [41], [78]

There exist 2 main outer loops of the GSC control, the upper loop which regulates the active power (APL) and the lower loop which regulates the reactive power (RPL). The inner control of Synchronverter involves the 4 equations:

$$e = M_f i_f \omega \widetilde{\sin\theta} \tag{38}$$

$$T_e = M_f i_f \langle i_{c,grid}, \widetilde{\sin\theta} \rangle \tag{39}$$

$$P = \omega M_f i_f \langle i_{c,grid}, \widetilde{\sin\theta} \rangle \tag{40}$$

$$Q = -\omega M_f i_f \langle i_{c,grid}, \widetilde{\cos\theta} \rangle \tag{41}$$

From the 4 equations given above and the control structure, it is clear that the GSC control need 4 inputs: P_{ref}, Q_{ref}, $i_{c,grid}$, and v_{pcc} where each of them are the active power reference, reactive power reference, output current from the inverter, and the PCC voltage respectively. In the WECS, it can also be seen from the schematics that the P_{ref} comes from the wind speed, v_w which has been feeded to the MPPT algorithm as modelled in equation (9). In this thesis, the wind speed will be assumed constant. Hence, no MPPT algorithm modelling involved.

The mechanical torque, T_m is obtained from the following equation

$$T_m = \frac{P_{ref}}{\omega_n} \tag{42}$$

where ω_n is the nominal frequency. Q_{ref} is defined by the TSO's request since usually power plants are operating in (P,PF) control mode. In this thesis, Q_{ref} is set as 0, assuming that

the WECS operate at unity PF. The grid parameters such as current and voltage are obtained through measurement sensors.

3.1.1 Active Power Control

As introduced previously, the APL is one of the outer loop controls that is shown in the upper part of the GSC control structure. The APL is utilising the swing equation using the T_m, T_e and $D_p\omega$ as follows,

$$\dot{\omega} = \frac{1}{J}\left(T_m - T_e - D_p\omega\right) \tag{43}$$

where T_m can be calculated using equation (42), T_e using equation (39). D_p is the frequency droop coefficient which can be considered as the droop coefficient of a conventional SG [33]. By feeding the difference of the torque and the $D_p\omega$ into an integrator with an inertia constant $\frac{1}{J}$, it will result in the converter speed ω. The droop constant is defined as

$$D_p = -\frac{\Delta T}{\Delta\omega} \tag{44}$$

Conventionally, droop constant in power system dynamics is referred to the percentage that extracts the full rated power from the SG, R. This droop constant D_p is related to that by the following equation.

$$\frac{1}{R} = \frac{2\pi S_n}{D_p\omega_n} \tag{45}$$

where S_n is the full power of the power plants, ω_n in this equation is the synchronous angular frequency of the grid [79].

From the swing equation and the control structure, the frequency regulation strategy can be explained. The droop feedback will be depending on the error between the converter speed and the frequency reference. If, for example, the error is positive i.e., $\omega > \omega_n$, the droop feedback will be negative. This will deliver a decrease of torque set-point in the Synchronverter, achieving the required frequency regulation. The same can be explained if the error is negative i.e., $\omega < \omega_n$. In this case, the droop feedback will be positive and the torque set-point will be increased to achieve the required frequency.

By integrating the obtained ω, the phase angle θ can be obtained. From this, equation (38), (39), (40), and (41) can be utilised to obtain the desired variable of e, T_e, P, and Q.

3.1.2 Reactive Power Control

While the APL is in the upper part of the control scheme, the lower part is the RPL and it is the other part of the outer loop control. It has 2 main parts, which are the voltage droop part and the reactive power regulation part. As explained previously, the Q_{ref} is set by the TSO since power plants are usually operating at (P,PF) control mode. The actual reactive power injected to the grid will be calculated from equation (41). By feeding the reactive power error to the $\frac{1}{K_q}$ integrator block, the virtual excitation $M_f i_f$ will be obtained. This virtual excitation will be used to calculate the e, T_e, P, and Q.

The voltage droop works similarly as in the frequency droop of the APL. The error of the voltage amplitude between the PCC voltage, $v_{m,pcc}$ and the reference voltage $v_{m,g}$ will be feeded to the voltage droop constant, D_q. This will serve as one of the inputs to the reactive

power error measurements. Switch B is included to set the operating mode of the GSC, whether to operates in droop control mode or in islanded (isochronous) mode. The D_q is also similar to D_p as follows,

$$D_q = -\frac{\Delta Q}{\Delta V} \tag{46}$$

where ΔQ is the required change in reactive power needed to change the voltage ΔV volts. Note that the voltage droop in Figure 3.2 can be disabled by opening switch B. The voltage regulation strategy is also very similar to the frequency regulation strategy, i.e., positive error will result in negative damping to decrease the reactive power injection, leading to decrease in voltage.

It can be seen that the RPL resulting in $M_f i_f$. Considering that the inner control of Synchronverter consist of equations involving $M_f i_f$ and ω, both APL and RPL is a must to ensure that the Synchronverter operation works.

3.1.3 Amplitude Detection

From the RPL, it has been explained that the voltage droop works by comparing the voltage amplitude. Therefore, an amplitude detection system needs to be implemented as well inside the control strategy. Usually, a PLL is used to obtain this variable. However, in this thesis, the converter will not implement PLL at all. The synchronisation strategies without PLL will be explained in the next section and this section will focus on technique to obtain the voltage amplitude without utilising PLL.

Here, the Clarke transform will be used to obtain the voltage amplitude. The Clarke transform will transform the abc signals to $\alpha\beta\gamma$ signals. The transformation matrix is as follows [80],

$$v_{\alpha\beta\gamma} = \begin{bmatrix} v_\alpha \\ v_\beta \\ v_\gamma \end{bmatrix} = \frac{2}{3}\begin{bmatrix} 1 & -\frac{1}{2} & -\frac{1}{2} \\ 0 & \frac{\sqrt{3}}{2} & -\frac{\sqrt{3}}{2} \\ \frac{1}{2} & \frac{1}{2} & \frac{1}{2} \end{bmatrix}\begin{bmatrix} v_a \\ v_b \\ v_c \end{bmatrix} \tag{47}$$

In a balanced three phase system, $\boldsymbol{v_\gamma} = 0$. Therefore, the transformation matrix can be simplified as

$$v_{\alpha\beta} = \begin{bmatrix} v_\alpha \\ v_\beta \end{bmatrix} = \frac{2}{3}\begin{bmatrix} 1 & -\frac{1}{2} & -\frac{1}{2} \\ 0 & \frac{\sqrt{3}}{2} & -\frac{\sqrt{3}}{2} \end{bmatrix}\begin{bmatrix} v_a \\ v_b \\ v_c \end{bmatrix} \tag{48}$$

From equation (48), it is clear that

$$v_\alpha = \frac{2}{3}v_a - \frac{1}{3}(v_b + v_c) \tag{49}$$

$$v_\beta = \frac{\sqrt{3}}{3}(v_b - v_c) \tag{50}$$

The amplitude will then obtainable from simple resultant as

$$v_m = \sqrt{v_\alpha^2 + v_\beta^2} \tag{51}$$

3.1.4 Self-Synchronisation

It was mentioned in the previous section that PLL is not being implemented in this thesis. Therefore, a new strategy to synchronise with the grid without PLL will be presented here in this section [76].

The active and reactive powers injected to the grid by an SG as follows,

$$P = \frac{3V_g E}{2X} sin(\theta - \theta_g) \tag{52}$$

$$Q = \frac{3V_g}{2X}\left[Ecos(\theta - \theta_g) - V_g\right] \tag{53}$$

Here, the variables in the equation are in the forms of amplitude i.e., V_g is the grid voltage amplitude and E is the amplitude of the SG's EMF. Also, θ is the phase angle of machine and θ_g is the phase angle of the grid, and X is the synchronous reactance of the machine. To synchronise the converter with the grid, there are 3 things that need to be considered: *voltage*, *frequency*, and *phase angle*. Since the frequency can be tracked later after the synchronisation with the grid, the only variables needed to be considered now is the voltage and the phase angle [76]. Mathematically, it can be expressed as

$$E\angle\theta = V_g\angle\theta_g \tag{54}$$

To fulfil equation (54), it can be seen that $E = V_g$ and $\theta = \theta_g$. And by having those two conditions, equation (52) and (53) will be 0. In the synchronverter algorithm, it is simple to realise this by setting P_{ref} and Q_{ref} as 0.

However, before the converter is connected to the grid, the output current of the inverter will be 0 as well. Therefore, $i_{c,grid}$ will not be able to be used as the feedback variable of the control algorithms. Hence, a virtual impedance will be implemented to obtain a virtual synchronising current $\boldsymbol{i_s}$, creating a specific self-synchronisation algorithm which will be switched-off when the converter has synchronised with the grid successfully. The formula can be seen as described below.

$$i_s = \frac{1}{s \times L_{sync} + R_{sync}}\left(e - v_{pcc}\right) \tag{55}$$

This synchronising current will be feeded to the control system to track the e so that equation (54) can be satisfied i.e., GSC synchronised with the grid. It is noticeable that i_s will be controlled to be 0 so that the condition for equation (54) fulfilled, i.e., $e = v_{pcc}$.

From equation (55), R_{sync} is the virtual resistor and L_{sync} is the virtual inductor. The virtual impedance value can be chosen arbitrarily since the virtual synchronising current will only used to control the e. Small values of the virtual impedance might cause a large transient current that might hasten up the synchronisation process. However, if the chosen values of the virtual impedance is too small, it might cause oscillations [76]. Normally, the virtual impedance value will be slightly smaller than the stator impedance.

It is also worth to note that during the synchronisation process, the virtual impedance block acts as a filter [76]. Therefore, the chosen values of the virtual impedance have an impact for filtering the harmonics in v_{pcc} at the synchronisation process. The cut-off frequency of the filter can be determined from the ratio of the virtual impedance, i.e., $\frac{R_{sync}}{L_{sync}}$.

3.1.5 Set-Point Limiter and Saturation

During the operation of the GSC, sometimes the control algorithms might cause the operating point to operate beyond the capability curve of the converters. This might cause

an issue since converters are one of the most expensive components and it is prone to damages due to the power electronics component. Therefore, an algorithm to ensure the injected power of the converter will not exceed the rated apparent power is needed and will be described below. The desired operating point is

$$\sqrt{P_{set}^2 + Q_{set}^2} \leq S_n \tag{56}$$

From the Synchronverter mathematical model, the desired set-point can be re-expressed as

$$P_{set} = \left(T_m - D_p(\omega - \omega_n)\right)\omega_n \tag{57}$$

$$Q_{set} = Q_{ref} + D_q\left(V_{m,g} - V_{m,pcc}\right) \tag{58}$$

An IF logic is implemented if equation (56) not fulfilled. By prioritising active power over reactive power, a simple resultant operation can be used to determine the Q_{set}.

$$Q_{set} = \sqrt{S_n^2 - P_{set}^2} \tag{59}$$

To ensure the GSC does not absorb reactive power, it can be added other criteria of Q_{set} as $Q_{set} \geq 0$. In this case, the GSC will always operate in inductive (generator inductive, not load inductive, i.e., will never absorb reactive power) mode. Hence, the GSC will operate only on the 1st quadrant of the capability curve shown below. Dotted line indicates the III and the IV-quadrant, in which the inverter will not operate.

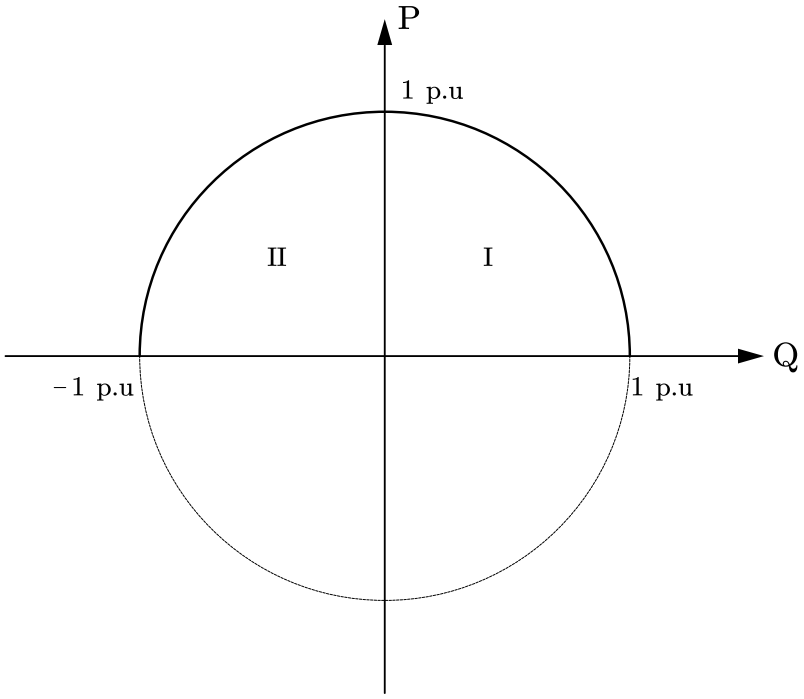

Figure 3.3 Inverter Capability Curve

3.2 Rotor Side - Rectifier Control

In this thesis, the RSC part of the WECS will also be using Synchronverter algorithm. While for GSC it mostly for active and reactive power control, the RSC will be utilised for the DC link voltage control. The rectifier now will be operated as an SM instead of the rectifier where it was operated as an SG. Consider the following schematics.

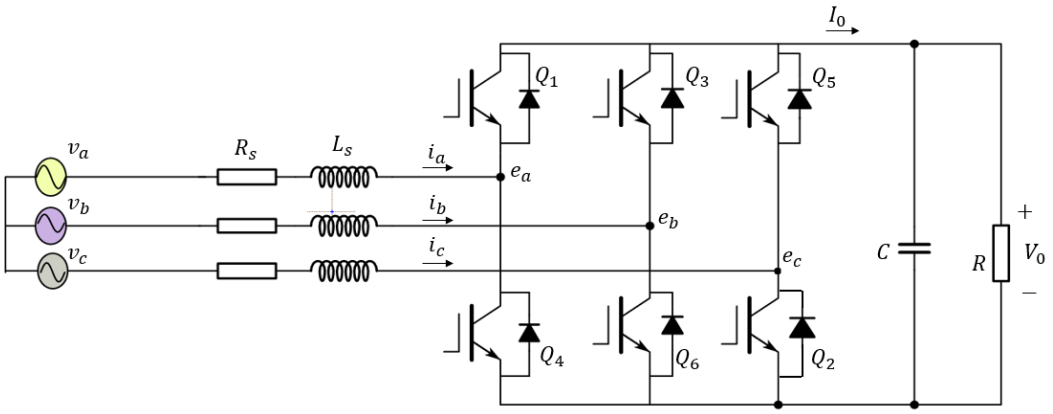

Figure 3.4 Schematics of a Typical Rectifier

From Figure 3.4, L_s and R_s are the rotor inductance and resistance of the virtual SG, similar to the GSC part. It can also be deduced that the terminal voltages of the converter will be the EMF, e. The Synchronverter controller will implement the mathematical model derived in Section 2.3.2. The control scheme can be seen in the following figure.

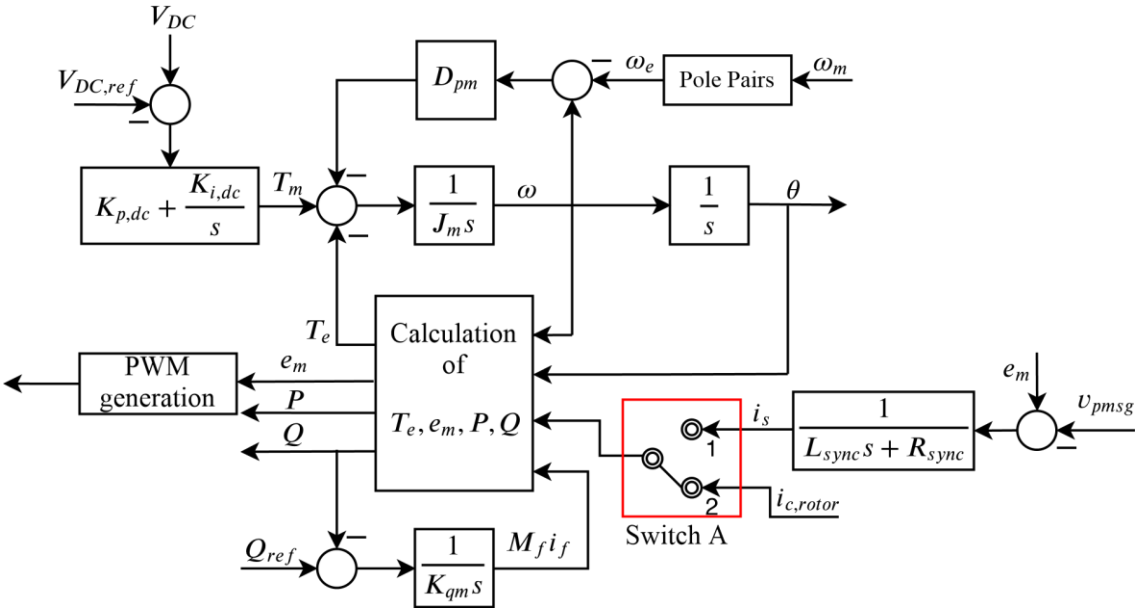

Figure 3.5 WECS-RSC Control Structure [33], [78]

It can be seen (and have been explained in the previous chapter and section) that the inner loop control is exactly the same as in the GSC part. The only difference is the control objective and the input. The output from the control system will generate a signal for the PWM, which will be used to control the IGBT switching of the rectifier. The RSC will consider the DC link voltage, the rectifier current, Q_{ref}, and the mechanical rotation speed as the input.

3.2.1 DC Voltage Control

From the control topology, it can be seen that the DC voltage control loop is located at the upper loop and is utilising the swing equation for frequency droop. To obtain the mechanical torque as the reference for the swing equation, the DC voltage error will be feeded to a PI controller. The PI controller will be a typical PI controller, i.e., $K_{p,DC} + \frac{K_{i,DC}}{s}$.

For the frequency, the motor rotational speed ω_m will be multiplied by the pole pairs to obtain the electrical frequency of the motor ω_e. All the other parameters, such as D_{pm} and J_m have the same definition as the GSC counterpart.

3.2.2 Reactive Power Control

The RPL of the RSC part is also in the lower part, similar to the GSC control part. The difference is that there is no droop control mode being implemented in the RSC part. This is due to the interaction of the RSC is not with the grid directly, but with the DC link capacitor and the GSC. Therefore, a droop control mode is not required.

Again, similar to the GSC counterpart, the reactive power error will be feeded to an integrator with the gain of $\frac{1}{K_{q,m}}$. This will create a virtual excitation $M_f i_f$ which will be used to obtain every parameter required in the inner loop control.

3.2.3 Self-Synchronisation

The synchronisation is required for the RSC to synchronise with the frequency and the voltage of the PMSG. This is important since previously, the rectifier works as an uncontrolled 3-phase diode rectifier [81]. Therefore, it is necessary to limit the high inrush currents flowing into the rectifier from the PMSG due to the transients [81].

The synchronisation method applied here is similar as shown in section 3.1.4. By applying virtual impedance, then the virtual synchronising current will be

$$i_s = \frac{1}{s \times L_{sync} + R_{sync}} \left(v_{pmsg} - e\right) \tag{60}$$

But since it is a SM, then the feedback current will be $-i_s$. Therefore, the virtual current will need to be rearranged as follows,

$$i_s = \frac{1}{s \times L_{sync} + R_{sync}} \left(e - v_{pmsg}\right) \tag{61}$$

i_s will then be feeded to the control system to track the e so that $e = v_{pmsg}$ by setting $i_s = 0$.

3.3 System Schematics

Both of the GSC and RSC control techniques based on Synchronverter have been explained in Sections 3.1 and 3.2 and will be used to control a wind farm which will be connected to the grid. The full system schematics (both the SLD and the control block) is shown at Figure 3.6.

The system being studied in this thesis depicts an SMIB which instead of a SG connected to the grid, will consists of a type IV wind turbine connected to an infinite bus. The wind turbine is driving a PMSG. On the DC link between the converters, there is a capacitor, C_{DC}, and a chopper resistor, $R_{chopper}$. The chopper resistor is connected using a controlled IGBT, and the objective of $R_{chopper}$ is to protect the DC link from overvoltage [82]. Excess energy can be dissipated in the chopper resistor instead of the converters by connecting the resistor when the DC voltage reaches a certain threshold, preventing damage to the converters. $R_{chopper}$ is designed based on the rated power of the system and can be calculated as follows [83],

$$R_{chopper} = \frac{V_{DC,ref}^2}{P_{rated}} \quad (62)$$

Besides the WECS and the grid part (which includes R_g and L_g as the grid impedance), the system also has a filter. This filter is used to filter harmonics so the power quality from the WECS will comply with the grid codes [84].

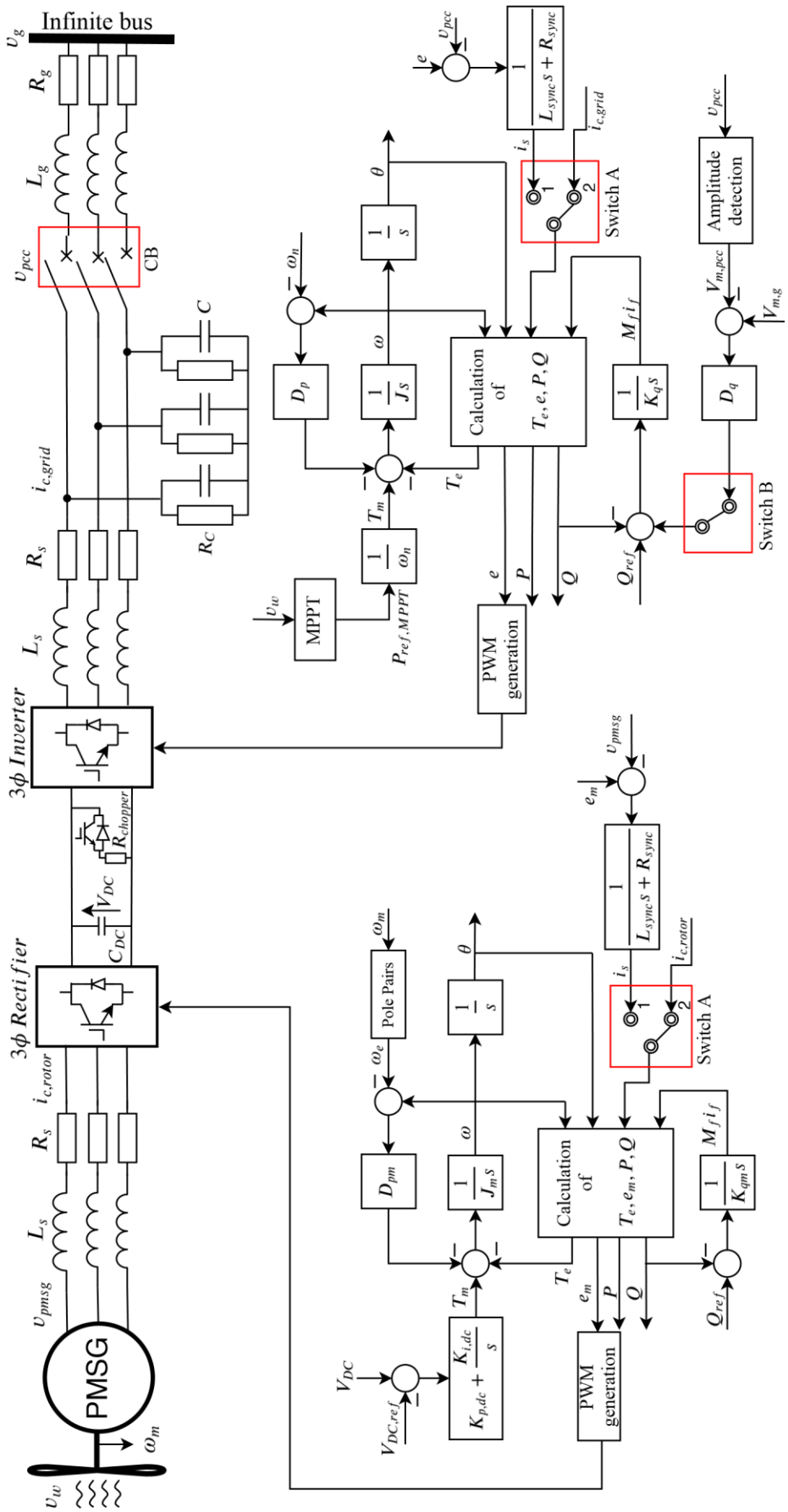

Figure 3.6 Complete System Schematics [78]

3.4 Simulations and Results

The model explained in this chapter will be the base model which will be used for all studies in this thesis. Therefore, a validation needs to be conducted to ensure that the WECS built here works properly.

The scenario to conduct the experiment will be based on Texas Panhandle Wind Power Systems validation scenario with some modifications [23]. The operating mode of the WECS will be in droop mode. However, the impact of the voltage droop here will be assessed and analysed.

The simulation scenario is as follows:

1. With initial wind speed of 12 m/s, all IGBT off to let the RSC operates as a diode rectifier i.e., self-sync mode with $Q_{ref} = 0$.
2. GSC also operates at self-sync mode with $P_{ref} = Q_{ref} = 0$ and CB opened.
3. At $t = 0.5\,s$, IGBT of RSC operates with $Q_{ref} = 0$. $V_{ref} = 1126.8\,V$ as stated in the Appendix.
4. At $t = 1\,s$, IGBT of GSC operates with $P_{ref} = Q_{ref} = 0$ and CB closed.
5. At $t = 2\,s$, DC load is disconnected and GSC operates with $P_{ref} = 0.8P_w$ and $Q_{ref} = 0$.
6. At $t = 3.5\,s$, 50% grid voltage drop is applied, which is recovered after 5 cycles.

3.4.1 WECS with Voltage Droop

The following simulation results for the simulation of the WECS under voltage droop mode are obtained.

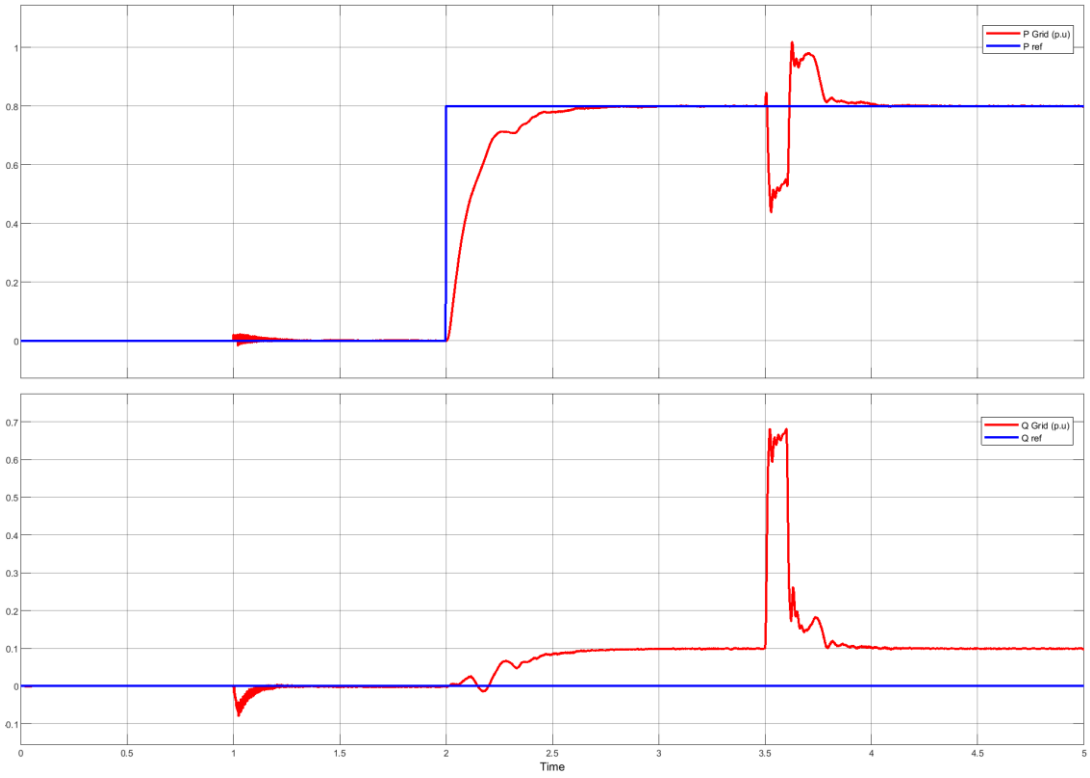

Figure 3.7 Active and Reactive Power in p.u. Injected to the Grid (Voltage Droop Mode)

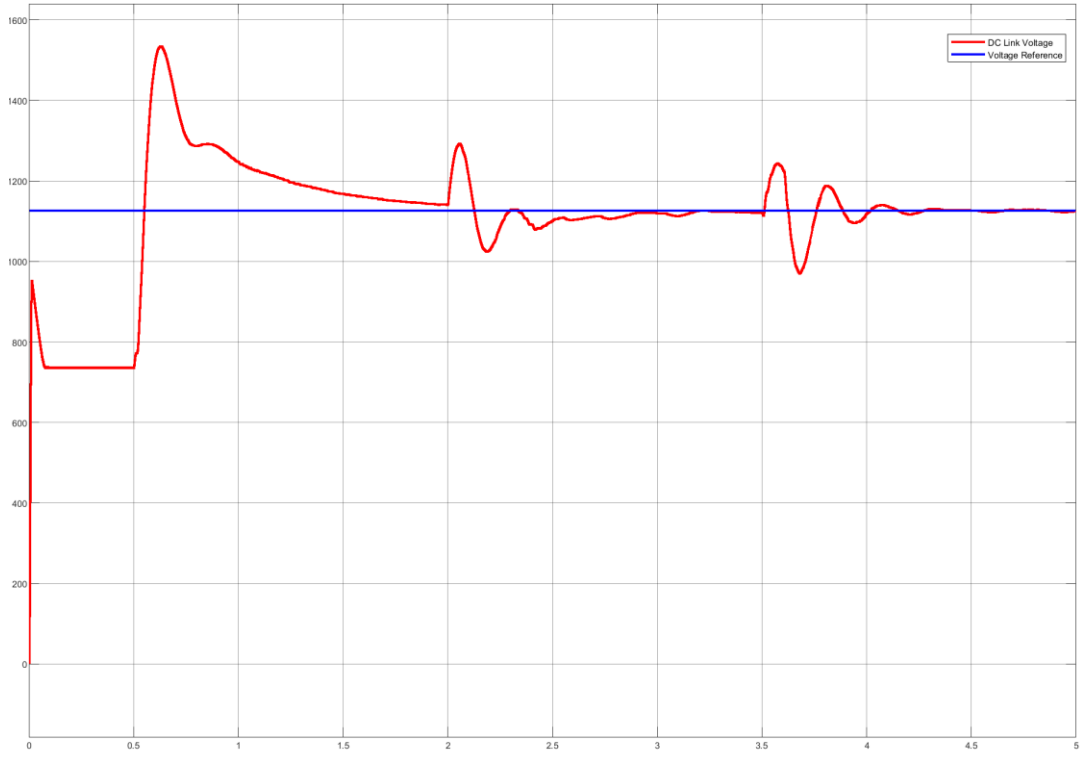

Figure 3.8 DC Link Voltage (Voltage Droop Mode)

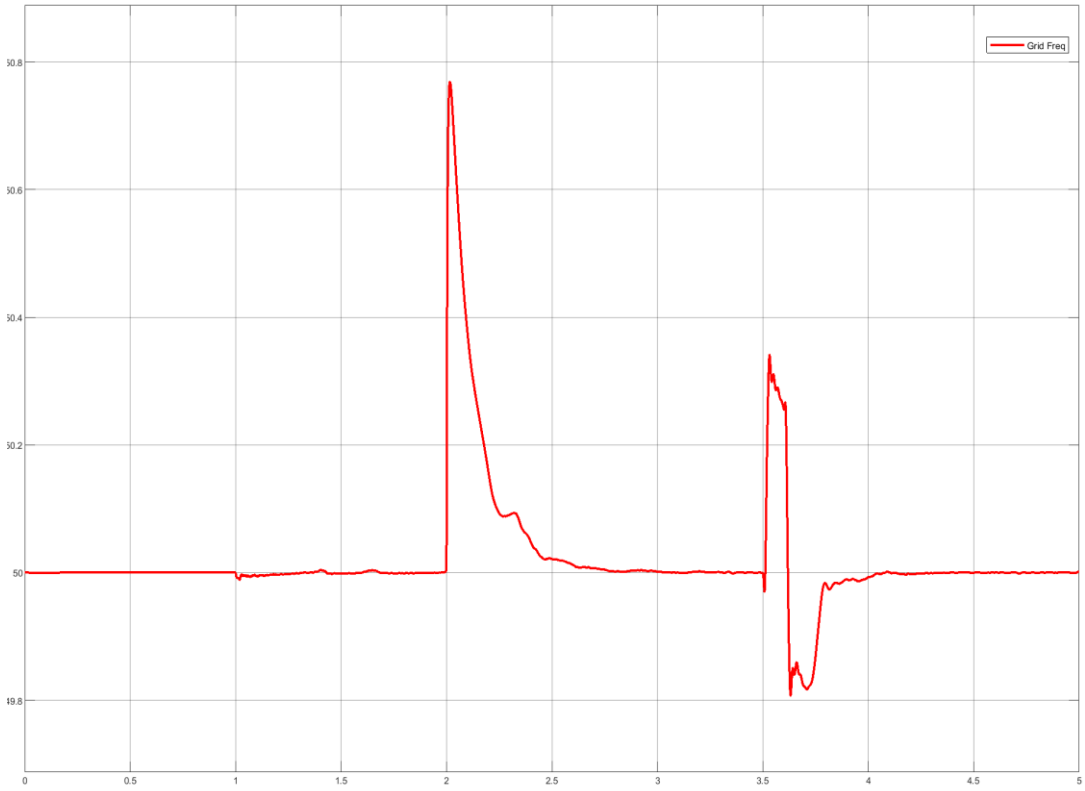

Figure 3.9 Grid Frequency (Voltage Droop Mode)

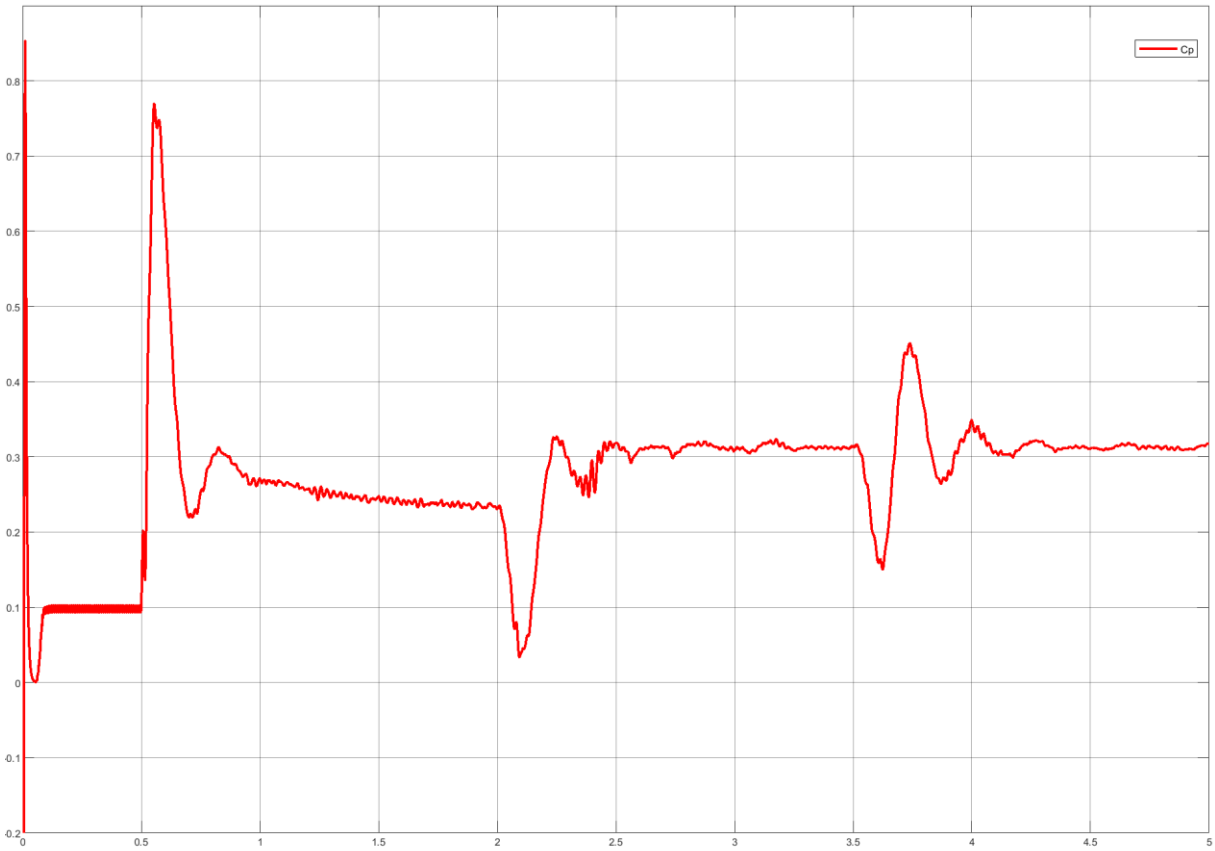

Figure 3.10 Wind Turbine Power Coefficient (Voltage Droop Mode)

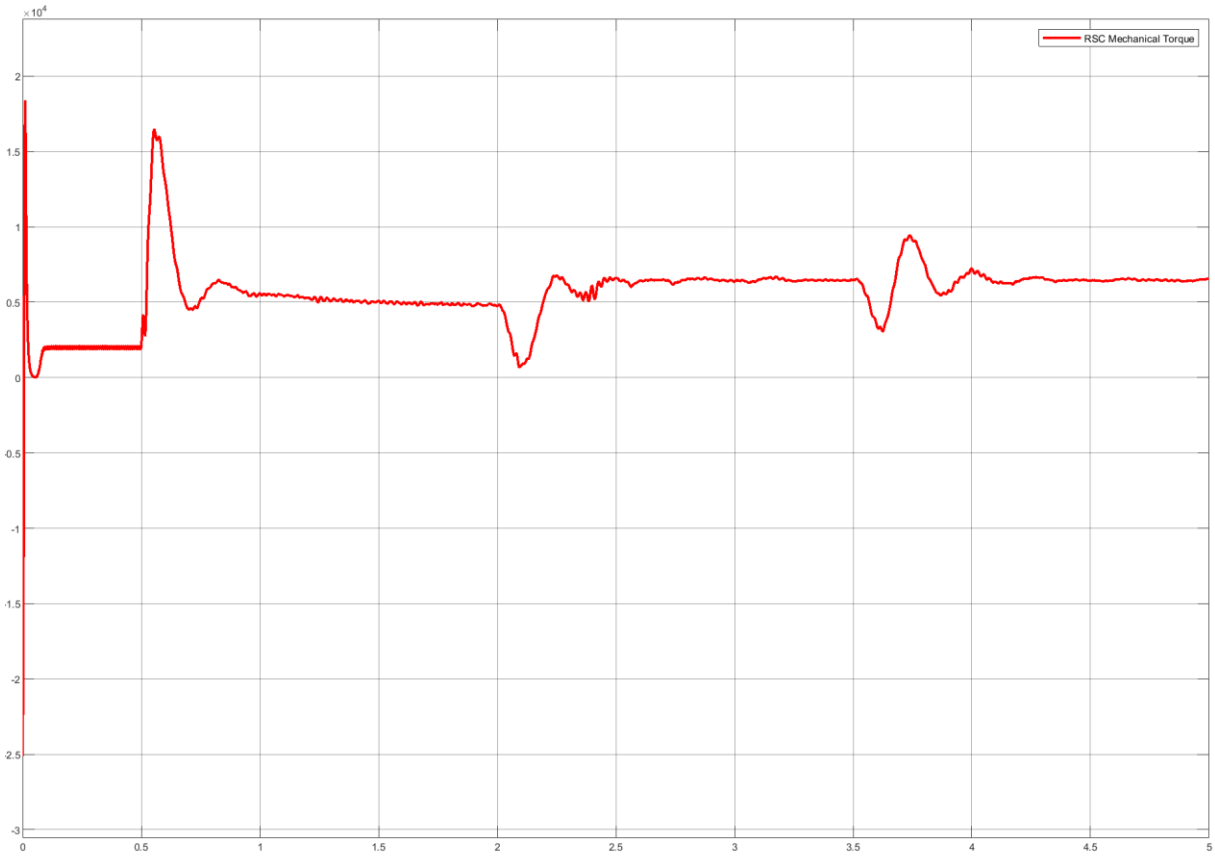

Figure 3.11 RSC Mechanical Torque (Voltage Droop Mode)

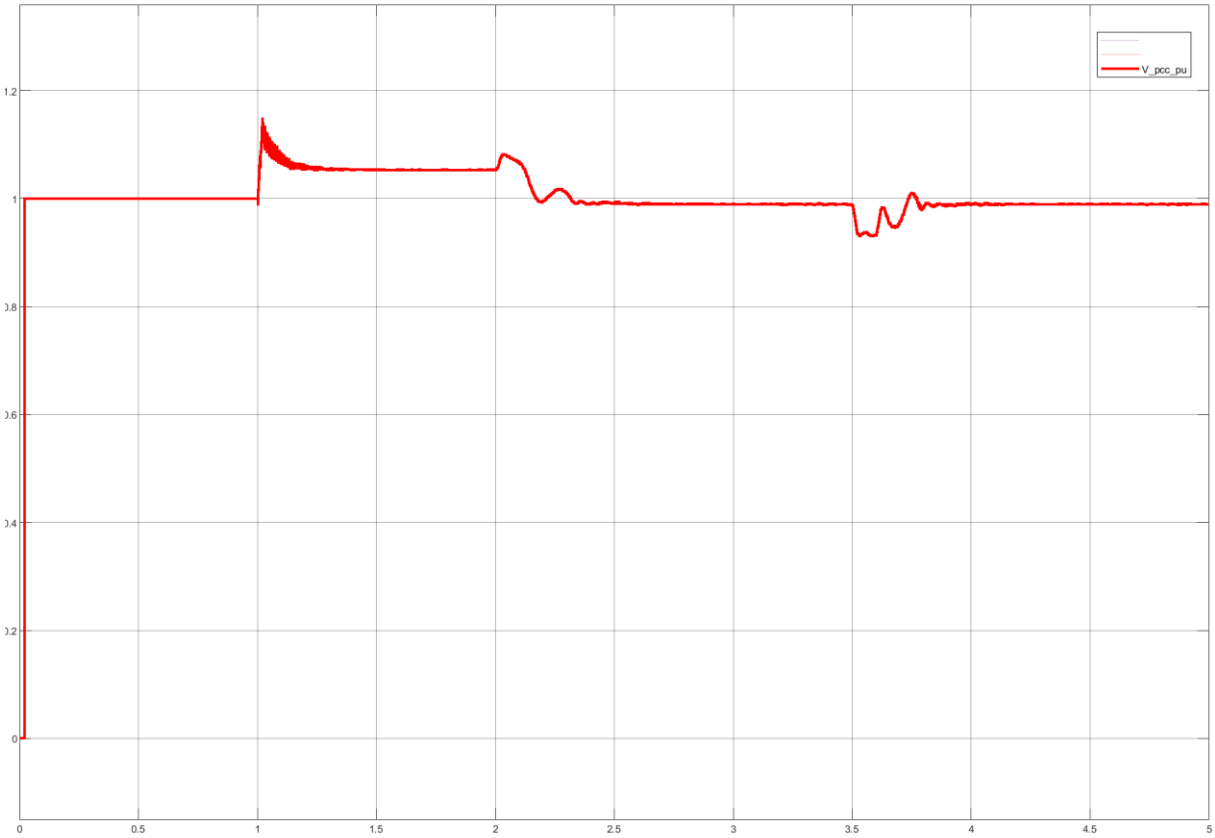

Figure 3.12 PCC Voltage in p.u. (Voltage Droop Mode)

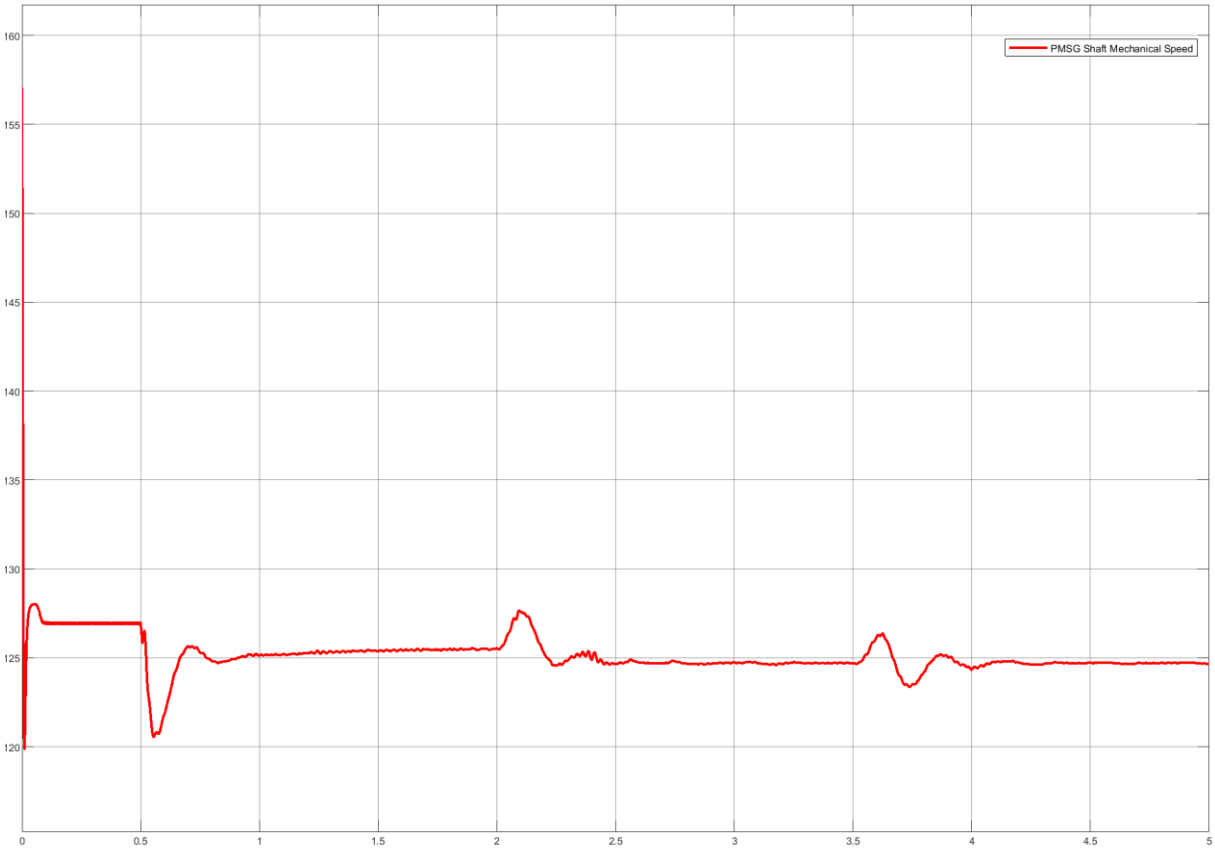

Figure 3.13 PMSG Shaft Mechanical Speed (Voltage Droop Mode)

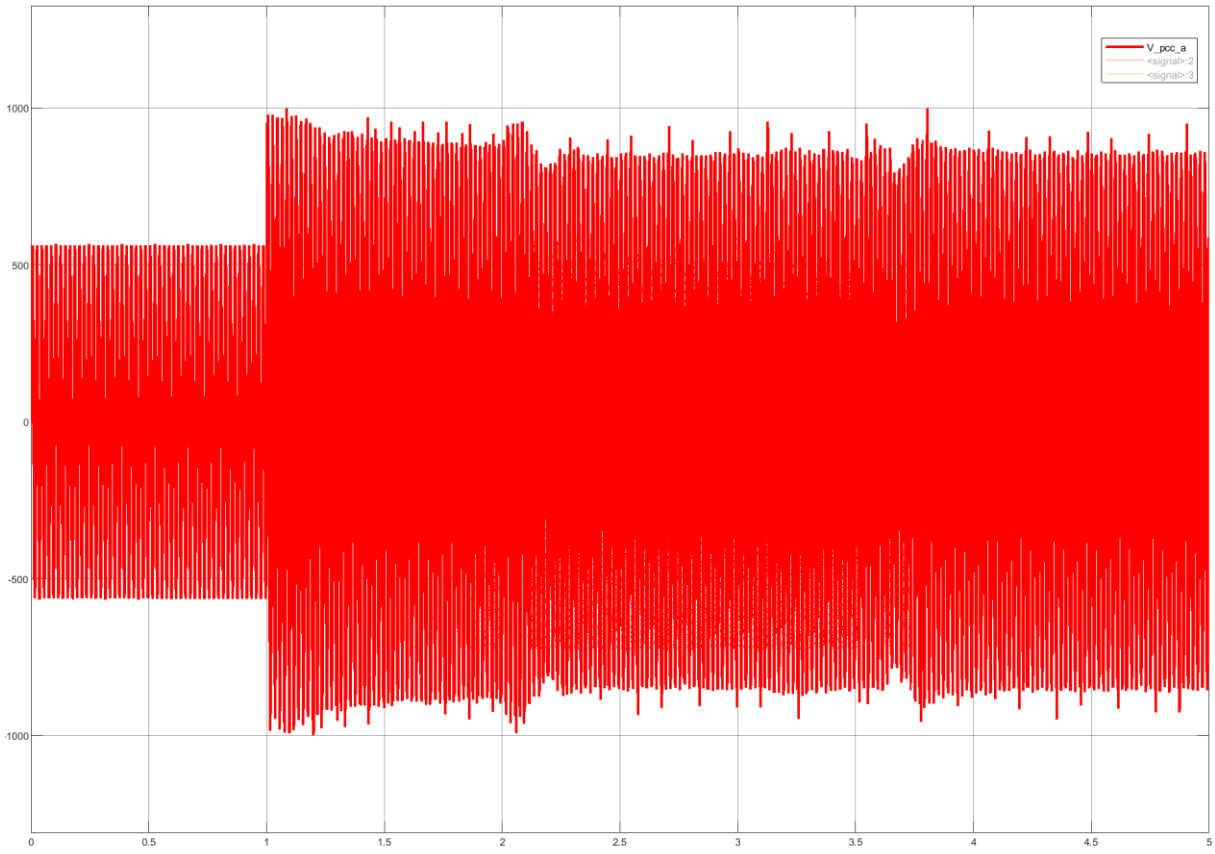

Figure 3.14 PCC Voltage in V (Voltage Droop Mode)

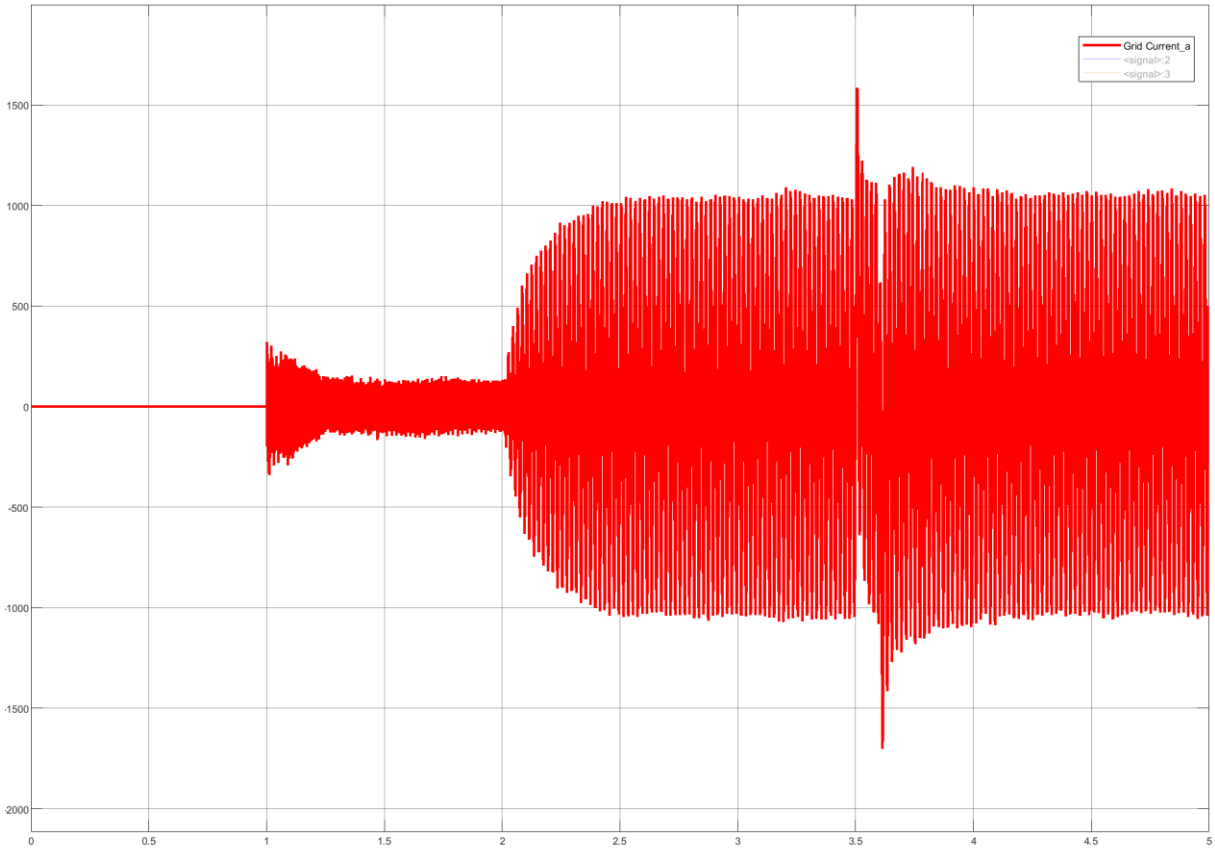

Figure 3.15 PCC Current in A (Voltage Droop Mode)

As shown in the figures above, both the GSC and the RSC works properly. It can be seen that the DC link voltage is regulated properly. It can also be seen that during the synchronisation process of the GSC, the dynamics of the power being injected oscillates a bit and settles in less than 0.5 s, indicating that the synchronisation works properly. Furthermore, the successful synchronisation can be assured from the PCC voltage and current which shows no unstable oscillation. Hence, the self-synchronisation technique by utlising virtual impedance proposed in this thesis works successfully.

It is interesting to see that at t = 2s, the PMSG rotates faster (the grid frequency increased as well) while the torque and the power coefficient decreases. It is due to the sudden load that felt by the wind turbine, in which after a quick moment, the PMSG slows down and the torque increases, and active power is started to be injected to the grid.

At t = 3.5s, when the voltage drops to 0.5 p.u, the active power sent to the grid drops to around 0.4 p.u while the reactive power increases to almost 0.7 p.u. This shows that the voltage droop works by injecting reactive power to properly balance the voltage according to the droop constant being used. When the voltage recovers, transient period exist for both the active and reactive power, reaching the initial stable condition.

The simulation results show that the WECS model built with voltage droop worked as expected.

3.4.2 WECS without Voltage Droop

The following simulation results for the simulation of the WECS without voltage droop mode are obtained.

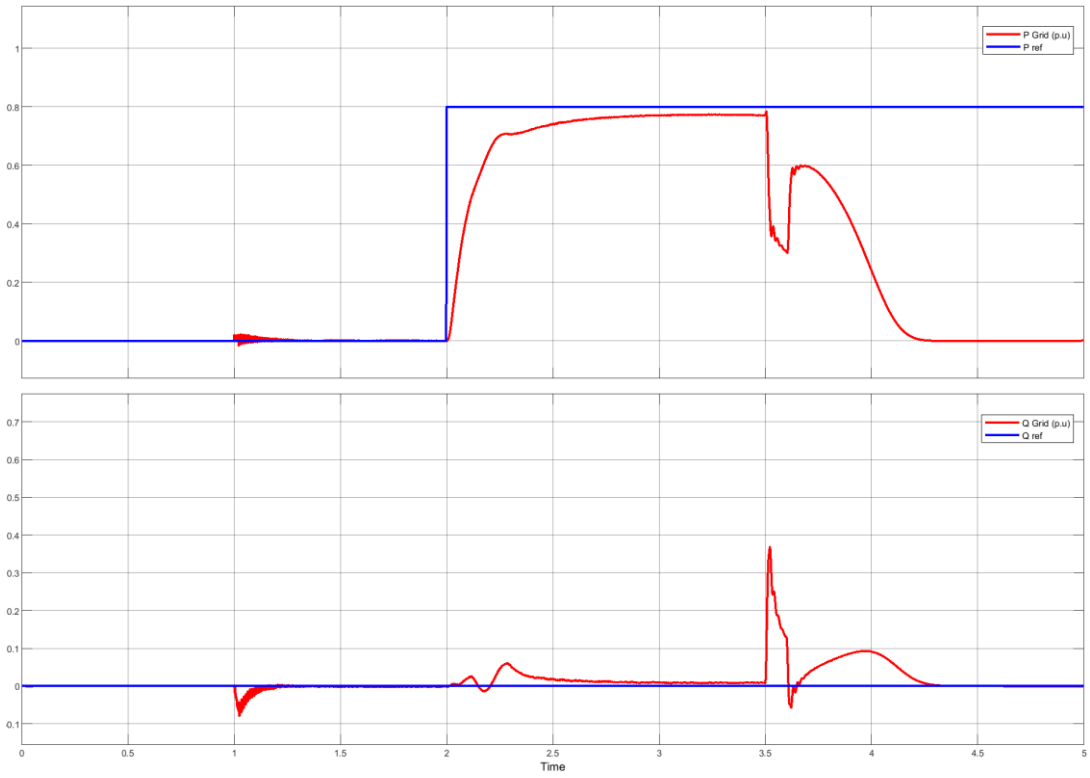

Figure 3.16 Active and Reactive Power in p.u. Injected to the Grid (Without Voltage Droop Mode)

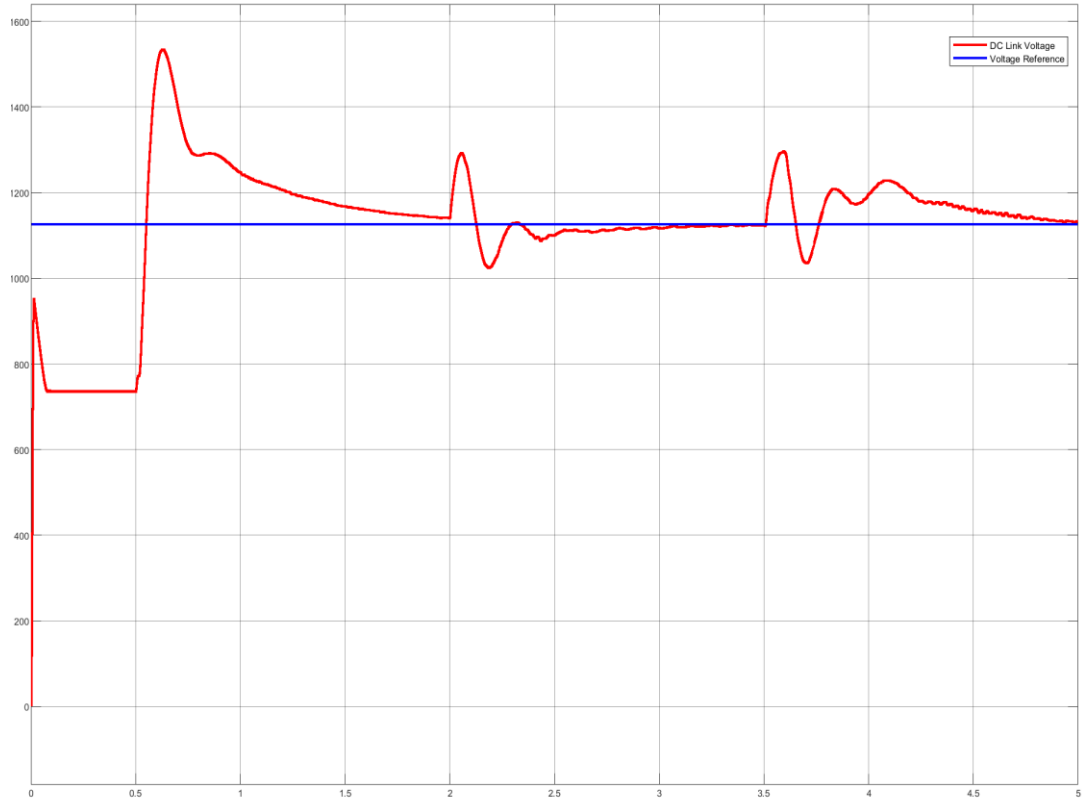

Figure 3.17 DC Link Voltage (Without Voltage Droop Mode)

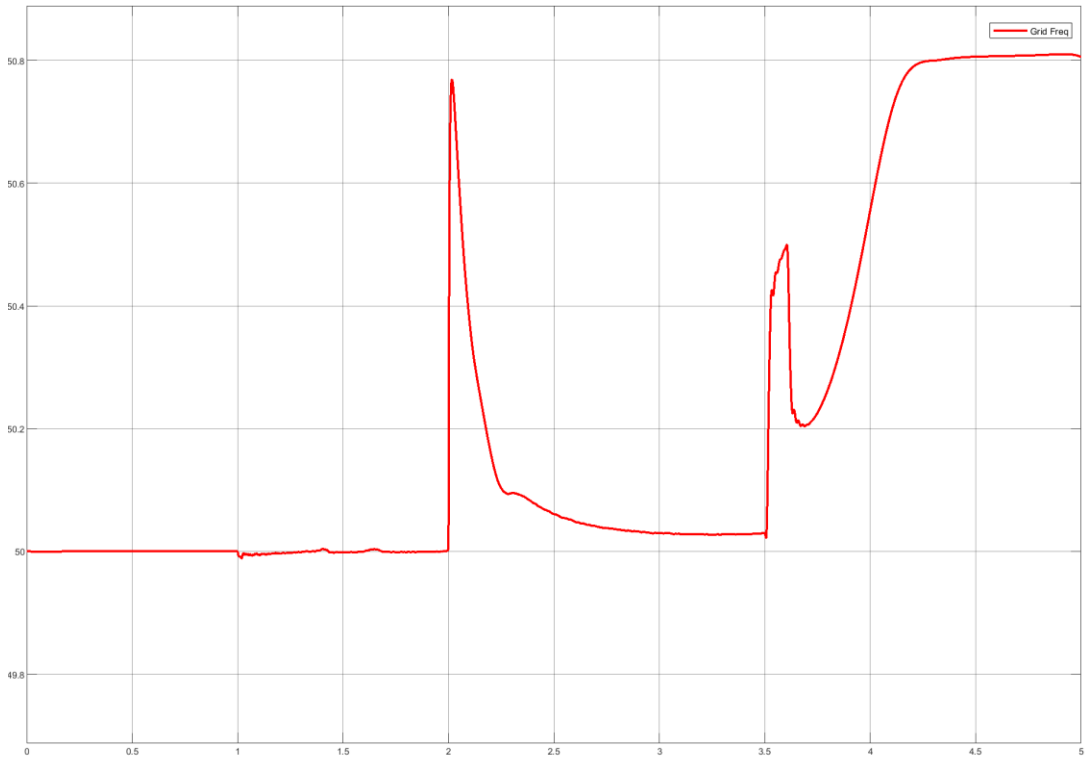

Figure 3.18 Grid Frequency (Without Voltage Droop Mode)

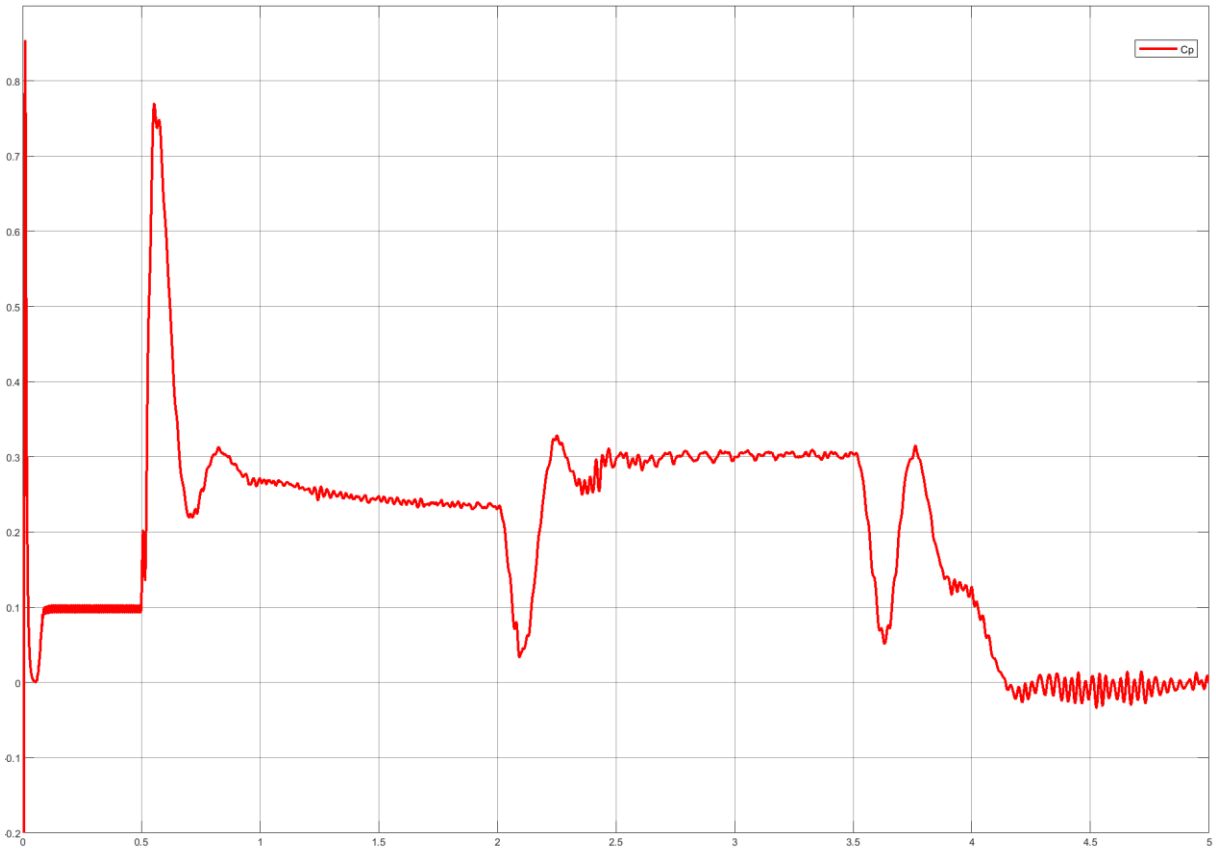

Figure 3.19 Wind Turbine Power Coefficient (Without Voltage Droop Mode)

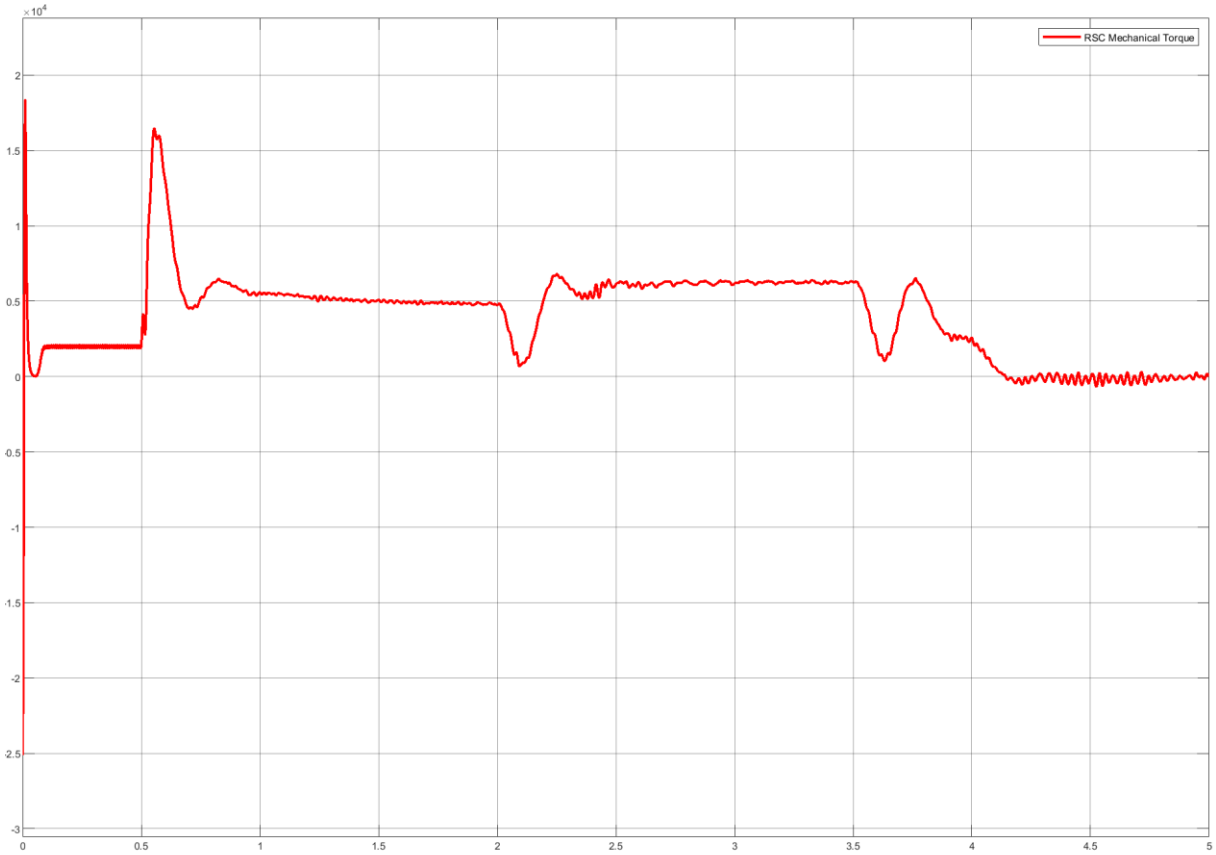

Figure 3.20 RSC Mechanical Torque (Without Voltage Droop Mode)

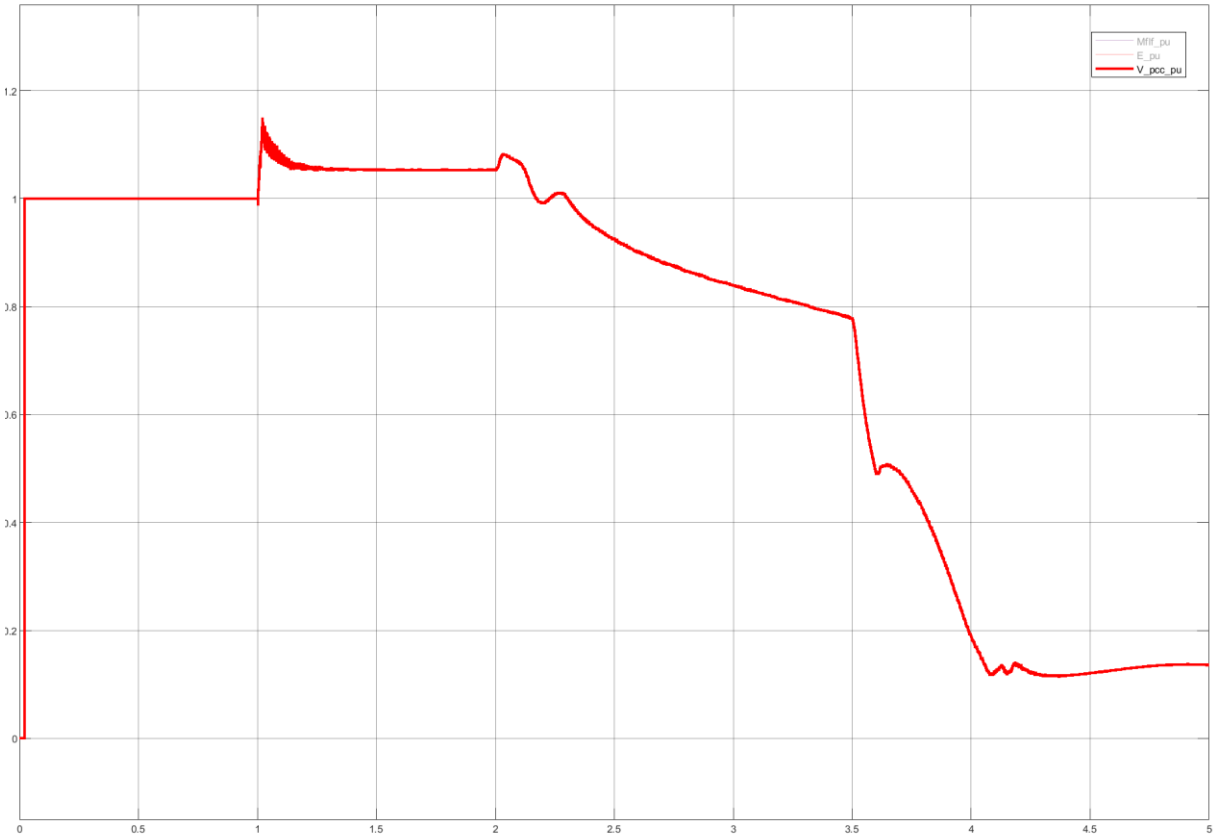

Figure 3.21 PCC Voltage in p.u. (Without Voltage Droop Mode)

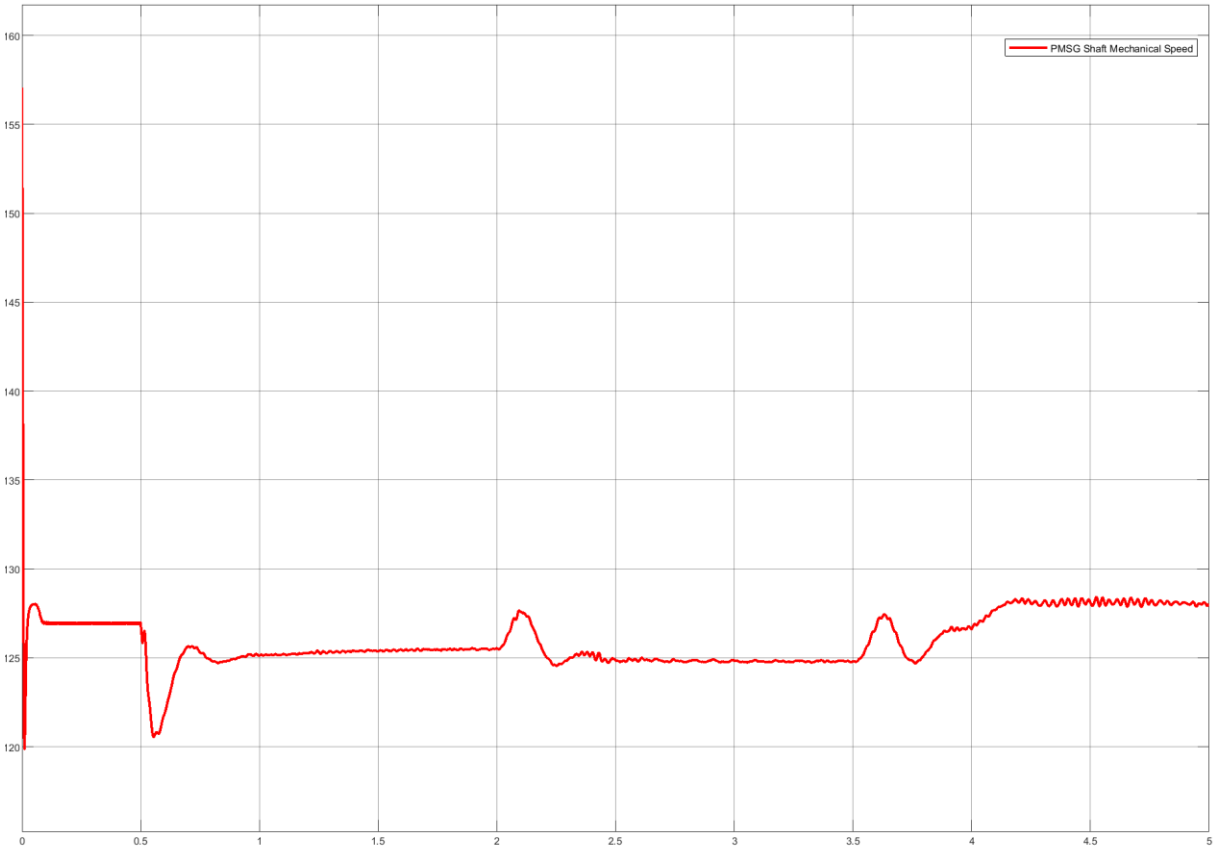

Figure 3.22 PMSG Shaft Mechanical Speed (Without Voltage Droop Mode)

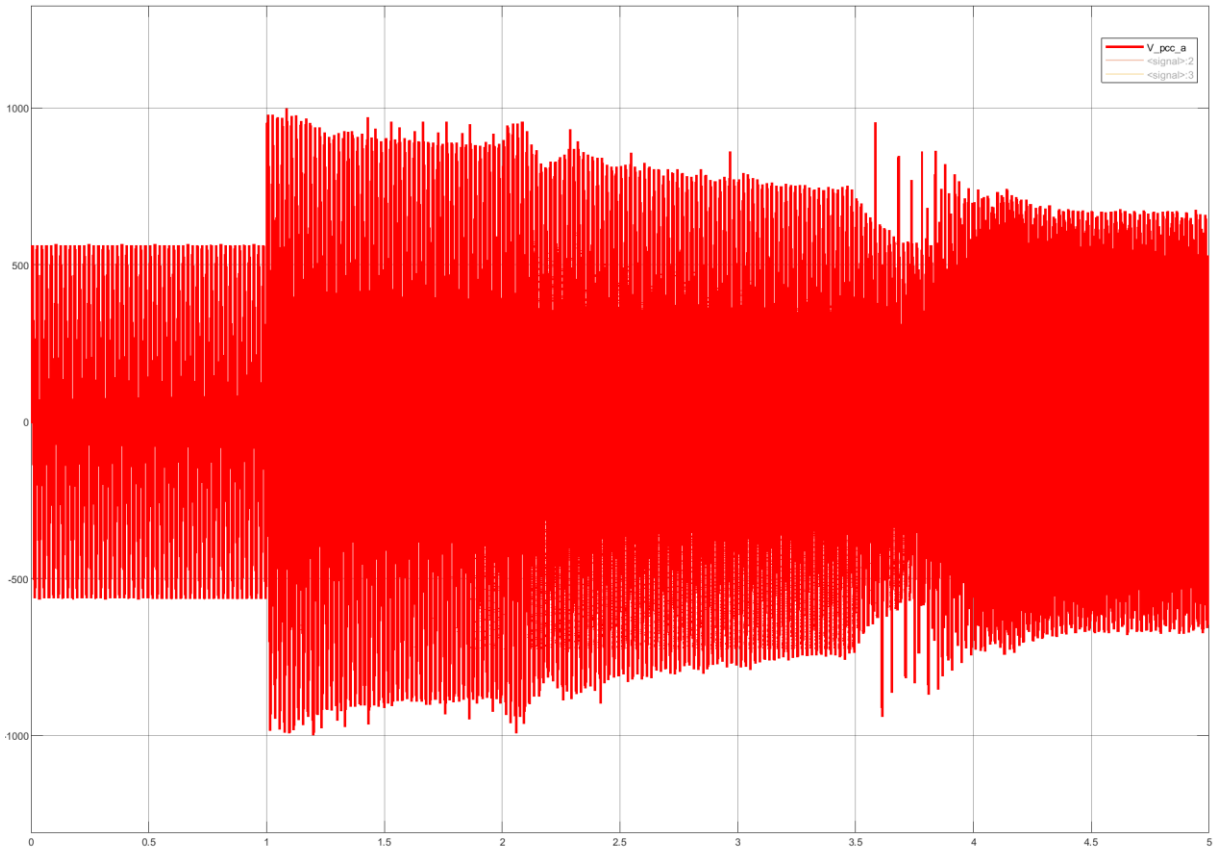

Figure 3.23 PCC Voltage in V (Without Voltage Droop Mode)

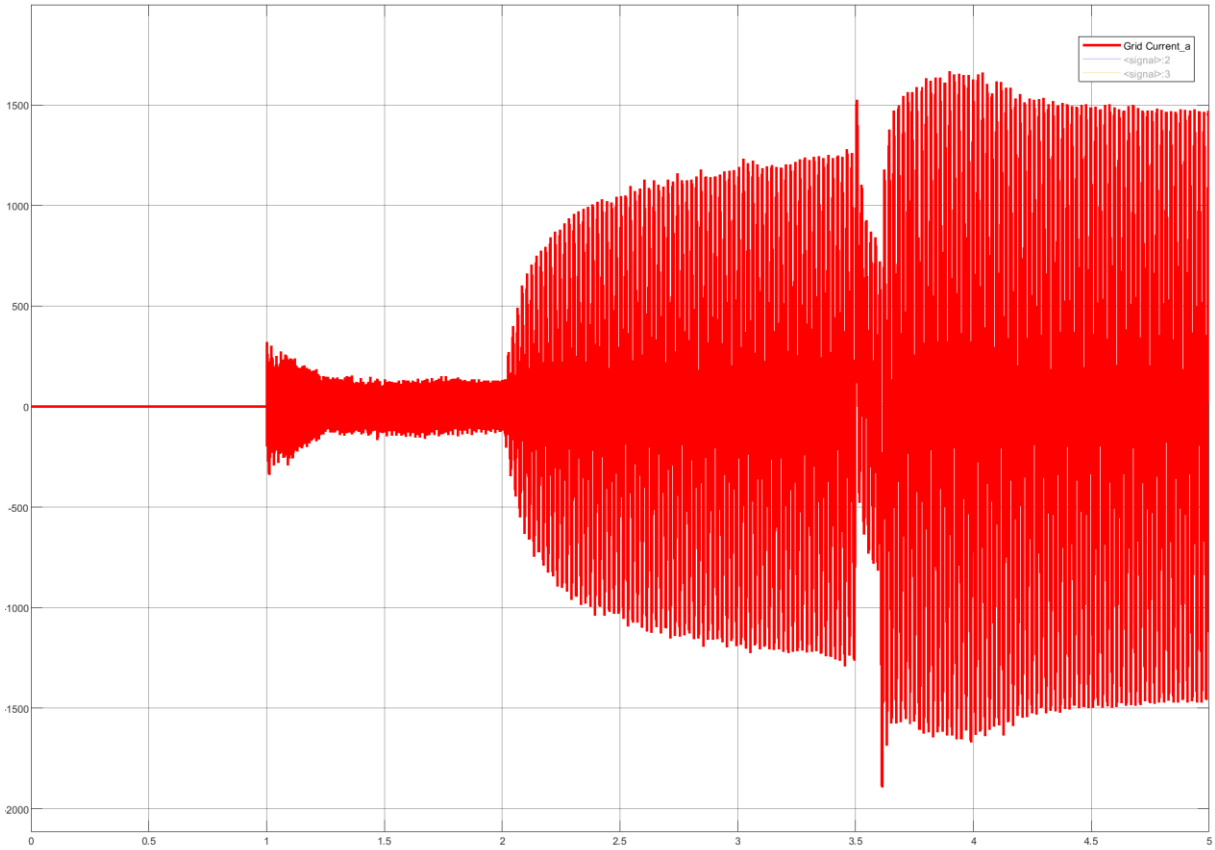

Figure 3.24 PCC Current in A (Without Voltage Droop Mode)

It is shown clearly the differences between the voltage droop implementation and without the voltage droop implementation. With the voltage droop implementation, the reactive power is tracked to ensure that the grid voltage is intact. Without the voltage droop, the reactive power is forced to be 0, and it turns out that forcing the reactive power to be 0 will not let the active power to be a bit less than 0.8 p.u. This indicates that the system's voltage stability is already at the limit, and when the grid voltage is dropping to 0.5 p.u, the knee point/critical point of the P-V curves is passed, causing voltage collapse of the system. Since voltage stability is out of scope of this thesis, it will not be discussed further. An example of PV-QV curves are attached here to visualise the reader.

It is interesting to see that even though the WECS is unstable, the DC link voltage is still regulated although the response is not as good as with the voltage droop implementation. The rotor part of the WECS operates as if the GSC operates in self-sync, but the response oscillates compared to the initial condition during the energisation period. Therefore, the dynamic operation between the RSC and the GSC can be assumed as **decoupled** (this will be an important point of assumption for Chapter 4 and 5).

In the nutshell, it is confirmed that the WECS works as modelled and as expected.

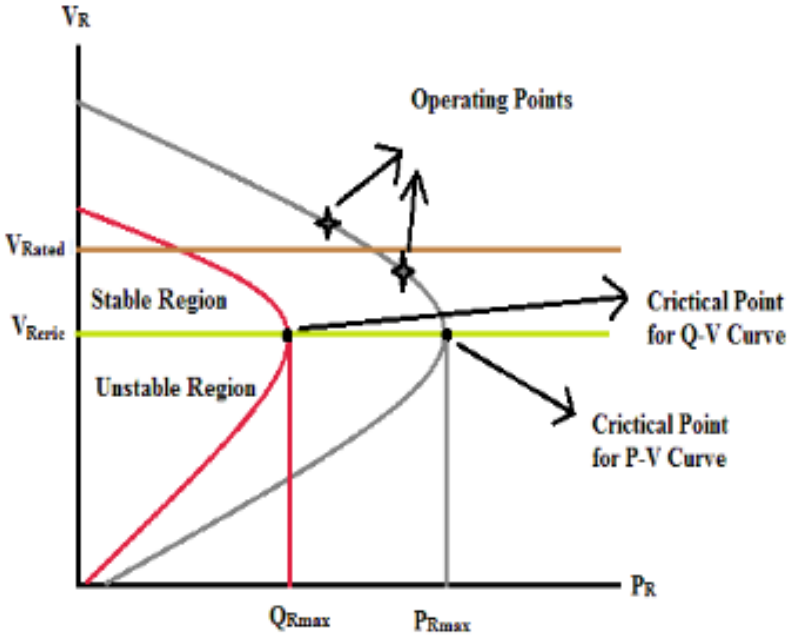

Figure 3.25 PV-QV Curves Example [85]

Chapter 4

Impedance Modelling and Measurement of the Synchronverter-based Wind Energy Conversion System

This chapter will analytically derive the impedance model of the WECS that have been developed in the previous chapter. Theoretical explanation regarding the small-signal impedance modelling and how the common representation of impedance modelling in 3-phase systems will be explained. Also, the frequency sweep simulation will also be explained. This chapter last part will analyse and compare the impedance obtained analytically with the frequency sweep results.

4.1 Introduction

As mentioned in Chapter 1, there are two main ways to conduct the stability analysis. While the state space method is more established and more commonly used, it brought complexity on the analysis, especially if the systems being studied are too complex which easily bring the dimension of the state space matrix to over bound. Therefore, an impedance-based approach will be explored and investigated in this thesis.

Impedance-based approach in detail can be divided into 3 domains of representations: *Modified Sequence Domain, Sequence Domain,* and *dq-Domain* as can be seen in Figure 4.1. It will be explained further in the following sections.

A concise explanation on how to obtain the impedance model by simulation will also be elaborated in this chapter.

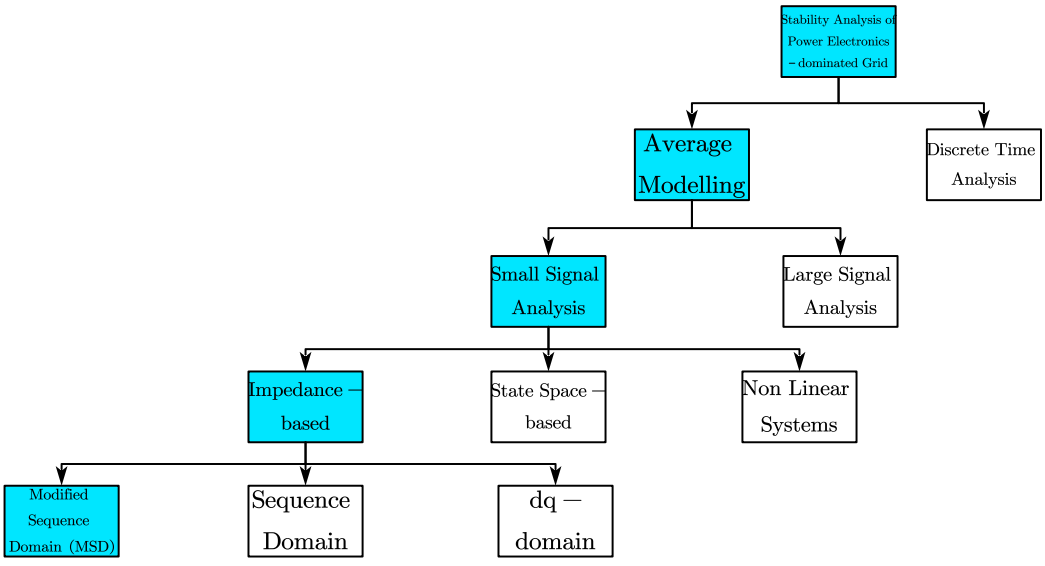

Figure 4.1 Methods for Stability Analysis of Power Electronics-dominated Grids

4.2 Small-Signal Impedance Modelling

Small-signal analysis has been commonly used in electronics and control theory to study the system response due to a small excitation or perturbation around a certain operation point. The analysis can be done either in the time domain, *s* domain, or the frequency domain. Therefore, small-signal impedance measures the time, *s*, or the frequency domain response of a small disturbance that is applied to a power systems terminal. Consider the following figure for more clarity.

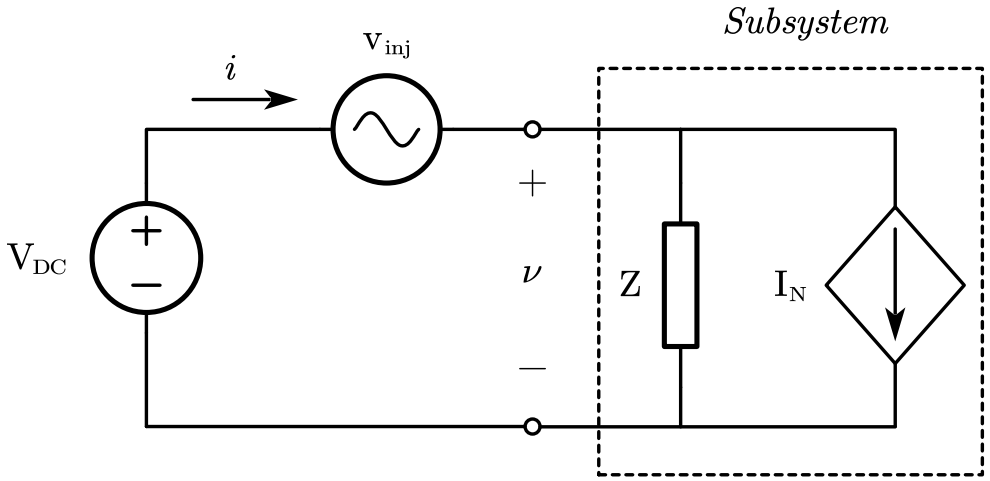

Figure 4.2 DC Voltage Source with Small Signal Voltage Perturbation and Norton Representation of Subsystem

A small sinusoidal voltage component is injected to the system, in which the voltage coming from the sources in time domain will be

$$v(t) = V_{dc} + v_{inj}\sin(\omega_{inj}t), \qquad v_{inj} \ll V_{dc}$$

The assumption $\boldsymbol{v_{inj} \ll V_{dc}}$ is due to the small-signal assumption. By superposition theorem at the steady state condition, the subsystem will produce an output current of

$$i(t) = I_{dc} + i_{inj}\sin(\omega_{inj}t + \phi), \qquad i_{inj} \ll I_{dc}$$

Then the small-signal impedance can be defined as

$$Z(j\omega_{inj}) = \frac{v_{inj}}{i_{inj}}e^{j\phi} \tag{63}$$

Other than frequency domain, by moving to a *s* domain, similar expression can also be obtained.

$$Z(s) = \frac{V(s)}{I(s)} \tag{64}$$

One thing worth an attention is that, the representation and the derivation works for both the Norton equivalent or Thevenin equivalent of the subsystem. It is easy to show that both of the impedance is actually the same with circuit theory. Therefore, the representation of the subsystem does not really affect the small-signal impedance definition per se [86].

4.3 Impedance Modelling of 3-phase AC Systems

To do the impedance modelling in 3-phase AC systems, it is a bit similar but will be more complex than the DC modelling shown previously. There are 2 main factors why 3-phase AC systems impedance modelling will be more complex [18]:

1. AC systems are oscillating along the fundamental frequency. Therefore, there is no equilibrium point for the variables i.e., time-varying state variables.
2. Since it is 3-phase, then the subsystem will be represented as a 3x3 matrix compared to a DC system which only consists of 1-phase.

For the time-varying state variables, it is solvable by transforming from the abc-domain into the $dq0$-domain or the 012-domain (sometimes can be written as $0pn$ as well, and it will interchangeably used in this thesis). And the system dimension can also be reduced to a 2x2 by assuming that the system being studied is in balance condition. In this thesis, the 012-domain or the sequence domain will be focused on, therefore the $dq0$-domain will not be discussed further.

4.3.1 Impedance Modelling in the 012-domain

As explained previously, transforming the 3-phase signals from the abc-domain into the 012-domain will help reducing the complexity of the systems. The transformation is called the Fortescue's transformation [87], or the symmetrical component transformation and mathematically can be expressed as

$$\begin{bmatrix} V_0(j\omega) \\ V_1(j\omega) \\ V_2(j\omega) \end{bmatrix} = \frac{1}{3}\begin{bmatrix} 1 & 1 & 1 \\ 1 & a & a^2 \\ 1 & a^2 & a \end{bmatrix}\begin{bmatrix} V_a(j\omega) \\ V_b(j\omega) \\ V_c(j\omega) \end{bmatrix} \tag{65}$$

where a is the $120°$ degree phase shift, i.e., $a = 1\angle 120°$. V_a, V_b, and V_c are the phase voltages, and V_0, V_1, and V_2 are the zero, positive, and negative sequence components. The frequency domain is used here to indicate that the Fortescue's transform is valid for any frequency.

Equation (65) is also valid for current, and mathematically can be presented as

$$\begin{bmatrix} I_0(j\omega) \\ I_1(j\omega) \\ I_2(j\omega) \end{bmatrix} = \frac{1}{3}\begin{bmatrix} 1 & 1 & 1 \\ 1 & a & a^2 \\ 1 & a^2 & a \end{bmatrix}\begin{bmatrix} I_a(j\omega) \\ I_b(j\omega) \\ I_c(j\omega) \end{bmatrix} \tag{66}$$

Having the sequence domain expression for both the voltages and the currents, then the sequence domain impedance will be

$$Z_1(j\omega) = \frac{V_1(j\omega)}{I_1(j\omega)} \tag{67}$$

$$Z_2(j\omega) = \frac{V_2(j\omega)}{I_2(j\omega)} \tag{68}$$

In s-domain, the sequence domain impedance will be [88]

$$Z_1(s) = \frac{V_1(s)}{I_1(s)} \tag{69}$$

$$Z_2(s) = \frac{V_2(s)}{I_2(s)} \tag{70}$$

The sequence domain definition of the impedance for application in power electronics was brought to light for the first time in [88], and has been the foundation of impedance-based modelling and stability analysis. In [89], sequence impedance of grid-feeding converters has been derived, while for grid connected VSC has been explored in [16]. Sequence impedance for HVDC transmission and AC collection system has also been explored in [20]. Also, sequence impedance modelling has been studied in an MMC as shown in [90].

One assumption in the sequence domain is that there is no coupling between the positive and the negative sequences, resulting in $Z_1 = Z_2$. However, it has been studied in [18], [87], and [91] that it is not necessarily true. Some components and controllers in power systems have been known to introduce a coupling between the positive and negative sequences at 2 distinct frequencies, which are [18]:

1. PLL
2. Converter current control
3. DC-link voltage control
4. Active power and reactive power control
5. Salient-pole SM

By extending the derived sequence domain impedance definition, it will be possible to capture this phenomenon. The extended definition is called the Modified Sequence Domain, and will be concisely explained in the following section.

4.3.2 Impedance Modelling in the Modified Sequence Domain

As have been mentioned in the previous section, MSD is the extension of the original sequence domain, which mathematically expressed as follows,

$$\begin{bmatrix} V_1(s+j\omega_1) \\ V_2(s-j\omega_1) \end{bmatrix} = \boldsymbol{Z}_{12}(s) \begin{bmatrix} I_1(s+j\omega_1) \\ I_2(s-j\omega_1) \end{bmatrix}$$

$$\boldsymbol{Z}_{12}(s) = \begin{bmatrix} Z_{11}(s) & Z_{12}(s) \\ Z_{21}(s) & Z_{22}(s) \end{bmatrix} \tag{71}$$

where ω_1 indicates the fundamental frequency. The impedance matrix indicates the following:

1. Z_{11}: response of the positive sequence voltage at $s+j\omega_1$ induced by a positive sequence current at $s+j\omega_1$
2. Z_{12}: response of the positive sequence voltage at $s+j\omega_1$ induced by a negative sequence current at $s-j\omega_1$
3. Z_{21}: response of the negative sequence voltage at $s-j\omega_1$ induced by a positive sequence current at $s+j\omega_1$
4. Z_{22}: response of the negative sequence voltage at $s-j\omega_1$ induced by a negative sequence current at $s-j\omega_1$

This coupling phenomena was first investigated in [92], and the impact on the MSD is studied in detail in [18] and [86] and can be referred for further details.

To obtain the MSD impedance model, the general framework is by utilising the harmonic transfer function/harmonic state space, or harmonic linearisation [20], [59]. In this thesis, however, an analytical derivation based on the Synchronverter mathematical equation will be used. The drawback of such method will be in accuracy compared to the harmonic state space or harmonic linearisation, but it offers simplicity in deriving the impedance model of the systems.

One assumption is also used in this thesis, in which there is no mirror frequency coupling, i.e., $\boldsymbol{Z_{12}} = \boldsymbol{Z_{21}} = 0$. This is because the analytical model derived will not be able to capture such phenomena, and hence will be disregarded and will not be discussed any further.

4.4 Impedance Model Measurement

After obtaining the impedance models of a system, a validation needs to be conducted to ensure the accuracy. One advantage of impedance-based technique is that the impedance model can be obtained purely using the current and voltage measurement at the terminals, so that a 'black-box' modelling is possible.

The concept to obtain the small-signal impedance model by measurement, is by measuring the changes in the terminal voltage and the terminal current. By Ohm's Law, then the small signal impedance will be the ratio of the voltages and the current, as shown in Equation (63). By that concept, several techniques exist to obtain the impedance model by measurement, which can be categorised into 2: *passive* and *active* methods. Short introduction will be presented in the following sections.

4.4.1 Passive Methods

Passive methods are called passive since they utilise disturbances which are already exist in the systems. In other words, passive methods will not introduce a new disturbance source to the system. Hence, the methods will not violate the grid codes, especially the power quality compliance.

One of the earliest example that falls under the passive method can be traced back to 2009, and called the *Linear Regression Method* [93]. This method will construct a set of linear equations from the measurements of several operating point, then linear regression will be utilised to obtain the approximate equivalent grid impedance.

Another example is called the *Error Function Method* [94]. This method works by making use of a grid model, in which a measured voltage perturbation will be inputted. Therefore, a current estimate will be produced, and the error between the measured current and the estimated current will be used to update the model parameters.

Even though such methods will not violate the power quality compliance, it has several disadvantages. For example, in the Error Function Method, a solid assumption regarding the grid model needs to be obtained. Or else, the simulation will just iterate indefinitely without producing a fruitful result.

Another disadvantage that is valid for all passive methods is that it relies on the existing disturbance in the power grids. This is a very sound disadvantage since the operation of the grid itself fully focused on having high security and reliability. Therefore, the disturbance that exist might be not high enough to be measured and utilised.

4.4.2 Active Methods

While passive methods are utilising existing disturbances in the grids, active methods will be injecting the disturbances to the grids. From there, the response will be analysed as explained. Therefore, these methods offer flexibilities on choosing the disturbances signals

being injected (can be either voltage or current injection, flexibility on the amplitude, phase, and frequency).

Active methods can be further classified into two sub-categories: *Transient methods* and *Steady-state methods*. The difference lies on the amount of the signal being injected. Transient methods inject a single signal or a few signals while steady-state methods inject repeated periodic signals.

One example of transient method is called *Pulse Injection* as shown in [95]. The pulse injected is a current impulse and is implemented in the control systems of the converter. Since the pulse injected is a single pulse, it results in a very fast simulation time, and so far, has been considered as the fastest method for impedance estimation. Other than pulse injection, *Load Switching* has also been studied previously in [96]. The concept behind it is that switching on-off the load (or any components) results in voltage and current changes, in which the impedance can be obtained. In [96], the OLTC is varied.

For steady-state method, several methods exist, such as *Maximum Length Binary Sequences* (MLBS) [97], *Pseudo-Random Binary Sequences* (PRBS) [98], and *Sinusoidal Sweep* [99]. MLBS and PRBS are similar to the pulse injection of the transient method. However, the difference lies in the sequence of pulses. PRBS is actually the generalisation of MLBS, in which the duty cycle can be determined from the number of bits and ones while for MLBS, the duty cycle is $\frac{1}{2}$ [100]. As the name indicates, sinusoidal sweep injects sinusoidal signals of different frequencies.

Sinusoidal sweep itself have 2 variants: *single-tone* and *multi-tone*. Single-tone injects the perturbation at a single frequency to calculate the system's response at that frequency. Therefore, the simulation will be iterated for a range of frequencies. Multi-tone will superimpose all the frequencies, resulting in a combined perturbation signal. The advantage is that in the multi-tone, the simulation time will be much faster compared to the single-tone. However, in this thesis, a single-tone sinusoidal frequency sweep (from here onwards will be referred simply as frequency sweep) will be used since it is much simpler. The explanation of how to obtain the response will be explained in the following section.

4.4.3 Single-Tone Frequency Sweep

As the previous section explains, the sinusoidal signal being injected can be a voltage or current. Therefore, two ways of injecting the perturbation signals into the system will be shown in the schematics below.

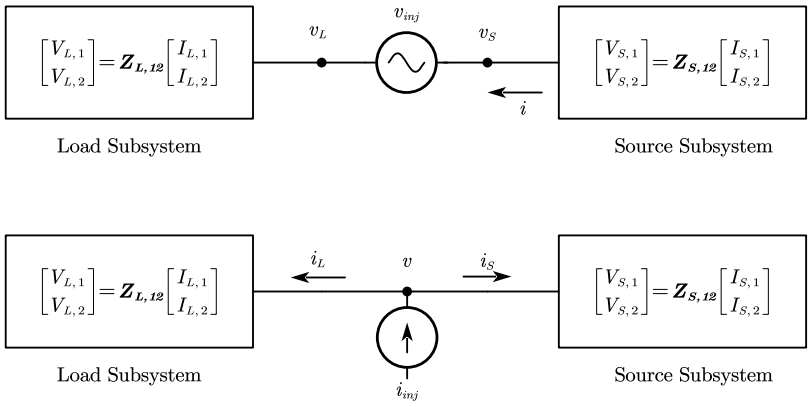

Figure 4.3 Illustration of the 2 Injection Method

In an ideal, numerical simulation condition, choosing between series or shunt injection has negligible impact on the results. But practically, injection method should be selected in accordance to the most important subsystem [18]. For example, if an impedance model of VSC is the point of interest, then series voltage injection is recommended. This is due to the perturbation voltage injected will be distributed between the two subsystems in proportion to their impedance. Since usually VSC have higher impedance than the grid, series voltage injection will be resulting in higher accuracy compared to shunt current injection. If a subsystem impedance is significantly lower, then using shunt current injection will be the best choice since almost all the perturbation current will flow to the respective subsystem, yielding higher voltage response measurement, hence a higher impedance accuracy will be obtained.

Also, since this thesis will measure the impedance in MSD, it will be impossible to obtain a 2x2 impedance matrix with a single frequency sweep. Therefore, 2 linear independent sweeps will be performed. The detailed flowchart of the steps on doing the frequency sweep in this thesis is shown in Figure 4.4.

First, a vector of frequencies is created to estimate the impedance. The frequency value can be chosen arbitrarily. Then, the 2 perturbation signals will be injected independently. A pure positive sequence signal will be the first injection, and a pure negative sequence signal will be the second injection. In this thesis, series voltage injection is used, therefore the signals being injected will be in the form of

$$v_{inj,p} = \begin{bmatrix} v_{inj,p,a} \\ v_{inj,p,b} \\ v_{inj,p,c} \end{bmatrix} = V_{inj} \begin{bmatrix} \sin\left((\omega_{inj} + \omega_1)t\right) \\ \sin\left((\omega_{inj} + \omega_1)t - \frac{2\pi}{3}\right) \\ \sin\left((\omega_{inj} + \omega_1)t + \frac{2\pi}{3}\right) \end{bmatrix}$$

$$v_{inj,n} = \begin{bmatrix} v_{inj,n,a} \\ v_{inj,n,b} \\ v_{inj,n,c} \end{bmatrix} = V_{inj} \begin{bmatrix} \sin\left((\omega_{inj} - \omega_1)t\right) \\ \sin\left((\omega_{inj} - \omega_1)t + \frac{2\pi}{3}\right) \\ \sin\left((\omega_{inj} - \omega_1)t - \frac{2\pi}{3}\right) \end{bmatrix} \quad (72)$$

where the subscript p and n indicate positive and negative sequence signals respectively. As shown in the equation (72), the series voltage injection will exist in each phase. If the injection signals used are shunt current instead, equation (72) can easily be changed into the current by changing the magnitude. After injecting the perturbation signals, the voltage and current signal will be stored. The data required after injecting the signals is shown in Figure 4.3. In the case of a series voltage injection, the load subsystem voltage, v_L and the sources subsystem voltage, v_S are required. Also, the line current, i is also required.

Next, an FFT will be conducted to convert the voltages and the current to the frequency domain. Since the impedance here will be presented in the MSD, then the abc-waveforms will be applied for the FFT. After obtaining the complex spectra, Fortescue's transform will be conducted to convert the voltages and current into the sequence domain. Before conducting the FFT for the voltages and current, an FFT will be conducted first for the terminal voltage to obtain the fundamental frequency voltage angle, θ_1. This is required to shift the sequence components to be consistent with its *dq*-domain counterparts (it will not be explored in this thesis, however the author decided it is needed to ensure consistency for future works).

After obtaining θ_1, conducting FFT for the voltages and the current, and performing Fortescue's transform, phase shifting will be done by the following set of expressions

$$V_p = V_p' e^{-j\theta_1} \qquad V_n = V_n' e^{j\theta_1}$$
$$I_p = I_p' e^{-j\theta_1} \qquad I_n = I_n' e^{j\theta_1} \tag{73}$$

where prime indicates the old sequence components before shift, which are obtained directly from the FFT and the Fortescue's transform. After obtaining the sequence domain, a component extraction from the FFT results for each frequency depending on the sequence will be conducted. For positive sequence, it will be extracted at $f + f_1$ and $f - f_1$ for the negative sequence. Attentive reader might notice that for $f < f_1$, $f - f_1$ will be negative. In this case, the negative sequence components can be transformed to positive sequence with the same frequency with positive sign and conjugated phase angles [101].

Last step is to calculate the impedance at frequency f from the following formula

$$\begin{bmatrix} Z_{pp}(\omega) & Z_{pn}(\omega) \\ Z_{np}(\omega) & Z_{nn}(\omega) \end{bmatrix} = \begin{bmatrix} V_{p1}(\omega+\omega_1) & V_{p2}(\omega+\omega_1) \\ V_{n1}(\omega-\omega_1) & V_{n2}(\omega-\omega_1) \end{bmatrix} \begin{bmatrix} I_{p1}(\omega+\omega_1) & I_{p2}(\omega+\omega_1) \\ I_{n1}(\omega-\omega_1) & I_{n2}(\omega-\omega_1) \end{bmatrix}^{-1} \tag{74}$$

Here, the subscript 1 and 2 refer to the injection 1 or injection 2.

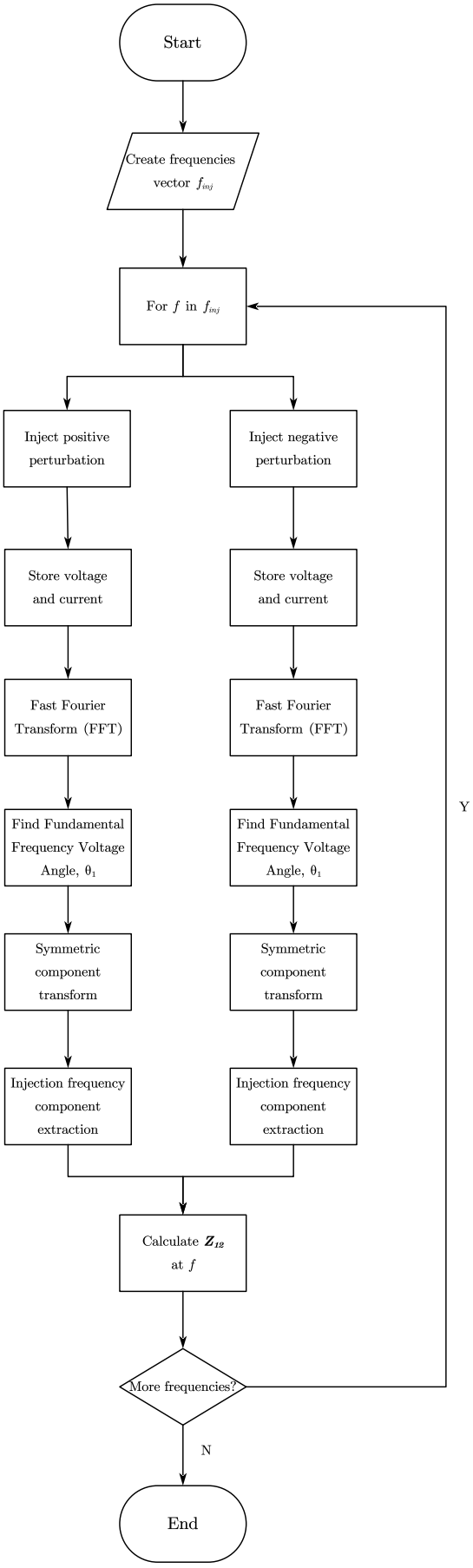

Figure 4.4 Single-Tone Frequency Sweep Flowchart

4.5 Analytical Impedance Modelling of the WECS

Based on the result from chapter 3, it has been concluded that the dynamic interaction between the GSC and the RSC is decoupled. Since this thesis are focused on the converter-driven stability for WECS and grid interaction, the main point of focus will be on the GSC and the grid part.

In this section, impedance for the grid subsystems and the GSC will be mathematically derived. Impedance for the RSC part will also be derived even though it will not be studied further in section 4.6 and Chapter 5. This is for the whole completeness of the thesis and can be referred later on for future works.

4.5.1 Grid Impedance Modelling

In this thesis, the perturbation is injected right at the converter terminal. Therefore, the grid impedance refers to the filter and the original grid impedance of the infinite bus.

The filter itself, as mentioned in section 3.3, consists of an RC connected in parallel. Therefore,

$$\frac{1}{Z_{filter}} = \frac{1}{R_{filter}} + \frac{1}{\frac{1}{sC_{filter}}}$$

$$\therefore Z_{filter} = \frac{R_{filter}}{1 + sC_{filter}R_{filter}} \tag{75}$$

Therefore, in MSD, the filter impedance will be

$$\boldsymbol{Z_{filter}} = \begin{bmatrix} \frac{R_{filter}}{1 + (s + j\omega_1)C_{filter}R_{filter}} & 0 \\ 0 & \frac{R_{filter}}{1 + (s - j\omega_1)C_{filter}R_{filter}} \end{bmatrix} \tag{76}$$

The non-diagonal elements of filter impedance are 0 since the components are passive components of RC, i.e., there will be no coupling. It is also worth mentioning that equation (75) is the original sequence domain form of Z_{filter}, where $Z_{filter,p} = Z_{filter,n} = \frac{\boldsymbol{R_{filter}}}{\boldsymbol{1+sC_{filter}R_{filter}}}$.

The original grid impedance consists of an RL connected in series. Therefore,

$$Z_g = R_g + sL_g \tag{77}$$

Similarly, the MSD of the original grid impedance will be

$$\boldsymbol{Z_g} = \begin{bmatrix} R_g + (s + j\omega_1)L_g & 0 \\ 0 & R_g + (s - j\omega_1)L_g \end{bmatrix} \tag{78}$$

The filter and the original grid impedance are in parallel with each other. Therefore, the grid impedance will be

$$\boldsymbol{Z_{grid}} = \left(\boldsymbol{Z_{filter}^{-1}} + \boldsymbol{Z_g^{-1}}\right)^{-1} \tag{79}$$

4.5.2 GSC Impedance Modelling

To derive the GSC impedance analytically, we will start from the Ohm's law of the SG model in equation (27) as shown below,

$$e_{abc} - R_s i_{abc} - L_s \frac{di_{abc}}{dt} = v_{abc} \tag{80}$$

where

$$e_{abc} = M_f i_f \omega \widetilde{\sin\theta} \tag{81}$$

The excitation can be derived as follows,

$$M_f i_f = \frac{1}{sK_q}\left(Q_{ref} - Q + D_q V_{m,g} - D_q V_{m,pcc}\right) \tag{82}$$

Now, going back to the swing equation of the GSC, the following expressions will be obtained,

$$J\frac{d\omega}{dt} = T_m - T_e - D_p(\omega - \omega_n) \tag{83}$$

Since $T_m = \frac{P_{ref}}{\omega_n}$, equation (83) can be rewritten as

$$J\frac{d\omega}{dt} = \frac{P_{ref}}{\omega_n} - T_e - D_p\omega + D_p\omega_n \tag{84}$$

Substituting equation (28) and (82) to (84), and assuming that $Q_{ref} = Q = 0$, also taking the Laplace transform, the swing equation of the GSC will be

$$sJ\omega = \frac{P_{ref}}{\omega_n} - \frac{\left(D_q V_{m,g} - D_q V_{m,pcc}\right)}{sK_q} i_a \sin\theta - D_p\omega + D_p\omega_n \tag{85}$$

Notice that in equation (85), only 1-phase is being considered. This is due to the balanced system being simulated; hence all phase is equal. Rearranging equation (85),

$$(sJ + D_p)\omega = \frac{P_{ref}}{\omega_n} + D_p\omega_n - \frac{\left(D_q V_{m,g} - D_q V_{m,pcc}\right)}{sK_q} i_a \sin\theta \tag{86}$$

Since P_{ref} and ω_n is constant for a certain wind speed, linearising (86) will results in

$$\widetilde{\omega} = \frac{D_q I_{a0}\sin\theta_0}{sK_q(sJ + D_p)}\widetilde{v_a} - \frac{M_{f0} I_{f0}\sin\theta_0}{(sJ + D_p)}\widetilde{i_a} \tag{87}$$

where the tilde indicates the small-signal. $\sin\theta_0 = 1$ from the assumption that $Q_{ref} = Q = 0$. Now, e_a needs to be expressed in terms of $\widetilde{v_a}$ and $\widetilde{i_a}$ by linearising equation (81).

$$\widetilde{e_a} = \left(\widetilde{M_f i_f}\omega_0 + M_{f0} I_{f0}\widetilde{\omega}\right)$$

$$\therefore \widetilde{e_a} = G_{v,GSC}\widetilde{v_a} + G_{i,GSC}\widetilde{i_a} \tag{88}$$

where

$$G_{v,GSC} = \frac{M_{f0} I_{f0} D_q I_{a0}}{sK_q(sJ + D_p)} - \frac{D_q\omega_0}{sK_q} \tag{89}$$

$$G_{i,GSC} = -\frac{\left(M_{f0} I_{f0}\right)^2}{(sJ + D_p)} \tag{90}$$

Substituting (88), (89), and (90) back to (80) will results in

$$G_{v,GSC}\widetilde{v_a} + G_{i,GSC}\widetilde{i_a} - R_s\widetilde{i_a} - sL_s\widetilde{i_a} = \widetilde{v_a}$$

$$\therefore Z_{GSC} = -\frac{\widetilde{v_a}}{\widetilde{i_a}} = \frac{R_s + sL_s - G_i}{1 - G_v} \tag{91}$$

Therefore, in MSD, the GSC impedance will be

$$\boldsymbol{Z_{GSC}} = \begin{bmatrix} \dfrac{R_s + (s+j\omega) \times L_s - G_i(s-j\omega)}{1 - G_v(s-j\omega)} & 0 \\ 0 & \dfrac{R_s + (s-j\omega) \times L_s - G_i(s+j\omega)}{1 - G_v(s+j\omega)} \end{bmatrix} \tag{92}$$

where $G_i(s-j\omega)$ indicates G_i as a function of $(s-j\omega)$, not a multiplication.

4.5.3 RSC Impedance Modelling

Deriving the RSC impedance is similar to the GSC counterpart. Starting from the Ohm's law as in equation (32),

$$e_{abc} + R_r i_{abc} + L_r \frac{di_{abc}}{dt} = v_{abc} \tag{93}$$

Recalling equation (81),

$$e_{abc} = M_f i_f \omega \widetilde{\sin\theta}$$

And with the same assumption as in previous section, the excitation can be derived as

$$M_f i_f = \frac{1}{sK_q}\left(Q_{ref} - Q\right) \tag{94}$$

Now, going back to the swing equation of the RSC, the following expressions will be obtained,

$$J_m \frac{d\omega}{dt} = T_m - T_e - D_{pm}(\omega - \omega_n) \tag{95}$$

From the RSC control schematics, the T_m is obtained from the PI controller, regulating the DC link voltage. Therefore,

$$T_m = H_{vDC}(s) \times (V_{DC} - V_{DC,ref}) \tag{96}$$

where

$$H_{vDC}(s) = K_{P,DC} + \frac{K_{i,DC}}{s}$$

Here, $K_{P,DC}$ and $K_{i,DC}$ are the proportional and the integral constant. Substituting equation (96) back to equation (95) and taking the Laplace transform will results in,

$$sJ_m\omega = H_{vDC}V_{DC} - H_{vDC}V_{DC,ref} - T_e - D_{pm}\omega + D_{pm}\omega_n \tag{97}$$

Recalling equation (28) and (94), and assuming that $Q_{ref} = Q = 0$, equation (97) can be re-written as

$$(sJ_m + D_{pm})\omega = H_{vDC}V_{DC} - H_{vDC}V_{DC,ref} + D_{pm}\omega_n \tag{98}$$

Since $V_{DC,ref}$ and ω_n is constant, linearising (98) will results in

$$\widetilde{\omega} = \frac{H_{vDC}}{(sJ_m + D_{pm})}\widetilde{v_{DC}} \tag{99}$$

Now, the $\widetilde{v_{DC}}$ needs to be represented in terms of $\widetilde{v_a}$ and $\widetilde{i_a}$. By considering that the power sent from the DC side should be equal to the power received in the AC side, i.e., $P_{AC} = P_{DC}$ then mathematically,

$$\frac{v_{DC}^2}{3R} = v_a i_a \tag{100}$$

R comes from the power generated by the wind. For a certain wind speed, the output power will be constant, and can be assumed as a constant power load. Therefore, it will be represented by an impedance R. Linearising equation (100) gives,

$$\widetilde{v_{DC}} = \frac{3R}{2V_{DC}}(V_0\widetilde{i_a} + I_0\widetilde{v_a}) \tag{101}$$

Substituting (101) to (99), and substituting further back to equation (81) will results in

$$\widetilde{e_a} = \left(\widetilde{M_f i_f}\omega_0 + M_{f0}I_{f0}\widetilde{\omega}\right)$$

$$\therefore \widetilde{e_a} = G_{v,RSC}\widetilde{v_a} + G_{i,RSC}\widetilde{i_a} \tag{102}$$

where

$$G_{v,RSC} = \frac{3RM_{f0}I_{f0}H_{vDC}I_{a0}}{2V_{DC}(sJ_m + D_{pm})} \tag{103}$$

$$G_{i,RSC} = \frac{3RM_{f0}I_{f0}H_{vDC}V_{a0}}{2V_{DC}(sJ_m + D_{pm})} \tag{104}$$

Substituting further to equation (93) yields

$$G_{v,RSC}\widetilde{v_a} + G_{i,RSC}\widetilde{i_a} + R_r\widetilde{i_a} + sL_r\widetilde{i_a} = \widetilde{v_a}$$

$$\therefore Z_{RSC} = \frac{\widetilde{v_a}}{\widetilde{i_a}} = \frac{R_r + sL_r + G_{i,RSC}}{1 - G_{v,RSC}} \tag{105}$$

Therefore, in MSD, the RSC impedance will be

$$\boldsymbol{Z_{RSC}} = \begin{bmatrix} \dfrac{R_r + (s + j\omega) \times L_r + G_i(s - j\omega)}{1 - G_v(s - j\omega)} & 0 \\ 0 & \dfrac{R_r + (s - j\omega) \times L_r - G_i(s + j\omega)}{1 - G_v(s + j\omega)} \end{bmatrix} \tag{106}$$

where $G_i(s - j\omega)$ indicates G_i as a function of $(s - j\omega)$, not a multiplication. Notice the difference of the impedance formula in GSC and RSC regarding the negative sign. This is due to the fact that in GSC, it is considered as a power dissipating component, in which it generates power. For RSC, as a power absorbing component, it dissipates power. Therefore, there is no negative sign in the RSC impedance formula.

4.6 Simulations and Results

As mentioned previously, this chapter will focus on the simple impedance derivation analytically, and validation by frequency sweep of the system. The frequency sweep simulation's configuration are as follows:

1. Series voltage injection is used
2. 24 injection frequencies will be used between 1 and 5000 Hz. The specific frequency was determined by logarithmic spacing, and are a multiple of 1 Hz
3. Duration of FFT is 1 second
4. Simulation time step is 20 μs
5. Injection magnitude is 0.01 p.u

4.6.1 Grid Impedance

The result of the simulation for the grid impedance can be seen in the following figure,

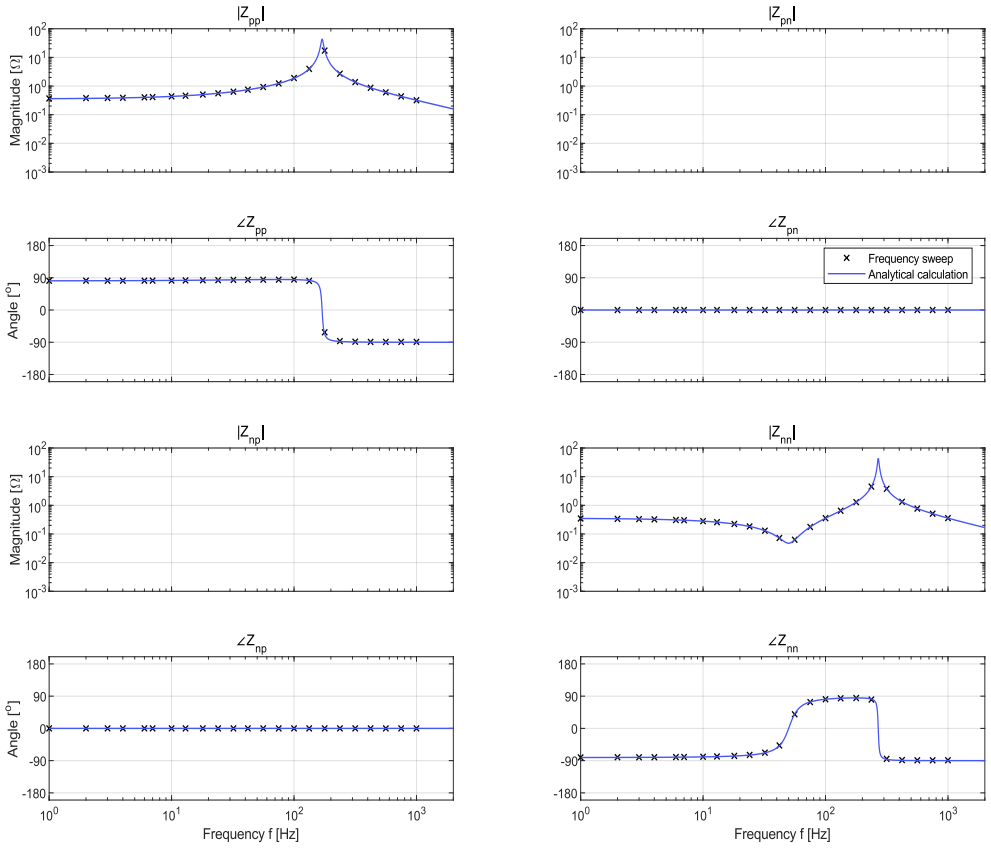

Figure 4.5 Grid Impedance Analytical Calculation and Frequency Sweep

As can be seen from Figure 4.5, the frequency sweep results and the analytical derivation is aligned perfectly, indicating that all components are estimated accurately. The positive sequence and the negative sequence component of the grid impedance also shows some differences. For the positive sequence, the resonant frequency is at around 170 Hz; while for negative sequence, there exist 2 resonant frequencies at 50 Hz and 270 Hz. It can also be seen that for the positive sequence, the response is similar to a simple second-order

system while for negative sequence, the response is similar to a fourth-order system. This indicates that the usual assumption used in similar previous research of $Z_p = Z_n$ is invalid.

4.6.2 GSC Impedance

The result of the simulation for the GSC impedance can be seen in the following figure,

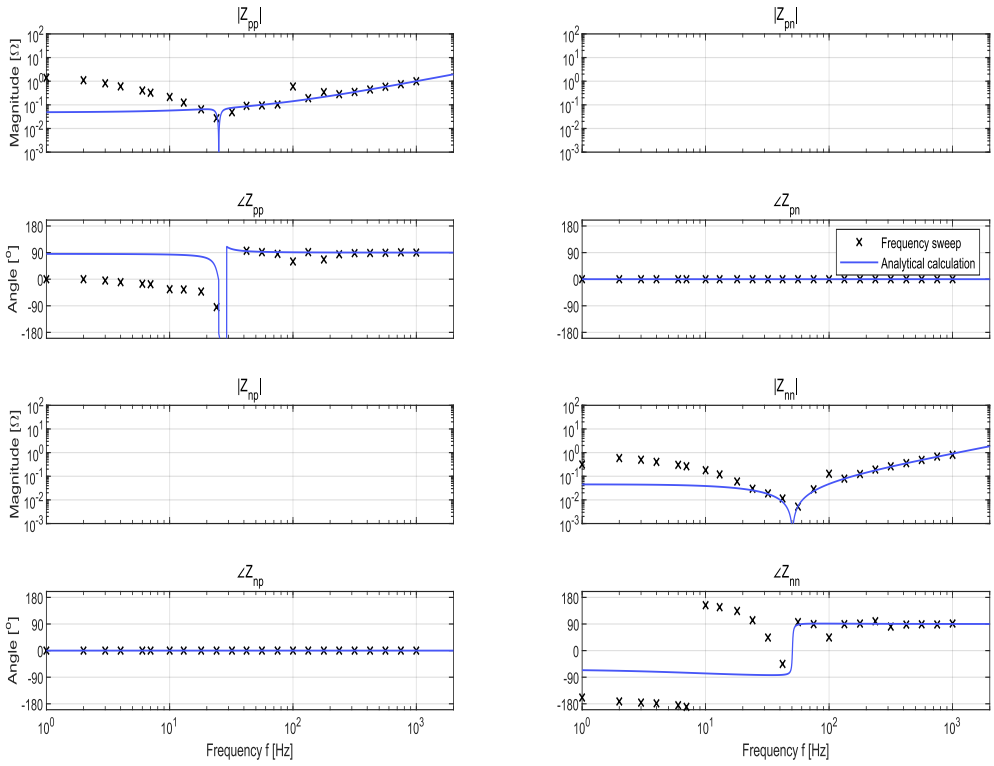

Figure 4.6 GSC Impedance Analytical Calculation and Frequency Sweep

It can be seen from Figure 4.6 the frequency sweep and the analytical calculation differs to a certain extent. By analysing the bode plots, the analytical and frequency sweep is aligned at $f > 27\,Hz$ while for negative sequence, it is aligned at $f > 50\,Hz$. This indicates that the analytical derivation is not really accurate for the low frequency region.

From the frequency sweep, it can also be seen that the impedance response is similar to a capacitive circuit at the low frequency, and to an inductive circuit at the high frequency. While for the analytical calculation, it shows a similar response to an RL circuit with a certain resonant frequency. This is understandable and an expected results since Synchronverter itself is a VSM algorithm which mimic the characteristic of an SG. Since SG is an inductive component, the analytical derivation of Synchronverter will be similar an SG characteristic as well.

For accuracy in doing the stability analysis for chapter 5, a new impedance model for the GSC part based on curve fitting will be used. This will also be assessed with the derived analytical model to see the difference on stability analysis accuracy between the two models. The curve fitting model for the GSC impedance is as follows,

$$\boldsymbol{Z_{GSC,fit}} = \begin{bmatrix} Z_{11,fit} & 0 \\ 0 & Z_{22,fit} \end{bmatrix} \tag{107}$$

where

$$Z_{11,fit} =$$

$$\frac{0.001082s^6 + 23.49s^5 + 2120s^4 - 2.354 \times 10^4 s^3 + 1.792 \times 10^6 s^2 - 1.058 \times 10^7 s - 2.649 \times 10^8}{s^5 + 2.348 \times 10^4 s^4 + 1.494 \times 10^6 s^3 + 1.815 \times 10^7 s^2 - 6.395 \times 10^6 s - 1.745 \times 10^8}$$

and

$$Z_{22,fit} =$$

$$\frac{0.0007705s^6 + 2.946s^5 + 3.097 \times 10^4 s^4 + 3.324 \times 10^5 s^3 + 4.407 \times 10^6 s^2 + 7.535 \times 10^8 s + 5.429 \times 10^8}{s^5 + 3081s^4 + 3.406 \times 10^7 s^3 - 8.991 \times 10^7 s^2 - 1.195 \times 10^9 s - 2.077 \times 10^9}$$

The result of the curve fitting is shown below,

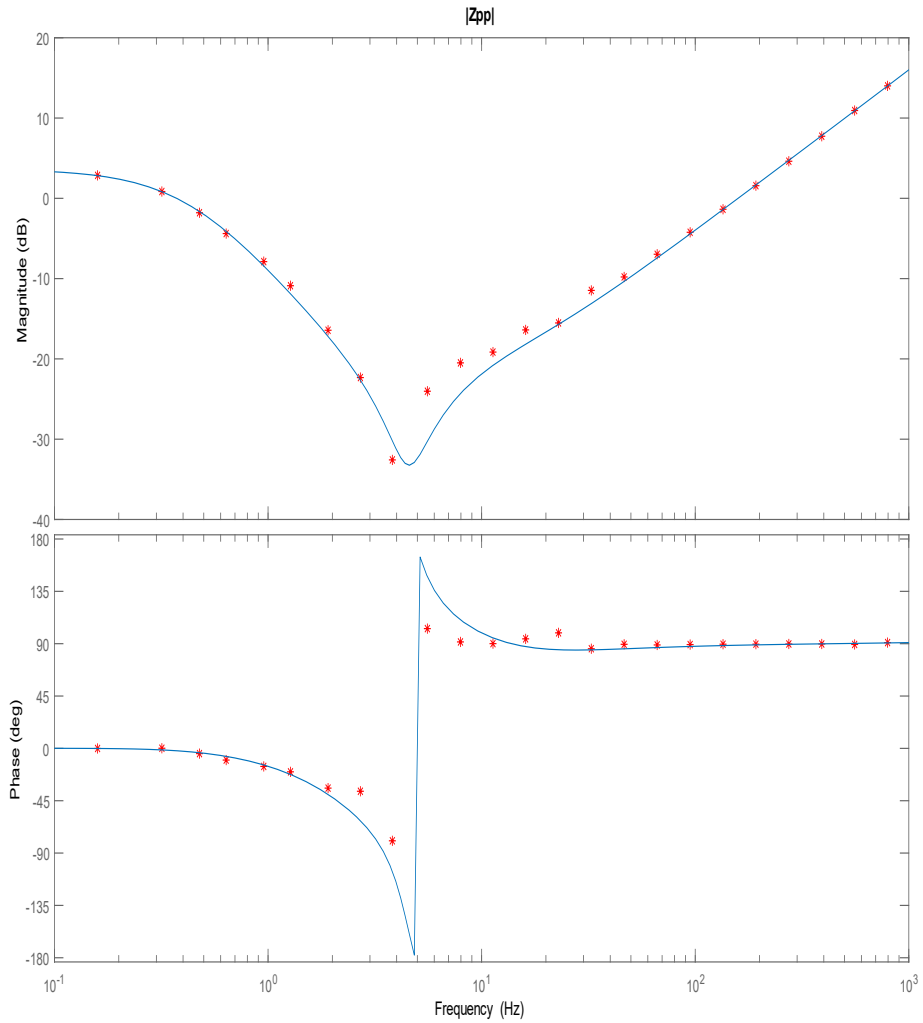

Figure 4.7 GSC Positive Sequence Impedance by Curve Fitting

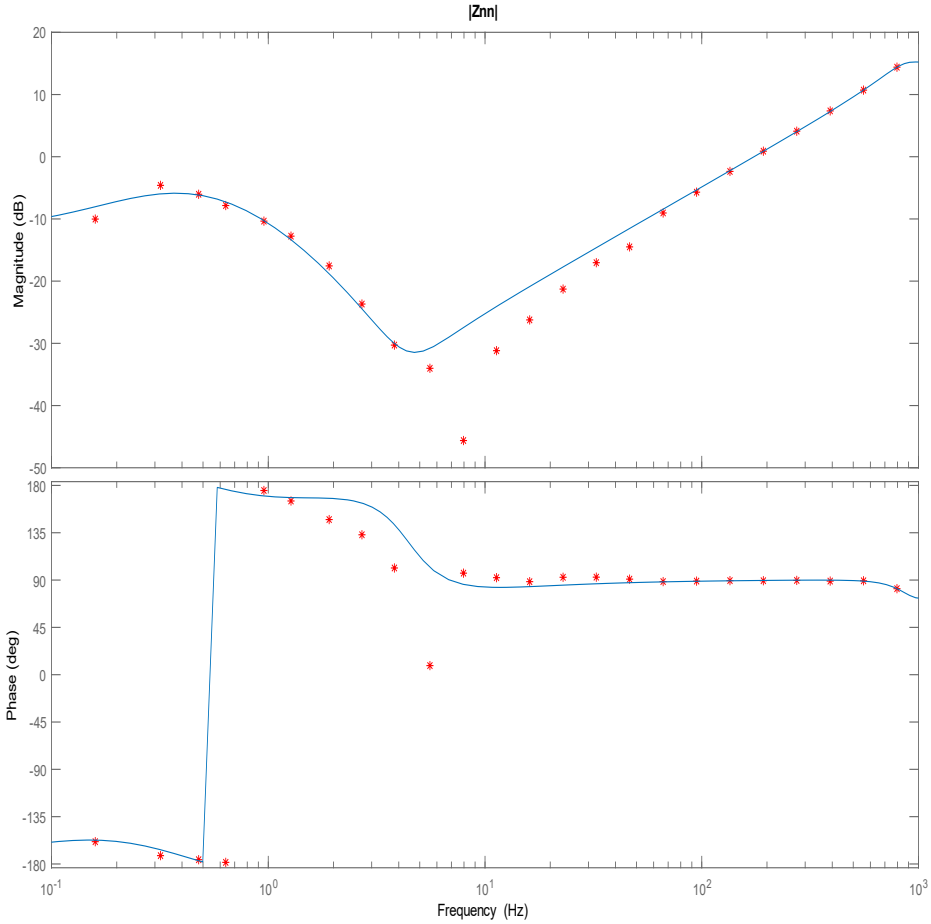

Figure 4.8 GSC Negative Sequence Impedance by Curve Fitting

Chapter 5

Impedance-based Converter-driven Stability Analysis under Weak AC Grid Conditions

This chapter puts forward a sensitivity analysis of the WECS' parameters for converter-driven stability. First, an introduction of the chapter regarding the existing methods for impedance-based stability analysis of power electronics systems will be presented. Then, a concise explanation of weak grid's characteristics will be given, along with the concept for Generalised Nyquist Criterion (GNC). Lastly, simulations are carried out to investigate the effect of several parameters of the WECS for converter-driven stability.

5.1 Introduction

With the increasing amount of renewable energy to the grids, it has been explained that there are a lot of impacts it will bring that changes the overall power systems scenario worldwide.

Connecting renewable energy power plants will be constrained by geographic location, in which they need to be connected to a location where the resources are abundant. However, these areas are typically very distant from the main grids. These far distances cause the grid impedance as seen from the VRE power plants to be very high, and is usually referred to a weak grid. Weak grid might cause issues, ranging from steady-state issues to dynamic issues [102]. As elaborated in Chapter 2, stability issues due to interaction between the converters and/or converter-grid interactions is referred as converter-driven stability and will be the main focus on this chapter.

To investigate the converter-driven stability based on impedance analysis, there are several methods such as GNC [103], Impedance Specification [104], Impedance Sum Criterion/Impedance Network Model [105], and Multi-loop Nyquist Stability Criterion [106]. There are several advantages and disadvantages regarding each of the method. For example, in Impedance Sum Criterion and Impedance Specification, it is assumed that no open loop RHP pole exist in the impedance ratio and the impedance sum. For multi-loop NSC, it heavily depends on the system topology, in which for a complex system, the loop might be too complex to select [107]. This thesis will focus on GNC as one of the most basic techniques derived from the standard Nyquist criterion. This will be explained further in section 5.3.

Since this section will deal with converter-driven stability for weak AC grid, characteristics of a weak grid will also be explained so the reader can have deeper understanding regarding the issues.

5.2 Characteristics of a Weak Grid

Weak AC grids (from here onwards will be referred simply as weak grids) are a power systems/grids that are very vulnerable to sudden changes in operating conditions [108]. This indicates that any major changes in the operating conditions, such as active power set point might result in significant voltage and frequency fluctuations. Whereas, strong grids are more robust to any changes in the system. In other words, strong grids are more resilient to faults and disturbances.

The grid strength is commonly defined by the SCR, and this is conceptually incorrect. Grid strength is actually determined by its impedance and mechanical inertia [109]. SCR is only a numerical ratio which compares the system's short circuit AC power compared to real power injection. However, this ratio turns out as a good measurement in checking the robustness to changes of the grid. Therefore, SCR is now an acceptable approximation of the grid strength [110].

As mentioned in previous paragraph, SCR can be determined mathematically as

$$SCR = \frac{S_{SC}}{P_n} \tag{108}$$

where S_{SC} is the 3-phase short circuit power as seen from the PCC and P_n is the nominal power of the power plants. By modelling the grid as a Thevenin circuits, S_{SC} can be mathematically expressed as

$$S_{SC} = \frac{V_{PCC}^2}{Z_{th}} \tag{109}$$

Here, V_{PCC} is the PCC voltage. Assuming that the power plants nominal power is 1 p.u., then the SCR can be simplified to

$$SCR = \frac{1}{Z_{Th}} \tag{110}$$

For a grid to be defined as weak, usually the SCR < 2 - 3 [67]–[72]. One thing worth to understand is that SCR is dynamic. Therefore, grid strength can be very much different depending on the bus we are trying to analyse. Also, during transient conditions such as contingencies or fault, SCR will also change.

Integrating a wind farm which have limited capability curve to a weak grid can cause several issues, such as [68]:

1. Decreased voltage stability limits
2. Limited active power transfer capability due to the SIL and the PV stability limit
3. Limited ramp rate capability of the active and reactive power, causing poor frequency and voltage regulation
4. Instability of the control loops of the WECS
5. Tripping on TOV during fault recovery period
6. Poor FRT response

5.3 Generalised Nyquist Stability Criterion and Its Application in Power Systems

NSC is one of the most basic graphical techniques to determine a stability of dynamical system. Other graphical techniques include Root Locus, Bode Plot, and Nichols Plot. The stability criterion is used when the dynamical system is described by a closed-loop negative feedback transfer function. Consider the following system for more clarity.

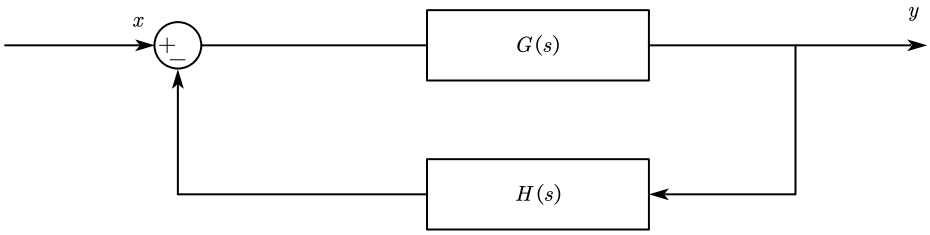

Figure 5.1 General Block Diagram of a Closed-Loop Negative Feedback Dynamic Systems

Then, the CLTF can be mathematically expressed as

$$CLTF = \frac{G}{1 + GH} \tag{111}$$

Here, the denominator of the CLTF, i.e., $1 + GH$ is known as characteristic equation, and the roots of this polynomial is called pole, while the roots of the polynomial in the numerator is called zero. From control theory, it is known that the stability of the system is determined by the real-part of the located in the RHP.

In Nyquist diagram, the OLTF, GH will be plotted in the complex plane with s as a variable. This s will be varied from zero to infinity, then to minus infinity, and back to zero. This will create a vector with origin at (-1,0), coming from the characteristic equation of the CLTF. From here, the NSC can be formally stated as [103]

> *"A closed-loop system is stable if the number of RHP poles in GH equals the number of counter-clockwise encirclements of the point (-1,j0) by the Nyquist plot of GH"*

Interestingly, the CLTF discussed above is assumed to be proper, i.e., the order of the numerator will be less than the order of the denominator. In the case of an improper CLTF, then the *Inverse Nyquist Stability Criterion* is valid, and can be formally stated as [103]

> *"A closed-loop system is stable if the Nyquist plot of in $\frac{1}{GH}$ has number of counter-clockwise encirclements of the point (-1,j0) equals to the number of RHP zeros of GH"*

If we take a closer look at Figure 5.1, then it is clear the dynamic system modelled is SISO. However, dynamic systems especially in power systems application are usually modelled in MIMO. Therefore, the NSC definition needs to be extended to MIMO system, resulting in GNC. Consider the following figures,

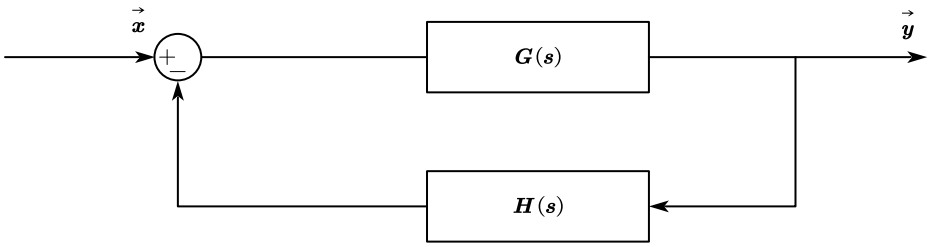

Figure 5.2 General Block Diagram of a Closed-Loop Negative Feedback MIMO Systems

Then, the CLTM can be mathematically expressed as

$$CLTM = [\boldsymbol{I} + \boldsymbol{GH}]^{-1}\boldsymbol{G} \tag{112}$$

$$OLTM = \boldsymbol{GH} \tag{113}$$

where bold indicates a transfer matrix. Therefore, the GNC can be formally expressed as [103]

> *"A closed-loop system is stable if the Nyquist contour of **GH** with P RHP poles has P number of counter-clockwise encirclement of (-1,j0) made by all the eigenvalue loci of **GH**"*

Note that the GINC is also valid here by taking $\boldsymbol{G^{-1}H}$ as the OLTM, and performing GNC to such OLTM.

In the applications for power systems studies, consider the following figure.

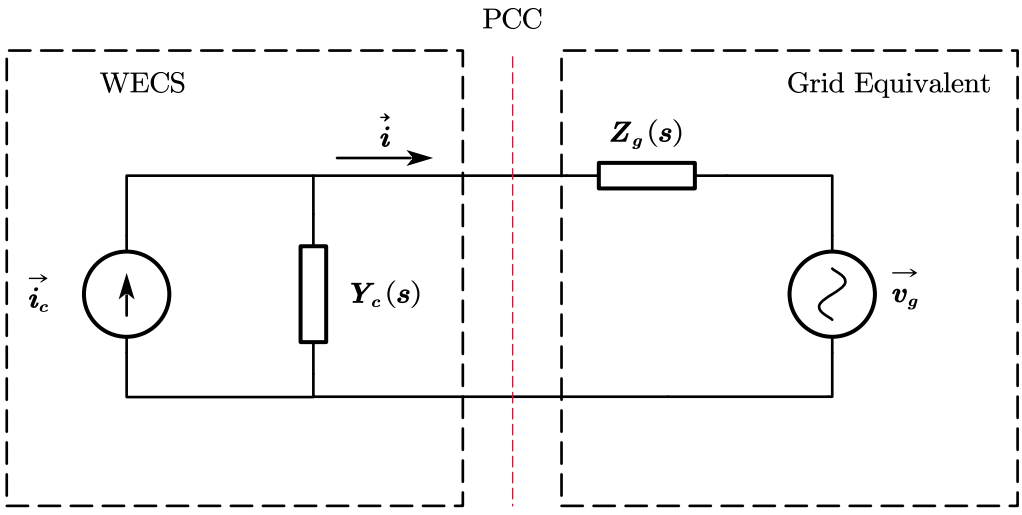

Figure 5.3 Impedance Model of WECS Connected to the Grid

Take a closer look at Figure 5.3, the current that flows in the system can be mathematically expressed using Ohm's law as follows,

$$\vec{\boldsymbol{i}} = \left(\vec{\boldsymbol{i_c}} - \boldsymbol{Y_c}\vec{\boldsymbol{v_g}}\right)\left[\boldsymbol{I} + \boldsymbol{Y_c Z_g}\right]^{-1} \tag{114}$$

From the impedance derived in chapter 4, the WECS admittance is equal to

$$\boldsymbol{Y_c} = \boldsymbol{Z_g^{-1}} = \boldsymbol{Z_{WECS}^{-1}} \tag{115}$$

By using the GNC in $\boldsymbol{Y_c Z_g}$, the converter-driven stability of the WECS interaction with the power grids can be analysed.

5.4 Simulations and Results

As mentioned previously, this chapter will conduct sensitivity analysis to study the several parameters of the WECS which might be related to the converter-driven stability. There are 3 parameters being studied:

1. Grid strength
2. Virtual damping
3. Virtual inertia

For the modelling in this chapter, the previous assumption regarding the decoupling of the dynamics of both GSC and the RSC is still valid. This section will only model the GSC part with a constant DC voltage source and the external grid. Therefore, the impact of the DC link capacitor and voltage regulator will not be studied since it is under the RSC control schemes.

5.4.1 Default Parameters

First, an assessment of the stability for the default case will be done, and shown as below.

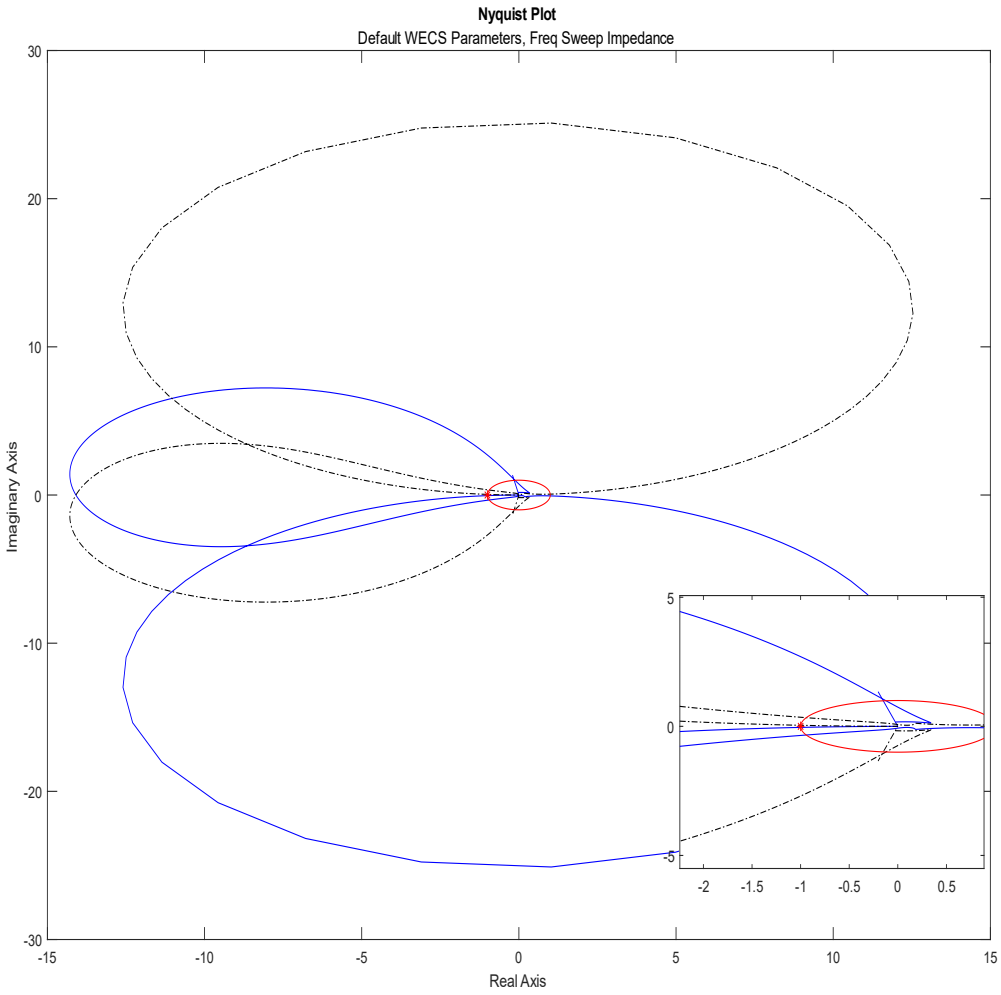

Figure 5.4 Nyquist Plot of $Y_c Z_g$ by Frequency Sweep (Default Parameter)

As can be seen from Figure 5.4, the Nyquist plot does encircle point (-1,j0) 2 times. Without knowing the characteristic equations, we might make a mistake by deducing that the system is unstable. However, encircling the (-1,j0) might still make the system stable if there exist 2 open loop poles in the RHP. By combining the analysis with the time domain response, we can reassure if the system is stable or not as follows,

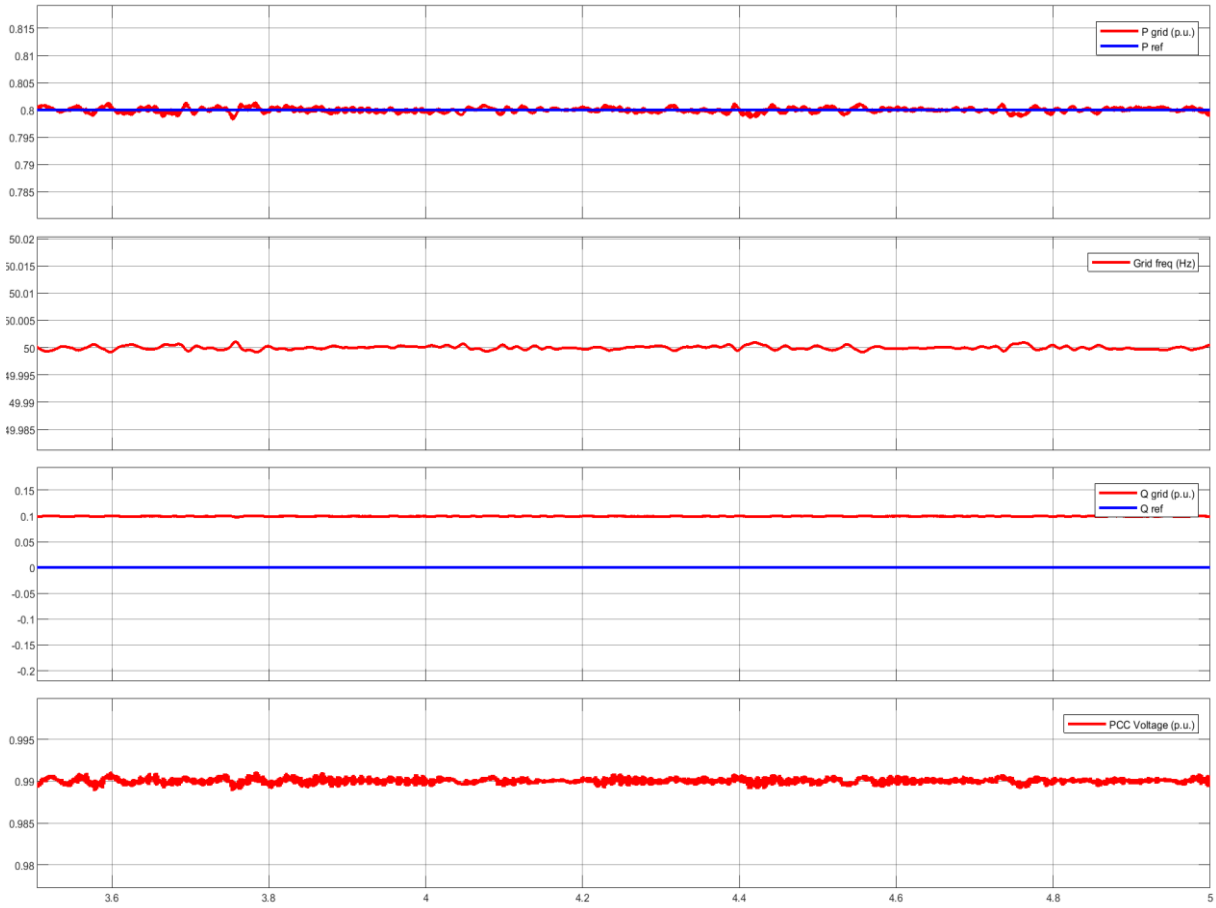

Figure 5.5 Time Domain Simulation Results (Default Parameter)

From Figure 5.5, it is shown that the system response is stable. Therefore, from eigenvalue loci of the OLTM, there exists at least 2 open loop poles on the RHP. This comes from the SISO NSC encirclement condition as follows,

$$N = P - Z \tag{116}$$

where N indicates the number of encirclements. N can be positive and negative depending on the direction of the encirclements. In the case of equation (116), N indicates the number of encirclements in counter-clockwise directions. P and Z is the number of RHP poles and RHP zeros respectively.

Since it is clear that from Figure 5.4 the Nyquist plot encircle the critical point (-1,j0) 2 times, it can be concluded that at least 2 RHP poles exist on the OLTM.

It can also be seen that some oscillation exist which might happen due to harmonics, and it might cause instability if some parameters that govern the stability are varied. Qualitatively speaking from the Nyquist plot, it is clear that the gain margin of the open loop system is relatively small since the Nyquist contour is located really close to the critical

point (-1,j0). Hence, the system is clearly very prone to instability, as hypothesised in previous chapters.

Now, it is interesting to see the difference of performance in stability assessment between the impedance obtained from analytical derivation and the impedance obtained from frequency sweep directly. The Nyquist plot of the analytical derivation can be seen in the following figure.

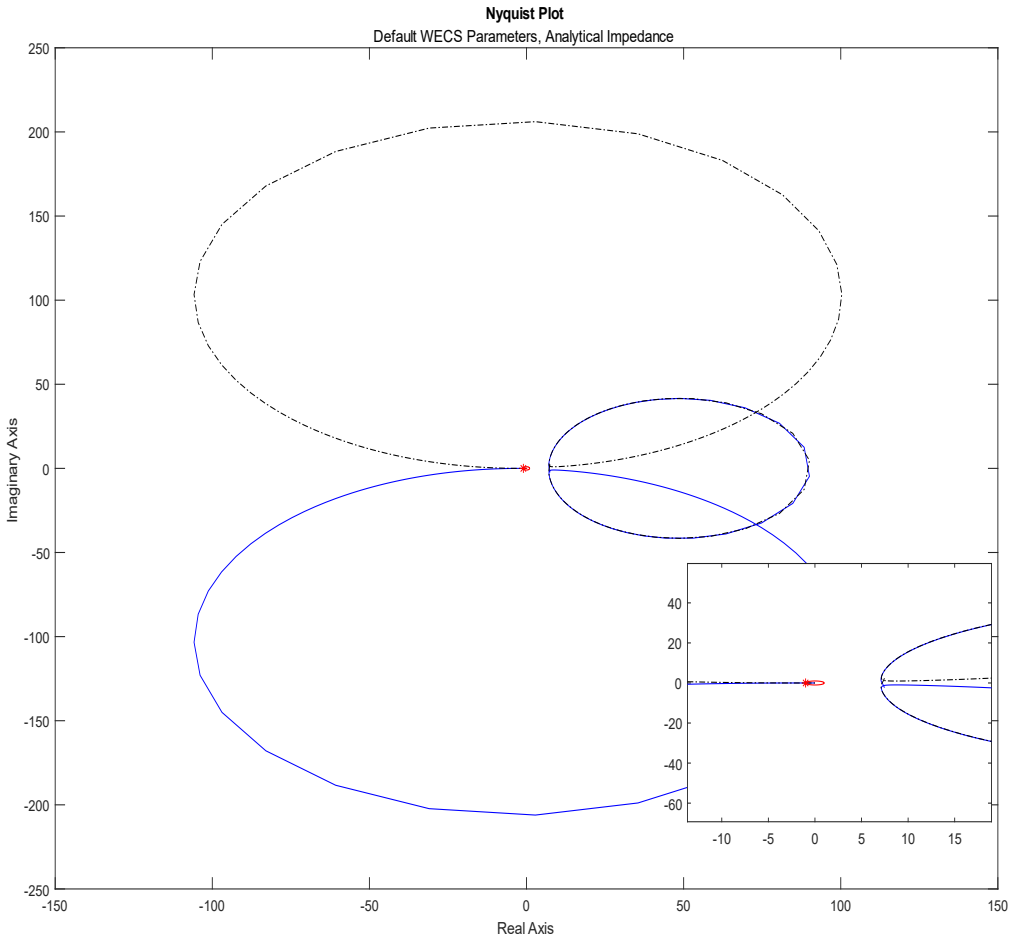

Figure 5.6 Nyquist Plot of $Y_c Z_g$ by Analytical Derivation (Default Parameter)

Even though the Nyquist contour shape is quite different between the analytical impedance and between the frequency sweep, turns out the most important features are exactly the same. From Figure 5.6, it is clear that the Nyquist contour cut through the critical point (-1,j0) 2 times. Therefore, same conclusion can be achieved either by applying GNC to the simple analytical derivation of impedance or the frequency sweep impedance.

Also, since the Nyquist plot of Figure 5.6 cut through the critical point directly, it can be deduced that the system is marginally stable with very low stability margin. Hence, the WECS interconnection to the grid is very prone to instability.

In the following section, the sensitivity analysis regarding the grid strength will be conducted to see the impact of the interconnection to the weak AC grid.

5.4.2 Grid Strength Sensitivity

First, the SCR of the default case will need to be calculated. By taking the grid equivalent impedance as the parallel connection between the filter and the original grid impedance as derived in the previous chapter, the SCR of the default case is

$$SCR_{def} = \frac{1}{|Z_{eq}|} = \frac{1}{\left(\frac{1}{\frac{R_{filter}}{1+sC_{filter}R_{filter}}} + \frac{1}{R_g + sL_g}\right)^{-1}} = 2.8168$$

Considering that the SCR is already quite low in the region of typical weak AC grid, it will be interesting to vary the SCR further to the region of ultra-weak grid (SCR = 1) and the region of strong grid (SCR = 10). To vary the SCR, the grid inductance, L_g will be varied. From MATLAB equation solver, we obtain $L_g = 0.00275\ H$ for SCR = 1 and $L_g = 0.000275\ H$ for SCR = 10.

The Nyquist plot obtained from the frequency sweep for SCR = 1 are as follows,

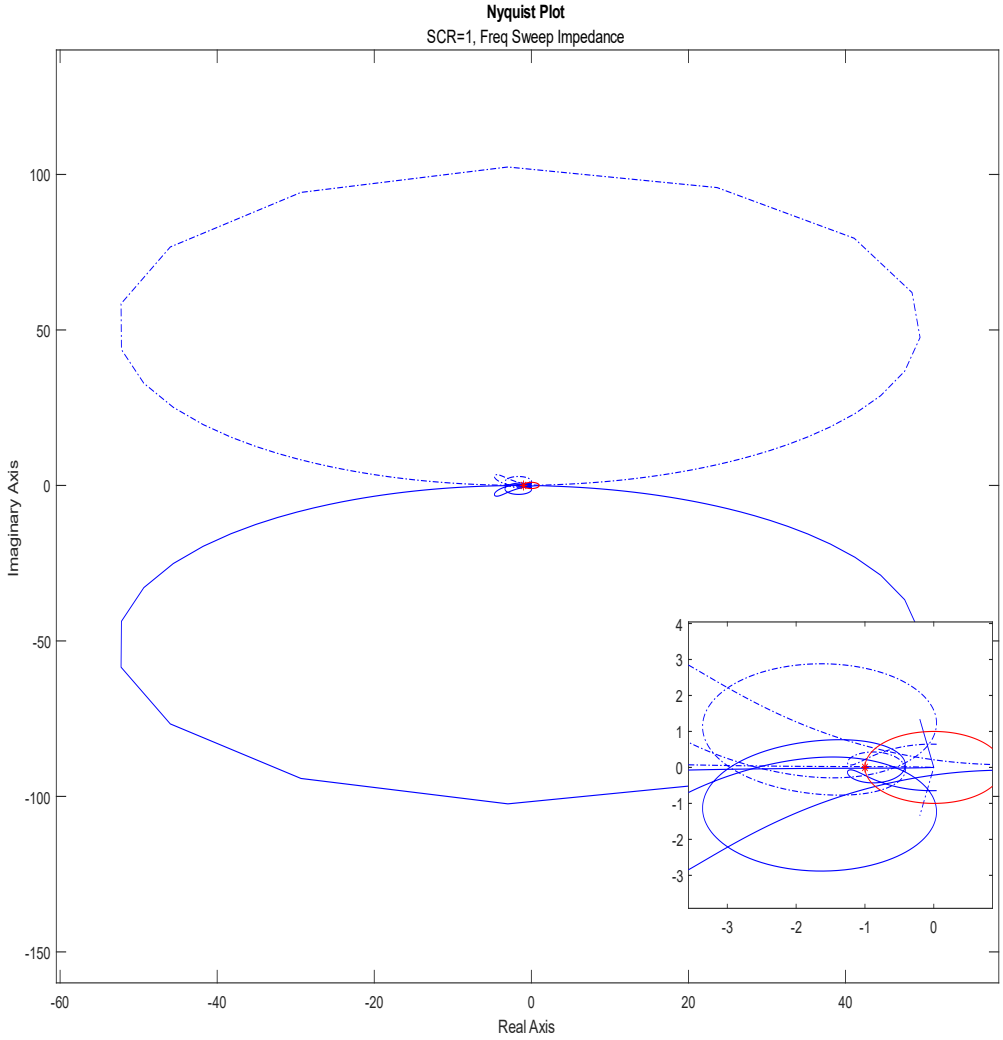

Figure 5.7 Nyquist Plot of Y_cZ_g by Frequency Sweep (SCR = 1)

As seen from Figure 5.7, there are a lot of encirclement around the critical point (-1,j0). Considering that the grid's strength is under ultra-weak condition, we can safely deduce that the system will be unstable. Even though there is still possibility for the system to be stable according to the encirclement condition N = P-Z, it is safer to assume that the system is unstable due to the weak grid vulnerability characteristics.

However, with GINC, we can check whether the stable is system or not. The GINC results are as follows,

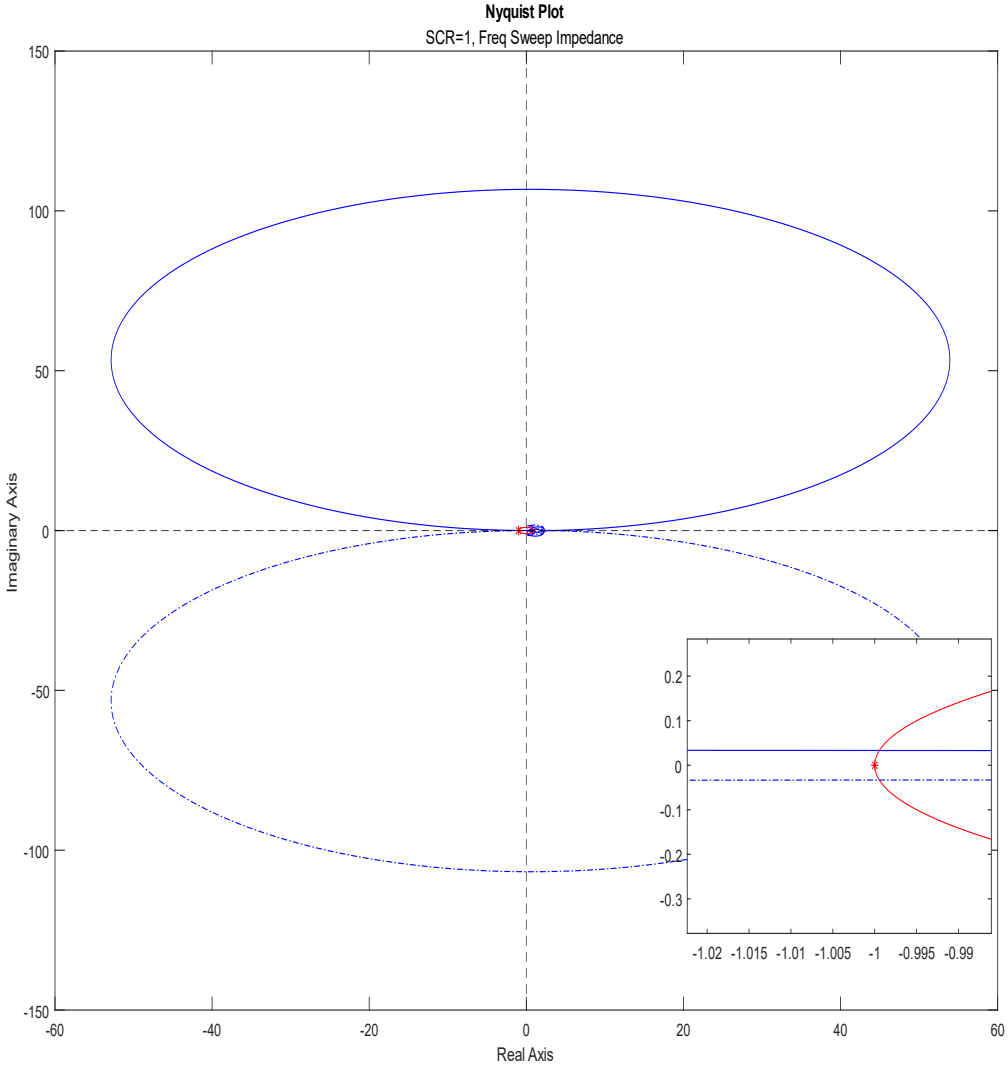

Figure 5.8 Inverse Nyquist Plot of $Y_c Z_g$ by Frequency Sweep (SCR = 1)

From the inverse Nyquist plot, obtained by using GINC, it is crystal clear that the critical point (-1,j0) is not encircled. Therefore, we can now be certain that the encirclement in Figure 5.7 is still stable since there exists RHP zeros.

To ascertain our deduction, analysing the time domain simulation results is a must and the results are as follows,

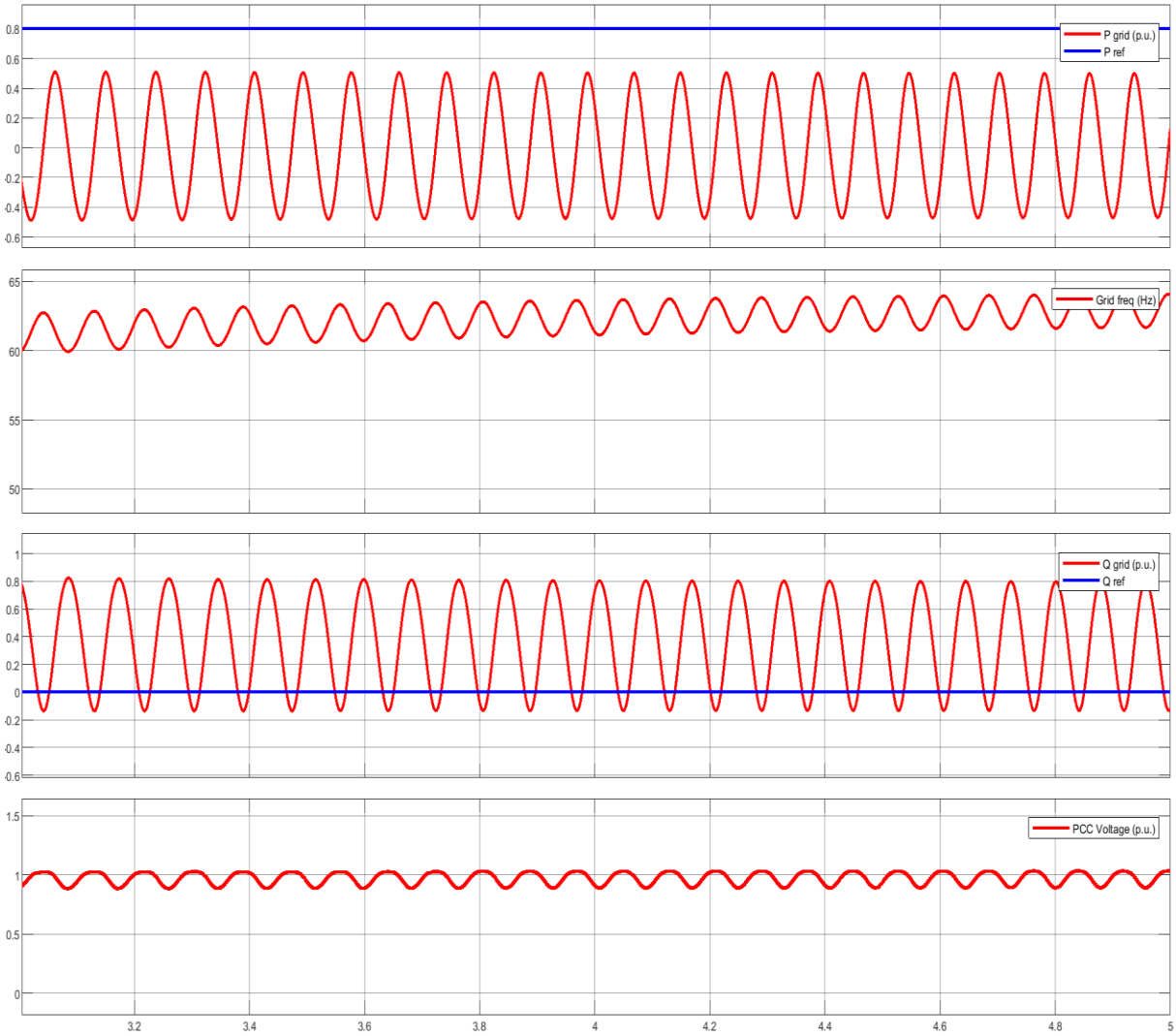

Figure 5.9 Time Domain Simulation Results (SCR = 1)

It can be seen clearly from the time domain results that it is marginally stable. It can be considered marginally stable since from the results, the oscillation is pretty bad for all 4 important parameters in power systems, in terms of grid codes compliance. However, the oscillation itself is clearly bounded. Hence, it can be deduced that impedance-based stability analysis is only concerned on the harmonics or oscillation behaviour, but it cannot stand alone and needs to be equipped with other stability assessment and the grid codes to fully understand the impact on the grids.

In the nutshell, it is correct according to the theory regarding the weak grid characteristics. The system is unstable (from the power system's perspective) since the grid's strength is very low and can be considered as an ultra-weak grid. While interconnecting the WECS, a variation of active and reactive power during the transient period causes the system's voltage stability margin to be violated, hence an oscillation happened. This scenario successfully shows how the GNC combined with time domain results can ascertain the converter-driven stability of the WECS.

The Nyquist plot for the same scenario of the analytically derived impedance is as follows,

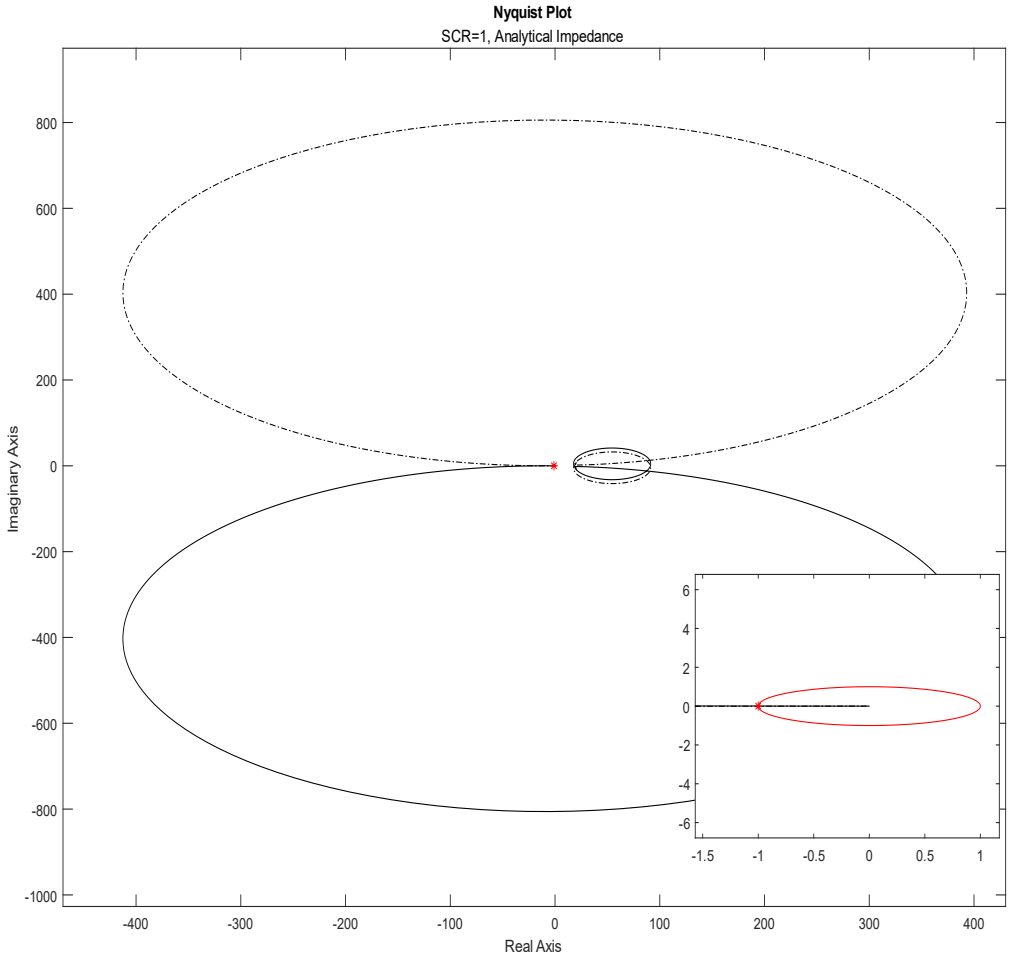

Figure 5.10 Nyquist Plot of $Y_c Z_g$ by Analytical Derivation (SCR = 1)

It can be seen that Figure 5.10 have a very similar shape and characteristics with Figure 5.7. It is predictable since for the high frequency part, the analytical derivation and the frequency sweep is actually quite consistent with each other. Therefore, the difference in shape is due to the low frequency differences. It can also be seen from Figure 5.10 that the critical point (-1,j0) is being cut through by the Nyquist contour. Therefore, the system can be deduced as marginally stable or unstable, consistent with the previous obtained results.

Now, we would like to investigate the WECS interconnection in a strong grid with SCR = 10. Again, the Nyquist plot obtained from the frequency sweep for SCR = 10 is as follows,

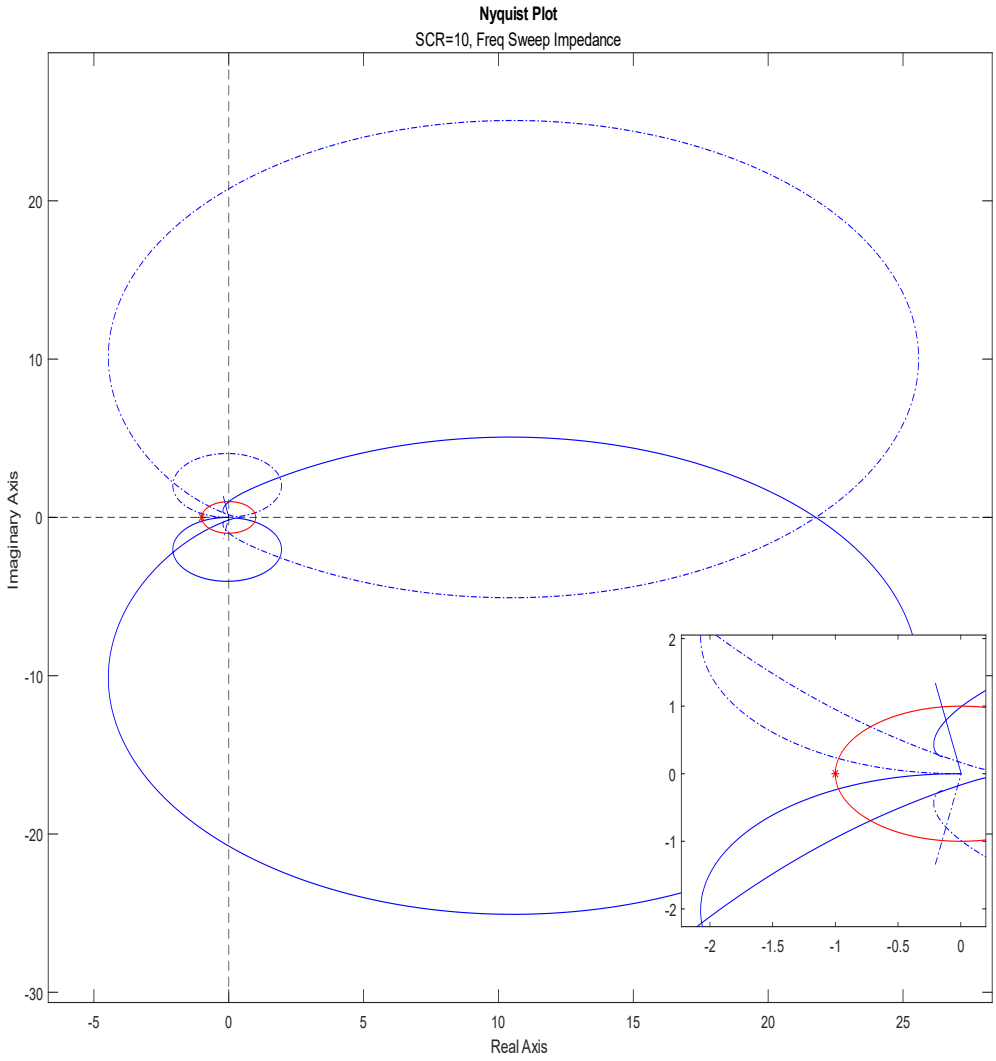

Figure 5.11 Nyquist Plot of $Y_c Z_g$ by Frequency Sweep (SCR = 10)

As seen from Figure 5.11, there is no encirclement around the critical point (-1,j0). Hence, we can conclude that the system is stable. No encirclement indicates that there are no unstable open loop poles in the RHP.

By visually analysing the figure, we can also conclude that the stability margin of the system with SCR = 10 is better than the default scenario, where the stability margin is very low. This indicates that the system with higher SCR have a higher 'spare-capacity' for flexibility operation during contingencies to prevent fault.

To reaffirm our deduction on the system's converter-driven stability, the time domain simulation responses are as follows,

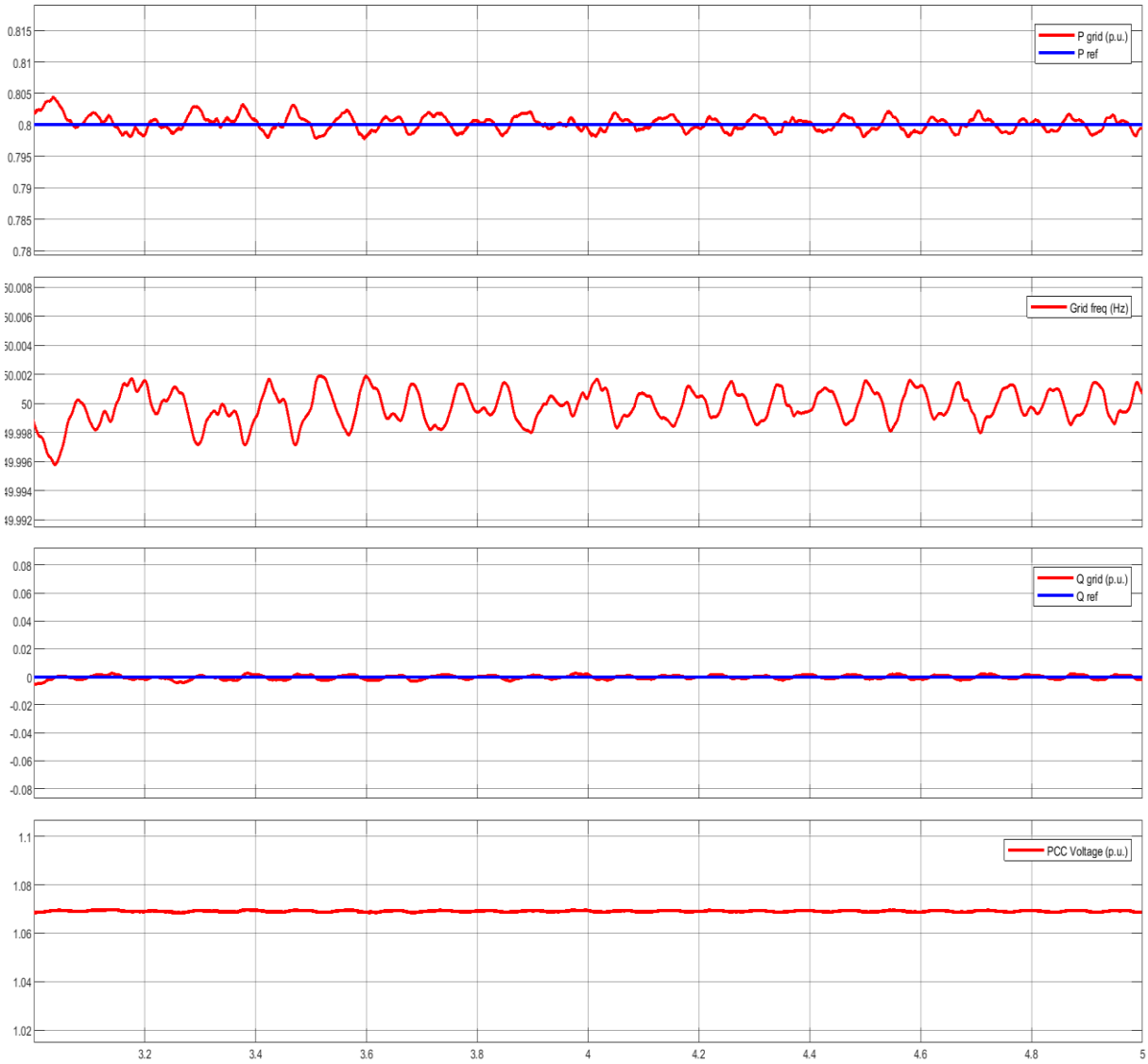

Figure 5.12 Time Domain Simulation Results (SCR = 10)

It can be seen clearly from the time domain results that it is stable. Therefore, it is correct according to the theory regarding the weak grid characteristics. The system is now stable since the grid's strength is relatively high and can be considered as a strong grid. In this scenario, for interconnecting the WECS, a variation of active and reactive power during the transient period will not violates the system's stability margin, hence no significant oscillation happened. This scenario, again, successfully shows how the GNC combined with time domain results can ascertain the converter-driven stability of the WECS.

It is interesting to see that the amplitude of the small oscillation that occurs in Figure 5.12 is higher compared to the default parameters in Figure 5.5. This might happen due to the control tuning which is not optimised for the varying value of SCR. However, this will not affect the results much, hence the stability is still confirmed.

The Nyquist plot for the same scenario of the analytically derived impedance is as follows,

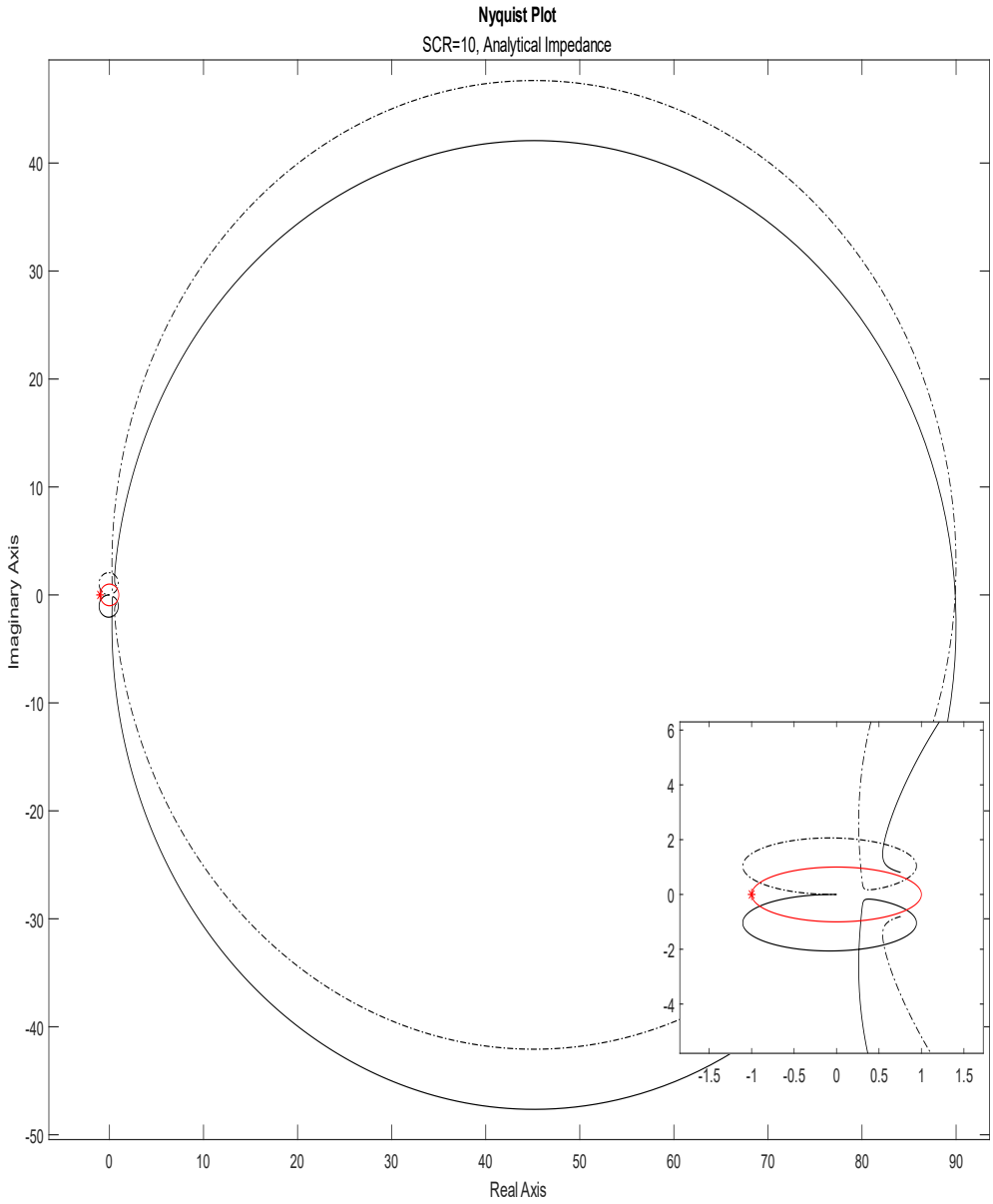

Figure 5.13 Nyquist Plot of $Y_c Z_g$ by Analytical Derivation (SCR = 10)

It can be seen that Figure 5.13 have a very similar shape and characteristics with Figure 5.11. It is predictable since for the high frequency part, the analytical derivation and the frequency sweep is actually quite consistent with each other. Therefore, the difference in shape is due to the low frequency differences. It can also be seen from Figure 5.13 that the critical point (-1,j0) is not being encircled by the Nyquist contour. Therefore, the system can be deduced as stable, consistent with the previous obtained results.

5.4.3 Virtual Damping Sensitivity

In this section, one of the most important parameters for the WECS will be assessed which is the virtual damping, D_p. A sensitivity analysis will be conducted for 2 varying values of D_p, which is $D_p = 50$ and $D_p = 1500$. The default value of D_p is 506.6059.

The Nyquist plot obtained from the frequency sweep for $D_p = 50$ is as follows,

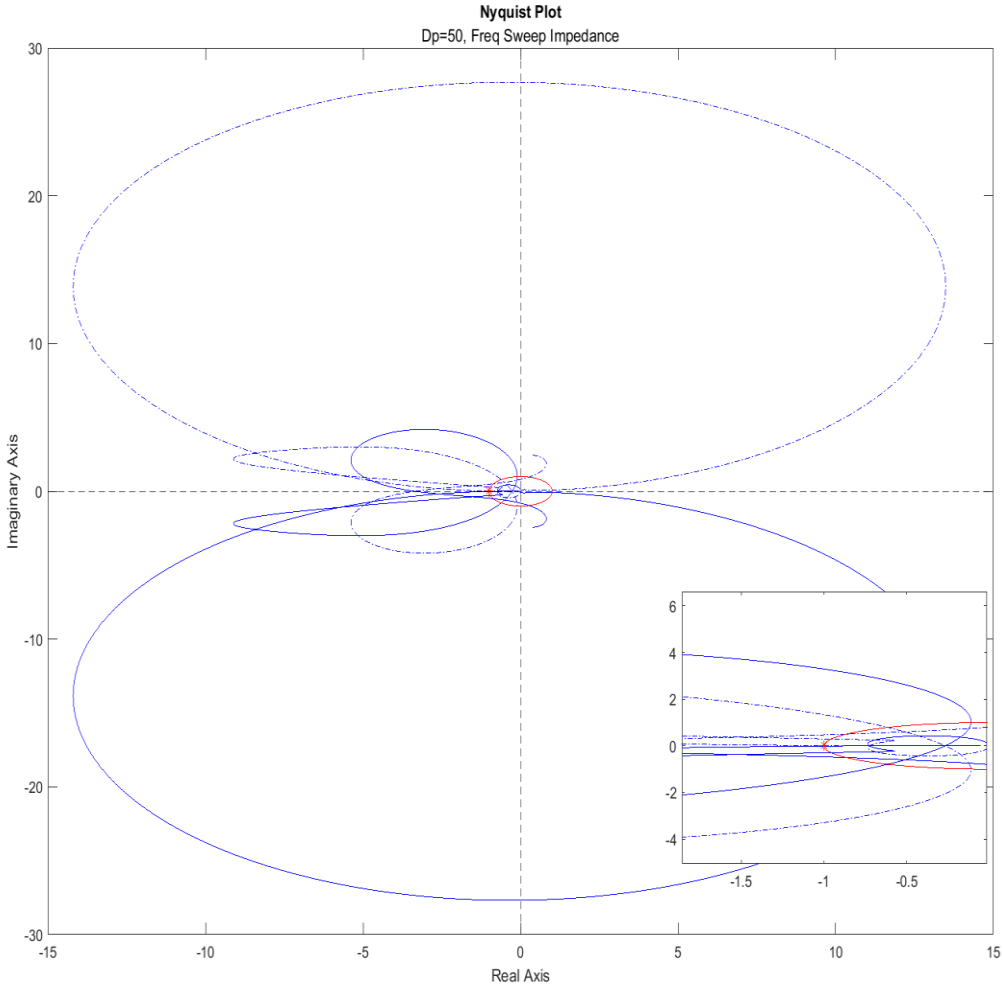

Figure 5.14 Nyquist Plot of $Y_c Z_g$ by Frequency Sweep (Dp = 50)

As seen from Figure 5.14, there are a lot of encirclement around the critical point (-1,j0). Therefore, we have difficulties on determining the stability, similar to previous section. To help our analysis, we can utilise again the GINC plot.

The result of the GINC plot is as follows,

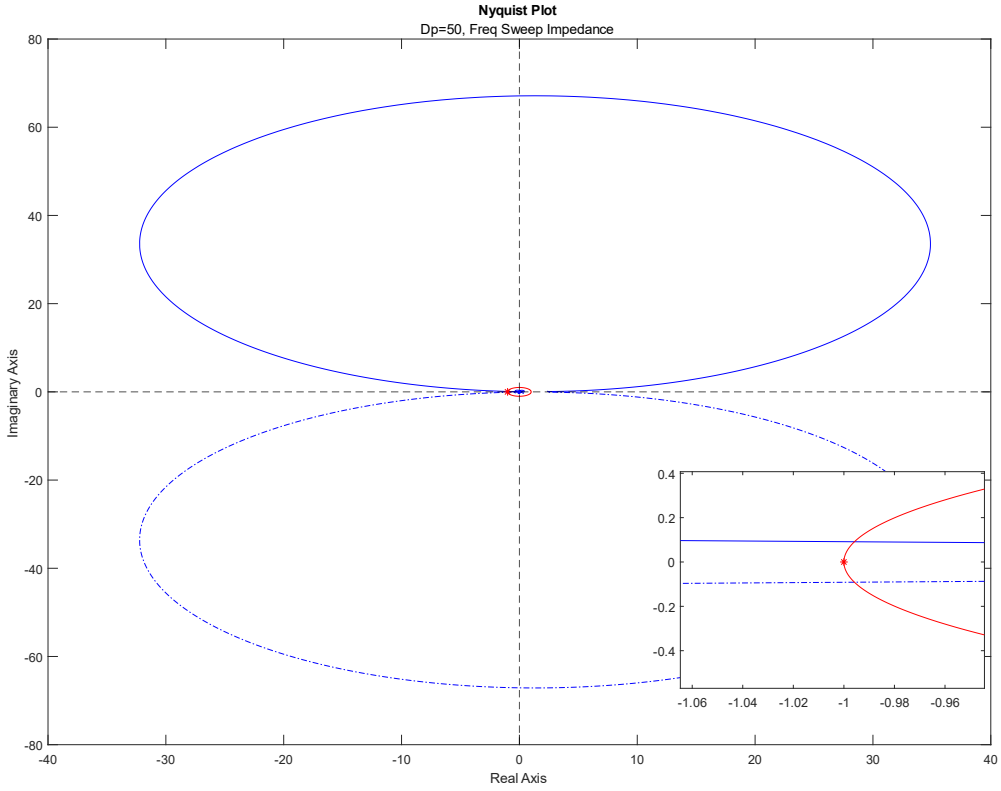

Figure 5.15 Inverse Nyquist Plot of $Y_c Z_g$ by Frequency Sweep (Dp = 50)

As seen from Figure 5.15, there is no encirclement around the critical point (-1,j0). Hence, we can conclude that the system is stable. No encirclement indicates that there are no unstable open loop poles in the RHP.

Virtual damping is one of the most important aspects in the Synchronverter control since it is directly involved with the frequency regulation. With reduced damping, we can infer that the oscillation will be higher.

To reaffirm our deduction on the system's converter-driven stability, the time domain simulation responses are as follows,

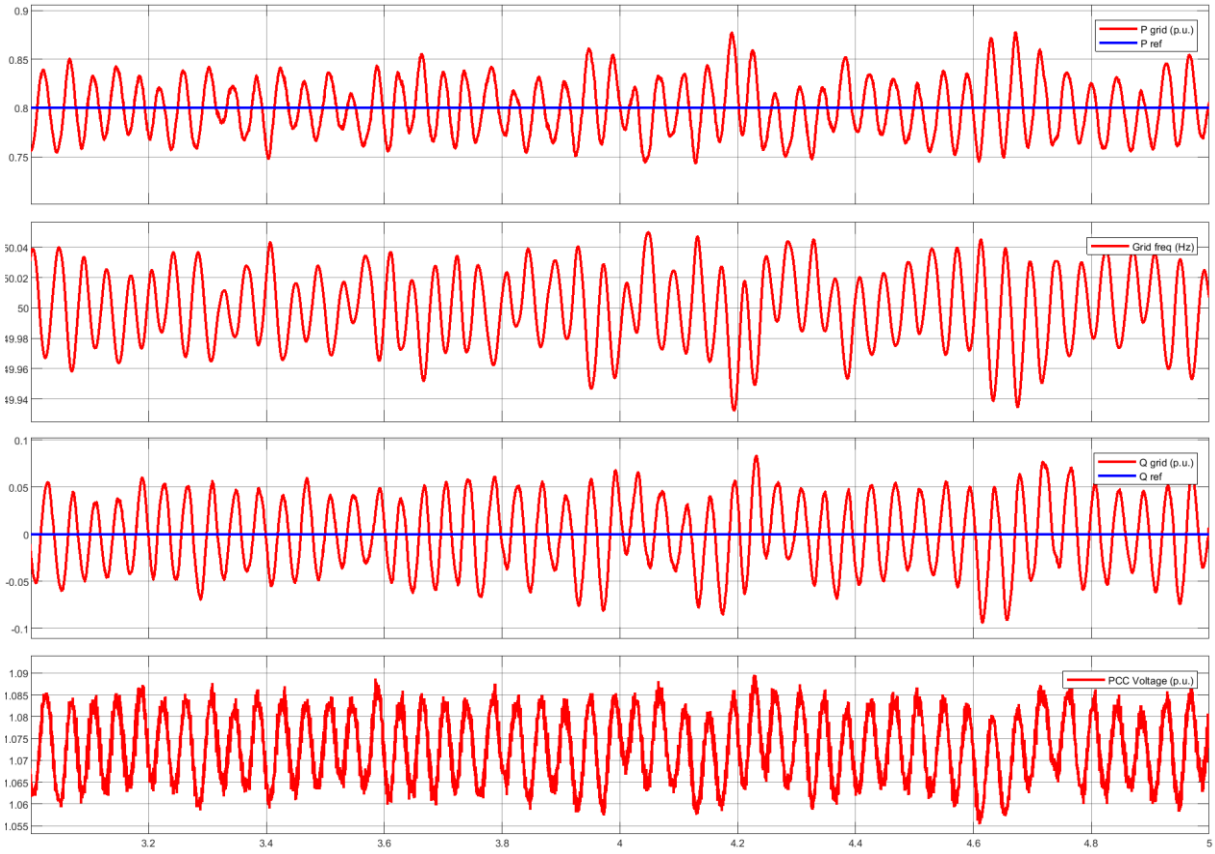

Figure 5.16 Time Domain Simulation Results (Dp = 50)

It can be seen clearly from the time domain results that it is stable since the oscillation is bounded. It is worth to note as well that the oscillation does indeed get higher compared to the default case. This is well-expected since as explained previously, the virtual damping affects the frequency regulation and plays a significant part in the APL of the GSC part of the WECS.

This scenario successfully shows how the GNC combined with time domain results can ascertain the converter-driven stability of the WECS.

The Nyquist plot for the same scenario of the analytically derived impedance is as follows,

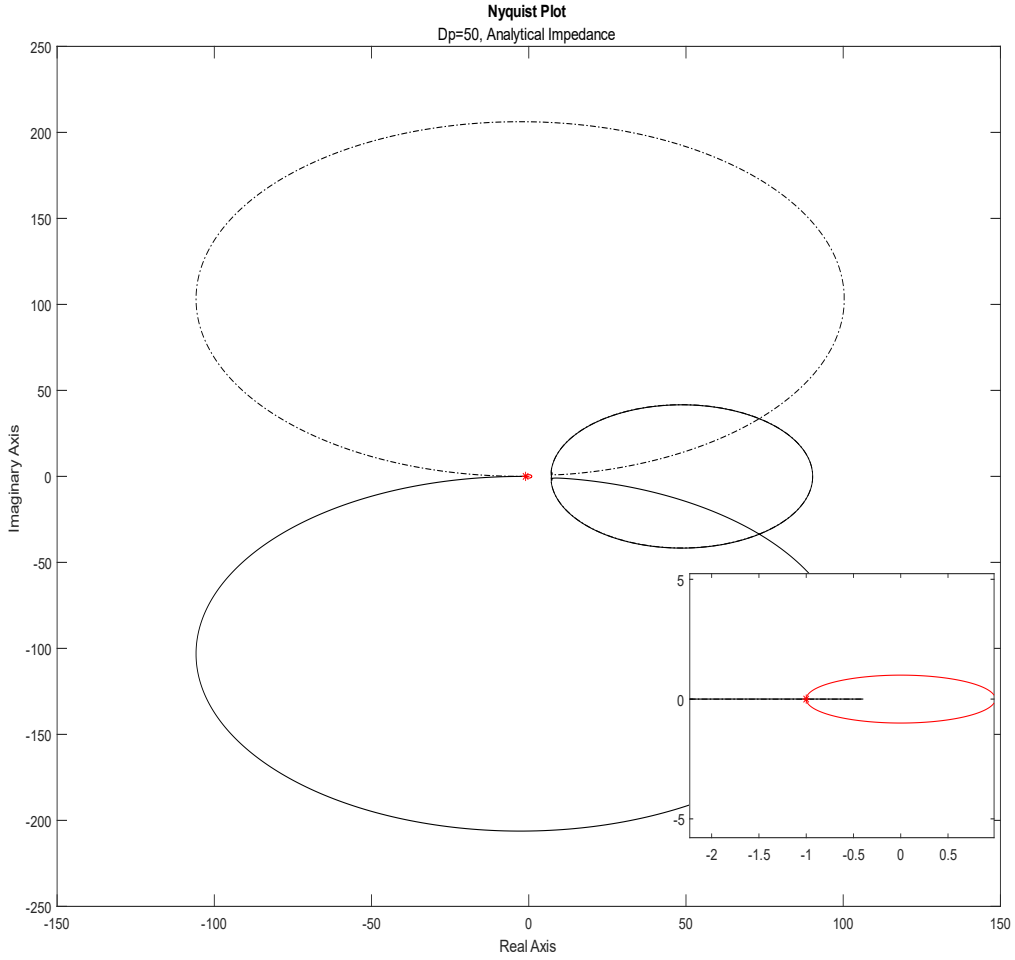

Figure 5.17 Nyquist Plot of $Y_c Z_g$ by Analytical Derivation (Dp = 50)

It can be seen that Figure 5.17 have a very similar shape and characteristics with Figure 5.14. It is predictable since for the high frequency part, the analytical derivation and the frequency sweep is actually quite consistent with each other. Therefore, the difference in shape is due to the low frequency differences. It can also be seen from Figure 5.17 that the critical point (-1,j0) is being cut through by the Nyquist contour. Therefore, the system can be deduced as either marginally stable or unstable. Now we do know that the system is marginally stable, but we are now interested whether the inverse Nyquist plot for the analytical impedance derivation in case of $D_p = 50$ will be consistent with the previous obtained results.

The result for the GINC plot is as follows,

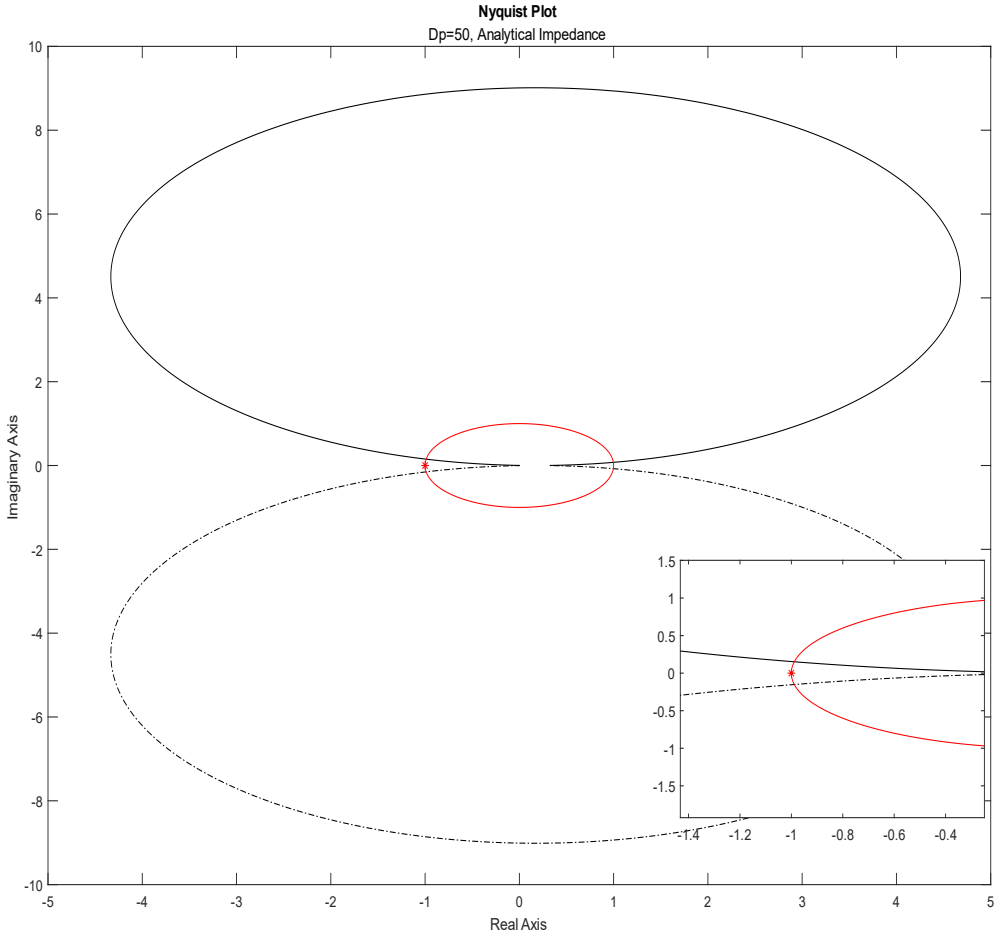

Figure 5.18 Inverse Nyquist Plot of $Y_c Z_g$ by Analytical Derivation (Dp = 50)

Again, from Figure 5.18, it is clear that the critical point (-1.j0) is not encircled. Therefore, the system is indeed stable with a pretty low stability margin, inferred from the figure.

Now, we would like to investigate the case where the $D_p = 1500$. Since for case of low D_p itself the system is stable, we can figure that with higher D_p, the system will still be stable with higher stability margin. The simulation results can be seen in the next pages.

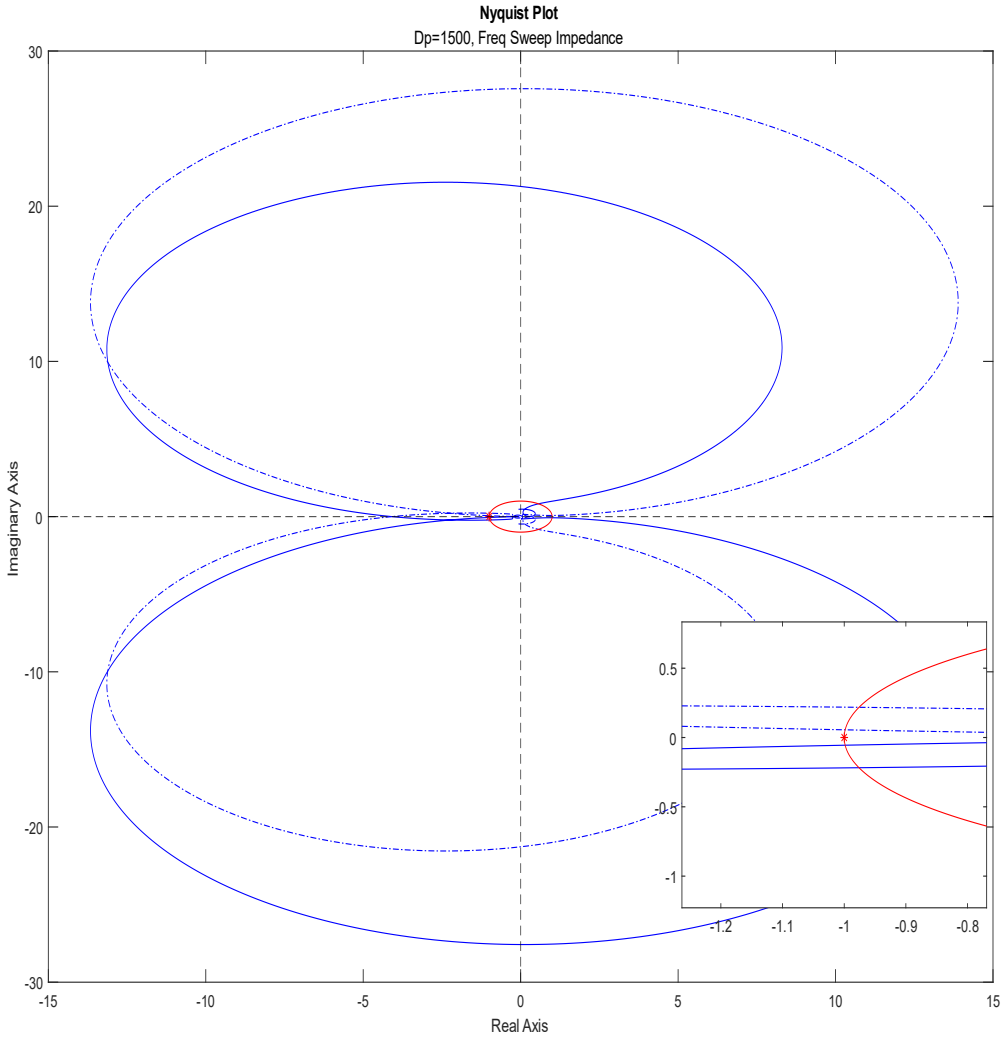

Figure 5.19 Nyquist Plot of $Y_c Z_g$ by Frequency Sweep (Dp = 1500)

From Figure 5.19, we can see 4 encirclements around the critical point (-1,j0). Similar to the previous cases, we do not know the exact characteristic of the open loop poles and zeros, therefore, visual inspection of the Nyquist plot cannot be used to determine the stability unless it is a totally non-encirclement.

We have our hypothesis that for higher virtual damping, the system will still be stable with higher stability margin. To confirm our hypothesis, the following GINC plot will be analysed.

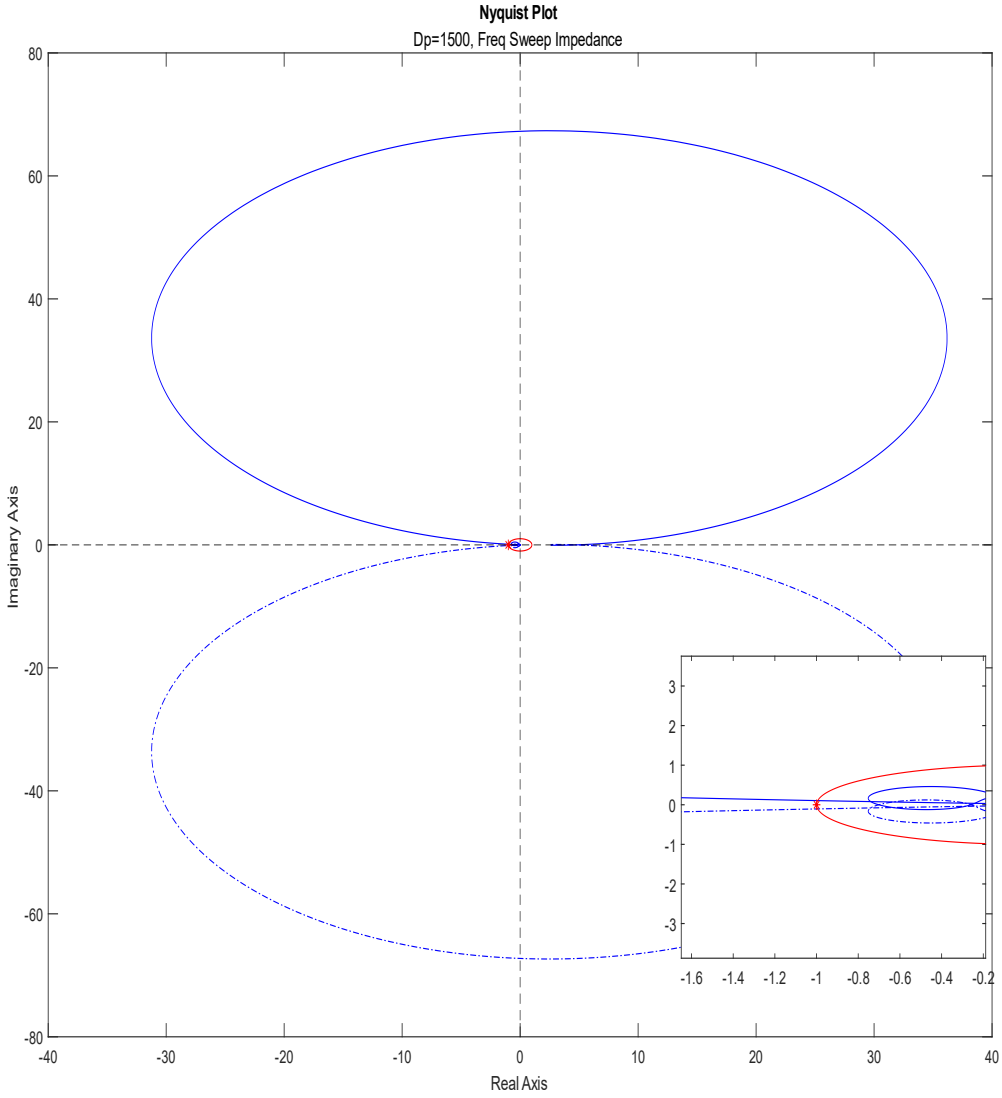

Figure 5.20 Inverse Nyquist Plot of $Y_c Z_g$ by Frequency Sweep (Dp = 1500)

As expected, from the GINC plot, our hypothesis can be affirmed as true. However, it turns out that the stability margin is not differ by much even though it still increases compared to the stability margin when $D_p = 50$. This indicates that even though the D_p might plays an important part for the frequency regulation, D_p's part in the oscillation response due to the converter-driven stability is not as much as we thought.

Next, the time domain simulation results will be analysed and the results are as follows,

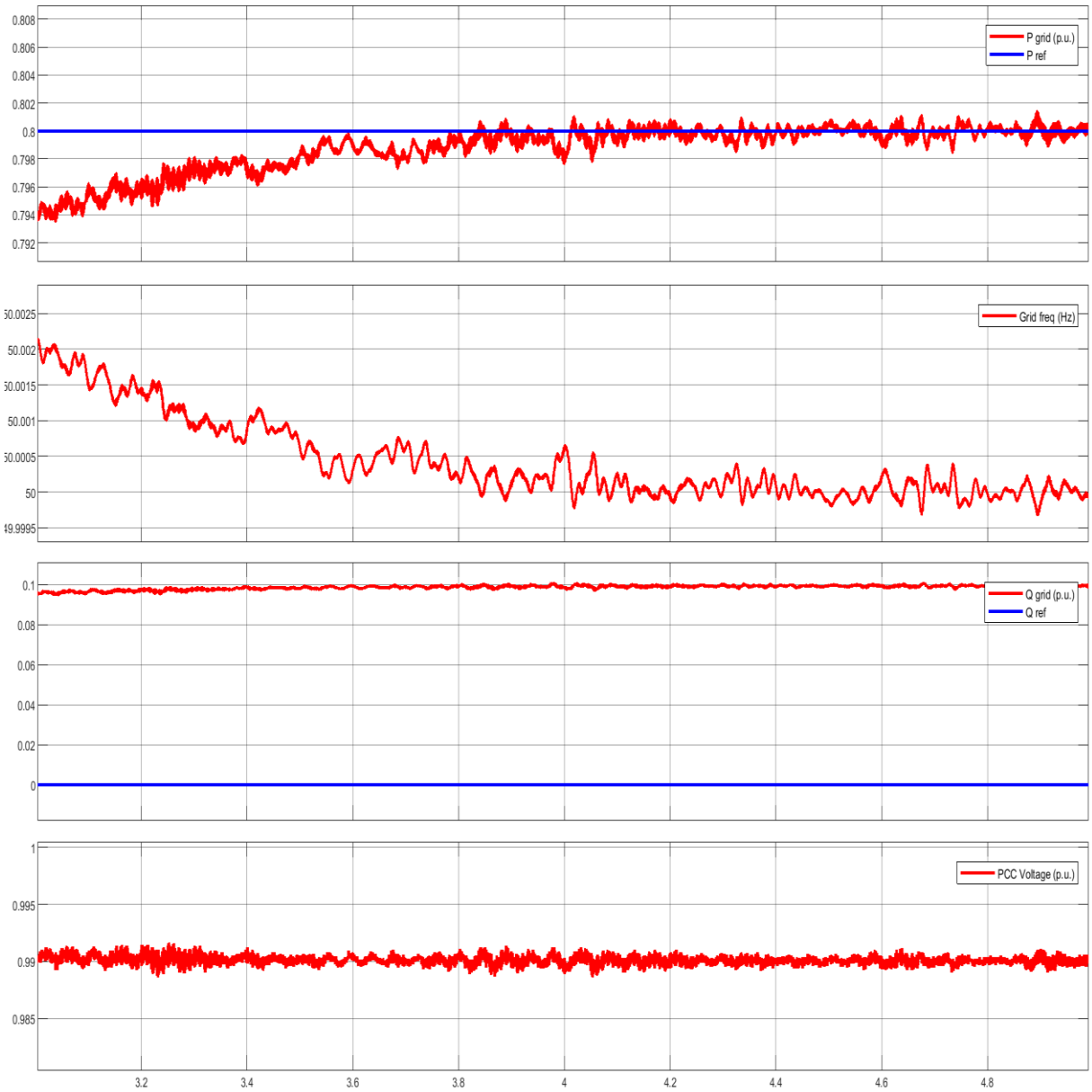

Figure 5.21 Time Domain Simulation Results (Dp = 1500)

It can be seen clearly from the time domain results that it is indeed stable. One thing worth an attention is that the D_p's role for the slow response of the system to achieve the steady state. This makes sense since from basic control theory, damping plays a major part in the transient response. With higher damping, the time constant of a control system will be higher, resulting in slower time to achieve steady state.

This scenario, again, successfully shows how the GNC combined with time domain results can ascertain the converter-driven stability of the WECS.

The Nyquist plot for the same scenario of the analytically derived impedance is as follows,

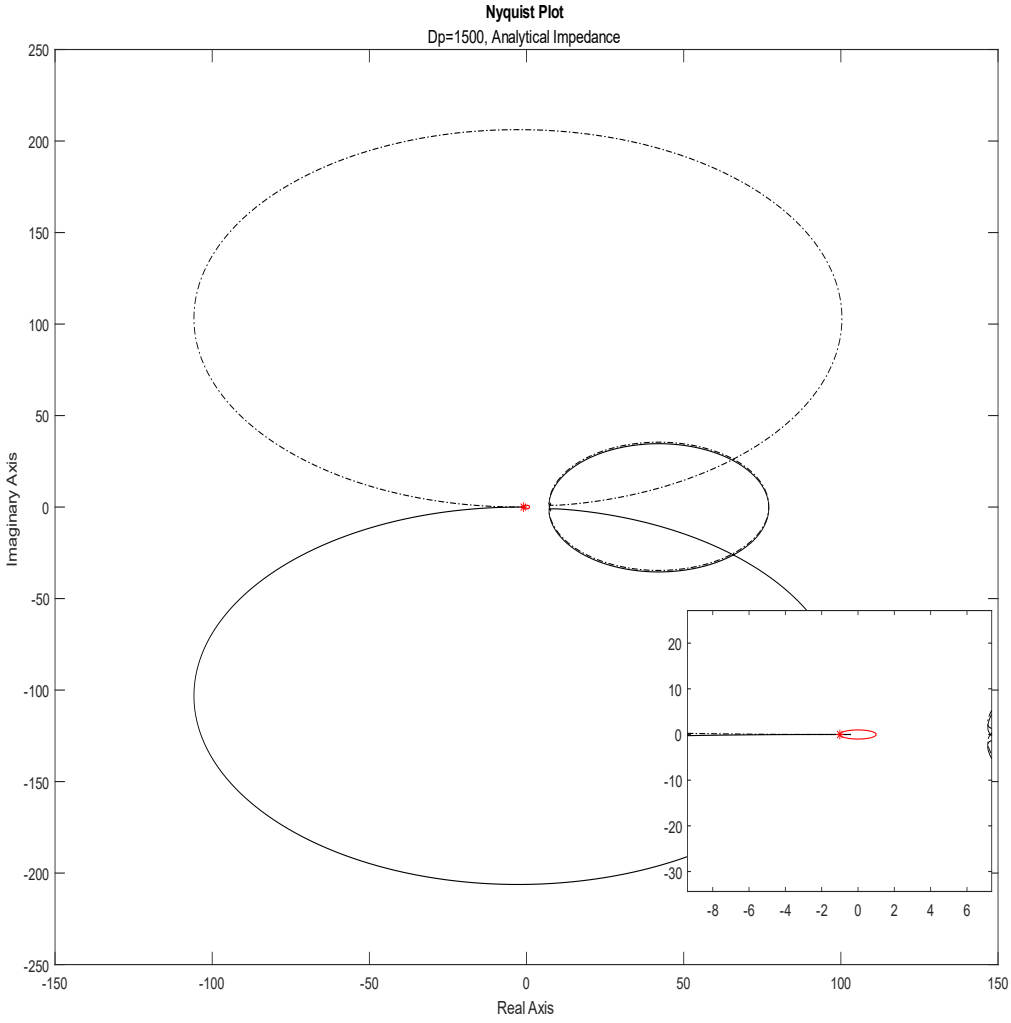

Figure 5.22 Nyquist Plot of $Y_c Z_g$ by Analytical Derivation (Dp = 1500)

It can be seen that Figure 5.22 have a very similar shape and characteristics with Figure 5.19. It has been consistent so far since for the high frequency part, the analytical derivation and the frequency sweep is actually quite consistent with each other. Therefore, the difference in shape is due to the low frequency differences. It can also be seen that the critical point (-1,j0) being cut-through by the Nyquist contour. Therefore, the system can be deduced as either stable or unstable depending on the open-loop pole characteristics.

To ascertain our conclusion, the GINC of the analytical impedance is shown below.

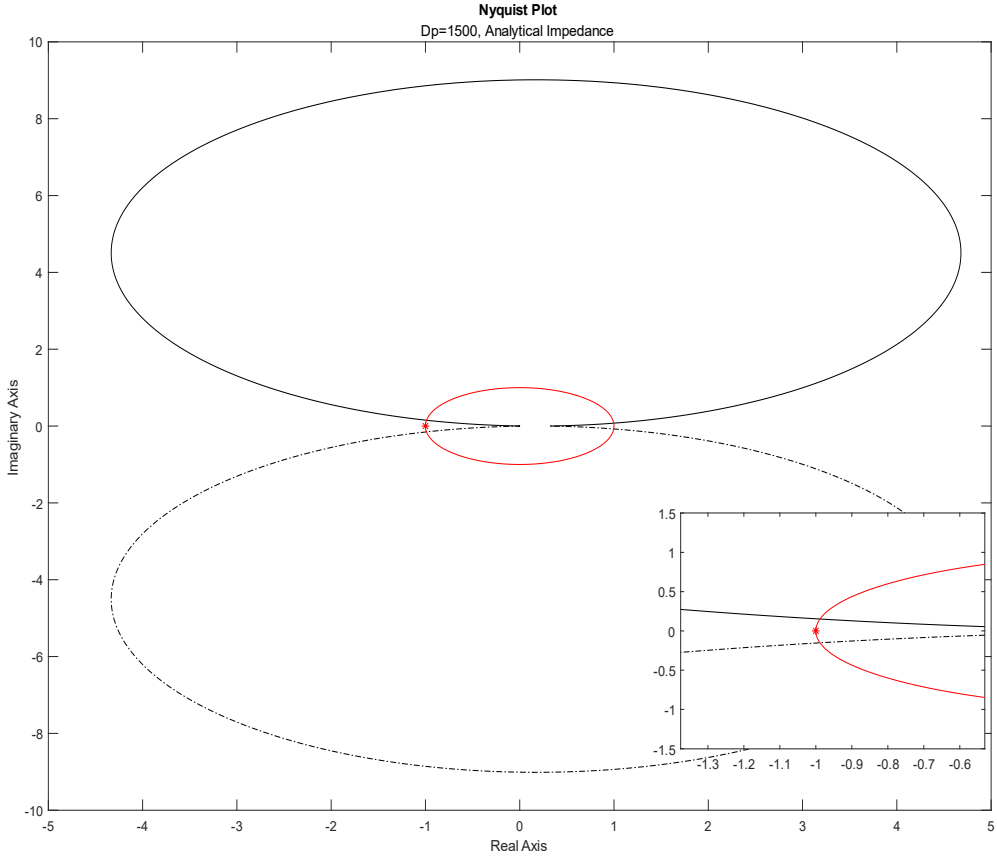

Figure 5.23 Inverse Nyquist Plot of $Y_c Z_g$ by Analytical Derivation (Dp = 1500)

It is crystal clear that from the GINC of the analytical derivation of impedance, the system is stable since there is no encirclement around the critical point (-1,j0). We can conclude that the system is clearly stable.

These results shows the advantage of using simple analytical derivation of impedance. So far, all the results obtained have been consistent regarding the stability, whether by analytical derivation or frequency sweep.

In the last section, we will analyse the impact of the virtual inertia to the converter-driven stability of the WECS based on the GNC.

5.4.4 Virtual Inertia Sensitivity

In this section, the impact of virtual inertia, J on converter-driven stability will be assessed. A sensitivity analysis will be conducted for 2 varying values of J, which are $J = 0.5$ and $J = 20$. The default value of J is 2.

The Nyquist plot obtained from the frequency sweep for $J = 0.5$ is as follows,

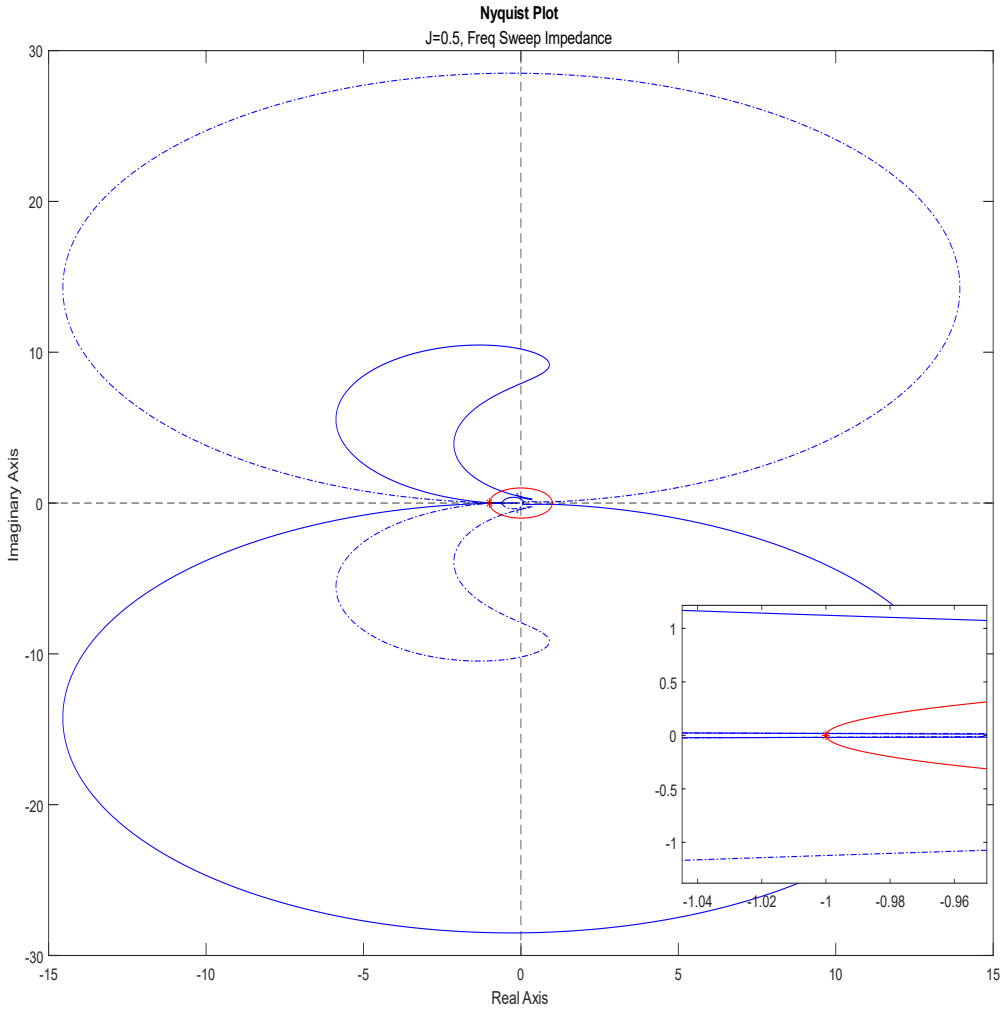

Figure 5.24 Nyquist Plot of $Y_c Z_g$ by Frequency Sweep (J = 0.5)

As shown in Figure 5.24, there is no encirclement around the critical point (-1,j0). Therefore, we can conclude that the system is stable in this condition. Similar to previous section. We will see the results of the time domain simulation to see the actual response.

The time domain results are as follows,

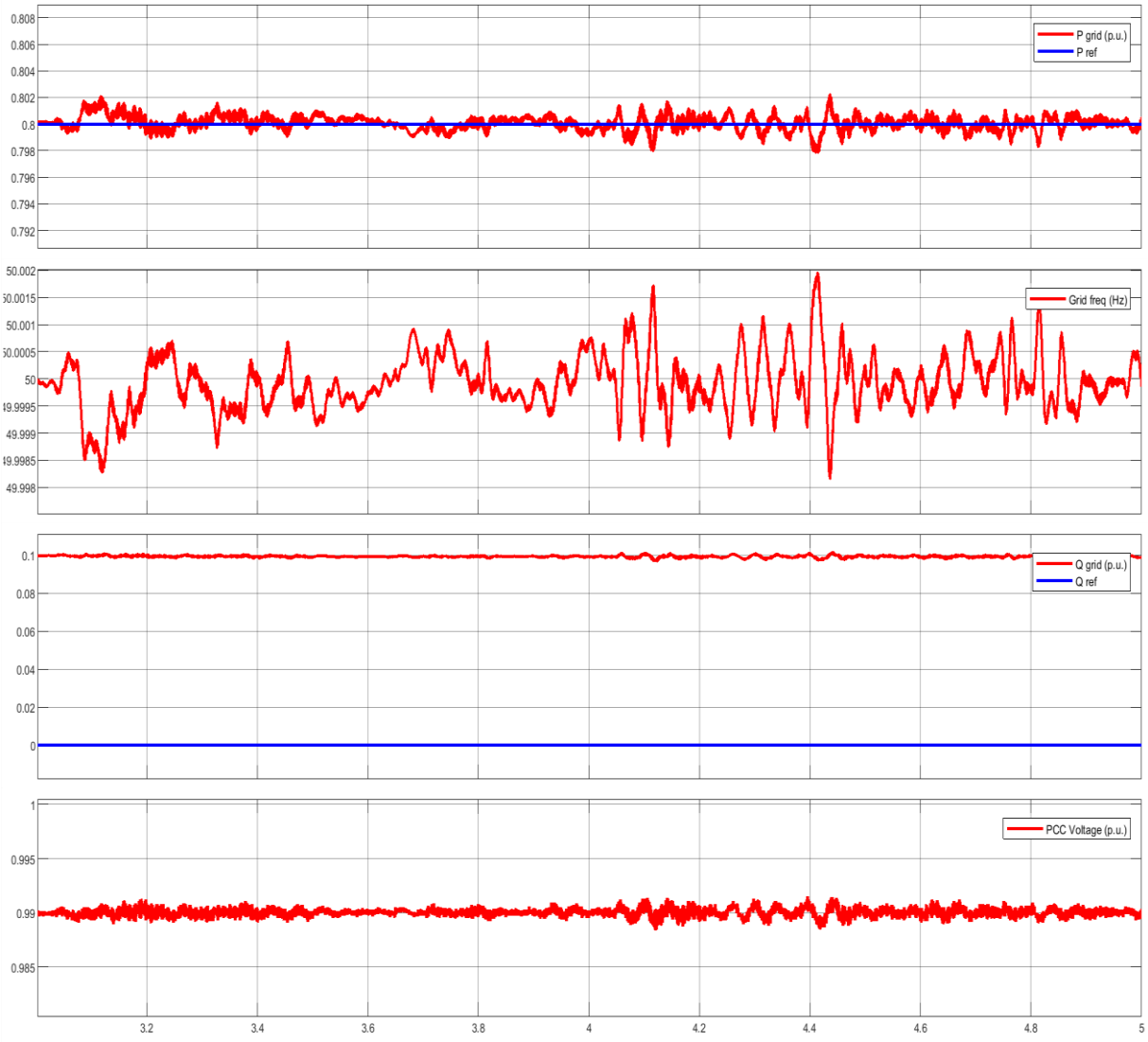

Figure 5.25 Time Domain Simulation Results (J = 0.5)

As can be seen from Figure 5.25, the response is indeed stable. There is no oscillation, and the oscillation shown in the figure is a ripple coming from the power electronics switching.

Virtual inertia is one of the most important aspects in the Synchronverter control since it is directly involved with the swing equation. Together with virtual damping, it is in charge for the frequency regulation of the Synchronverter.

This scenario successfully shows how the GNC combined with time domain results can ascertain the converter-driven stability of the WECS.

Again, we would like compare the Nyquist plot of the frequency sweep and the analytical derivation to see the accuracy. The analytical derivation Nyquist plots are as follows,

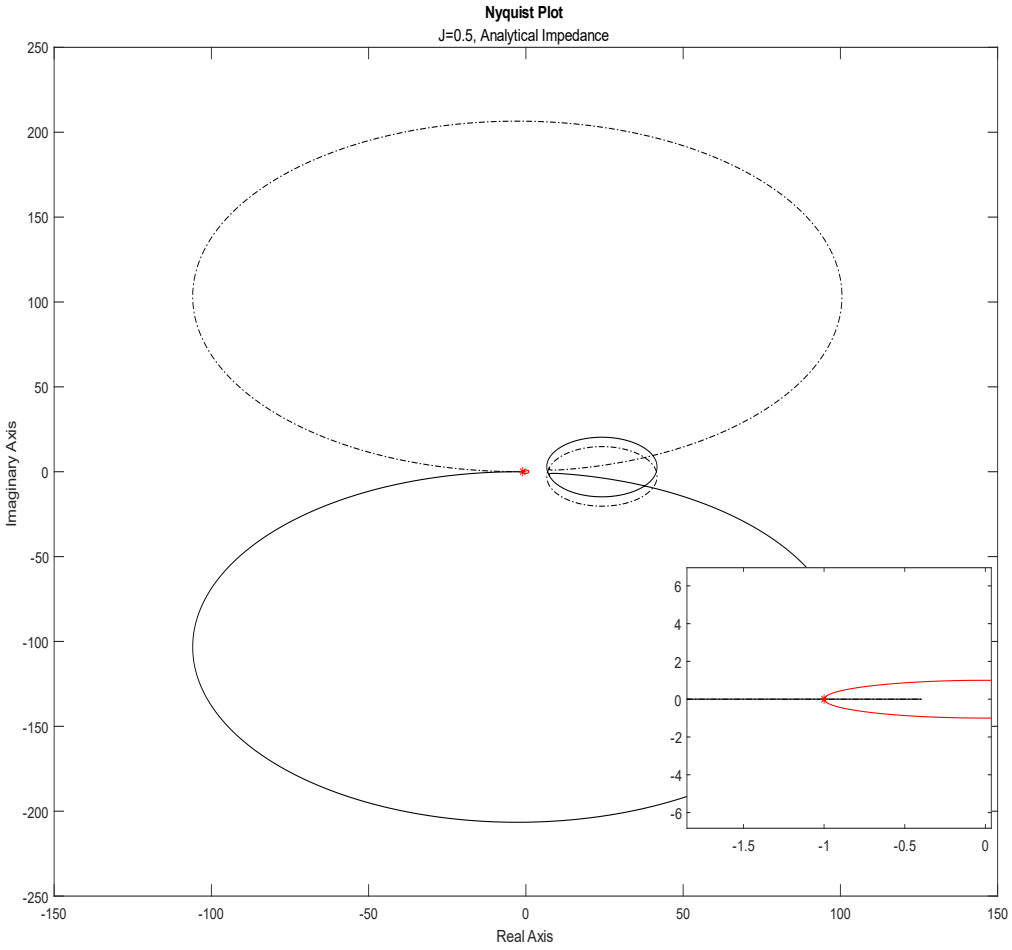

Figure 5.26 Nyquist Plot of $Y_c Z_g$ by Analytical Derivation (J = 0.5)

It can be seen that Figure 5.26 have a very similar shape and characteristics with Figure 5.24. It is again, accurate since for the high frequency part, the analytical derivation and the frequency sweep is quite consistent with each other. Therefore, the difference in shape is due to the low frequency differences. It can also be seen from Figure 5.26 that the critical point (-1,j0) is being cut through by the Nyquist contour. Therefore, the system can be deduced as either marginally stable or unstable.

Now we do know that the system is stable, but we are interested whether the inverse Nyquist plot for the analytical impedance derivation in case of $J = 0.5$ will also be consistent with the previous obtained results and other cases.

The result for the GINC plot is as follows,

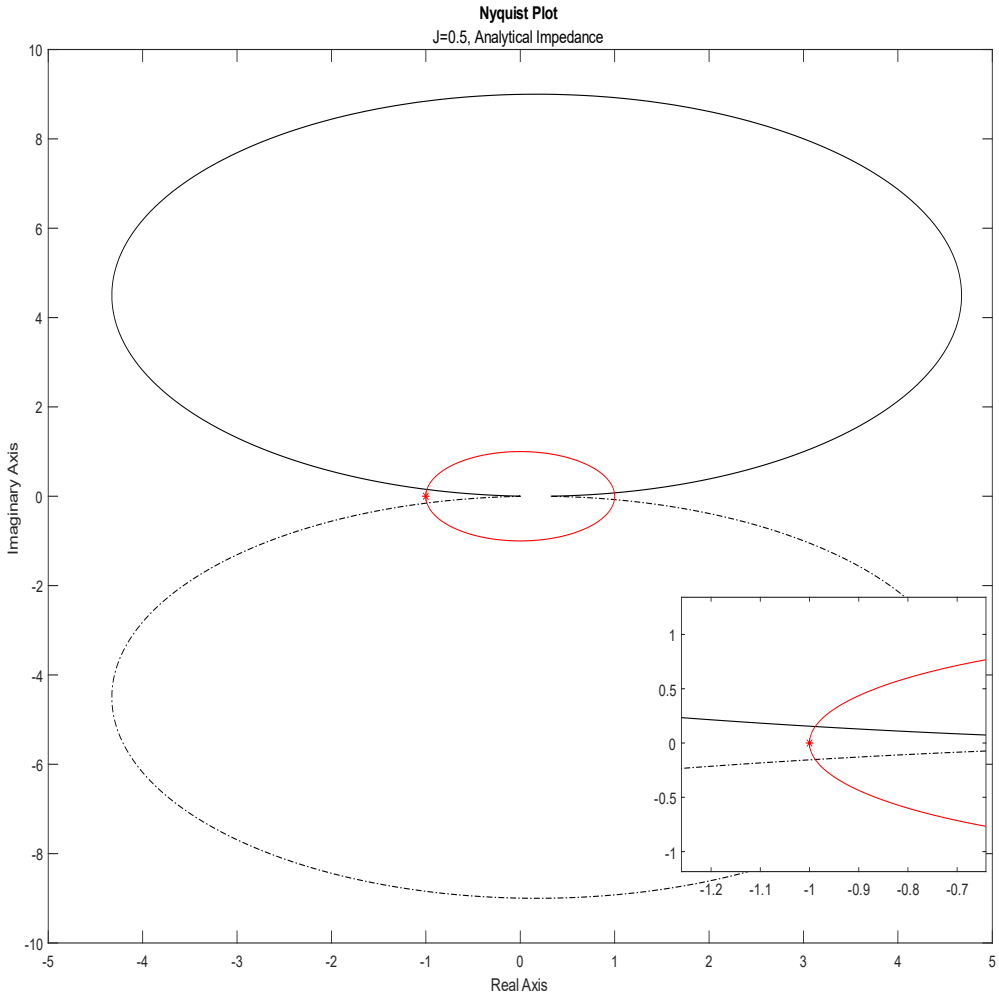

Figure 5.27 Inverse Nyquist Plot of $Y_c Z_g$ by Analytical Derivation (J=0.5)

Similar to the results from all other sections, the Inverse Nyquist plot of the analytical impedance derivation is not encircling the critical point (-1.j0). Therefore, the system is indeed stable.

Now, we would like to investigate the case where the $J = 20$. Since for case of low J itself the system is stable, we can figure that with higher J, the system will also be stable. The simulation results can be seen in the next pages.

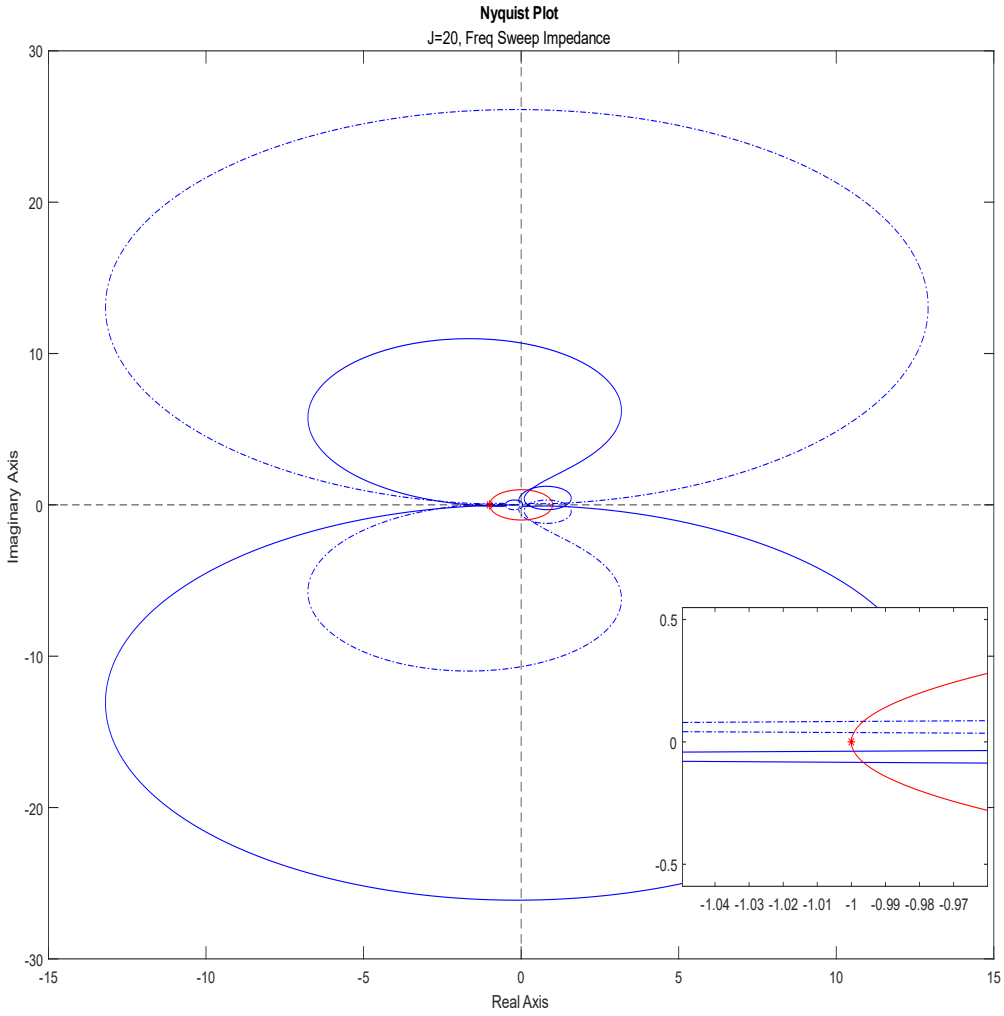

Figure 5.28 Nyquist Plot of $Y_c Z_g$ by Frequency Sweep (J=20)

From Figure 5.28, we can see that there is no encirclement around the critical point (-1,j0). Therefore, the system can be deduced as stable.

However, visually, it is still a bit difficult to be certain whether there is encirclement or not. Therefore, by GINC, we obtain the following figure in the next page.

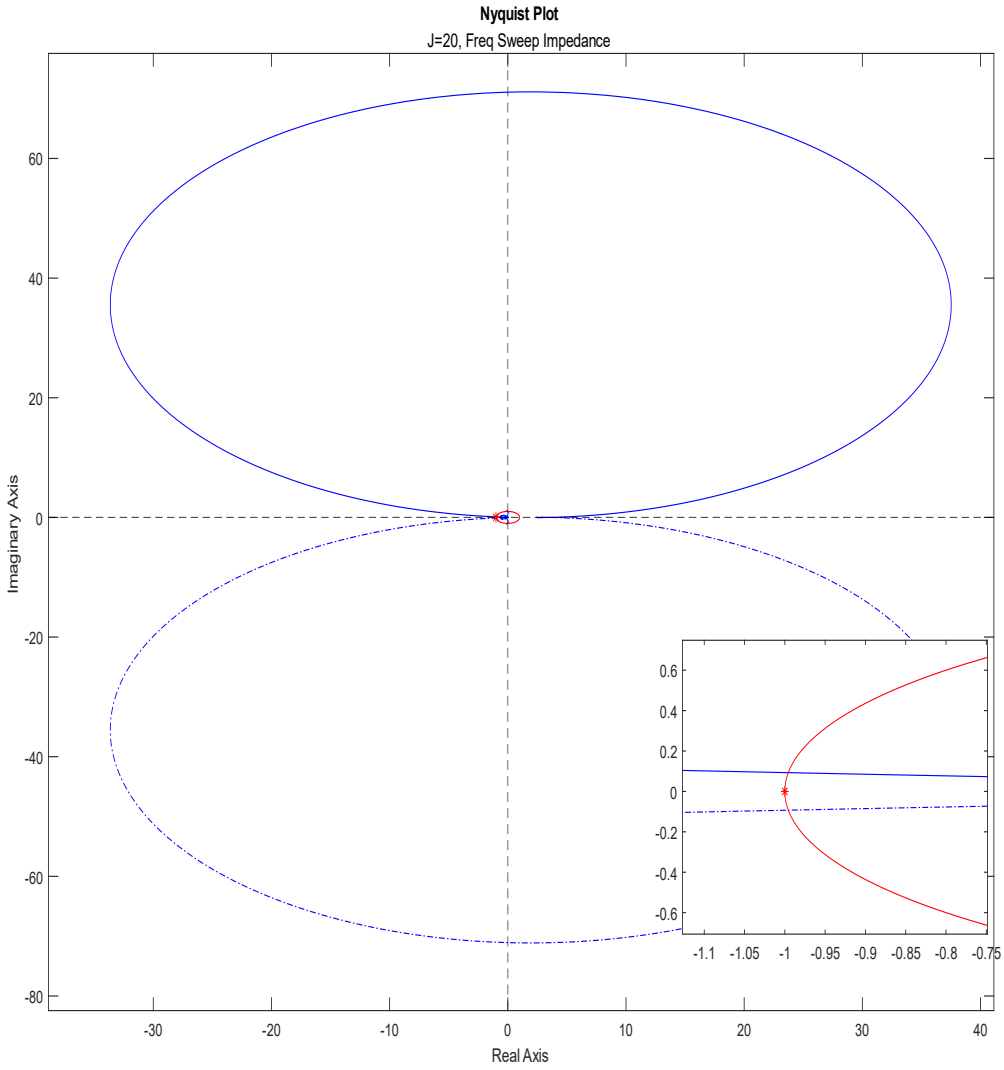

Figure 5.29 Inverse Nyquist Plot of $Y_c Z_g$ by Frequency Sweep (J = 20)

As expected, from the GINC plot, our hypothesis can be affirmed as true. However, it turns out that the stability margin is not differ by much even though it still increases compared to the stability margin when $J = 0.5$. This indicates that the virtual inertia, J may not affect the converter-driven stability much.

Next, the time domain simulation results will be analysed and the results are as follows,

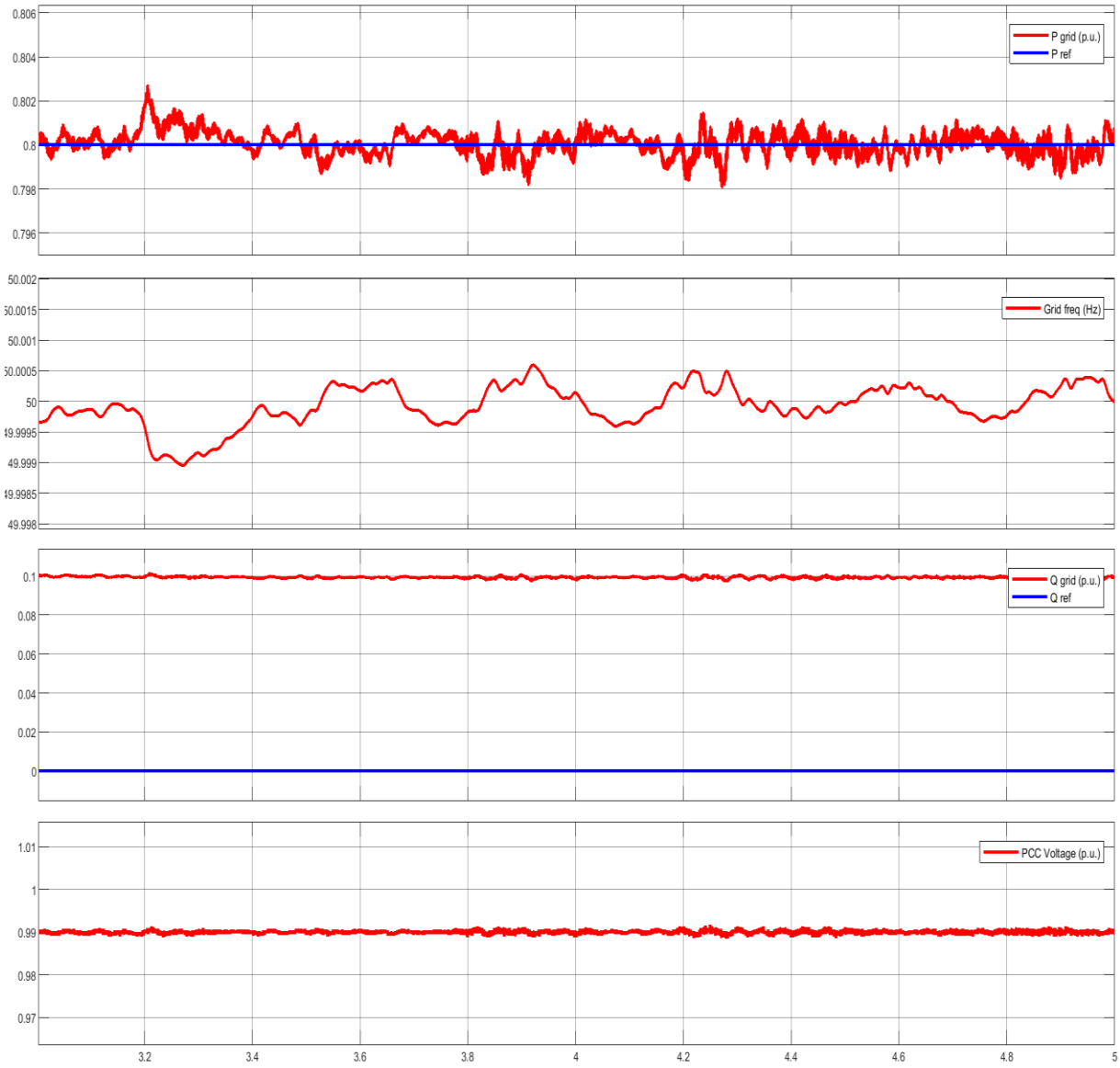

Figure 5.30 Time Domain Simulation Results (J = 20)

It can be seen clearly from the time domain results that it is indeed stable. One thing worth an attention is that with increasing J, the oscillation is getting much lower. This is because, with increasing inertia, the changes in the frequency are resisted (similar to damping). The difference between damping and inertia, is the physical meaning between those two. Damping, comes from the mechanical friction of an SG while inertia is the stored energy in the form of rotating mass. Despite the physical differences in meaning and definition, the responses of both of the parameter to frequency changes are very similar.

This scenario, again, successfully shows how the GNC combined with time domain results can ascertain the converter-driven stability of the WECS.

The Nyquist plot for the same scenario of the analytically derived impedance is as follows,

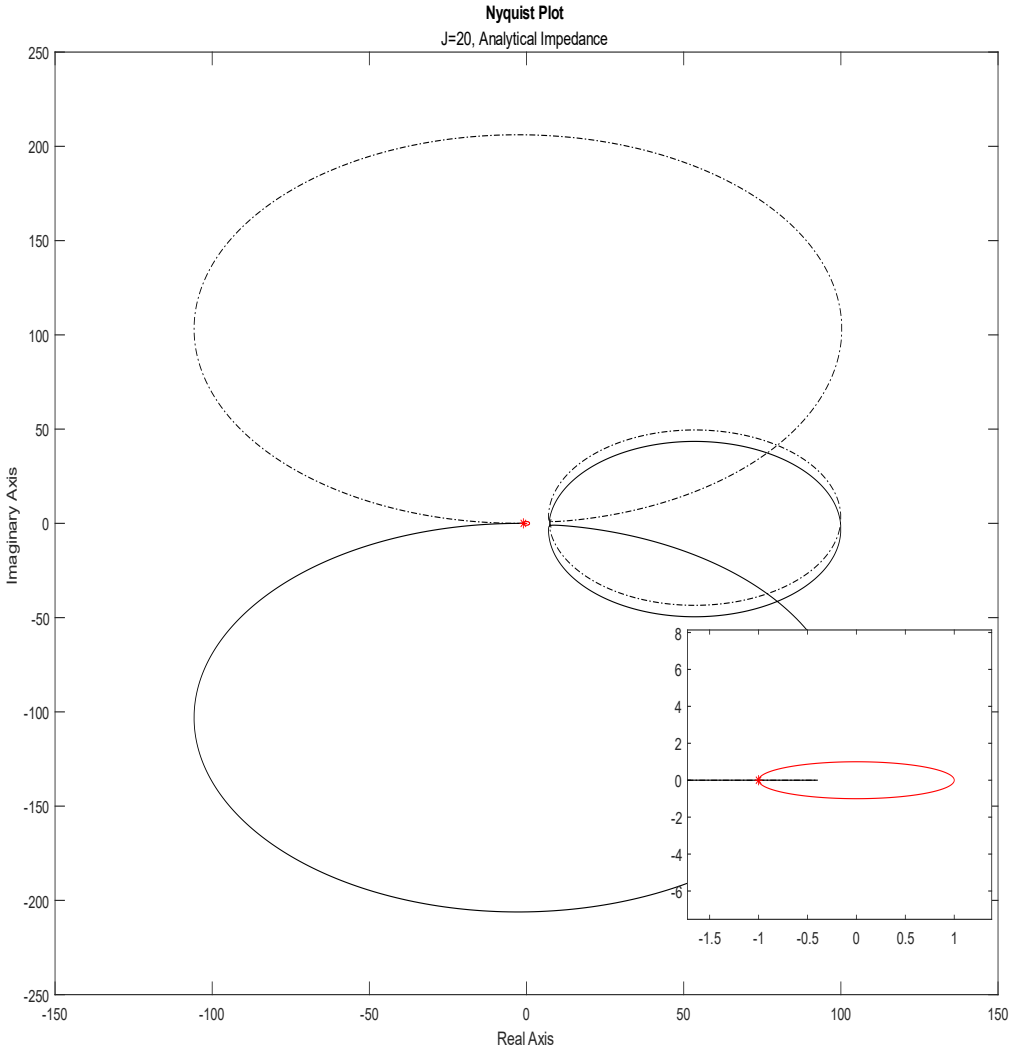

Figure 5.31 Nyquist Plot of $Y_c Z_g$ by Analytical Derivation (J = 20)

It can be seen that Figure 5.31 have a very similar shape and characteristics with Figure 5.19. This has been explained previously, which comes from the similarities of the impedance obtained in high frequency, while both of the impedance model differs in the low frequency region.

It can also be seen that the critical point (-1,j0) being cut-through by the Nyquist contour. Therefore, the system can be deduced as either stable or unstable depending on the open-loop pole characteristics.

To ascertain our conclusion, the GINC of the analytical impedance is shown below.

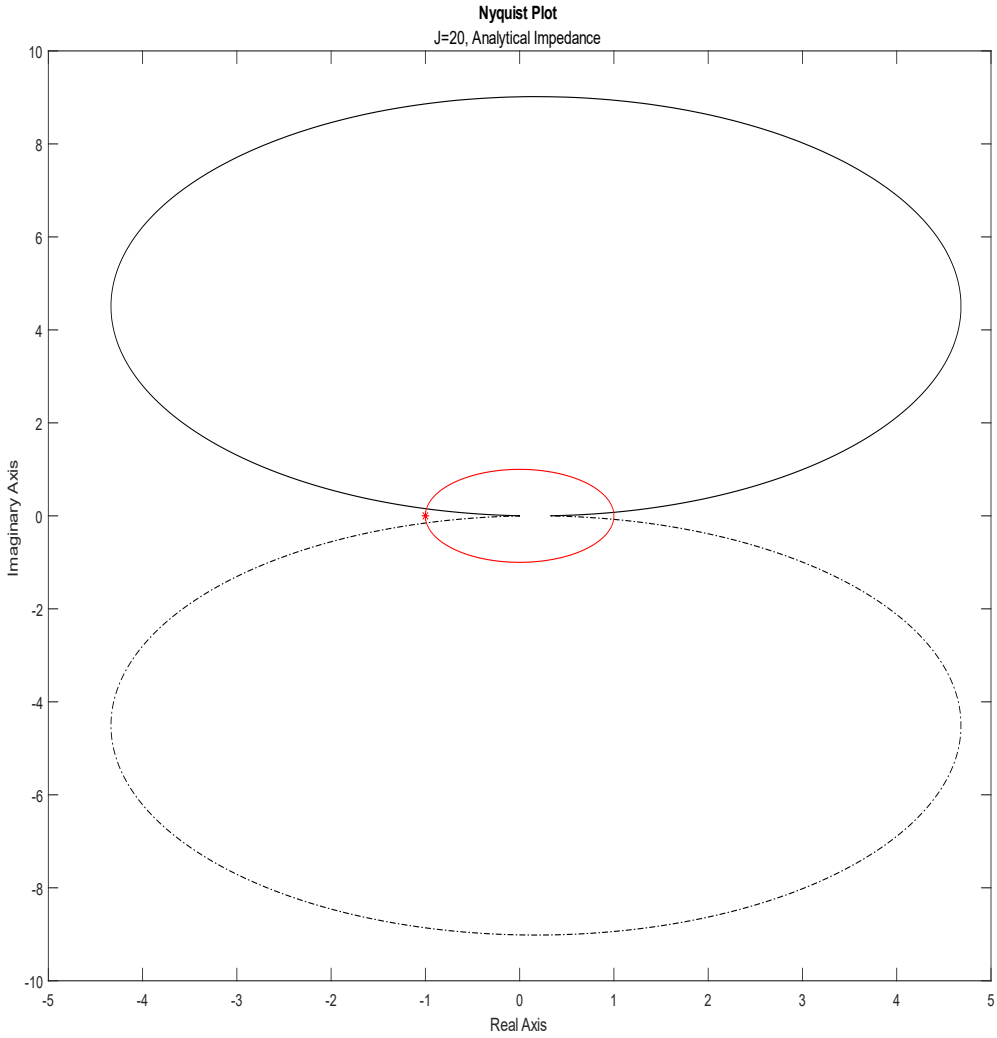

Figure 5.32 Inverse Nyquist Plot of $Y_c Z_g$ by Analytical Derivation (J = 20)

It is crystal clear that from the GINC of the analytical derivation of impedance, the system is stable since there is no encirclement around the critical point (-1,j0). We can conclude that the system is clearly stable.

Once again, these results prove the advantage of using simple analytical derivation of impedance. So far, all the results obtained have been consistent regarding the stability, whether by analytical derivation or frequency sweep.

By using simple analytical derivation, a simple stability assessment of a CIG or CIL can be conducted without loss of generalisation. It offers simplicity due to no sophisticated mathematical techniques required to obtain the impedance model. However, for in-depth studies, it is not recommended to be used since for proper interconnection or other power systems studies, an accurate model is required to obtain a holistic approach and response of the interactions between the components, and between the WECS and the power grids.

Chapter 6

Conclusions

This chapter will outline conclusions for the Synchronverter-based WECS modelling, impedance derivation based on the analytical model and the frequency sweep, and the impedance-based stability analysis based on GNC for interconnection to a weak AC grid. The goals and specific contribution of the thesis will be connected to the findings. Finally, based on the conclusions and analyses offered by the research presented in this thesis, suggestions for further study will be put forth.

6.1 Concluding Statements

In this thesis, the Synchronverter control strategy has been implemented to a type IV WECS, in which a B2B converter is used for grid interconnection. Both of the converters are controlled with Synchronverter strategy, but each of them regulates different variables. The RSC is controlling the DC link voltage, and the GSC is regulating the active and reactive power transfer to the grid.

By building the model, it is clear that the operation of Synchronverter-based WECS is similar to a synchronous machine. It is also clear that the voltage droop block for voltage regulation is vital in the GSC part to ensure the reactive power is tracked properly, especially in case of weak grid interconnection where slight change in voltage might cause voltage collapse to the system.

The first main objective of this thesis was to derive the impedance model of the Synchronverter-based WECS analytically. It was done by deriving it directly from the Synchronverter mathematical model combined with linearisation technique. The impedance obtained is validated with a single-tone sinusoidal frequency sweep for some ranges of frequency, and the results are compared.

The results show that for the high frequency part, both model shows resemblance while for the low frequency part, it differs to a certain extent. This indicates that the low frequency response of the WECS cannot be captured simply by the mathematical model, and a more sophisticated technique is needed, such as Harmonic Linearisation or Harmonic State Space. However, this analytical derivation technique is also advantageous, in a way that it offers simplicity on obtaining an impedance model. Therefore, it is a matter of simplicity vs accuracy between a simple model or a more sophisticated model.

The last main objective was to investigate the converter-driven stability of the WECS for interconnection under weak AC grid conditions. This was done by implementing Generalised Nyquist Criterion (GNC), a fundamental technique in control theory which was extended from the classic Nyquist Criterion.

The object of interest in analysing the converter-driven stability is on the effect of the WECS parameters for weak AC grid integration. There are several WECS parameters that can be studied, but this thesis will focus on 3 main aspects on the GSC part of the WECS and the grid interconnection: *Grid Strength (SCR), Virtual Damping,* and *Virtual Inertia*.

From the results obtained, varying the SCR affects the systems stability greatly. Having low SCR indicates that the bus is weak, and is prone to instability. It is shown in this thesis on how the impact of varying SCR to the WECS interconnection converter-driven stability by means of impedance-based analysis.

It is also shown that virtual damping and virtual inertia does not really affect the converter-driven stability of the WECS, especially for grid interconnection. Some interesting responses are also obtained and can be seen in section 5.4.3 and 5.4.4 for more details.

Another important finding is that the simple analytical derivation impedance model used in this thesis has a pretty good accuracy for stability analysis, as shown by comparing the results with the Nyquist plot of the impedance obtained from the frequency sweep. Therefore, for simple stability studies, a sophisticated technique might not be needed to save computing power and resources.

Other important finding regarding the GNC technique, is that this technique is focused on assessing the stability of the response in terms of bounded input-bounded output (BIBO). As we know, the definition of the stability in control theory might differ a bit compared to the power systems stability. From the simulation, it is clear that in converter-driven stability based on GNC technique, the output might still be considered stable as long as it is BIBO. However, in regards for classical power system stability, such condition might be considered as unstable especially if the swing is way too high. One suggestion to help solve this, is by applying the impedance-based technique together with the classical power systems stability theory to ensure that the stability in both of the theory is fulfilled

These objectives and the intended the thesis significance were successfully linked. The analytical impedance model that could be used to investigate the WECS small-signal response were successfully developed, and a detailed comparison between the simple analytical model derived and the frequency sweep model was shown. Then, the impedance obtained is used to assess the converter-driven stability of the WECS, analysing the various parameters which affect the synchronising stability of WECS for interconnection to an AC weak grid.

Regarding the aims and targeted contributions of the thesis, in relation to the aforementioned findings, there is no doubt that the goals have been well met and that the targeted contributions have been made.

6.2 Future Works

Based on the results, discussions and conclusions in Chapters 4 and 5, as well as Section 6.1, several improvements and new direction for further research topics to improve based on this thesis can be pointed out. The suggested future works can be seen in the following list.

- One of the most signification assumptions in this thesis is by assuming static wind speed, subsequently resulting in a constant active power extracted from the wind turbine. In real life operation, wind speed is always varying. Therefore, it will be a challenge and will be interesting to assess the stability of such scenario. While for larger transient studies, a sudden change in wind speed might be required, a small change in wind speed is enough for small-signal stability studies of the WECS.

- This thesis focuses only on one of the VSM topology, which is Synchronverter. It will be interesting to analyse other VSM topology based on the simple mathematical model impedance derivation to affirm the potency in this simple way of modelling.
- This thesis only focused on assessing the converter-driven stability while not designing or tuning a controller to help alleviate the issues. Therefore, further studies regarding the accuracy of the impedance-based model used for control design will be needed.
- The WECS modelling used in this thesis is an SMIB model. To understand the impact of the parameters better, the test case should be extended to a larger area, such as the use of IEEE 3-bus with several converters and other SG/SM interconnection. A fully renewable-based studies are also possible to investigate the use of impedance-based modelling for power electronics-dominated power systems.
- For a more detailed power system studies, a more realistic and real-life representations might be needed.
- For a more programming type of work, an automation of impedance-based modelling and stability might be interesting to study, in which the results can be used as a baseline for commercial development to be used by power system engineers worldwide.

Bibliography

[1] IEA, "Electricity Market Report," 2022. [Online]. Available: https://www.iea.org/reports/electricity-market-report-january-2022.

[2] Ofgem, "Price cap to increase by £693 from April," 2022. https://www.ofgem.gov.uk/publications/price-cap-increase-ps693-april (accessed Jun. 09, 2022).

[3] National World, "Which energy firms have gone bust? How many companies have collapsed or at risk - Together Energy latest to go," 2022. https://www.nationalworld.com/lifestyle/money/which-energy-firms-have-gone-bust-how-many-companies-have-collapsed-or-at-risk-together-energy-latest-to-go-3389971 (accessed Jun. 09, 2022).

[4] European Commission, "A policy framework for climate and energy in the period from 2020 to 2030," 2014.

[5] European Commission, "Delivering the EU's 2030 climate target on the way to climate neutrality," 2021. [Online]. Available: https://eur-lex.europa.eu/legal-content/EN/TXT/?uri=CELEX:52021DC0550.

[6] World Energy Council, "World Energy Trilemma Index," 2021. [Online]. Available: www.worldenergy.org.

[7] ING, "Energy Outlook 2022: Solid growth for wind and solar amid energy crisis," 2022.

[8] European Commission, "Eurostat: From where do we import energy?," 2020. https://ec.europa.eu/eurostat/cache/infographs/energy/bloc-2c.html (accessed Jun. 09, 2022).

[9] European Commission, "REPowerEU: EU external energy engagement in a changing world," 2022, [Online]. Available: https://eur-lex.europa.eu/legal-content/EN/TXT/?uri=JOIN%3A2022%3A23%3AFIN&qid=1653033264976.

[10] C. Kost, S. Shammugam, V. Fluri, D. Peper, A. D. Memar, and T. Schlegel, "Levelized Cost of Electricity Renewable Energy Technologies," no. June, pp. 1–45, 2021, [Online]. Available: www.ise.fraunhofer.de%0ADirectors.

[11] N. Hatziargyriou *et al.*, "Definition and Classification of Power System Stability - Revisited & Extended," *IEEE Trans. Power Syst.*, vol. 36, no. 4, pp. 3271–3281, 2021, doi: 10.1109/TPWRS.2020.3041774.

[12] IEEE Power System Dynamic Performance Committee, "IEEE PES-TR77: Stability definitions and characterization of dynamic behavior in systems with high penetration of power electronic interfaced technologies," 2020.

[13] Y. Hu, S. Bu, B. Zhou, Y. Liu, and C. W. Fei, "Impedance-Based Oscillatory Stability Analysis of High Power Electronics-Penetrated Power Systems-A Survey," *IEEE Access*, vol. 7, pp. 120774–120787, 2019, doi: 10.1109/ACCESS.2019.2937395.

[14] X. Wang, M. G. Taul, H. Wu, Y. Liao, F. Blaabjerg, and L. Harnefors, "Grid-Synchronization Stability of Converter-Based Resources—An Overview," *IEEE Open J. Ind. Appl.*, vol. 1, no. June, pp. 115–134, 2020, doi: 10.1109/ojia.2020.3020392.

[15] D. Yang and X. Wang, "Unified Modular State-Space Modeling of Grid-Connected Voltage-Source Converters," *IEEE Trans. Power Electron.*, vol. 35, no. 9, pp. 9702–9717, 2020, doi: 10.1109/TPEL.2020.2965941.

[16] M. Cespedes and J. Sun, "Impedance modeling and analysis of grid-connected

voltage-source converters," *IEEE Trans. Power Electron.*, vol. 29, no. 3, pp. 1254–1261, 2014, doi: 10.1109/TPEL.2013.2262473.

[17] F. Loku, M. Quester, C. Brantl, and A. Monti, "MMC control optimization approach to facilitate DC-side interoperability in MTDC networks," *Electr. Power Syst. Res.*, vol. 203, 2022, doi: 10.1016/j.epsr.2021.107639.

[18] A. Rygg, "Impedance-based methods for small-signal analysis of systems dominated by power electronics," Norwegian University of Science and Technology, 2018.

[19] S. Wang, Z. Liu, and J. Liu, "Modeling of D-Q Small-Signal Impedance of Virtual Synchronous Generator," *Proc. - 2018 IEEE Int. Power Electron. Appl. Conf. Expo. PEAC 2018*, vol. 2, no. 1, pp. 3–8, 2018, doi: 10.1109/PEAC.2018.8590285.

[20] H. Liu and J. Sun, "Voltage stability and control of offshore wind farms with AC collection and HVDC transmission," *IEEE J. Emerg. Sel. Top. Power Electron.*, vol. 2, no. 4, pp. 1181–1189, 2014, doi: 10.1109/JESTPE.2014.2361290.

[21] M. Amin, A. Rygg, and M. Molinas, "Self-Synchronization of Wind Farm in an MMC-Based HVDC System: A Stability Investigation," *IEEE Trans. Energy Convers.*, vol. 32, no. 2, pp. 458–470, 2017, doi: 10.1109/TEC.2017.2661540.

[22] I. Ray, "Review of impedance-based analysis methods applied to grid-forming inverters in inverter-dominated grids," *Energies*, vol. 14, no. 9, 2021, doi: 10.3390/en14092686.

[23] Q. C. Zhong, *Power Electronics-Enabled Autonomous Power Systems: Next Generation Smart Grids*. Chicago: John Wiley & Sons, Ltd, 2020.

[24] B. Wen, D. Dong, D. Boroyevich, R. Burgos, P. Mattavelli, and Z. Shen, "Impedance-based analysis of grid-synchronization stability for three-phase paralleled converters," *IEEE Trans. Power Electron.*, vol. 31, no. 1, pp. 26–38, 2016, doi: 10.1109/TPEL.2015.2419712.

[25] J. Manwell, J. McGowan, and A. Rogers, *Wind Energy Explained: Theory, Design, and Application*. John Wiley & Sons, Ltd, 2009.

[26] T. M. Letcher, *Wind Energy Engineering: A Handbook for Onshore and Offshore Wind Turbines*. Academic Press, 2017.

[27] O. Anaya-Lara, J. O. Tande, K. Uhlen, and K. Merz, *Offshore Wind Energy Technology*, vol. 7, no. 2. John Wiley & Sons, Ltd, 2018.

[28] R. Gasch, *Wind Power Plants: Fundamentals, Design, Construction and Operation*. Springer, 2011.

[29] GE Renewable Energy, "Meet the Haliade-X 14 MW," 2020.

[30] S. Heier, *Grid Integration of Wind Energy*, vol. 21, no. 3–4. Chichester, UK: John Wiley & Sons, Ltd, 2014.

[31] P. M. Pardalos, S. Rebennack, M. V. F. Pereira, N. A. Iliadis, and V. Pappu, *Handbook of Wind Power Systems*. Berlin, Heidelberg: Springer Berlin Heidelberg, 2013.

[32] H. Knudsen and J. N. Nielsen, "Introduction to the Modelling of Wind Turbines," in *Wind Power in Power Systems*, vol. 8, 2012, pp. 523–554.

[33] Z. Ma, "Synchronverter-based Control for Wind Power," Loughborough University, 2012.

[34] Q. C. Zhong, Z. Ma, W. L. Ming, and G. C. Konstantopoulos, "Grid-friendly wind power systems based on the synchronverter technology," *Energy Convers. Manag.*, vol. 89, pp. 719–726, 2015, doi: 10.1016/j.enconman.2014.10.027.

[35] P. A. Dahono, "Lecture Notes of EP3072 - Power Electronics," Institut Teknologi Bandung, 2018.

[36] M. H. Rashid, *Power Electronics: Devices, Circuits, and Applications*. 2014.

[37] M. Amin, "Lecture Notes of ELK 21 - Electronics for Control of Power," Norwegian University of Science and Technology, 2021.

[38] Y. Haroen, *Elektronika Daya*. Bandung: Penerbit ITB, 2010.

[39] International Electrotechnical Commission (IEC), "IEC 60038 International Standard - IEC Standard Voltages," 2009.

[40] Y. Jiang, J. Li, S. Pan, X. Zhang, P. Hu, and H. Zhang, "Research on the comparison analyses of three-phase discrete and integrated LC filters in three-phase PV inverter," *Int. J. Photoenergy*, vol. 2013, 2013, doi: 10.1155/2013/217023.

[41] Q. C. Zhong and G. Weiss, "Synchronverters: Inverters that mimic synchronous generators," *IEEE Trans. Ind. Electron.*, vol. 58, no. 4, pp. 1259–1267, 2011, doi: 10.1109/TIE.2010.2048839.

[42] P. M. Anderson and A.-A. A. Fouad, *Power system control and stability*. IEEE Press, John Wiley & Sons, 2008.

[43] J. Machowski, Z. Lubosny, J. W. Bialek, and J. R. Bumby, *Power System Dynamics: Stability and Control*. Wiley, 2020.

[44] P. Kundur, *Power System Stability and Control*. 1994.

[45] P. Denholm, T. Mai, R. W. Kenyon, B. Kroposki, and M. O. Malley, "Inertia and the Power Grid : A Guide Without the Spin," 2020. [Online]. Available: https://www.nrel.gov/docs/fy20osti/73856.pdf.

[46] K. S. Ratnam, K. Palanisamy, and G. Yang, "Future low-inertia power systems: Requirements, issues, and solutions - A review," *Renew. Sustain. Energy Rev.*, vol. 124, no. July 2019, p. 109773, 2020, doi: 10.1016/j.rser.2020.109773.

[47] P. Tielens, "Operation and control of power systems with low synchronous inertia," *Arenb. Dr. Sch. Fac. Eng. Sci.*, no. November, 2017, [Online]. Available: https://lirias.kuleuven.be/bitstream/123456789/592208/1/phd_Pieter_Tielens.pdf.

[48] T. Funabashi, *Integration of Distributed Energy Resources in Power Systems*. Academic Press, 2016.

[49] H. P. Beck and R. Hesse, "Virtual synchronous machine," *2007 9th Int. Conf. Electr. Power Qual. Util. EPQU*, 2007, doi: 10.1109/EPQU.2007.4424220.

[50] T. Loix, S. De Breucker, P. Vanassche, J. Van Den Keybus, J. Driesen, and K. Visscher, "Layout and performance of the power electronic converter platform for the VSYNC project," *2009 IEEE Bucharest PowerTech Innov. Ideas Towar. Electr. Grid Futur.*, pp. 1–8, 2009, doi: 10.1109/PTC.2009.5282160.

[51] W. Zhang, D. Remon, and P. Rodriguez, "Frequency support characteristics of grid-interactive power converters based on the synchronous power controller," *IET Renew. Power Gener.*, vol. 11, no. 4, pp. 470–479, Mar. 2017, doi: 10.1049/iet-rpg.2016.0557.

[52] Y. Hirase, K. Abe, K. Sugimoto, and Y. Shindo, "A grid-connected inverter with virtual synchronous generator model of algebraic type," *Electr. Eng. Japan*, vol. 184, no. 4, pp. 10–21, Sep. 2013, doi: 10.1002/eej.22428.

[53] J. Alipoor, Y. Miura, and T. Ise, "Power System Stabilization Using Virtual Synchronous Generator With Alternating Moment of Inertia," *IEEE J. Emerg. Sel. Top. Power Electron.*, vol. 3, no. 2, pp. 451–458, Jun. 2015, doi: 10.1109/JESTPE.2014.2362530.

[54] M. Ashabani, F. D. Freijedo, S. Golestan, and J. M. Guerrero, "Inducverters: PLL-Less Converters With Auto-Synchronization and Emulated Inertia Capability," *IEEE Trans. Smart Grid*, vol. 7, no. 3, pp. 1660–1674, 2016, doi: 10.1109/TSG.2015.2468600.

[55] H. Alrajhi Alsiraji and R. El-Shatshat, "Comprehensive assessment of virtual

synchronous machine based voltage source converter controllers," *IET Gener. Transm. Distrib.*, vol. 11, no. 7, pp. 1762–1769, May 2017, doi: 10.1049/iet-gtd.2016.1423.

[56] N. Hatziargyriou *et al.*, "Definition and Classification of Power System Stability IEEE/CIGRE Joint Task Force on Stability Terms and Definitions," *IEEE Trans. Power Syst.*, vol. 19, no. 3, pp. 1387–1401, Aug. 2004, doi: 10.1109/TPWRS.2004.825981.

[57] IEEE Subsynchronous Resonance Working Group, "Terms, Definitions and Symbols for Subsynchronous Oscillations," *IEEE Trans. Power Appar. Syst.*, vol. PAS-104, no. 6, pp. 1326–1334, 1985, doi: 10.1109/TPAS.1985.319152.

[58] IEEE/NERC Task Force on Short-Circuit and System Performance Impact, "IEEE PES-TR68: Impact of Inverter Based Generation on Bulk Power System Dynamics and Short-Circuit Performance," 2018.

[59] X. Wang and F. Blaabjerg, "Harmonic Stability in Power Electronic-Based Power Systems: Concept, Modeling, and Analysis," *IEEE Trans. Smart Grid*, vol. 10, no. 3, pp. 2858–2870, 2019, doi: 10.1109/TSG.2018.2812712.

[60] F. Milano, F. Dorfler, G. Hug, D. J. Hill, and G. Verbič, "Foundations and challenges of low-inertia systems (Invited Paper)," *20th Power Syst. Comput. Conf. PSCC 2018*, pp. 1–25, 2018, doi: 10.23919/PSCC.2018.8450880.

[61] L. P. Kunjumuhammed, B. C. Pal, C. Oates, and K. J. Dyke, "Electrical oscillations in wind farm systems: Analysis and insight based on detailed modeling," *IEEE Trans. Sustain. Energy*, vol. 7, no. 1, pp. 51–62, 2016, doi: 10.1109/TSTE.2015.2472476.

[62] L. P. Kunjumuhammed, B. C. Pal, R. Gupta, and K. J. Dyke, "Stability analysis of a PMSG-based large offshore wind farm connected to a VSC-HVDC," *IEEE Trans. Energy Convers.*, vol. 32, no. 3, pp. 1166–1176, 2017, doi: 10.1109/TEC.2017.2705801.

[63] M. Liserre, F. Blaabjerg, and S. Hansen, "Design and control of an LCL-filter-based three-phase active rectifier," *IEEE Trans. Ind. Appl.*, vol. 41, no. 5, pp. 1281–1291, 2005, doi: 10.1109/TIA.2005.853373.

[64] D. Shu, X. Xie, H. Rao, X. Gao, Q. Jiang, and Y. Huang, "Sub- and Super-Synchronous Interactions Between STATCOMs and Weak AC/DC Transmissions With Series Compensations," *IEEE Trans. Power Electron.*, vol. 33, no. 9, pp. 7424–7437, Sep. 2018, doi: 10.1109/TPEL.2017.2769702.

[65] C. Yoon, X. Wang, F. M. F. Da Silva, C. L. Bak, and F. Blaabjerg, "Harmonic stability assessment for multi-paralleled, grid-connected inverters," *Proc. - 2014 Int. Power Electron. Appl. Conf. Expo. IEEE PEAC 2014*, pp. 1098–1103, 2014, doi: 10.1109/PEAC.2014.7038014.

[66] M. K. AL-Nussairi, R. Bayindir, S. Padmanaban, L. Mihet-Popa, and P. Siano, "Constant power loads (CPL) with Microgrids: Problem definition, stability analysis and compensation techniques," *Energies*, vol. 10, no. 10, 2017, doi: 10.3390/en10101656.

[67] D. Wu, G. Li, M. Javadi, A. M. Malyscheff, M. Hong, and J. N. Jiang, "Assessing Impact of Renewable Energy Integration on System Strength Using Site-Dependent Short Circuit Ratio," *IEEE Trans. Sustain. Energy*, vol. 9, no. 3, pp. 1072–1080, 2018, doi: 10.1109/TSTE.2017.2764871.

[68] M. Gupta, A. Martinez, and S. Saylors, "Experiences with Wind Power Plants with Low SCR," IEEE PES General Meeting, 2015.

[69] A. Asrari, M. Mustafa, M. Ansari, and J. Khazaei, "Impedance Analysis of Virtual Synchronous Generator-Based Vector Controlled Converters for Weak AC Grid Integration," *IEEE Trans. Sustain. Energy*, vol. 10, no. 3, pp. 1481–1490, 2019, doi: 10.1109/TSTE.2019.2892670.

[70] G. Han, S. Sang, and X. Cai, "Impedance analysis and stabilization control of the LCL-type wind power inverter under weak grid conditions," *J. Renew. Sustain. Energy*, vol. 10, no. 3, 2018, doi: 10.1063/1.5019462.

[71] R. Yin, Y. Sun, S. Wang, and L. Zhang, "Stability Analysis of the Grid tied VSC Considering the Influence of Short Circuit Ratio and X/R," *IEEE Trans. Circuits Syst. II Express Briefs*, vol. 69, no. 1, pp. 129–133, 2021, doi: 10.1109/TCSII.2021.3076058.

[72] J. Chen, X. Zhang, Y. Yang, J. Chen, and X. Chen, "Impedance modelling and grid integration stability evaluation of three-phase virtual synchronous generator," *IET Power Electron.*, vol. 15, no. 1, pp. 80–91, Jan. 2022, doi: 10.1049/pel2.12214.

[73] L. Fan and Z. Miao, "Wind in Weak Grids: 4 Hz or 30 Hz Oscillations?," *IEEE Trans. Power Syst.*, vol. 33, no. 5, pp. 5803–5804, 2018, doi: 10.1109/TPWRS.2018.2852947.

[74] L. Fan, "Modeling Type-4 Wind in Weak Grids," *IEEE Trans. Sustain. Energy*, vol. 10, no. 2, pp. 853–864, 2019, doi: 10.1109/TSTE.2018.2849849.

[75] Y. Li, L. Fan, and Z. Miao, "Stability Control for Wind in Weak Grids," *IEEE Trans. Sustain. Energy*, vol. 10, no. 4, pp. 2094–2103, 2019, doi: 10.1109/TSTE.2018.2878745.

[76] Q. C. Zhong, P. L. Nguyen, Z. Ma, and W. Sheng, "Self-synchronized synchronverters: Inverters without a dedicated synchronization unit," *IEEE Trans. Power Electron.*, vol. 29, no. 2, pp. 617–630, 2014, doi: 10.1109/TPEL.2013.2258684.

[77] K. R. Vasudevan, V. K. Ramachandaramurthy, T. S. Babu, and A. Pouryekta, "Synchronverter: A Comprehensive Review of Modifications, Stability Assessment, Applications and Future Perspectives," *IEEE Access*, vol. 8, pp. 131565–131589, 2020, doi: 10.1109/ACCESS.2020.3010001.

[78] H. Høstmark, "Transient Stability Assessment of VSM based Wind Energy Conversion System," Norwegian University of Science and Technology, 2020.

[79] W. Zhang, A. M. Cantarellas, J. Rocabert, A. Luna, and P. Rodriguez, "Synchronous Power Controller with Flexible Droop Characteristics for Renewable Power Generation Systems," *IEEE Trans. Sustain. Energy*, vol. 7, no. 4, pp. 1572–1582, 2016, doi: 10.1109/TSTE.2016.2565059.

[80] Q. C. Zhong and T. Hornik, *Control of Power Inverters in Renewable Energy and Smart Grid Integration*. 2012.

[81] Q. C. Zhong, Z. Ma, and Phi-Long Nguyen, "PWM-controlled rectifiers without the need of an extra synchronisation unit," *IECON Proc. (Industrial Electron. Conf.*, pp. 691–695, 2012, doi: 10.1109/IECON.2012.6388668.

[82] O. Anaya-Lara, "Lecture Notes of ELK 12 - Wind Power in Electric Power Systems," Norwegian University of Science and Technology, 2021.

[83] O. Anaya-Lara, D. Campos-Gaona, E. Moreno-Goytia, and G. Adam, *Offshore Wind Energy Generation*. 2014.

[84] S. D. Arco, "Lecture Notes of ELK 23 - Power Electronics in Future Power Systems," Norwegian Unviersity of Science and Technology, 2021.

[85] F. B. K. Mahmood *et al.*, "Weakest location exploration in IEEE-14 bus system for voltage stability improvement using STATCOM, synchronous condenser and static capacitor," *ECCE 2017 - Int. Conf. Electr. Comput. Commun. Eng.*, no. February, pp. 623–629, 2017, doi: 10.1109/ECACE.2017.7912980.

[86] S. Shah, "Small and Large Signal Impedance Modeling for Stability Analysis of Grid-Connected Voltage Source Converters," Rensselaer Polytechnic Institute, 2018.

[87] C. L. Fortescue, "Method of Symmetrical Co-Ordinates Applied to the Solution of

Polyphase Networks," *Trans. Am. Inst. Electr. Eng.*, vol. XXXVII, no. 2, pp. 1027–1140, Jul. 1918, doi: 10.1109/T-AIEE.1918.4765570.

[88] J. Sun, "Small-signal methods for AC distributed power systems-A review," *IEEE Trans. Power Electron.*, vol. 24, no. 11, pp. 2545–2554, 2009, doi: 10.1109/TPEL.2009.2029859.

[89] M. Dokus and A. Mertens, "Sequence Impedance Characteristics of Grid-Feeding Converters," *2020 IEEE 9th Int. Power Electron. Motion Control Conf. IPEMC 2020 ECCE Asia*, no. 359921210, pp. 1216–1223, 2020, doi: 10.1109/IPEMC-ECCEAsia48364.2020.9367825.

[90] J. Sun and H. Liu, "Sequence Impedance Modeling of Modular Multilevel Converters," *IEEE J. Emerg. Sel. Top. Power Electron.*, vol. 5, no. 4, pp. 1427–1443, 2017, doi: 10.1109/JESTPE.2017.2762408.

[91] Y. Liao, "Impedance Modeling and Stability Analysis of Grid-Interactive Converters," Aalborg University, 2021.

[92] M. K. Bakhshizadeh *et al.*, "Couplings in Phase Domain Impedance Modeling of Grid-Connected Converters," *IEEE Trans. Power Electron.*, vol. 31, no. 10, pp. 6792–6796, 2016, doi: 10.1109/TPEL.2016.2542244.

[93] S. Cobreces, E. J. Bueno, D. Pizarro, F. J. Rodriguez, and F. Huerta, "Grid impedance monitoring system for distributed power generation electronic interfaces," *IEEE Trans. Instrum. Meas.*, vol. 58, no. 9, pp. 3112–3121, 2009, doi: 10.1109/TIM.2009.2016883.

[94] M. Ciobotaru, V. Agelidis, and R. Teodorescu, "Line impedance estimation using model based identification technique," in *Proceedings of the 2011 14th European Conference on Power Electronics and Applications*, 2011, no. 1, pp. 15–21.

[95] M. Cespedes and J. Sun, "Online grid impedance identification for adaptive control of grid-connected inverters," *2012 IEEE Energy Convers. Congr. Expo. ECCE 2012*, pp. 914–921, 2012, doi: 10.1109/ECCE.2012.6342721.

[96] M. Bahadornejad and N. K. C. Nair, "System Thevenin Impedance Estimation Through On-Load Tap Changer Action," in *2010 20th Australasian Universities Power Engineering Conference*, 2010, pp. 3–7.

[97] T. Roinila, J. Puukko, L. Nousiainen, and M. Vilkko, "Designing MLBS excitation for the frequency-response measurement of AC-connected power electronics systems," *IFAC Proc. Vol.*, vol. 16, no. PART 1, pp. 1329–1334, 2012, doi: 10.3182/20120711-3-BE-2027.00082.

[98] N. Mohammed, M. Ciobotaru, and G. Town, "Performance evaluation of wideband binary identification of grid impedance using grid-connected inverters," in *2019 21st European Conference on Power Electronics and Applications, EPE 2019 ECCE Europe*, 2019, pp. 1–10, doi: 10.23919/EPE.2019.8915509.

[99] A. Knop and F. W. Fuchs, "High frequency grid impedance analysis by current injection," *IECON Proc. (Industrial Electron. Conf.*, pp. 536–541, 2009, doi: 10.1109/IECON.2009.5414978.

[100] L. Naszódi, "On digital filtration in correlation time-of-flight spectrometry," *Nucl. Instruments Methods*, vol. 161, no. 1, pp. 137–140, Apr. 1979, doi: 10.1016/0029-554X(79)90371-9.

[101] A. Rygg, M. Molinas, C. Zhang, and X. Cai, "A Modified Sequence-Domain Impedance Definition and Its Equivalence to the dq-Domain Impedance Definition for the Stability Analysis of AC Power Electronic Systems," *IEEE J. Emerg. Sel. Top. Power Electron.*, vol. 4, no. 4, pp. 1383–1396, 2016, doi: 10.1109/JESTPE.2016.2588733.

[102] N. R. Chaudhuri, *Integrating Wind Energy to Weak Power Grids using High Voltage*

Direct Current Technology. 2019.

[103] M. Amin, C. Zhang, A. Rygg, M. Molinas, E. Unamuno, and M. Belkhayat, "Nyquist Stability Criterion and its Application to Power Electronics Systems," *Wiley Encycl. Electr. Electron. Eng.*, pp. 1–22, 2019, doi: 10.1002/047134608x.w1026.pub2.

[104] S. Shah, P. Koralewicz, V. Gevorgian, H. Liu, and J. Fu, "Impedance Methods for Analyzing Stability Impacts of Inverter-Based Resources: Stability Analysis Tools for Modern Power Systems," *IEEE Electrif. Mag.*, vol. 9, no. 1, pp. 53–65, 2021, doi: 10.1109/MELE.2020.3047166.

[105] H. Liu, X. Xie, X. Gao, H. Liu, and Y. Li, "Stability Analysis of SSR in Multiple Wind Farms Connected to Series-Compensated Systems Using Impedance Network Model," *IEEE Trans. Power Syst.*, vol. 33, no. 3, pp. 3118–3128, 2018, doi: 10.1109/TPWRS.2017.2764159.

[106] X. Wang, F. Blaabjerg, and P. C. Loh, "An impedance-based stability analysis method for paralleled voltage source converters," in *2014 International Power Electronics Conference (IPEC-Hiroshima 2014 - ECCE ASIA)*, May 2014, pp. 1529–1535, doi: 10.1109/IPEC.2014.6869788.

[107] Y. Liao and X. Wang, "Impedance-Based Stability Analysis for Interconnected Converter Systems with Open-Loop RHP Poles," *IEEE Trans. Power Electron.*, vol. 35, no. 4, pp. 4388–4397, 2020, doi: 10.1109/TPEL.2019.2939636.

[108] Ö. S. Mutlu, "Evaluating the Impacts of Wind Farms on Power System Operation," *J. Nav. Sci. Eng.*, vol. 6, no. 2, pp. 166–185, 2010, [Online]. Available: http://dergipark.gov.tr/jnse/issue/9992/123487.

[109] K. Uhlen, "Lecture Notes of TET4180 - Power Systems Stability," Norwegian University of Science and Technology, 2022.

[110] A. Gavrilovic, "AC/DC system strength as indicated by short circuit ratios," in *International Conference on AC and DC Power Transmission*, 1991, pp. 27–32.

APPENDIX

Appendix A

Per Unit Systems

S_b	3-phase rated VSM power
V_b	Rated grid LG peak voltage
$I_b = \frac{S_b}{\sqrt{\frac{3}{2}}V_b}\sqrt{\frac{2}{3}}$	Base current = peak value of rated RMS current
$Z_b = \frac{V_b}{I_b}$	Base impedance
$f_b = f_n$	Base frequency = nominal grid frequency
$\omega_b = \omega_n$	Base angular speed = nominal angular speed
$M_f i_{f_b} = \frac{V_b}{\omega_b}$	Base flux excitation
$L_b = \frac{Z_b}{\omega_b}$	Base inductance
$R_b = Z_b$	Base resistance
$C_b = \frac{1}{Z_b \omega_b}$	Base capacitance
$T_b = \frac{S_b}{\omega_b}$	Base torque of electrical system
$V_{DC_b} = 2V_b$	Base DC link voltage
$T_{b,wind} = \frac{P_{rated,turb}}{\omega_{rated,turb}}$	Base torque of wind turbine

Appendix B

System Parameters

B.1 Base Values for Per Unit Calculations

Base Values for Per Unit Calculations

Parameter	Value
Electrical system base power, S_b	1 MVA
Electrical system base frequency, f_b	50 Hz
Electrical system base frequency, ω_b	100π rad/s
Electrical system base torque, T_b	3183.1 Nm
Wind turbine mechanical base power, $P_{mech,b}$	1.0603 MW
Wind turbine mechanical base rotational speed, $\omega_{mech,b}$	79.59 rad/s
Wind turbine mechanical base torque, $T_{mech,b}$	13332 Nm
Base AC voltage, V_b	563.3826 V
Base AC current, I_b	1183.3 A
Base impedance, Z_b	0.4761 Ohm
Base inductance, L_b	0.0015 H
Base resistance, R_b	0.4761 Ohm
Base capacitance, C_b	0.0067 F
Base DC voltage, $V_{DC,b}$	1126.8 V
Base DC current, I_b	887.4963 A
Base resistance DC link, $R_{DC,b}$	1.2696 Ohm
Base capacitance DC link, $C_{DC,b}$	0.0025 F
Base flux excitation, $M_f i_{f,b}$	1.7933 Vs

B.2 Wind Turbine and PMSG Parameters

Turbine parameters

Parameter	Value
Turbine radius, R	1.2 m
Number of turbines, aggregated model	550
Air density, ρ	1.2 kg/m^3
Optimal tip speed ratio, λ_{opt}	7.95
Maximum power coefficient, $C_{p,max}$	0.411
Rated wind speed, $v_{w,rated}$	12 m/s
Aggregated rated mechanical power, $P_{mech,rated}$	1.0603 MW

PMSG parameters

Parameter	Value
Number of pole pairs PMSG, p	2
Permanent magnet flux, Ψ	1.7933 Vs
Inertia of the PMSG, J	5.4713 kgm^2
Friction factor of the PMSG, D	0 Nms

B.3 Power Grid Parameters

Grid parameters

Parameter	Absolute Value	Per Unit Value
Grid inductance, L_g	1.1 mH	0.7
Grid resistance, R_g	0.0476 Ohm	0.1
Filter capacitance, C	494.75 µF	0.074
Parallel resistance, R_C	1000 Ohm	2100.4
"Stator"/filter inductance, L_s	0.15155 mH	0.1
Grid side "stator"/filter resistance, R_s	0.4761 mOhm	0.001
Rotor side resistance, $R_{s,rotor}$	0.0024 Ohm	0.005

DC link capacitance, C_{DC}	0.1003 F	40
Chopper resistance, $R_{chopper}$	2.1583 Ohm	1.7
Breaker resistance, R_B	0.001 Ohm	0.0021

Electrical parameters

Parameter	Value
Rated power, S_{rated}	1.0MVA
Nominal Line-Line voltage, $V_{gn,L-L}$	690V
Nominal DC link voltage, $V_{DC,ref}$	1126.8V
Nominal DC link current, $I_{n,DC}$	177.5A
Nominal grid frequency, f_n	50Hz

B.4 Synchronverter Parameters

Inverter Controller Parameters.

Parameter	Value
J	2
K_q	40000
D_p	506.6059
D_q	17750
Virtual synchronising resistance, R_{sync}	0.0476Ω
Virtual synchronising inductance, L_{sync}	0.53042mH
Switching frequency, f_s	5kHz

Rectifier Controller Parameters

Parameter	Value
J_m	4.0528
K_{qm}	223050

$K_{p,dc}$	18.3624
$K_{i,dc}$	45.9061
D_{pm}	2026.4
Switching frequency, f_s	5kHz
Virtual synchronising resistance, R_{sync}	0.0024Ω
Virtual synchronising inductance, L_{sync}	0.75774mH

Appendix C

Simulink Models

C.1 Original System

C.1.1 Full Original System

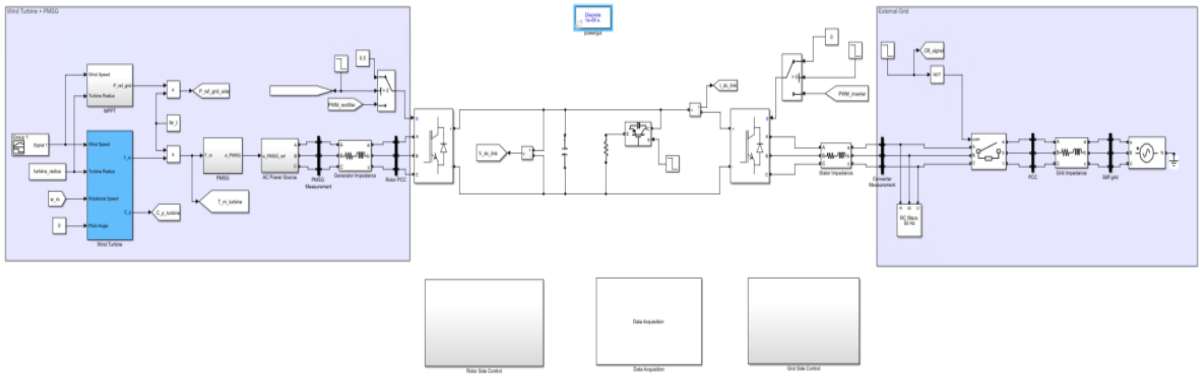

Figure C.1: Full system Simulink model.

C.1.2 Wind turbine

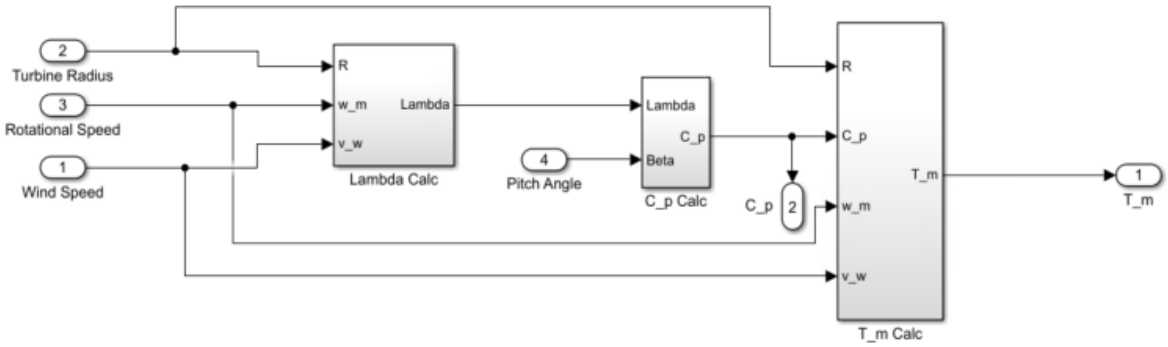

Figure C.2: Wind turbine Simulink model.

C.1.3 Drive Train and PMSG

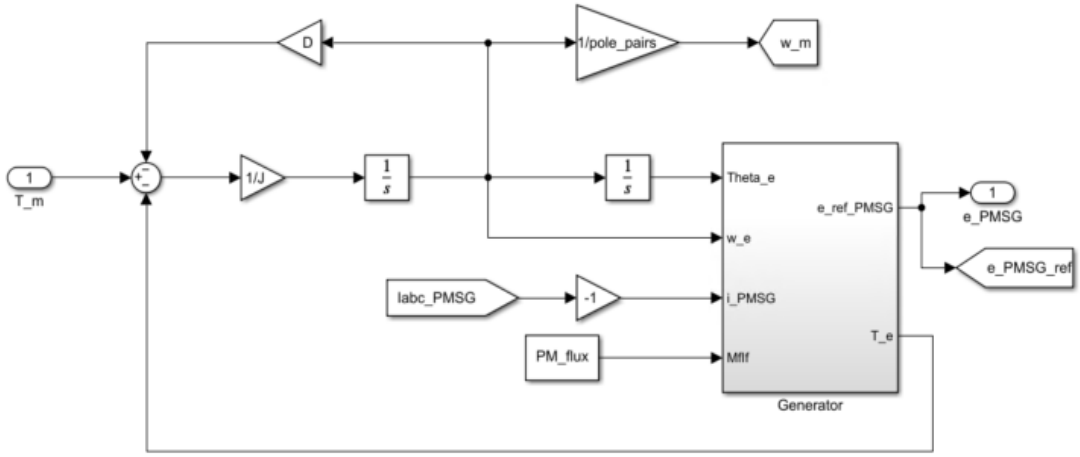

Figure C.3: Drive train and PMSG Simulink model.

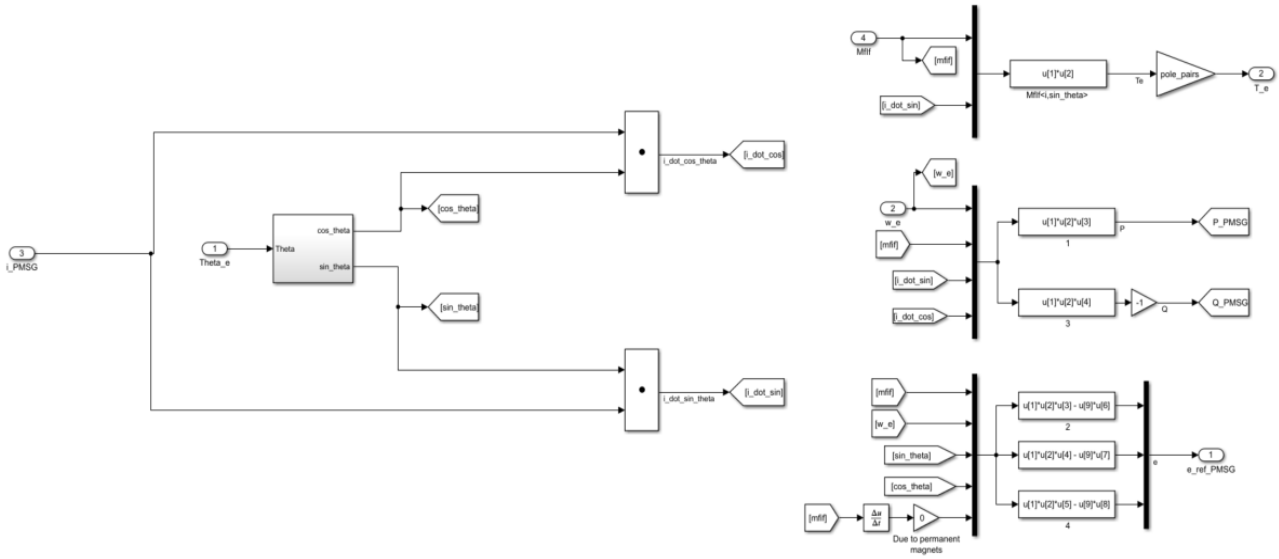

Figure C.4: PMSG Generator Simulink model.

C.1.4 Grid Side Controller

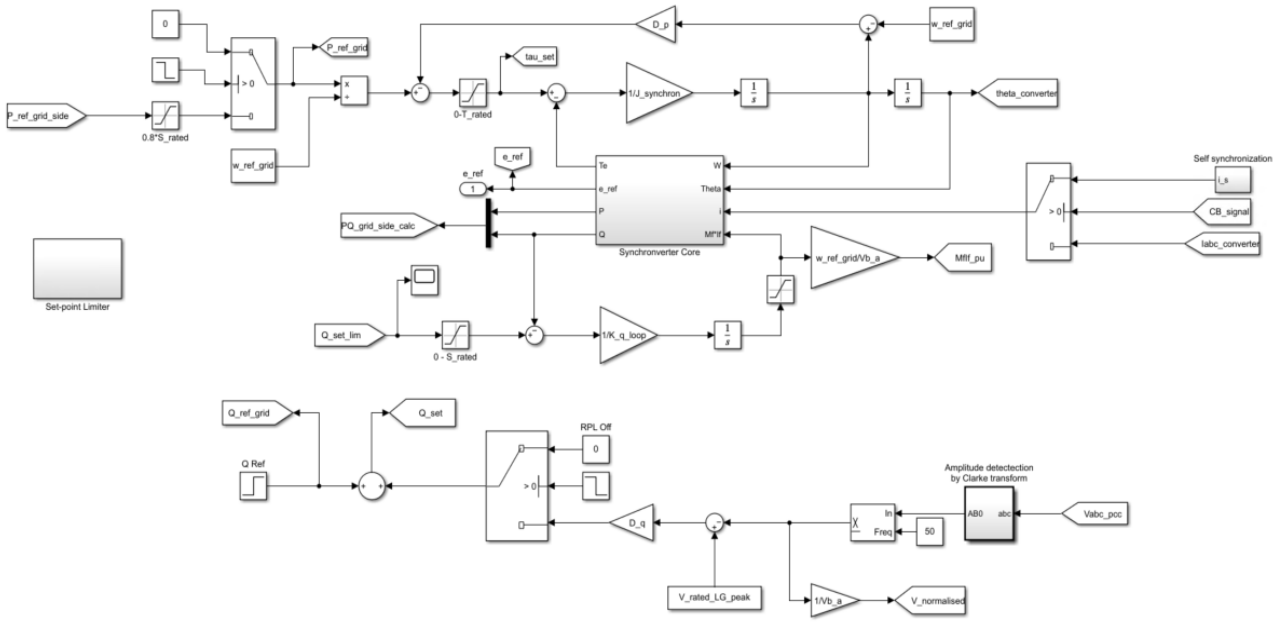

Figure C.5: Grid Side Control Simulink model.

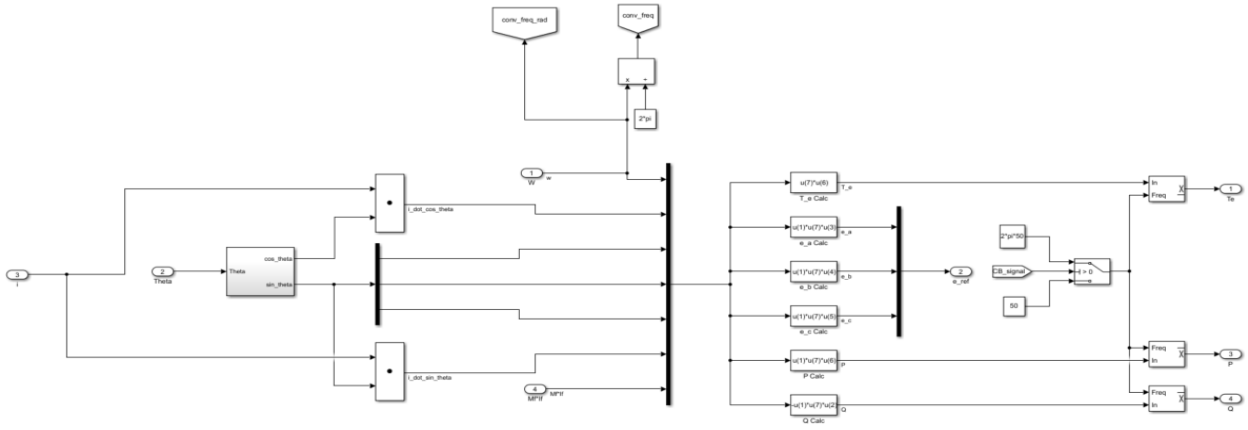

Figure C.6: Synchronverter core constituting the Synchronverter calculations.

C.1.5 Rotor Side Controller

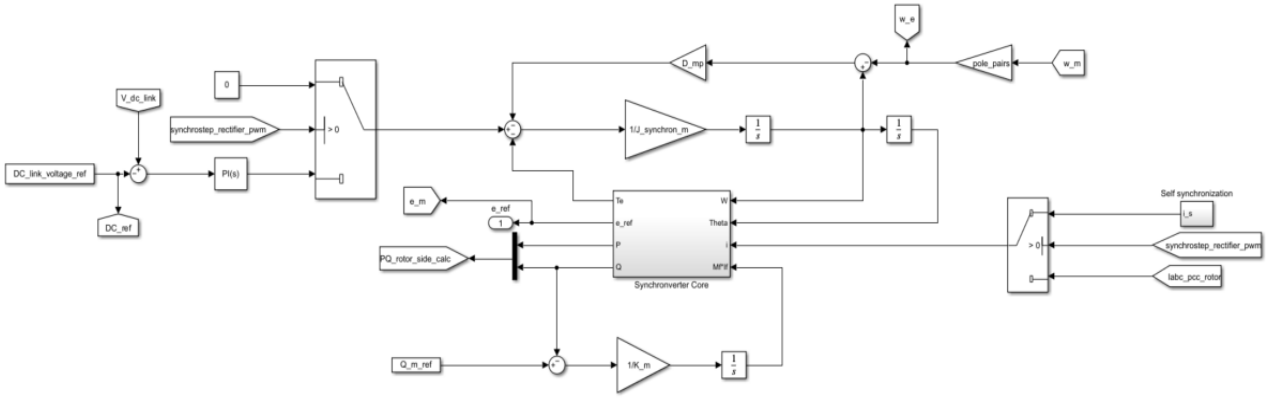

Figure C.7: Rotor Side Control Simulink model

Appendix D

Scientific Paper

Low-Inertia Power Systems: A Comprehensive Review

Claysius Dewanata Widjaja, *Student Member, IEEE,* Mohammad Amin, *Senior Member, IEEE*

***Abstract*—With massive penetration of Converter-Interfaced Generation (CIGs), new challenges emerge regarding the inertia of the systems. Since CIGs have no rotating part, it provides no inertia to the system, bringing several issues such as low short circuit level (SCL), higher ROCOF, lower frequency nadir and more significant frequency deviations. Low-inertia has been investigated since a few years ago. However, the new framework regarding this has just been developed in 2021, contained in the official publication of IEEE PES TR-77. With the massive research on the CIGs, especially in low inertia, this paper tries to discuss holistically the transition of power systems and what impacts this low inertia brings to the systems in terms of stability. Several solutions that have been proposed by researchers worldwide are also reviewed, and possible future works and challenges in low-inertia systems are also proposed and advised.**

***Index Terms*—Low-Inertia, Stability, Frequency, Rotor Angle, Virtual Inertia, Deloaded, Hidden Inertia,**

I. Introduction

CONVERTER based renewable energy systems have been massively integrating in power systems, which causes the displacement of conventional generating units, hence reducing system inertia. This emerging grid is known as a low inertia power system. An ample amount of inertia is significant to make sure a secure and reliable power supply. A decade ago, the low inertia power systems were just a theoretical concept that is now a reality [1]. Some countries have more than 100% of their demand from solar or maybe from wind [1]. In traditional power systems, the inertia is provided by the rotating masses, and the system operators evaluate the system inertia by the approximate method based on the part of the resource or based on a simplified empirical relation [2]. However, the massive involvement of CIG system operators requires more reliable and more flawless methods to estimate instantaneous and forecast future inertia. This paper has discussed the importance of inertia estimation and further research on inertia estimation techniques. Also, inertia plays a vital role in power system stability, especially in rotor angle stability and frequency stability. Here in this paper, both stability issues are briefly explained. Furthermore, the current measures for low inertia power systems and future works are also articulated in this paper.

II. Evolutions of the Power Systems

A. Power Systems Transition

In the last couple of years, the contribution from renewable energy resources has been increased eminently. Because of the environmental protection rules, less availability of fossil fuels, and uninterrupted power supply for future [3]. The traditional power system uses a synchronous generator that provides robust frequency and voltage control. On the other hand, converter dominated power systems uses variable generation and has more fragile and volatile frequency and voltage control. The traditional power systems have large rotational inertia, self-synchronisation, slow actuation and control. However, the converter-based power systems do not have rotational inertia and self-synchronisation. Even for the transmission systems, the modern transmission is based on converters such as Flexible AC Transmission Systems (FACTS) and High Voltage DC (HVDC) transmission systems [4]. One report published by EPRI stated that "the 21st century is the golden age for applying power electronics technology".

B. Impact of CIGs Penetration on the Grid

The significant advancement of scientific and technological power electronics made a massive transition from conventional energy to renewable energy [5]. The use of power electronics in power systems have increased immensely in recent years, and it is expected to be more in the future [6]. The increase of CIGs penetration to the grid will create lots of issues. The power electronics control plays a vital role in grid connection also in defining the device level characteristics. Multiple control loops are used to control power electronics devices such as outer control loop, inner control loop, pulse width modulation (PWM). Hence the control algorithm other than the physical characteristic like the traditional devices determines the steady-state response, dynamic response, and response in the fault conditions [7]. The inertia support from the CIGs is low compared to the SGs. The SGs or prime movers are decoupled from the grid due to the power electronics converter interface, resulting in no inertia support based on rotational kinetic energy. The inertia support from the traditional SGs is very high compared to the power electronics converter [3]. The short circuit current for CIGs is low compared to SGs. When a short circuit fault occurs, there is no sub transient process in power electronics devices. The short circuit current for the initial state is very low, normally 1.5pu range, but it decreases very fast for

C. D. Widjaja and M. Amin is with the Department of Electric Power Engineering, Norwegian University of Science and Technology (NTNU), Trondheim, Norway (e-mail: claysius@ieee.org; mohammad.amin@ntnu.no)

the steady state short circuit current because of aloft internal reactance and prompt controllable reference current [8]. This causes challenges for the control and protection devices.

III. Inertia and Its Relevance in Power Systems

A. Inertia from Power Systems Perspective

Most of the power generating modules are from gas, coal, nuclear, hydroelectric power for a typical power system. The typical device in all these power generating modules is the Synchronous generator. The rotating parts of these SGs stores kinetic energy, which plays an important role in the dynamics of frequency and stability. Synchronous generators have a built-in property of inertia support. When there is a supply/demand variation, or a grid fault, the SGs change the rotational speed based on the controllers' actions and rotor inertia. The SGs make sure grid synchronism and protect the grid from collapsing or a possible blackout [3]. During any frequency variation, the SGs absorb or supply kinetic energy to the grid through the rotational mass [9].

When the system's frequency starts to fall, the SGs release their stored kinetic energy even before the primary frequency controllers are activated to restore the frequency deviation. System frequency change will always be the proportion to the system inertia in any power system for a supply/demand mismatch.

Utterly, the resistance to the change in the rotational speed of the SG is defined as the inertia of a power system [10].

The inertia of the synchronous generators can be written as,

$$J = \int r^2 dm = r^2 dm$$

Where r (in m) is the radius of the rotating part and m is the mass (in kg)

The kinetic energy can be written as,

$$E_K = \frac{1}{2} J w_m^2$$

The rate of change of kinetic energy of the power system is equal to the difference between the mechanical power and electrical power, which is known as the swing equation of the power system [11] and can be expressed as,

$$\frac{d}{dt}\left(\frac{1}{2} J \omega_m^2\right) = P_m - P_e$$

From the swing equation, it can be expressed that if the average acceleration power is zero, the power system is in stable operation. Any discrepancy between the mechanical and absorbed electrical power will generate dislodgement in the steady-state angular rotor speed [12]. The moment of inertia constant can be expressed then,

$$H = \frac{E_{KE}}{S} = \frac{\frac{1}{2} J \omega_m^2}{S}$$

B. Inertia and Power Systems Stability

Power system stability is the ability to go back to initial or normal operation after having some disturbances. From classical point of view, power system instability means loss of synchronism when the system subjected to some disturbances [13]. Addition of CIGs in the power systems means reduction of inertia hence issues in the stability of the power system. If the renewable energy sources penetration is equivalent to or greater than the capacity of the SG, then the power system stability related issues arise [14]. A new definition and classification for power system stability have been given by IEEE PES-TR77 [15].

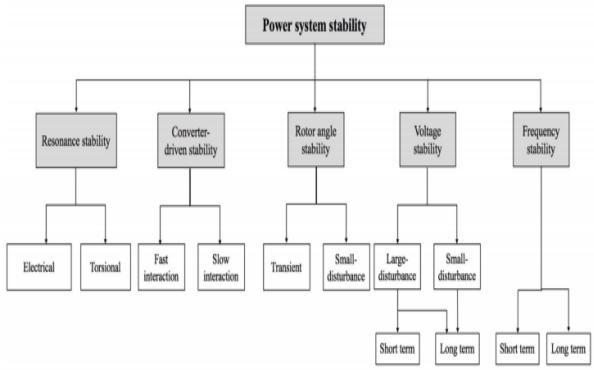

Fig. 1. New classification of power system stability [15]

C. Impact of Inertia on Rotor Angle Stability

Rotor angle stability is defined as the ability of the power systems to maintain synchronism after a disturbance happens. Rotor angle stability itself can be divided in two main categories, which is generally more known as Transient Stability and Oscillatory Stability (or Small-signal Stability). These two categories are defined based on the severity of the disturbance. These severity levels of disturbance affect the linearisation of the system equations, resulting in the two most significant methods used worldwide: Equal Area Criterion (EAC) for transient stability and the Modal-based approach for small-signal stability.

EAC comes from the swing equation as follows,

$$\frac{d^2\delta}{dt^2} = \frac{\omega_s}{2H}(P_m - P_e)$$

By integrating the above equation, we can obtain what we called the Critical Clearing Time (CCT), or the time to reach Critical Clearing Angle (CCA) as follows

$$CCT = \sqrt{\frac{2H(\delta_{cr} - \delta_0)}{\pi f \omega_s}}$$

Where the CCA is defined as the maximum fault clearance angle, where the Equal Area Criterion can still be satisfied without loss of synchronism. CCT and CCA are used as system transient stability indicators, since the difference between the actual clearing time and clearing angle with the CCT and CCA measures the transient stability margin of the system [16].

From the previous equation, it is clear that inertia affects the CCT proportionally, where the increase in inertia will increase the CCT. However, we need to recall that this is only valid for the SMIB system, where this formula for CCT is mainly derived. If, say, the network is extended into two-machine two-area systems, it can be seen that the distribution of the inertia also plays a role in the change of CCT, depending on the type of the load [17]. The test system is as follows,

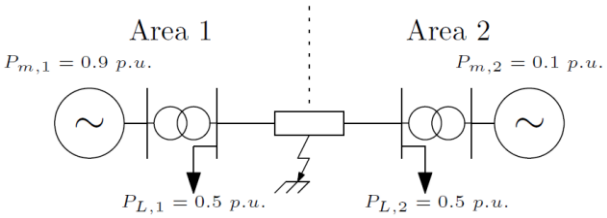

Fig. 2. Two-area two-machines test systems [17]

By implementing the extended EAC [18] and also changing the load types (constant power and constant impedance), we can obtain the following contour plots distribution of CCT

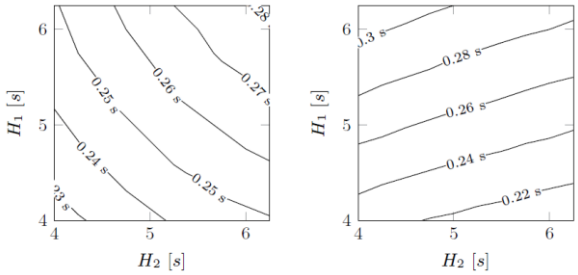

Fig. 3. Contour plots of CCT for constant power and constant impedance load [17]

From the results, we can see that in constant power load, increasing both inertia constants of the two generators give rise to the CCT, while in constant impedance load, the higher CCT is obtained by reducing the inertia constant of generator 1 while increasing the inertia constant of generator 2. Therefore, we can safely conclude that to improve the system's transient stability better, a simple increase in inertia might not be the optimal solution since many parameters also play a part. Further study is required in this, by investigating the system's overall inertia to arrive in much convincing conclusion.

For small-signal stability, it is related to the Eigenvalues mode due to the linearisation near the operating point of the system equations. In SMIB, the relation between the natural frequency and damping ratio of the rotor angle mode and the inertia is given according to the following equation [11].

$$\omega = \sqrt{\frac{P_{max}\cos(\delta_0)\omega_s}{2}}\sqrt{\frac{1}{H}}$$

$$\zeta = \frac{K_D}{2\sqrt{P_{max}\cos(\delta_0)\omega_s}}\sqrt{\frac{1}{H}}$$

From the two equations, we can see that the inertia constant will be inversely proportional to the rotor angle mode's natural frequency and damping ratio. However, similar to what the two-area two-machines study case shows in transient stability, the electro-mechanical modes for the two area systems are as follows [17],

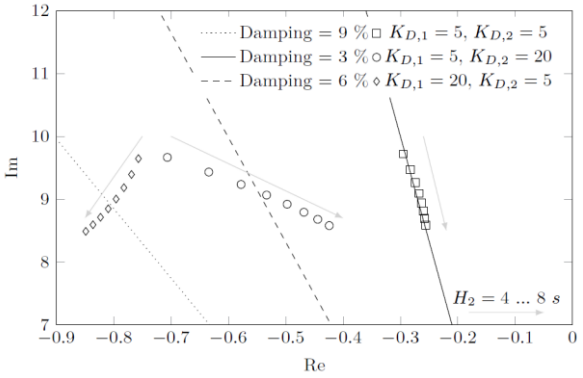

Fig. 4. Eigenvalue loci for two-area systems, where $H_1 = 4\ s$ and H_2 is varied from 4 to 8 s in steps of 0.5 s [17]

Again, we can see from Fig. 3. that the damping ratio is determined not simply by inertia but also by damping torque coefficients.

D. Impact of Inertia on Frequency Stability

In the case of frequency stability, it is already widely discussed in the industry and academia and a consensus has been reached that low inertia will increase the rate of change of frequency (ROCOF), decreasing the nadir frequency response further as follows.

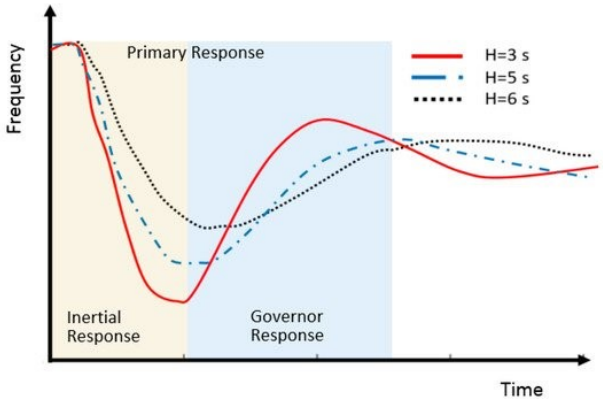

Fig. 5. Frequency response with varying total systems inertia [19]

As can be seen in Fig. 4, lower inertia of the systems will cause the nadir to be lower, and the ROCOF to be faster to reach the nadir, causing the deviation from the nominal frequency to be higher. This is true according to the formula

$$ROCOF = -\frac{\Delta P f_n}{2H_{sys}}$$

Where ΔP is the power imbalance in the system, f_n is the nominal frequency, and H_{sys} is the total inertia of the system.

IV. Current Measures for Low-Inertia Power Systems

A. Synchronous Condensers

Synchronous condensers are synchronous machines that are connected to a high voltage network. By controlling the field current of the synchronous condenser, the reactive power and voltage are controlled [17]. Its main objective is to control the voltage by injecting or absorbing the reactive power but as it is a rotating machine, inertia support is an inherent feature of it

[20]. SC normally operates in motoring mode but it can be transferred to the generation mode if the frequency drops [21]. It contributes to the limitations of ROCOF. The SC can absorb or release the kinetic energy stored in its rotating mass during a disturbance to protect the system from frequency instability. For instance, if a generator suddenly tripped then the system frequency will start to drop as the demand increases because of the loss of a generator then the SC will release the rotational energy to the grid to against the frequency drop. On the contrary, if load or demand decreases, the SC will absorb extra active power from the network to stop the frequency increase. The inertia constant for a typical SC is 1-1.25 s [22]. The increased use of SCs in low inertia power systems helps limit the ROCOF and frequency discrepancy [23]. SCs are capable of providing other services like short circuit level to enhance system strength [24], [25], fault-ride through capability [26], [27], oscillation damping and so on. Because of these reasons this device becoming very popular globally. However, there are some disadvantages of SCs like for instant load changes it cannot be controlled fast enough and it requires high cooling for thermal consideration [22]. In this perspective the thermal and hydroelectric power plants that is going to be retired can be converted to synchronous condensers for inertia support [28]. To improve the system's inertia, the Australian authorities plan to install SCs to ensure large integration of renewable energy sources. In ref [29] it is stated that with the increase of SCs the frequency nadir starts to get better. With the increase of system inertia, the frequency deviation starts to decrease. That buys more time to deploy headroom which finally makes sure improvement of frequency nadir. It also needs to be considered that adding of SCs in power systems is not cheap which requires further study for cost reduction. In Fig. 6 it can be seen that the frequency nadir without SC is 48.0 Hz but if SC is added then the frequency nadir increases to 48.2 Hz.

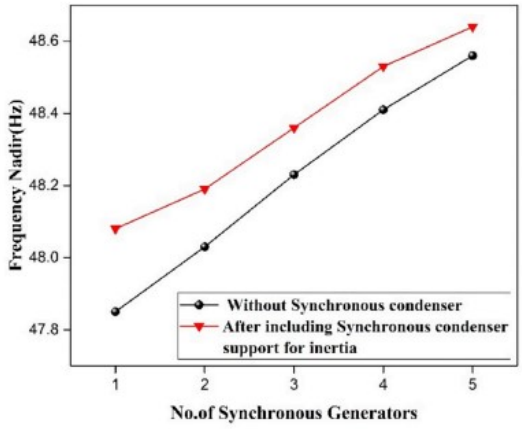

Fig. 6. Comparison of frequency nadir with and without the synchronous condenser

B. Demand-side Management

For many years it was assumed that the demand side of a power system is uncontrollable, so the system's stability is only manageable by controlling the generation side or the generators only [30]. But now because of the high integration of RES in grids, the generation side also becomes uncontrollable, leading to a frequency deviation. Hence control of the generation side or the demand side is imminent. Self-regulating loads can regulate when there is a power imbalance from the demand side of the power system. This helps decrease the frequency deviation created from a power imbalance by injecting active power support from the demand side [31]. In a demand side management plan the participating clients decrease their consumption to maintain system stability when there is an effective loss of generation. Demand side management plan has been implemented in GB, and trials have been given to see the effectiveness [32]. On the demand side, there are many motors connected with the system which provide inertia to the system and this inertia is a potential contribution for a low inertia power system [33]. Self-regulating loads or to be more specific, thermostatically controlled loads like freezers, refrigerators, air-conditioner tracks the frequency and turn on or turn off the device accordingly [34]. These devices have relays and these relays calculate frequency deviation and ROCOF during a power imbalance and turn the device off.

Implementation of demand-side management is a cost-effective solution for a low inertia power system, and many TSOs recommend it. Initial implementation cost for DSM is high as it requires a redesign of power system with a communication channel. With the addition of a communication channel, some drawbacks arise, like it is challenging to manage the communication channel when it reaches the maximum number of ports; thus, it can lead to the failure of the channel, and the whole grid can collapse because of that.

C. Energy Storage

Energy storage systems are becoming popular for inertia support to the power system. For renewable energy plants, the energy storage systems can be used to improve the uses of the plants by storing energy at night when there is less demand and can be discharged and sent to the grid in the daytime when the demand increases. This will balance the supply/ demand criteria and will balance the system [35]. Batteries operate at direct current, so a power electronics converter must control it to get inertia supports from batteries. Nevertheless, inertia support from batteries depends on what type of battery is being used. Sodium-sulfur batteries usually have a response time of 1 ms, which is good for inertia emulation control [36]. However, hydrogen-based energy systems have greater response time and cannot be used in inertia support [37]. Lithium-ion batteries have a faster response time, and it is used in inertia support. But an unexpected draw of power puts large stress on it and can affect the battery's lifetime. Ultra-capacitors are a kind of energy storage that can store a large amount of and can discharge the same amount within a short period. To reduce this, ultra-capacitor can be used with the lithium-ion battery.

So far, the prominent energy storage system is pumped hydro energy storage. PHES method is the lowest cost energy storage system available in the market [38]. PHES storing energy principle is transferring water between lower and upper reservoir [39]. PHES can support for inertia both in generation and pumping modes. One major advantage of LHES is it can be used as synchronous condenser when it is not using for pumping or generating. By this PHES can support inertia to limit the ROCOF when there is a disturbance in power system. The inertia constant for a typical PHES is 2-4 s and it can also

take or give power from the system. But its response time is not fast enough to compare with super-capacitors.

Compressed air energy storage is another method of energy storage that can be use in inertia support. This helps to connect large RES into grid. CAES is the technic in which air is compressed and pressurised by using electrical power and then it is stored in a chamber which air tight. To get electrical energy this pressurised air is then supply through an air turbine [40]. Inertia constant for CAES is 3-4s [3]. But there is a challenge of building it in any location as it has geographical restriction.

D. Inertia Emulation Techniques for Inverter (Virtual Synchronous Generator)

Inertia emulation techniques, or much more familiar to be called virtual inertia, are a control method to imitate the inertial characteristics of rotating machines. In general, the virtual inertia techniques for inverters mimics two machines: induction machine, which is called inducverters [41] and synchronous machine. Currently, the research trend is more focused on synchronous machines, which can be categorised further into a higher order model pioneered by VISMA [42] and a lower order model such as synchronverter [43]. Higher order and lower order model indicates the order of the machine model being implemented, with higher order sometimes refer to the 5th order or 7th order and lower order usually utilise the 2nd order of the model of SG. This virtual inertia technique combines renewable energy systems, short-term energy storage, power electronics components, and controller combined. In this case, the inertia constant can be defined as

$$H = \frac{C_{DC} V_{DC}^2}{2S}$$

Where C_{DC} is the capacitance of the DC-link capacitor, V_{DC} is the DC bus voltage, and S is the apparent power of the VSG [44].

E. Inertia Emulation Techniques for Wind Turbine

There are 4 types of wind turbines currently used worldwide. Type 1 and type 2 wind turbines are connected directly to the grid through an induction generator. Hence the rotation of the wind turbine and the rotation of the induction generator will contribute to the total inertia of the systems even though the value might be too small compared to conventional generators.

However, in type 3 and type 4 wind turbines, it is connected via a converter that can regulate the rotation speed. Hence, by utilising a control algorithm, this variable can be regulated to contribute to the system's inertia by extracting the kinetic energy from the rotor. This is referred to as the 'hidden' inertia of wind turbines [45]. The 'hidden' inertia techniques can be employed by either 1 control loop or 2 control loops (ROCOF only, or ROCOF and frequency) [46].

F. Inertia Emulation Techniques for PV Array

The techniques being used to emulate inertia in PV array are similar to VSG, such as synchronverter [47]. Other than the VSG techniques, a deloading control method can also be implemented to regulate the power by increasing the DC bus voltage so it works outside the maximum power point, a technique that can also be implemented in wind turbines [48].

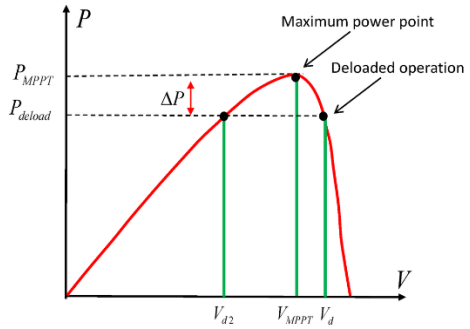

Fig. 7. Deloading operation for PV array [47]

V. Possible Future Works

A. Main Challenges in Low-Inertia Solution Research

With the increase of RES integration in power systems stimulate low inertia challenges. Different control technologies (like VSG) that can mitigate this inertia problem are now used and will be greatly used in future power systems. Addition of these new technologies in modern power systems can be harmful to the existing one. Hence intense research is needed in this area to ensure smooth operation of the grid. Virtual synchronous generators give inertial support, which entirely depends on the frequency and ROCOF. Therefore, immaculate measurements of these values are obligatory. These values will be obtained from different nodes of the power systems, and under the transient mode, these values can vary for different measurement windows. Thus, high-speed measurement devices with an upper computing method are required for the smooth operation of VSGs. Further robust research is needed for these measurement devices and computing methods.

B. Inertia Estimation

Inertia estimation has become an essential role for the stable operation of future low inertia power systems. Inertia support from the RESs is variable, and it is increasing with the increase of high penetration of RES in the power systems. Hence estimation of inertia from RES is necessary to keep the power system stable. Proper and financially affordable inertia estimations will help the system operators analyse the characteristic of the system's frequency response [49]. Based on time, inertia estimation can be categorised in three different categories [49].

I. Offline, post-mortem inertia estimation: In this method, inertia is estimated after a significant frequency disturbance has already been taken place, and because of that, the power imbalance related to ROCOF is accurately known [49].

II. Online inertia estimation: In this method, the real-time measurements are done in real-time. It provides almost close to the real-time inertia information in the power system. This method has three more methods to estimate real-time inertia. 1) Total inertia from transmission-system-connected synchronous generation units. 2) Discrete inertia estimation. 3) Continuous inertia estimation [50].

III. Estimation of expected inertia (forecasting): This method estimates expected inertia that will be present in future [51]. Grid operators cannot always operate or take actions based on real-time values, so

they need to know how much inertia will be present in future to reflect fast on frequency disturbance.

C. Virtual Synchronous Generator

Virtual synchronous generator combines power electronics devices, control systems, storage systems, and renewable energy sources that provide inertia like a conventional power system [52]. For the low inertia power systems, it can be said that the VSG will be the future [53]. The VSG control technique can be implemented in all the rectifiers and inverters, which can maintain the stability of the power system. The rectifier in an HVDC transmission system can behave like a synchronous machine, and the Inverter at the grid connection point can act like an SG unit through inertia emulation control.

D. Economic and Standard Assessment for Virtual Inertia

Inertia support provided by the virtual inertia control units needs to be correctly valued. In a typical power system, inertia support is inherently provided. So, it is not recognised as a valuable resource that needs to be quantified. But now, with the increase of CIG, the virtual inertia control support will be quantified, and there can be a fair price for this support. By doing this, the demand for inertia service will increase. The virtual inertia control unit requires additional cost, so virtual inertia should be traded [54]. To determine the economic value of the inertia in the power system, an economic valuation toll was developed in [55].

But further research should be done to build a proper fair model considering both the investment cost and the provisional income of trading the inertia. Then also who will pay for the inertia service e.g. the consumer or the distributor. Some standard and regulation needs to be developed for connection of large RESs. It is necessary to maintain certain level of reliability for safe operation of the grid. Policy for integration of virtual inertia control units needs to be changed. Some of the key aspects that needs to be included can be VSG units location, the amount of inertia support and for how long, the size of the grid with capacity [56].

VI. Conclusion

To conclude, the high-level penetration of RESs in the power system will create stability issues. To maintain the stability of the power system, the inertia support needs to be maintained. This study focused on the challenges due to low inertia and their possible solution. Also, some inertia emulation control techniques are briefly discussed in this review. Current inertia support techniques, along with some future work, has also been discussed in this study. A brief study of an economic and standard assessment for virtual inertia has also been presented here. Furthermore, this study also recommends some further research on low inertia power systems.

VII. References

[1] F. Milano, F. Dorfler, G. Hug, D. J. Hill, and G. Verbič, "Foundations and challenges of low-inertia systems (Invited Paper)," *20th Power Syst. Comput. Conf. PSCC 2018*, pp. 1–25, 2018, doi: 10.23919/PSCC.2018.8450880.

[2] D. Wilson, J. Yu, N. Al-Ashwal, B. Heimisson, and V. Terzija, "Measuring effective area inertia to determine fast-acting frequency response requirements," *Int. J. Electr. Power Energy Syst.*, vol. 113, no. March 2019, pp. 1–8, 2019, doi: 10.1016/j.ijepes.2019.05.034.

[3] K. S. Ratnam, K. Palanisamy, and G. Yang, "Future low-inertia power systems: Requirements, issues, and solutions - A review," *Renew. Sustain. Energy Rev.*, vol. 124, no. July 2019, p. 109773, 2020, doi: 10.1016/j.rser.2020.109773.

[4] J. Shair, H. Li, J. Hu, and X. Xie, "Power system stability issues, classifications and research prospects in the context of high-penetration of renewables and power electronics," *Renew. Sustain. Energy Rev.*, vol. 145, 2021, doi: 10.1016/j.rser.2021.111111.

[5] A. Chakraborty, "Advancements in power electronics and drives in interface with growing renewable energy resources," *Renew. Sustain. Energy Rev.*, vol. 15, no. May, pp. 1816–1827, 2011, doi: 10.1016/j.rser.201 0.12.005.

[6] G. Zhang, Z. Li, B. Zhang, and W. A. Halang, "Power electronics converters: Past, present and future," *Renew. Sustain. Energy Rev.*, vol. 81, no. May 2016, pp. 2028–2044, 2018, doi: 10.1016/j.rser.2017.05.290.

[7] M. Beza and M. Bongiorno, "Impact of converter control strategy on low- and high-frequency resonance interactions in power-electronic dominated systems," *Int. J. Electr. Power Energy Syst.*, vol. 120, no. February, p. 105978, 2020, doi: 10.1016/j.ijepes.2020.105978.

[8] A. K. Elnaggar, J. L. Rueda, and I. Erlich, "Comparison of short-circuit current contribution of Doubly-Fed induction generator based wind turbines and synchronous generator," *2013 IEEE Grenoble Conf. PowerTech, POWERTECH 2013*, 2013, doi: 10.1109/PTC.2013.6652307.

[9] M. Dreidy, H. Mokhlis, and S. Mekhilef, "Inertia response and frequency control techniques for renewable energy sources: A review," *Renew. Sustain. Energy Rev.*, vol. 69, pp. 144–155, 2017, doi: 10.1016/j.rser.2016.11.170.

[10] P. Tielens and D. Van Hertem, "The relevance of inertia in power systems," *Renewable and Sustainable Energy Reviews*, vol. 55. pp. 999–1009, 2016, doi: 10.1016/j.rser.2015.11.016.

[11] P. Kundur, *Power System Stability and Control*. 1994.

[12] M. P. N. Van Wesenbeeck, S. W. H. De Haan, P. Varela, and K. Visscher, "Grid tied converter with virtual kinetic storage," *2009 IEEE Bucharest PowerTech Innov. Ideas Towar. Electr. Grid Futur.*, no. 1, pp. 1–7, 2009, doi: 10.1109/PTC.2009.5282048.

[13] A. Ulbig, T. S. Borsche, and G. Andersson, "Impact of Low Rotational Inertia on Power System Stability and Operation," 2014.

[14] Y. Hirase, K. Abe, O. Noro, K. Sugimoto, and K. Sakimoto, "Stabilisation effect of virtual synchronous generators in microgrids with highly penetrated renewable energies," *2016 IEEE 17th Work. Control Model. Power Electron. COMPEL 2016*, 2016, doi: 10.1109/COMPEL.2016.7556690.

[15] N. Hatziargyriou *et al.*, "Definition and Classification of Power System Stability - Revisited & Extended," *IEEE Trans. Power Syst.*, vol. 36, no. 4, pp. 3271–3281, 2021, doi: 10.1109/TPWRS.2020.3041774.

[16] M. Reza, "Stability analysis of transmission systems with high penetration of distributed generation," Delft University of Technology, 2006.

[17] P. Tielens, "Operation and control of power systems with low synchronous inertia," *Arenb. Dr. Sch. Fac. Eng. Sci.*, no. November, 2017, [Online]. Available: https://lirias.kuleuven.be/bitstream/123456789/592208/1/phd_Pieter_Tielens.pdf.

[18] Y. Xue and M. Pavella, "Extended equal-area criterion: an analytical ultra-fast method for transient stability assessment and preventive control of power systems," *Int. J. Electr. Power Energy Syst.*, vol. 11, no. 2, pp. 131–149, 1989, doi: 10.1016/0142-0615(89)90021-5.

[19] A. Mujcinagic, M. Kusljugic, and E. Nukic, "Wind Inertial Response Based on the Center of Inertia," *Energies*, vol. 2, pp. 1–17, 2020.

[20] H. T. Nguyen, G. Yang, A. H. Nielsen, and P. H. Jensen, "Frequency stability improvement of low inertia systems using synchronous condensers," *2016 IEEE Int. Conf. Smart Grid Commun. SmartGridComm 2016*, pp. 650–655, 2016, doi: 10.1109/SmartGridComm.2016.7778835.

[21] Q. Hong, M. A. U. Khan, C. Henderson, A. Egea-Àlvarez, D. Tzelepis, and C. Booth, "Addressing Frequency Control Challenges in Future Low-Inertia Power Systems: A Great Britain Perspective,"

Engineering, vol. 7, pp. 1057–1063, 2021, doi: 10.1016/j.eng.2021.06.005.

[22] Y. Liu, S. Yang, S. Zhang, and F. Z. Peng, "Comparison of synchronous condenser and STATCOM for inertial response support," *2014 IEEE Energy Convers. Congr. Expo. ECCE 2014*, pp. 2684–2690, 2014, doi: 10.1109/ECCE.2014.6953761.

[23] Nahid-Al-Masood, N. Modi, and R. Yan, "Low inertia power systems: Frequency response challenges and a possible solution," in *Australasian Universities Power Engineering Conference*, 2016, pp. 1–6, doi: 10.1109/aupec.2016.7749335.

[24] D. Tzelepis, Q. Hong, C. Booth, P. N. Papadopoulos, J. Ramachandran, and G. Yang, "Enhancing Short-Circuit Level and Dynamic Reactive Power Exchange in Gb Transmission Networks under Low Inertia Scenarios," *SEST 2019 - 2nd Int. Conf. Smart Energy Syst. Technol.*, pp. 1–6, 2019, doi: 10.1109/SEST.2019.8849020.

[25] E. Marrazi, G. Yang, and P. Weinreich-Jensen, "Allocation of synchronous condensers for restoration of system short-circuit power," *J. Mod. Power Syst. Clean Energy*, vol. 6, no. 1, pp. 17–26, 2018, doi: 10.1007/s40565-017-0346-4.

[26] F. O. Igbinovia, G. Fandi, I. Ahmad, Z. Muller, and J. Tlusty, "Modeling and simulation of the anticipated effects of the synchronous condenser on an electric-power network with participatingwind plants," *Sustain.*, vol. 10, no. 12, 2018, doi: 10.3390/su10124834.

[27] A. O. Rousis, D. Tzelepis, Y. Pipelzadeh, G. Strbac, C. D. Booth, and T. C. Green, "Provision of Voltage Ancillary Services through Enhanced TSO-DSO Interaction and Aggregated Distributed Energy Resources," *IEEE Trans. Sustain. Energy*, vol. 12, no. 2, pp. 897–908, 2021, doi: 10.1109/TSTE.2020.3024278.

[28] J. Banks, A. Bruce, and I. Macgill, "Fast Frequency Response Markets for High Renewable Energy Penetrations in the Future Australian NEM," *Sol. Res. Conf.*, no. January 2018, 2017, [Online]. Available: http://www.ceem.unsw.edu.au/sites/default/files/documents/024_J-Banks_DI_Peer-reviewed.pdf.

[29] Nahid-Al-Masood, R. Yan, T. K. Saha, and N. Modi, "Frequency response and its enhancement using synchronous condensers in presence of high wind penetration," *IEEE Power Energy Soc. Gen. Meet.*, vol. 2015-September, 2015, doi: 10.1109/PESGM.2015.7285801.

[30] V. Trovato, S. H. Tindemans, and G. Strbac, "Demand response contribution to effective inertia for system security in the GB 2020 gone green scenario," *2013 4th IEEE/PES Innov. Smart Grid Technol. Eur. ISGT Eur. 2013*, pp. 6–10, 2013, doi: 10.1109/ISGTEurope.2013.6695253.

[31] M. Nedd, C. Booth, and K. Bell, "Potential solutions to the challenges of low inertia power systems with a case study concerning synchronous condensers," *2017 52nd Int. Univ. Power Eng. Conf. UPEC 2017*, vol. 2017-January, pp. 1–6, 2017, doi: 10.1109/UPEC.2017.8232001.

[32] E. Kuriakose and F. Francis, "Enhancement of Power System Stability by Optimal Adaptive Under Frequency Load Shedding Using Artificial Neural Networks," pp. 12–20, 2013.

[33] Y. Bian, H. Wyman-Pain, F. Li, R. Bhakar, S. Mishra, and N. P. Padhy, "Demand Side Contributions for System Inertia in the Gb Power System," *IEEE Trans. Power Syst.*, vol. 33, no. 4, pp. 3521–3530, 2018, doi: 10.1109/TPWRS.2017.2773531.

[34] N. Chakraborty, A. Mondal, and S. Mondal, "Intelligent scheduling of thermostatic devices for efficient energy management in smart grid," *IEEE Trans. Ind. Informatics*, vol. 13, no. 6, pp. 2899–2910, 2017, doi: 10.1109/TII.2017.2695241.

[35] K. Kpoto, A. M. Sharma, and A. Sharma, "Effect of Energy Storage System (ESS) in Low Inertia Power System with High Renewable Energy Sources," *5th Int. Conf. Electr. Energy Syst. ICEES 2019*, no. February, pp. 1–7, 2019, doi: 10.1109/ICEES.2019.8719294.

[36] S. A. Hosseini, M. Toulabi, A. Ashouri-Zadeh, and A. M. Ranjbar, "Battery energy storage systems and demand response applied to power system frequency control," *Int. J. Electr. Power Energy Syst.*, vol. 136, no. September 2021, p. 107680, 2022, doi: 10.1016/j.ijepes.2021.107680.

[37] Y. Qiu *et al.*, "Feasibility analysis of utilising underground hydrogen storage facilities in integrated energy system: Case studies in China," *Appl. Energy*, vol. 269, 2020, doi: 10.1016/j.apenergy.2020.115140.

[38] A. Blakers, M. Stocks, B. Lu, C. Cheng, and R. Stocks, "Pathway to 100% Renewable Electricity," *IEEE J. Photovoltaics*, vol. 9, no. 6, pp. 1828–1833, 2019, doi: 10.1109/JPHOTOV.2019.2938882.

[39] P. Vasko, A. Verbovij, A. Moroz, S. Pazych, M. Ibragimova, and L. Sahno, "Concept of Accumulation of Energy from Photovoltaic and Wind Power Plants by Means of Seawater Pumped Hydroelectric Energy Storage," *2019 IEEE 6th Int. Conf. Energy Smart Syst. ESS 2019 - Proc.*, pp. 188–191, 2019, doi: 10.1109/ESS.2019.8764167.

[40] W. T. Pfeiffer, F. Witte, I. Tuschy, and S. Bauer, "Coupled power plant and geostorage simulations of porous media compressed air energy storage (PM-CAES)," *Energy Convers. Manag.*, vol. 249, 2021, doi: 10.1016/j.enconman.2021.114849.

[41] M. Ashabani, F. D. Freijedo, S. Golestan, and J. M. Guerrero, "Inducverters: PLL-Less Converters With Auto-Synchronization and Emulated Inertia Capability," *IEEE Trans. Smart Grid*, vol. 7, no. 3, pp. 1660–1674, 2016, doi: 10.1109/TSG.2015.2468600.

[42] H. P. Beck and R. Hesse, "Virtual synchronous machine," *2007 9th Int. Conf. Electr. Power Qual. Util. EPQU*, 2007, doi: 10.1109/EPQU.2007.4424220.

[43] Q. C. Zhong and G. Weiss, "Synchronverters: Inverters that mimic synchronous generators," *IEEE Trans. Ind. Electron.*, vol. 58, no. 4, pp. 1259–1267, 2011, doi: 10.1109/TIE.2010.2048839.

[44] L. Xiong, X. Liu, F. Wang, and F. Zhuo, "Static Synchronous Generator model for investigating dynamic behaviors and stability issues of grid-tied inverters," *Conf. Proc. - IEEE Appl. Power Electron. Conf. Expo. - APEC*, vol. 2016-May, no. 9, pp. 2742–2747, 2016, doi: 10.1109/APEC.2016.7468251.

[45] G. Lalor, A. Mullane, and M. O'Malley, "Frequency control and wind turbine technologies," *IEEE Trans. Power Syst.*, vol. 20, no. 4, pp. 1905–1913, 2005, doi: 10.1109/TPWRS.2005.857393.

[46] H. Knudsen and J. N. Nielsen, "Introduction to the Modelling of Wind Turbines," in *Wind Power in Power Systems*, vol. 8, 2012, pp. 523–554.

[47] R. V. Ferreira, S. M. Silva, D. I. Brandao, and H. M. A. Antunes, "Single-phase synchronverter for residential PV power systems," *Proc. Int. Conf. Harmon. Qual. Power, ICHQP*, vol. 2016-December, pp. 861–866, 2016, doi: 10.1109/ICHQP.2016.7783378.

[48] C. Rahmann and A. Castillo, "Fast frequency response capability of photovoltaic power plants: The necessity of new grid requirements and definitions," *Energies*, vol. 7, no. 10, pp. 6306–6322, 2014, doi: 10.3390/en7106306.

[49] E. Heylen, F. Teng, and G. Strbac, "Challenges and opportunities of inertia estimation and forecasting in low-inertia power systems," *Renew. Sustain. Energy Rev.*, vol. 147, 2021, doi: 10.1016/j.rser.2021.111176.

[50] F. Zhang, I. Sharf, A. Misra, and P. Huang, "On-line estimation of inertia parameters of space debris for its tether-assisted removal," *Acta Astronaut.*, vol. 107, pp. 150–162, 2015, doi: dx.doi.org/10.1016/j.actaastro.2014.11.016.

[51] E. M. Carlini, F. Del Pizzo, G. M. Giannuzzi, D. Lauria, F. Mottola, and C. Pisani, "Online analysis and prediction of the inertia in power systems with renewable power generation based on a minimum variance harmonic finite impulse response filter," *Int. J. Electr. Power Energy Syst.*, vol. 131, 2021, doi: 10.1016/j.ijepes.2021.107042.

[52] U. Tamrakar, D. Galipeau, R. Tonkoski, and I. Tamrakar, "Improving transient stability of photovoltaic-hydro microgrids using virtual synchronous machines," *2015 IEEE Eindhoven PowerTech, PowerTech 2015*, 2015, doi: 10.1109/PTC.2015.7232663.

[53] A. Hirsch, Y. Parag, and J. Guerrero, "Microgrids: A review of technologies, key drivers, and outstanding issues," *Renew. Sustain. Energy Rev.*, vol. 90, pp. 402–411, 2018, doi: 10.1016/j.rser.2018.03.040.

[54] H. Thiesen, C. Jauch, and A. Gloe, "Design of a system substituting today's inherent inertia in the European continental synchronous area," *Energies*, vol. 9, no. 8, 2016, doi: 10.3390/en9080582.

[55] T. Xu, W. Jang, and T. Overbye, "An Economic evaluation tool of inertia services for systems with integrated wind power and fast-acting storage resources," *Proc. Annu. Hawaii Int. Conf. Syst. Sci.*, vol. 2016-March, pp. 2456–2465, 2016, doi: 10.1109/HICSS.2016.307.

[56] T. Kerdphol, F. S. Rahman, M. Watanabe, and Y. Mitani, *Virtual Inertia Synthesis and Control*. 2020.

VIII. BIOGRAPHIES

Claysius Dewanata Widjaja (S'19) received his B.Sc degree in electrical power engineering from Institut Teknologi Bandung, Indonesia in 2020. Currently he is working towards the M.Sc degree in renewable energy in the marine environment under Department of Electric Power Engineering, Norwegian University of Science and Technology (NTNU), Trondheim, Norway under the Erasmus Mundus scholarship from the European Union.

He worked as a Power System Engineer in PLN UIP2B (Indonesian Java-Bali Grid's TSO) and Quadran Energi Rekayasa, an energy and electricity consulting company back in Indonesia. His current research interests are in power systems dynamics and stability, power systems optimisation, machine learning application for power systems and renewable energy, and applications of power electronics in future power systems.

Mr. Widjaja is registered under The Indonesian Power Engineers Association, and published several international level IEEE proceedings in power systems, high voltage, and renewable energy.

Mohammad Amin (Senior Member, IEEE) received the B.Sc. degree in electrical and electronic engineering from the Chittagong University of Engineering and Technology, Bangladesh, in 2008, the M.Sc. degree in electric power engineering from the Chalmers University of Technology, Sweden, in 2011, and the Ph.D. degree in engineering cybernetics from the Norwegian University of Science and Technology, Trondheim, Norway, in 2017.,From 2008 to 2013, he was with the Department of Electrical and Electronic Engineering, International Islamic University Chittagong, Chittagong, Bangladesh. In 2015, he was a Ph.D. Visiting Scholar with Wind Power Research Center, Shanghai Jiao Tong University, Shanghai, China. From 2017 to 2019, he was a Senior Research Associate with the Department of Electrical and Computer Engineering, Illinois Institute of Technology, Chicago, IL, USA. He is currently an Associate Professor with the Department of Electric Power Engineering, Norwegian University of Science and Technology. His research interests include power electronics application to power system, application of artificial intelligence in power electronics system, robust integration of wind and solar energy, high voltage direct current (HVDC) transmission, microgrid, smart grids, and robust control theory for power electronics system. He was the recipient of the 2018 IEEE JESTPE First Prize Paper Award from IEEE Power Electronics Society and The 2020 Premium Award for Best Paper in IET Generation, Transmission & Distribution.

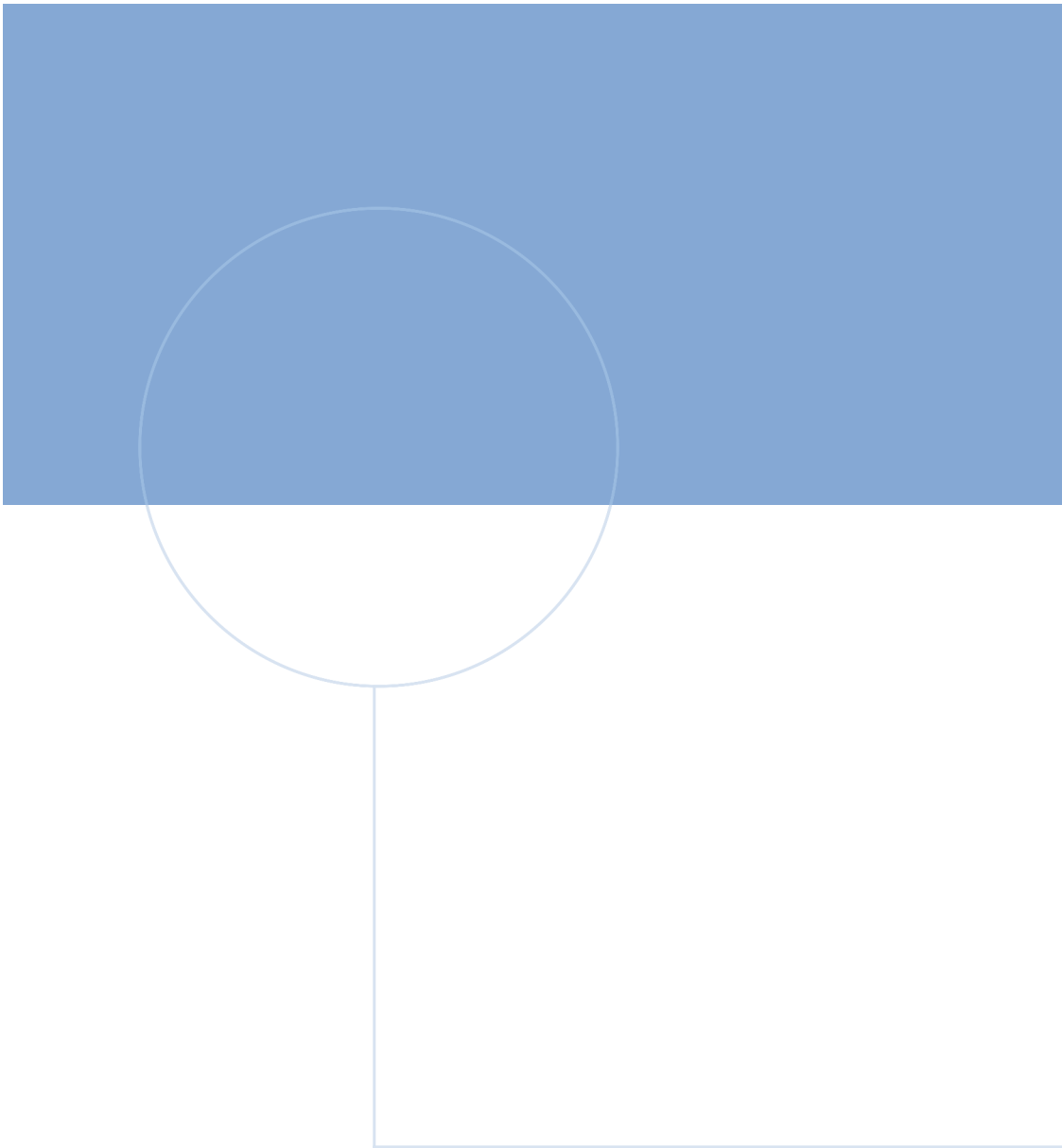

NTNU

Norwegian University of
Science and Technology